4-16-2021

Studies of the rectification behavior of the PDT ligand and the active site of MsrP

Laura J. Ingersol
University of New Mexico - Main Campus

Laura Jane Ingersol

Candidate

Chemistry

Department

This dissertation is approved, and it is acceptable in quality and form for publication:

Approved by the Dissertation Committee:

Martin Kirk

, Chairperson

Christopher Johnston

Brian Gold

Mark Walker

Studies of the rectification behavior of the PDT ligand and

the active site of MsrP

by

Laura Jane Ingersol

B.A. Biology Chemistry, University of Colorado at Colorado

Springs, 2011

M.S. Biomedical Sciences, University of New Mexico, 2014

DISSERTATION

Submitted in Partial Fulfillment of the
Requirements for the Degree of
Doctor of Philosophy

Chemistry

The University of New Mexico
Albuquerque, New Mexico
May, 2021

Studies of the rectification behavior of the PDT ligand and the active site of MsrP

by

Laura Jane Ingersol

B.A. Biology Chemistry, University of Colorado at Colorado Springs, 2011

M.S. Biomedical Sciences, University of New Mexico, 2014

Submitted in Partial Fulfillment of the Requirements for the Degree of Doctor of Philosophy Chemistry

Abstract

Molybdenum (Mo) is an essential element that plays an important role in global nitrogen, carbon, and sulfur cycles with a critical role in human metabolism and ecological balance. It becomes catalytically active when complexed with the pyranopterin dithiolene ligand (PDT), forming the nearly ubiquitous molybdenum cofactor (Moco). The complex biosynthetic pathway of Moco, its presence in all three domains of life, and its role as a constituent cofactor in the last universal common ancestor (LUCA) all point toward the importance of the PDT in the development of life on Earth. Molybdoenzymes catalyze the two-electron oxidation or reduction of substrates that is usually coupled to an oxygen atom transfer. The PDT adopts several tautomeric and oxidation states in proteins, and this has been suggested to contribute to enzyme function through its ability to facilitate redox

reactions by acting as an electron transfer conduit or a mediator of the enzyme redox potential.

In the following studies, the role of the PDT in electron transfer and catalysis is investigated. In the first of these studies, the potential role of the PDT as a directional electron transfer conduit during catalysis is assessed; in this, we have provided the first evidence that the PDT can function as biological unimolecular rectifier. Unimolecular rectifiers were first proposed by Aviram and Ratner over 40 years ago, but true rectification has been difficult to achieve, with RRs rarely exceeding 10. Our results indicate that the PDT can achieve RRs ~2-10, depending upon the tautomeric/oxidation state of the ligand and its relative connectivity to the electrodes. These results may elucidate how directional electron transfer is achieved in a biological system.

In the second of these studies, we sought an explanation for the conflicting crystallographic, kinetic, and spectroscopic data that has been published on the *E. coli* molybdoenzyme, MsrP. This enzyme functions as a periplasmic methionine sulfoxide reductase to “rescue” proteins damaged by oxidative stress from reactive chlorine species (RCS). The originally proposed active site of *as-isolated* MsrP, assigned by X-ray crystallography, is at odds with published spectroscopic data, and has led to the formulation of an unusual catalytic mechanism, in which the reducing equivalents necessary for catalysis are provided by the PDT ligand and not the metal. This mechanism, if correct, would represent a major paradigm shift from the accepted catalytic mechanisms of all other molybdoenzymes, in which the metal undergoes redox changes to provide the reducing equivalents necessary

for catalysis. In this study, we provide compelling evidence that this mechanism and the originally proposed active site structure of *as-isolated* MsrP is incorrect. We provide evidence that *as-isolated* MsrP represents a thiol-inhibited species and reconciles the conflicting spectroscopic data. Lastly, we propose a new mechanism for the catalytic cycle of MsrP, in which the PDT does not undergo redox changes and the reducing equivalents are provided by Mo.

Table of Contents

Table of Figures

Table of Tables

1. Chapter 1- An overview of molybdoenzymes

This chapter serves as a background of the different families of molybdoenzymes and the postulated role of the highly conserved pyranopterin dithiolene (PDT) ligand in facilitating electron transfer in the catalytic cycles of molybdoenzymes. The ability of the PDT to function as a directional electron transfer (ET) conduit is explored in the first half of this dissertation, necessitating a brief overview of some supporting evidence of this role in molybdoenzymes. The *E. coli* molybdoenzyme, MsrP, is also discussed briefly in terms of how it differs from other known molybdoenzymes. This serves as general background for the second half of this dissertation, in which the electronic structure of MsrP is explored spectroscopically and computationally to explain these differences.

1.1 Molybdenum and the pyranopterin dithiolene ligand

Molybdenum is a trace element essential for most forms of life and the only second-row transition metal found in the active sites of metalloenzymes.[1] These enzymes play critical roles in human health and metabolism, as well as global C, N, and S cycles.[2,3] They also are essential in maintaining ecological balance and in the formation of greenhouse gases; the processes of nitrogen fixation, denitrification, and dissimilatory nitrate reduction to ammonium in bacteria are reliant upon molybdoenzymes.[4] In bacteria, molybdoenzymes are also necessary for detoxification pathways and anaerobic respiration.

With the solitary exception of the nitrogenase enzyme, which utilizes the FeMo-cofactor, all molybdoenzymes possess at least one pyranopterin ene-1,2-dithiolate (PDT or MPT = molybdopterin) ligand; this arrangement forms a cofactor known as Moco.[2,5] The Mo ion is ligated by the PDT through the sulfur donors of a dithiolene chelate connected to a pyran ring; the pyran ring is fused to the heterocyclic pterin portion of the molecule, which consists of a pyrimidine fused to either a piperazine or pyrazine ring, depending upon the oxidation state of the pterin, as seen in Figure 1-1. The pyranopterin may be modified by the addition of a dinucleotide attached to the phosphate group in bacterial molybdoenzymes; a notable exception is the bacterial enzyme MsrP, which is the only known *E.coli* molybdoenzyme terminated by a H atom at this position, consistent with other members of the SO family of molybdoenzymes.[1,6,7] The orientation of the chelated PDT with respect to the apical oxo is stereospecific for the XO and SO families of molybdoenzymes, as seen in Figure 1-1.[8]

Molybdoenzymes commonly utilize catalytic cycles in which the oxidation state of the metal cycles between Mo(IV), Mo(V), and Mo(VI).[1] This redox cycling facilitates the oxidation or reduction of a particular substrate, which is usually coupled to either a formal oxygen atom transfer (OAT) or an oxidative hydroxylation.[9] Redox cycling between the Mo(IV) and Mo(VI) oxidation states facilitates the two-electron oxidation or reduction of the substrate; the catalytically competent active site is regenerated by two sequential one-electron transfers, with a Mo(V) state acting as an obligatory intermediate species. The Mo(V) catalytic intermediate is a paramagnetic d^1 species which has enabled the study of the electronic structures

of various molybdoenzymes using magnetic spectroscopies, including electron paramagnetic resonance (EPR) and magnetic circular dichroism (MCD) spectroscopies.[10–12] The use of synthetic models of the active sites of molybdoenzymes have provided further insight into the electronic structures of enzymes which possess chromophores such as hemes, flavins, and iron-sulfur clusters that complicate the use of direct spectroscopic techniques on the enzymes themselves.[13]

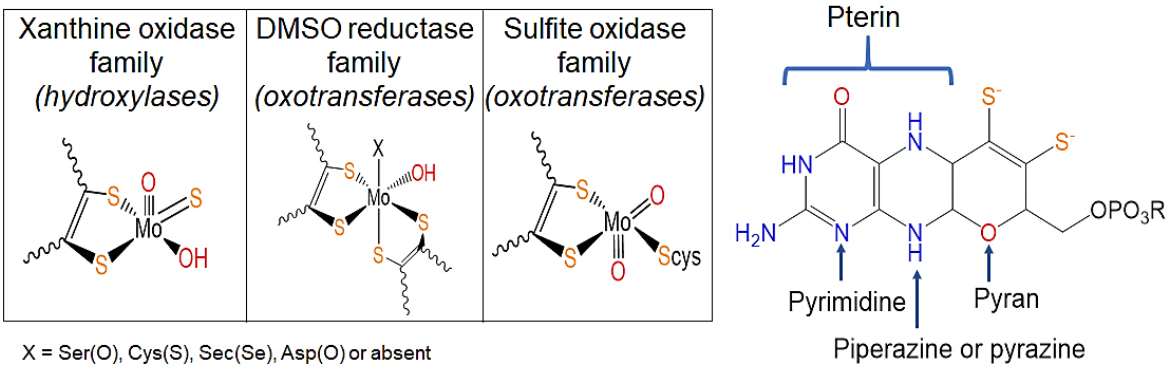

Figure 1-1 Molybdoenzyme active sites. The orientation of the apical oxo is pointed "down" in SO family enzymes and "up" in XO family enzymes, with respect to the orientation of the PDT ligand relative to the apical oxo. Members of the DMSOR family are coordinated by two PDT ligands, termed proximal and distal. The PDT ligand itself (shown on right) consists of a tricyclic structure that coordinates to Mo via its two dithiolene sulfurs.

1.2 Mononuclear molybdoenzyme families

Mononuclear molybdoenzymes are classified into three different families according the type of reactions they catalyze and the protein fold: the xanthine oxidase (XO), sulfite oxidase (SO), and dimethyl sulfoxide (DMSO) reductase (DMSOR) families.[1,2,14] DMSOR family enzymes, found in prokaryotes, are notable in that the Mo is coordinated by two PDT ligands, referred to as either

proximal or distal based upon their relative proximity to an Fe-S cluster referred to as FS0. These enzymes can serve as terminal reductases of a wide variety of substrates in the absence of oxygen as a more efficient alternative to energy generation via fermentation pathways.[15]

Eukaryotes only have five molybdoenzymes, two from the XO family which are aldehyde oxidase (AOX) and xanthine oxidoreductase/dehydrogenase (XOR/XDH), and three from the SO family, which are nitrate reductase (NR), sulfite oxidase (SO), and moonlighting enzyme mitochondrial Amidoxime Reducing Component (mARC).[16] Of these enzymes, only NR is absent from mammals; in plants, fungi, and algae, NO is critical for nitrate assimilation.[16,17] XOR enzymes catalyze hydroxylation reactions which are essential in the purine degradation pathway and are implicated in the maintenance of human health and metabolism.[18] Human AOX, mainly expressed in the liver, is necessary for the metabolism of drugs and xenobiotics.[19,20] The recently discovered mARC enzyme is critical for the reduction of *N*-hydroxylated substances and is thought to play a role in the detoxification of DNA-base analogs and the processing of amidoxime prodrugs.[21–24] SO oxidizes sulfite to sulfate, which is the final step in the degradation pathway of sulfur-containing amino acids.[25,26]

Deficiency in either SO or Moco in humans leads to progressive neurological damage resulting from high levels of sulfite; the symptoms, which include seizures and loss of muscle tone, usually manifest within a week of birth and is fatal shortly thereafter.[25,26] Deficiencies in the other molybdoenzymes in humans is not fatal. XOR enzyme deficiency may lead to a buildup of xanthine in muscle tissue and

kidneys, which may lead to the formation of xanthine stones in some patients.[25] There are no pathologies associated with deficiency in mARC of AOX in humans.

1.3 An evolutionarily ancient metallocofactor

The presence of Moco in bacteria, archaea, and eukaryota can be traced back to the last common universal ancestor (LUCA), from which all modern life on Earth descended.[27] There have been more than 50 molybdoenzymes discovered which possess the Moco cofactor, most of which are found in prokaryotes.[2,28] The evolutionary conservation and nearly ubiquitous presence of Moco in molybdoenzymes is indicative of the critical role that the PDT ligand plays in enzymatic function, although the role of the PDT is not yet fully understood. In addition to the presence of the PDT ligand in molybdoenzymes, enzymes possessing tungsten (W) complexed to the conserved PDT ligand in the active site have also been discovered in mostly thermophilic and hypo-thermophilic organisms that are obligate anaerobes.[29] As LUCA likely arose from hydrothermal vents in oceans, the hot, anaerobic environment make it likely that tungsten was first utilized by early organisms.[27–29] Tungsten complexes have lower reduction potentials than the corresponding molybdenum complexes and tungsten was likely more bioavailable, as tungsten sulfides are more water-soluble.[28,29] The Great Oxygenation Event (GOE) made the use of molybdenum in enzymes more favorable, as tungsten compounds tend to be oxygen sensitive and molybdenum oxides are generally more water-soluble than molybdenum sulfides.[28] As modern tungsten enzymes are not within the scope of this dissertation, they will not be further discussed here.

Molybdenum is predominately found in nature in the form of molybdate, $[MoO_4]^{2-}$, in ocean water at concentrations of ~105nM, making it the most abundant transition metal found in the ocean.[30,31]Molybdate is a highly bioavailable form of molybdenum and both prokaryotes and eukaryotes have efficient molybdate transporters to facilitate uptake. Bacteria and archaea both utilize an ATP-binding cassette (ABC) transport system to uptake molybdate into cells.[32–34] While molybdate uptake is less well understood in eukaryotes, high affinity molybdate transporters have been discovered in eukaryotes as well, including a molybdate transporter shared by both humans and algae (MOT2) and another found in plants (MOT1).[35,36]

1.4 Biosynthesis of Moco

Molybdenum itself is inactive until it is complexed to the PDT ligand as Moco.[34] The biosynthetic pathway for Moco and its insertion into apoenzymes is highly evolutionarily conserved. There are no pathways for the recycling of Moco or its precursors and therefore Moco must be synthesized *de novo* from molybdate.[37,38] There are four steps and six gene products leading to the biosynthesis of the cofactor; homologous genes involved in this process are found in humans, plants, fungi, and bacteria.[31,34,38,39] Briefly, the steps (Figure 1-2) consist of the conversion of GTP to cyclic pyranopterin monophosphate (cPMP), the subsequent adenylation and addition of two sulfurs to form MPT, the transfer of Mo to MPT to form Moco, and the insertion of Moco into the apoenzyme, which is catalyzed by the cleavage of the adenylate group.[34,38,40] For members of the bacterial DMSOR family of molybdoenzymes, two Moco subunits combine to create the final cofactor,

as these enzymes possess two PDT ligands chelated to Mo.[41] Bacterial molybdoenzymes are distinguished from those from eukaryotes by the addition of nucleotides such as CMP or GMP to the phosphate group of the final cofactor, with the notable exception of MsrP, which possesses the form of the PDT cofactor common to the eukaryotic SO family of molybdoenzymes.[6,41]

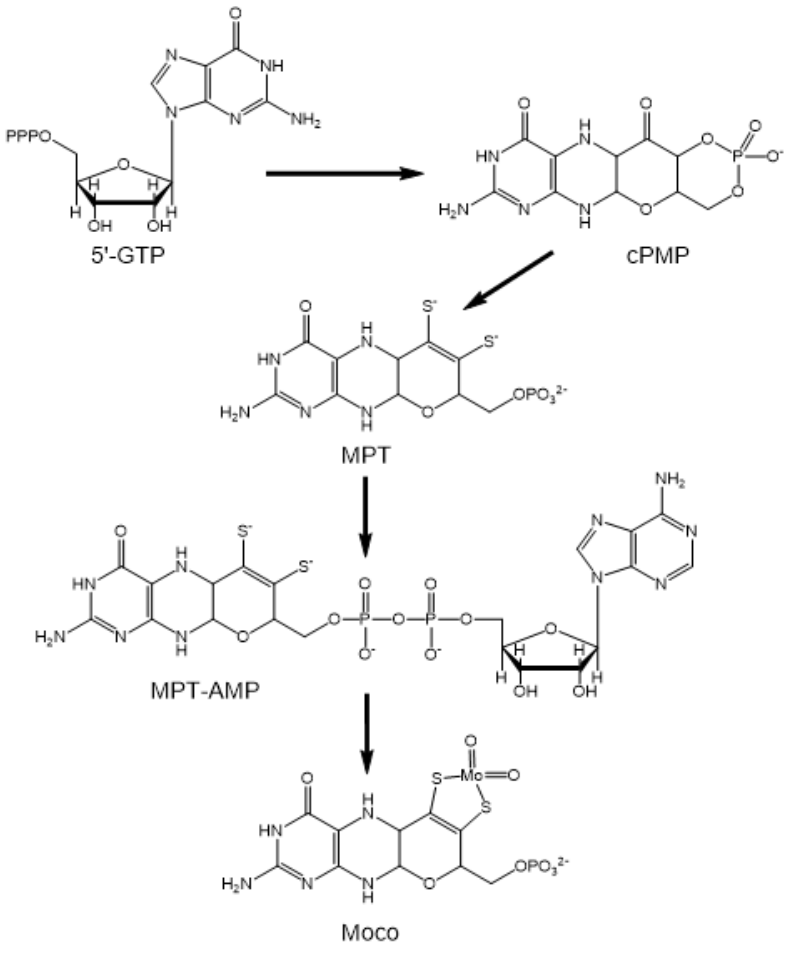

Figure 1-2 Moco biosynthetic pathway

1.5 Postulated roles of the PDT

The role of the conserved PDT ligand in catalysis is unclear. Several possibilities have been proposed, including anchoring the metal within the active site through a series of hydrogen bonds between the ligand and protein structure, modulating the redox potential of Mo, and acting as an electron transfer conduit so the enzyme active site can be regenerated following catalysis.[42–48] It has also been hypothesized to be the source of the two electrons used to reduce the substrate during the catalytic cycle of the *E. coli* enzyme,

MsrP.[49] The two electrons necessary for the reduction or oxidation of substrates by molybdoenzymes are normally accounted for by Mo(IV)/Mo(V)/Mo(VI) redox cycling, and with the exception of MsrP, oxidization state changes on the PDT during catalysis have not usually been suggested in proposed mechanisms.[49] However, the PDT ligand itself is capable of adopting alternative oxidation and tautomeric states and is potentially redox active, theoretically capable of providing four redox equivalents.[1,50] The pterin portion of the PDT is capable of assuming three different oxidation states which are interconvertible through two electron, two proton transfers: the fully reduced tetrahydro, a semi-reduced dihydro, and a fully oxidized pterin, as seen in Figure 1-3.[50] The dihydro form can theoretically assume several tautomeric forms, including the quinoid dihydro form and a dihydro that features an opened pyran ring.[51–54] Studies have sought to assign an oxidation state to the PDT in rat liver sulfite oxidase and bovine milk xanthine oxidase, but a

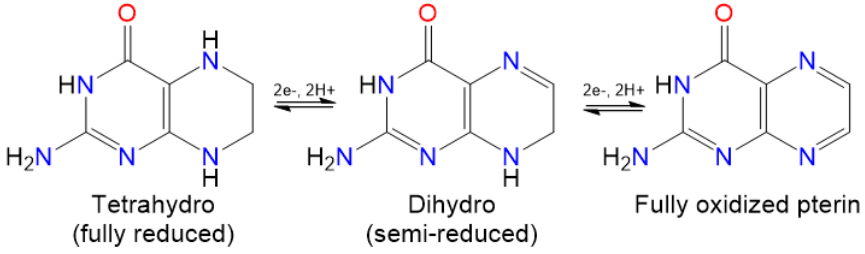

Figure 1-3. Redox states of the pterin

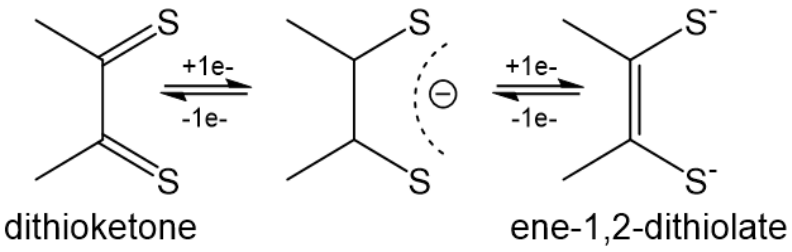

Figure 1-4. Dithiolene redox states

definitive assignment proved inconclusive due to contradictory conclusions presented by the authors.[55–57]

The dithiolene portion of the PDT ligand itself is capable of supplying 2e-, which in addition to the 4e- possessed by the fully reduced tetrahydro pterin, poises the PDT ligand to be capable of dramatic non-innocent redox behavior (Figure 1-4).[1,58] The dithiolene fold angle, defined as the angle between the planes formed by Mo bound by the two dithiolene sulfurs and the S-C=C-S of the remainder of the dithiolene fragment, is thought to contribute to reactivity and charge transfer between the metal and ligand by modulating the relative overlap of the S p and Mo d orbitals, as seen in Figure 1-5.[43,59] The fold angle contributes to "electronic buffering" of the relative electron density changes on Mo that accompany redox[91].[60] There are a range of dithiolene fold angles, from ~6.6-7.0° for SO to 18.2-33.1° for oxidized DMSO, that have been observed via X-ray crystal structures of molybdoenzymes, but definitive assignment of the oxidation states of the Mo and PDT are confounded by the low resolutions of the structures, which prevent the direct observation of hydrogen atoms, and autoreduction by X-ray radiation.[15,54,61–71] The fold angle in metallic dithiolene complexes is known to vary based upon the relative occupancy of the metal d-orbital in the equatorial plane, with d^0 molecules displaying a larger degree of folding than d^1 and d^2 electron configurations, which allows donation of electron density from the filled S_{π} orbitals of the dithiolene to the empty M_{ip} orbital.[63,72–74] The degree of metal-sulfur covalency due to the fold angle is attributed to a pseudo-Jahn-Teller effect, which permits the mixing of LMCT states into the ground state; this effect is strongly

dependent upon the d-electron count and therefore, doubly occupied M_{ip} orbitals show a decreased fold angle and a decrease in metal-sulfur covalency compared to a singly occupied or unoccupied M_{ip} orbital.[71] This effect is also thought to help stabilize metals with a d^1 electron configurations, such as the obligatory Mo(V) intermediate in the catalytic cycles of nearly every molybdoenzyme, providing a low energy pathway for the one-electron oxidation and geometric rearrangement necessary to regenerate the catalytically competent active site.[72,75] A study of various oxomolybdenum dithiolene fold angles concluded an average fold angle of ~12.5°; in enzymes, the fold angle may be dynamically dependent upon the relative oxidation states of both Mo and the PDT ligand and may serve to help stabilize the metal center at different d electron configurations.[59,75–77]

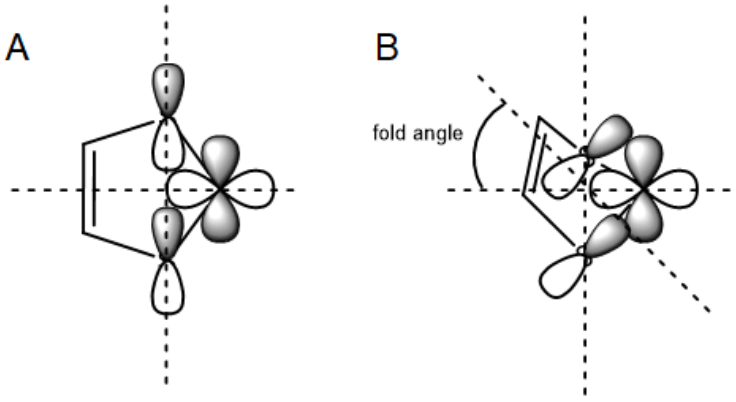

Figure 1-5. Depiction of the relative overlap between the two dithiolene S p orbitals and the Mo in-plane d orbital. A planer fold angle creates orthogonal p and d orbitals with no overlap (A). When the fold angle is increased, due to structural changes which may be influenced by the relative oxidation state of both metal and ligand, the S p orbitals begin to overlap with the Mo d orbital (B), facilitating charge transfer between orbitals and promoting non-innocent redox behavior of the PDT ligand.

The PDT is one of the most complex and electronically labile ligands in all of biology. It adopts several distinct geometries, characteristic of different families of

molybdoenzymes, that may correspond to different oxidation and tautomeric states.[48] Unfortunately, the direct study of the Moco cofactor outside of the enzyme environment is complicated by its rapid degradation to its stable, oxidized derivatives.[2,50,78] Recently, a detailed conformational analysis of 319 pyranopterins in 102 different Mo and W containing enzymes, characterized by X-ray crystallography, was performed.[48] The distortions of the pyranopterins in mononuclear Mo/W enzymes were compared to electronic structure calculations performed on the fully reduced tetrahydro and oxidized 10,10a dihydro and quinoid dihydro PDT structures. In this study, the PDT conformations in the X-ray crystal structures could be described by a well-defined distortion coordinate which encompassed conformations expected for quinoid dihydro, tetrahydro, and 10,10a dihydro PDT oxidation states (Figure 1-6). The evidence alludes to a critical relationship between PDT conformation and enzyme function, since specific distortions correlated to the protein fold for each enzyme family (SUOX, XDH, DMSOR, AOR families). The relationship between pyranopterin conformation and oxidation state provided the first structural evidence indicating that enzyme bound pyranopterins may exist in both tetrahydro and dihydro forms, with implications for the importance of PDT oxidation/tautomeric state in aiding catalysis in different

Mo/W enzyme families.

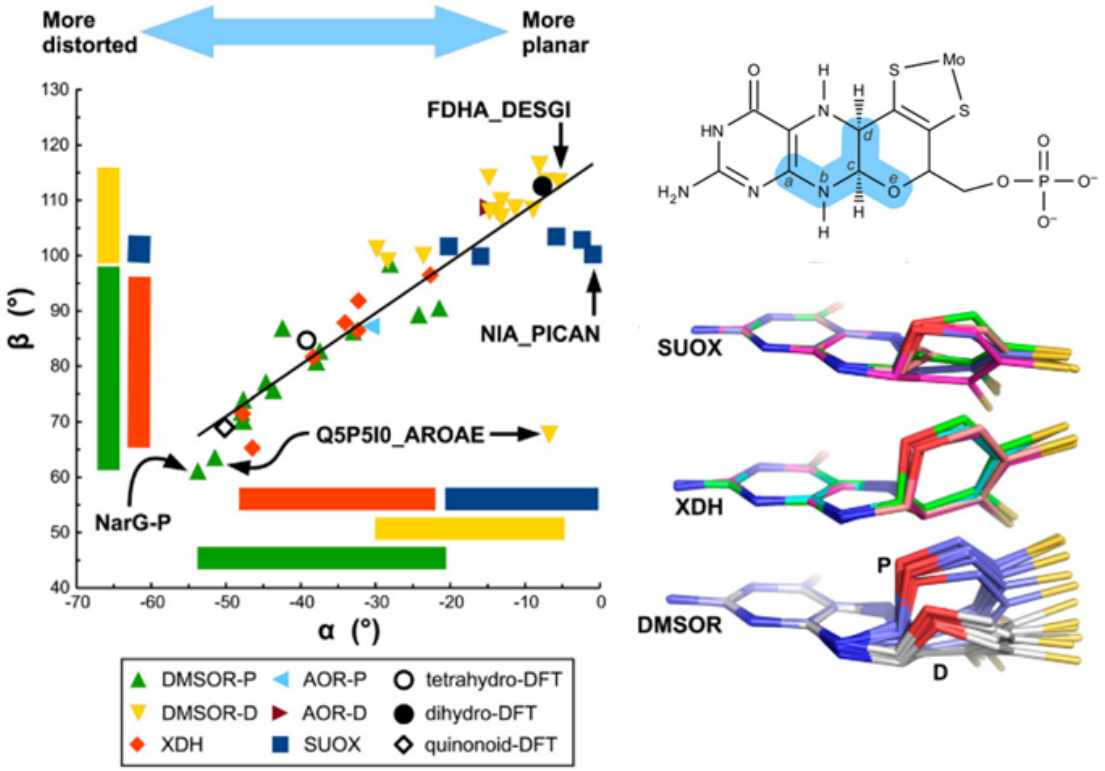

Figure 1-6. Distortion coordinate comparing PDT distortions from X-ray crystal structures of different molybdoenzyme families to those computed by DFT for the tetrahydro, 10,10a dihydro, and quinoid dihydro PDT states. The distortions are characterized by α and β angles, defined as the angles formed by atoms a-b-c-d and a-b-c-e, respectively. Shown at bottom right are the distortions from different molybdoenzymes superimposed on each other, categorized by family. Figure adapted from Rothery, R., et al. Proc. Natl. Acad. Sci. ***2012****, 109 (37), 14773–14778.*

Hydrogen bonding contacts between the protein and the PDT ligand may serve to stabilize oxidation states and geometric distortions which may be essential to enzymatic activity. A conserved Lys in the SO family is thought to play a role in maintaining PDT geometry within the active site by bridging the phosphate group off of the pyran ring with the pyrimidine ring of the PDT (Figure 1-7).[47] The relative importance of this distortion is not understood but mutation of the conserved Lys to Arg in human sulfite oxidase (SO) causes enzymatic deficiency, indicating that

the characteristic distortions of the PDT in SO family enzymes may play an indispensable role in catalysis.[48,79] The presence of a "bridging" residue, either a His or Arg, is conserved in DMSOR family enzymes, links the N-5 atoms of the piperazine rings on the proximal and distal PDT ligands (Figure 1-8).[47] The bridging residue is thought to facilitate direct electronic communication between the two PDT ligands; the relative charge donation between the ligands could be influenced by protonation state of His, which has a side chain pK_a that is close to neutral.[47,80] These enzymes also possess a "stabilizing" residue, either a His, Gln, or Ser, which H-bonds with the N-5 atom on the proximal PDT ligand; this is hypothesized to function to stabilize the presumed tetrahydro oxidation state of the PDT and prevent its oxidation into a dihydro form.[47,48]

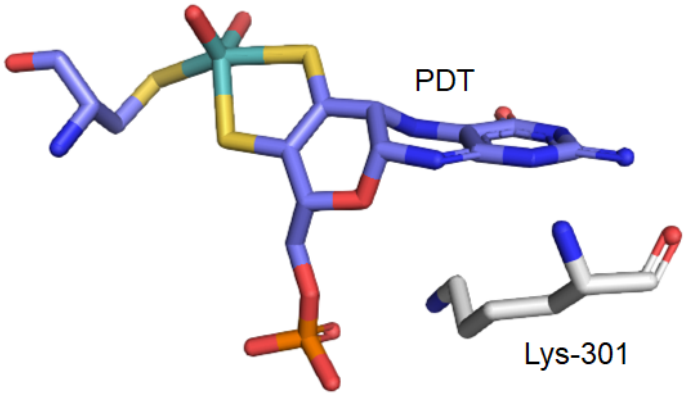

Figure 1-7. Crystal structure of chicken liver sulfite oxidase (PDB 1SOX).[90] A conserved Lys in SO family enzymes maintains the PDT distortion within the active site by bridging the phosphate group off of the pyran ring with the pyrimidine ring of the PDT.

The contacts between the PDT ligand and the protein may facilitate the postulated role of the PDT as an electron transfer conduit. In molybdoenzymes possessing the SUOX-fold, a conserved His in close proximity to the N-5 atom of the piperazine ring of the PDT, and a conserved Tyr that is positioned between the piperazine

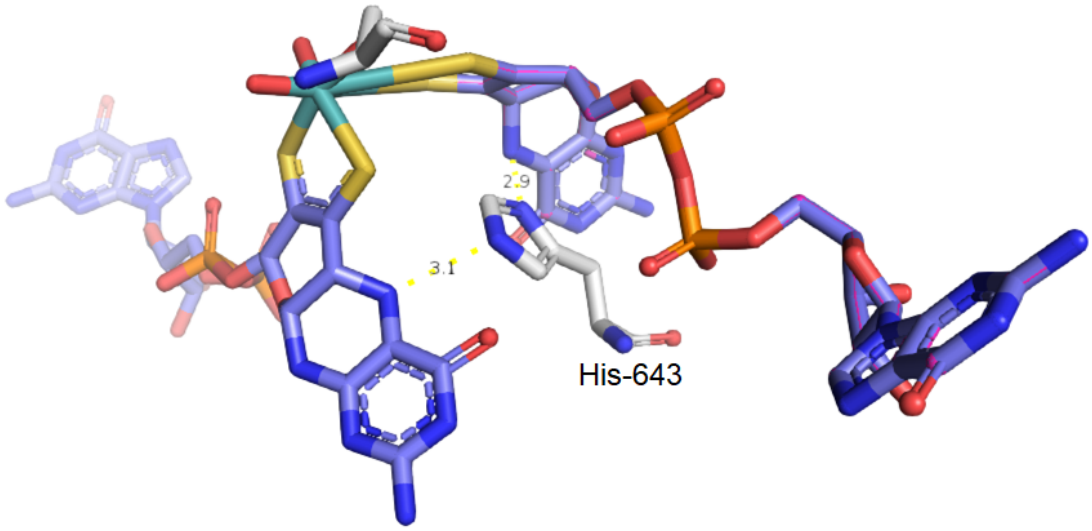

Figure 1-8. Crystal structure of DMSO reductase from R. capsulatus (PDB ID 1DMS).[9146,52] *A conserved His links the N-5 atoms of the piperazine rings on the proximal and distal PDT ligands and is thought to facilitate direct electronic communication between the two PDT ligands.*

ring and the substrate binding site is critical to catalysis.[81–83] It has been speculated that the positioning of these residues might form a charge transfer pathway to facilitate the deprotonation step in the oxidation of sulfite; these residues are absent in the SUOX-fold containing MsrP, which could partially explain why sulfite is not a substrate for this molybdoenzyme.[6,47] Conserved residues that link the PDT to other redox active centers in molybdoenzymes provide further evidence that the PDT can act as an electron transfer conduit. Within the DMSOR family, a conserved Arg positioned between a [4Fe-4S] cluster and the proximal PDT has been demonstrated as being essential for electron transfer in *E. coli* DmsABC and NarGHI.[61,84,85]

The idea that the non-innocent PDT ligand can undergo dynamic oxidation/tautomeric state changes to facilitate catalysis has been postulated by several groups. It has been speculated that the proximal PDT ligand in periplasmic nitrate reductase NapAB functions as an electron transfer conduit linking Mo to a nearby [4Fe-4S] cluster and that this process is facilitated by reversible cyclization of the pyran ring and oxidation state changes on the pterin, which modulates the exchange coupling between Mo and the [4Fe-4S] cluster.[86] The formation and tautomerization of an open ring form of the distal PDT in *E. coli* nitrate reductase A (NarGHI) is thought to be stabilized by two nearby His residues (His-1163 and His-1184), which form a postulated charge transfer relay; this charge transfer relay is speculated to help modulate the reduction potential of Mo and stabilize the obligatory Mo(V) catalytic intermediate (Figure 1-9).[46,52] In *E. coli* MsrP, an unusual catalytic cycle was presented in which the two redox equivalents are provided by redox cycling of the PDT ligand between the fully reduced tetrahydro and semi-

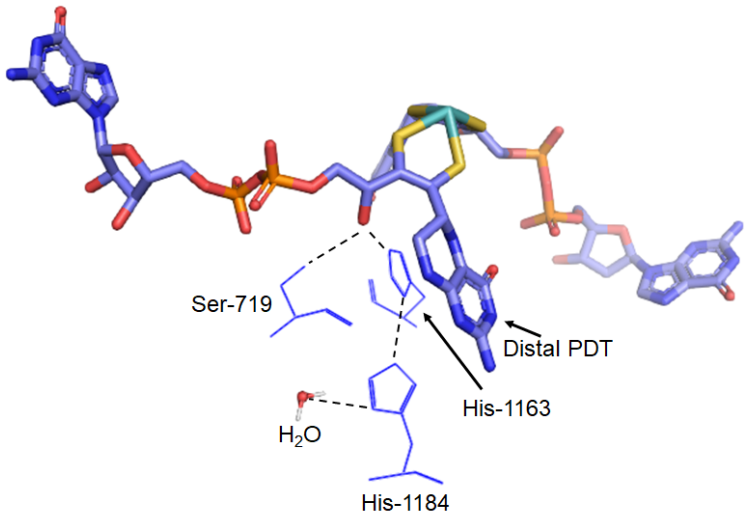

Figure 1-9. Postulated charge transfer relay in E. coli nitrate reductase A (NarGHI), PDB 1Q16. The distances between Ser-719 and His-1163 and the O of the opened pyran ring on the distal PDT are 2.0Å and 1.8Å, respectively.[46,52] The distance between His-1163 and His-1184 is 2.1Å.

reduced 10,10a dihydro oxidation states, while the metal remained in the Mo(IV) oxidation state throughout.[49] This proposed catalytic cycle represented a departure from the accepted catalytic cycles of all other Moco-containing molybdoenzymes, in which the metal redox cycles between the Mo(IV)/Mo(V)/Mo(VI) oxidation states during catalysis.

In xanthine oxidoreductase (XOR) family enzymes, the amino terminus of the pterin ring of the PDT ligand is positioned in close proximity to the first of two spinach ferredoxin type [2Fe-2S] clusters (Figure 1-10).[62] In these enzymes, the active site is regenerated through two sequential one-electron transfers from Mo to the [2Fe-2S] clusters, these electrons are then funneled to FAD and the terminal e- acceptors O_2 or NAD+.[1,2,62] The positioning of the presumed tetrahydro PDT between Mo and Fe/S I provides strong evidence that the non-innocent ligand may function as a directional electron transfer conduit.[48,62] At pH 8.5, the reduction potential difference between the Mo(VI)/Mo(V) and Fe/S I couples are ~40mV, which only provides a driving force of 0.9 kcal/mol to favor the reduction of Fe/S I.[87] The low

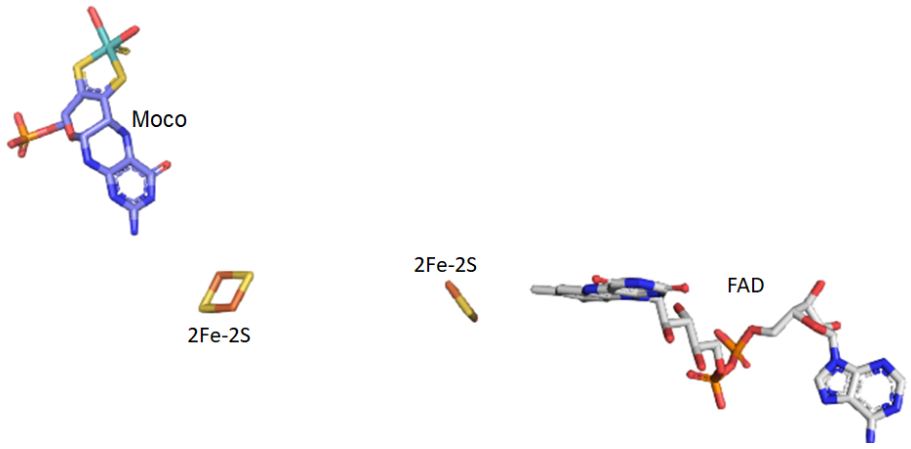

Figure 1-10. Electron transfer pathway in bovine milk xanthine oxidase (PDB 1FIQ).[62] Reducing equivalents are shuttled from the Moco active site to two spinach ferredoxin type [2Fe-2S] clusters and then to FAD and the terminal electron acceptor to regenerate the Mo active site.

driving force for ET between Mo and Fe/S I may necessitate rectification behavior from the PDT to promote the shuttling of reducing equivalents from Mo to regenerate the catalytically competent active site. It is the potential rectification behavior of the PDT that is of particular interest to us and is explored in detail in the first part of this dissertation.

A resonance Raman (rR) study of xanthine oxidase (XO) and xanthine dehydrogenase (XDH) provided evidence of PDT involvement in catalysis.[88] In this study, the one-electron oxidation of Mo(VI) to Mo(V) was linked to PDT vibrational distortions, indicating that ET in these enzymes is accompanied by geometric distortions of the PDT ligand and lending credibility to the hypothesized role of the PDT as a directional ET conduit. The involvement of the PDT in regeneration of the active site is further evidenced by the observed enhancement of low-frequency vibrations that involve PDT distortions that are linked to the one-electron oxidation of Mo in the active site of xanthine dehydrogenase (XDH).[44]

In the first part of this dissertation, the concept of directional electron transfer through the PDT ligand is explored computationally in order to assess its potential role as an electron transfer conduit during the regeneration of the active site of molybdoenzymes. We assess the ability of the PDT to function as a unimolecular rectifier as a function of oxidation state and tautomeric form and relate this to the proposed design criteria for unimolecular rectifiers delineated by Van Dyck and Ratner.[89] In the second part, the use of various spectroscopies, including EPR and XAS, is applied to resolve previously published and conflicting electronic structural data for the unusual molybdoenzyme MsrP from *E. coli*. We provide evidence that

the original interpretation of the crystal structure and the previously proposed mechanism of catalysis is incorrect, and we propose a new active site structure and mechanism based upon our results.

1.6 References

(1) Kirk, M. L.; Stein, B. *Molybdenum Enzymes*; Elsevier Ltd., 2013. https://doi.org/10.1016/B978-0-08-097774-4.00316-8.

(2) Hille, R. The Mononuclear Molybdenum Enzymes. *Chemical Reviews* **1996**, *96*, 2757–2816. https://doi.org/10.1021/cr950061t.

(3) Wang, D. Redox Chemistry of Molybdenum in Natural Waters and Its Involvement in Biological Evolution. *Frontiers in Microbiology* **2012**, *3* (DEC), 1–7. https://doi.org/10.3389/fmicb.2012.00427.

(4) Kraft, B.; Strous, M.; Tegetmeyer, H. E. Microbial Nitrate Respiration - Genes, Enzymes and Environmental Distribution. *Journal of Biotechnology* **2011**, *155* (1), 104–117. https://doi.org/10.1016/j.jbiotec.2010.12.025.

(5) Einsle, O.; Tezcan, F. A.; Andrade, S. L. a; Rees, D. C. Nitrogenase MoFe-Protein At. **2002**, *3123* (1988), 16–21.

(6) Loschi, L.; Brokx, S. J.; Hills, T. L.; Zhang, G.; Bertero, M. G.; Lovering, A. L.; Weiner, J. H.; Strynadka, N. C. J. Structural and Biochemical Identification of a Novel Bacterial Oxidoreductase. *The Journal of biological chemistry* **2004**, *279* (48), 50391–50400. https://doi.org/10.1074/jbc.M408876200.

(7) Mendel, R. R. The Molybdenum Cofactor. *Journal of Biological Chemistry* **2013**, *288* (19), 13165–13172. https://doi.org/10.1074/jbc.R113.455311.

(8) Schwarz, G.; Mendel, R. R. Molybdenum Cofactor Biosynthesis and Molybdenum Enzymes. *Annual Review of Plant Biology* **2006**, *57* (1), 623–647. https://doi.org/10.1146/annurev.arplant.57.032905.105437.

(9) Cerqueira, N. M. F. S. A.; Pakhira, B.; Sarkar, S. Theoretical Studies on Mechanisms of Some Mo Enzymes. *Journal of Biological Inorganic Chemistry* **2015**, *20* (2), 323–335. https://doi.org/10.1007/s00775-015-1237-7.

(10) Brondino, C. D.; Rivas, M. G.; Romão, M. J.; Moura, J. J. G.; Moura, I. Structural and Electron Paramagnetic Resonance (EPR) Studies of Mononuclear Molybdenum Enzymes from Sulfate-Reducing Bacteria. *Accounts of Chemical Research* **2006**, *39* (10), 788–796. https://doi.org/10.1021/ar050104k.

(11) Stein, B. W.; Kirk, M. L. Electronic Structure Contributions to Reactivity in Xanthine Oxidase Family Enzymes. *Journal of biological inorganic chemistry : JBIC : a publication of the Society of Biological Inorganic Chemistry* **2015**, *20* (2), 183–194. https://doi.org/10.1007/s00775-014-1212-8.

(12) Mtei, R. P.; Ganna, L.; Stein Benjamin, Rubie Nick, H. R. and M. L. K. Spectroscopic and Electronic Structure Studies of a DMSO Reductase Caltalytic Intermediate: Implications for Electron and Atom Transfer Reactivity. *Submitted to American Chemical Society* **2011**, 9762–9774. https://doi.org/10.1016/j.biotechadv.2011.08.021.Secreted.

(13) Majumdar, A. Structural and Functional Models in Molybdenum and Tungsten Bioinorganic Chemistry: Description of Selected Model Complexes, Present Scenario and Possible Future Scopes. *Dalton Transactions* **2014**, *43* (24), 8990–9003. https://doi.org/10.1039/c4dt00631c.

(14) Hille, R.; Hall, J.; Basu, P. The Mononuclear Molybdenum Enzymes. *Chemical Reviews* **2014**, *114* (7), 3963–4038. https://doi.org/10.1021/cr400443z.

(15) Kisker, C.; Schindelin, H.; Rees, D. C. MOLYBDENUM-COFACTOR– CONTAINING ENZYMES : Structure and Mechanism. *Annual review of biochemistry* **1997**, *66*, 233–267.

(16) Tejada-Jimenez, M.; Chamizo-Ampudia, A.; Calatrava, V.; Galvan, A.; Fernandez, E.; Llamas, A. From the Eukaryotic Molybdenum Cofactor Biosynthesis to the Moonlighting Enzyme MARC. *Molecules* **2018**, *23* (12). https://doi.org/10.3390/molecules23123287.

(17) Campbell, W. H. NITRATE REDUCTASE STRUCTURE, FUNCTION AND REGULATION: Bridging the Gap between Biochemistry and Physiology. *Annual Review of Plant Physiology and Plant Molecular Biology* **1999**, *50* (1), 277–303. https://doi.org/10.1146/annurev.arplant.50.1.277.

(18) Hille, R. Molybdenum-Containing Hydroxylases. *Archives of Biochemistry and Biophysics* **2005**, *433* (1), 107–116. https://doi.org/10.1016/j.abb.2004.08.012.

(19) Terao, M.; Romão, M. J.; Leimkühler, S.; Bolis, M.; Fratelli, M.; Coelho, C.; Santos-Silva, T.; Garattini, E. Structure and Function of Mammalian Aldehyde Oxidases. *Archives of Toxicology* **2016**, *90* (4), 753–780. https://doi.org/10.1007/s00204-016-1683-1.

(20) Terao, M.; Garattini, E.; Romão, M. J.; Leimkühler, S. Evolution, Expression, and Substrate Specificities of Aldehyde Oxidase Enzymes in Eukaryotes. *Journal of Biological Chemistry* **2020**, *295* (16), 5377–5389. https://doi.org/10.1074/jbc.REV119.007741.

(21) Llamas, A.; Chamizo-Ampudia, A.; Tejada-Jimenez, M.; Galvan, A.; Fernandez, E. The Molybdenum Cofactor Enzyme MARC: Moonlighting or Promiscuous Enzyme? *BioFactors* **2017**, *43* (4), 486–494. https://doi.org/10.1002/biof.1362.

(22) Havemeyer, A.; Bittner, F.; Wollers, S.; Mendel, R.; Kunze, T.; Clement, B. Identification of the Missing Component in the Mitochondrial Benzamidoxime Prodrug-Converting System as a Novel Molybdenum Enzyme. *Journal of Biological Chemistry* **2006**, *281* (46), 34796–34802. https://doi.org/10.1074/jbc.M607697200.

(23) Havemeyer, A.; Lang, J.; Clement, B. The Fourth Mammalian Molybdenum Enzyme MARC: Current State of Research. *Drug Metabolism Reviews* **2011**, *43* (4), 524–539. https://doi.org/10.3109/03602532.2011.608682.

(24) Ott, G.; Havemeyer, A.; Clement, B. The Mammalian Molybdenum Enzymes of MARC. *Journal of Biological Inorganic Chemistry* **2015**, *20* (2), 265–275. https://doi.org/10.1007/s00775-014-1216-4.

(25) Reiss, J.; Hahnewald, R. Molybdenum Cofactor Deficiency: Mutations in GPHN, MOCS1, and MOCS2. *Human Mutation* **2011**, *32* (1), 10–18. https://doi.org/10.1002/humu.21390.

(26) Johnson, J. L.; Coyne, K. E.; Garrett, R. M.; Zabot, M.-T.; Dorche, C.; Kisker, C.; Rajagopalan, K. v. Isolated Sulfite Oxidase Deficiency: Identification of 12 Novel SUOX Mutations in 10 Patients. *Human mutation* **2002**, *20* (1), 74. https://doi.org/10.1002/humu.9038.

(27) Weiss, M. C.; Sousa, F. L.; Mrnjavac, N.; Neukirchen, S.; Roettger, M.; Nelson-Sathi, S.; Martin, W. F. The Physiology and Habitat of the Last Universal Common Ancestor. *Nature Microbiology* **2016**, *1* (9), 1–8. https://doi.org/10.1038/nmicrobiol.2016.116.

(28) Hille, R. Molybdenum and Tungsten in Biology. *Trends in Biochemical Sciences* **2002**, *27* (7), 360–367. https://doi.org/10.1016/S0968-0004(02)02107-2.

(29) Miralles-Robledillo, J. M.; Torregrosa-Crespo, J.; Martínez-Espinosa, R. M.; Pire, C. DMSO Reductase Family: Phylogenetics and Applications of Extremophiles. *International Journal of Molecular Sciences* **2019**, *20* (13). https://doi.org/10.3390/ijms20133349.

(30) Mendel, R. R. The Molybdenum Cofactor. *Journal of Biological Chemistry* **2013**, *288* (19), 13165–13172. https://doi.org/10.1074/jbc.R113.455311.

(31) Schwarz, G.; Mendel, R. R. Molybdenum Cofactor Biosynthesis and Molybdenum Enzymes. *Annual Review of Plant Biology* **2006**, *57* (1), 623–647. https://doi.org/10.1146/annurev.arplant.57.032905.105437.

(32) Self, W. T.; Grunden, A. M.; Hasona, A.; Shanmugam, K. T. Molybdate Transport. *Research in Microbiology* **2001**, *152* (3–4), 311–321. https://doi.org/10.1016/S0923-2508(01)01202-5.

(33) Tomatsu, H.; Takano, J.; Takahashi, H.; Watanabe-Takahashi, A.; Shibagaki, N.; Fujiwara, T. An Arabidopsis Thaliana High-Affinity Molybdate Transporter Required for Efficient Uptake of Molybdate from Soil. *Proceedings of the National Academy of Sciences of the United States of America* **2007**, *104* (47), 18807–18812. https://doi.org/10.1073/pnas.0706373104.

(34) Mendel, R. R. Biology of the Molybdenum Cofactor. *Journal of Experimental Botany* **2007**, *58* (9), 2289–2296. https://doi.org/10.1093/jxb/erm024.

(35) Tejada-Jiménez, M.; Galván, A.; Fernández, E. Algae and Humans Share a Molybdate Transporter. *Proceedings of the National Academy of Sciences of the United States of America* **2011**, *108* (16), 6420–6425. https://doi.org/10.1073/pnas.1100700108.

(36) Demtröder, L.; Narberhaus, F.; Masepohl, B. Coordinated Regulation of Nitrogen Fixation and Molybdate Transport by Molybdenum. *Molecular Microbiology* **2019**, *111* (1), 17–30. https://doi.org/10.1111/mmi.14152.

(37) Reiss, J.; Hahnewald, R. Molybdenum Cofactor Deficiency: Mutations in GPHN, MOCS1, and MOCS2. *Human Mutation* **2011**, *32* (1), 10–18. https://doi.org/10.1002/humu.21390.

(38) Mendel, R. R.; Leimkühler, S. The Biosynthesis of the Molybdenum Cofactors. *Journal of Biological Inorganic Chemistry* **2015**, *20* (2), 337–347. https://doi.org/10.1007/s00775-014-1173-y.

(39) Iobbi-Nivol, C.; Leimkühler, S. Molybdenum Enzymes, Their Maturation and Molybdenum Cofactor Biosynthesis in Escherichia Coli. *Biochimica et Biophysica Acta - Bioenergetics* **2013**, *1827* (8–9), 1086–1101. https://doi.org/10.1016/j.bbabio.2012.11.007.

(40) Rizzi, M.; Schindelin, H. Structural Biology of Enzymes Involved in NAD and Molybdenum Cofactor Biosynthesis. *Current Opinion in Structural Biology* **2003**, *13* (1), 142. https://doi.org/10.1016/s0959-440x(03)00006-x.

(41) Leimkühler, S. The Biosynthesis of the Molybdenum Cofactors in Escherichia Coli. *Environmental Microbiology* **2020**, *22* (6), 2007–2026. https://doi.org/10.1111/1462-2920.15003.

(42) Inscore, F. E.; McNaughton, R.; Westcott, B. L.; Helton, M. E.; Jones, R.; Dhawan, I. K.; Enemark, J. H.; Kirk, M. L. Spectroscopic Evidence for a Unique Bonding Interaction in Oxo-Molybdenum Dithiolate Complexes:

Implications for a Electron Transfer Pathways in the Pyranopterin Dithiolate Centers of Enzymes. *Inorganic Chemistry* **1999**, *38* (7), 1401–1410. https://doi.org/10.1021/ic981126o.

(43) Inscore, F. E.; Knottenbelt, S. Z.; Rubie, N. D.; Joshi, H. K.; Kirk, M. L.; Enemark, J. H. Understanding the Origin of Metal-Sulfur Vibrations in an Oxo-Molybdenum Dithiolene Complex: Relevance to Sulfite Oxidase. *Inorganic Chemistry* **2006**, *45* (3), 967–976. https://doi.org/10.1021/ic0506815.

(44) Dong, C.; Yang, J.; Reschke, S.; Leimkühler, S.; Kirk, M. L. Vibrational Probes of Molybdenum Cofactor-Protein Interactions in Xanthine Dehydrogenase. *Inorganic Chemistry* **2017**, *56* (12), 6830–6837. https://doi.org/10.1021/acs.inorgchem.7b00028.

(45) Gisewhite, D. R.; Yang, J.; Williams, B. R.; Esmail, A.; Stein, B.; Kirk, M. L.; Burgmayer, S. J. N.; Mawr, B.; States, U.; States, U. Implications of Pyran Cyclization and Pterin Conformation on Oxidized Forms of the Molybdenum Cofactor. **2019**, *140* (40), 12808–12818. https://doi.org/10.1021/jacs.8b05777.Implications.

(46) Wu, S. Y.; Rothery, R. a.; Weiner, J. H. Pyranopterin Coordination Controls Molybdenum Electrochemistry in Escherichia Coli Nitrate Reductase. *Journal of Biological Chemistry* **2015**, *290* (41), 25164–25173. https://doi.org/10.1074/jbc.M115.665422.

(47) Rothery, R. a.; Weiner, J. H. Shifting the Metallocentric Molybdoenzyme Paradigm: The Importance of Pyranopterin Coordination. *JBIC Journal of Biological Inorganic Chemistry* **2015**, *20* (2), 349–372. https://doi.org/10.1007/s00775-014-1194-6.

(48) Rothery, R. a.; Stein, B.; Solomonson, M.; Kirk, M. L.; Weiner, J. H. Pyranopterin Conformation Defines the Function of Molybdenum and Tungsten Enzymes. *Proceedings of the National Academy of Sciences* **2012**, *109* (37), 14773–14778. https://doi.org/10.1073/pnas.1200671109.

(49) Adamson, H.; Simonov, a. N.; Kierzek, M.; Rothery, R. a.; Weiner, J. H.; Bond, a. M.; Parkin, a. Electrochemical Evidence That Pyranopterin Redox Chemistry Controls the Catalysis of YedY, a Mononuclear Mo Enzyme. *Proceedings of the National Academy of Sciences* **2015**, *112* (47), 1–6. https://doi.org/10.1073/pnas.1516869112.

(50) Basu, P.; Burgmayer, S. J. N. Pterin Chemistry and Its Relationship to the Molybdenum Cofactor. *Coordination chemistry reviews* **2011**, *255* (9–10), 1016–1038. https://doi.org/10.1016/j.ccr.2011.02.010.

(51) Nieter Burgmayer, S. J.; Pearsall, D. L.; Blaney, S. M.; Moore, E. M.; Sauk-Schubert, C. Redox Reactions of the Pyranopterin System of the Molybdenum Cofactor. *Journal of Biological Inorganic Chemistry* **2004**, *9* (1), 59–66. https://doi.org/10.1007/s00775-003-0496-x.

(52) Bertero, M. G.; Rothery, R. A.; Palak, M.; Hou, C.; Lim, D.; Blasco, F.; Weiner, J. H.; Strynadka, N. C. J. Insights into the Respiratory Electron Transfer Pathway from the Structure of Nitrate Reductase A. *Nature Structural Biology* **2003**, *10* (9), 681–687. https://doi.org/10.1038/nsb969.

(53) Jormakka, M.; Richardson, D.; Byrne, B.; Iwata, S. Architecture of NarGH Reveals a Structural Classification of Mo-BisMGD Enzymes. *Structure* **2004**, *12* (1), 95–104. https://doi.org/10.1016/j.str.2003.11.020.

(54) Kloer, D. P.; Hagel, C.; Heider, J.; Schulz, G. E. Crystal Structure of Ethylbenzene Dehydrogenase from Aromatoleum Aromaticum. *Structure* **2006**, *14* (9), 1377–1388. https://doi.org/10.1016/j.str.2006.07.001.

(55) Gardlik, S.; Rajagopalan, K. v. Oxidation of Molybdopterin in Sulfite Oxidase by Ferricyanide: Effect on Electron Transfer Activities. *Journal of Biological Chemistry* **1991**, *266* (8), 4889–4895.

(56) Gardlik, S.; Rajagopalan, K. v. The State of Reduction of Molybdopterin in Xanthine Oxidase and Sulfite Oxidase. *Journal of Biological Chemistry* **1990**, *265* (22), 13047–13054.

(57) Rajagopalan, K. v.; Kramer, S.; Gardlik, S. Studies on the Oxidation State of Molybdopterin. *Polyhedron* **1986**, *5* (1–2), 573–576. https://doi.org/10.1016/S0277-5387(00)84966-9.

(58) Hine, F. J.; Taylor, A. J.; Garner, C. D. Dithiolene Complexes and the Nature of Molybdopterin. *Coordination Chemistry Reviews* **2010**, *254* (13–14), 1570–1579. https://doi.org/10.1016/j.ccr.2010.01.017.

(59) Joshi, H. K.; Enemark, J. H. Geometrical Control of the Active Site Electronic Structure of Pyranopterin Enzymes by Metal-Dithiolate Folding: Aldehyde Oxidase. *Journal of the American Chemical Society* **2004**, *126* (38), 11784–11785. https://doi.org/10.1021/ja046465x.

(60) Westcott, B. L.; Gruhn, N. E.; Enemark, J. H. Evaluation of Molybdenum-Sulfur Interactions in Molybdoenzyme Model Complexes by Gas-Phase Photoelectron Spectroscopy. The “electronic Buffer” Effect. *Journal of the American Chemical Society* **1998**, *120* (14), 3382–3386. https://doi.org/10.1021/ja972674o.

(61) Rothery, R. A.; Bertero, M. G.; Spreter, T.; Bouromand, N.; Strynadka, N. C. J.; Weiner, J. H. Protein Crystallography Reveals a Role for the FS0 Cluster of Escherichia Coli Nitrate Reductase a (NarGHI) in Enzyme Maturation. *Journal of Biological Chemistry* **2010**, *285* (12), 8801–8807. https://doi.org/10.1074/jbc.M109.066027.

(62) Enroth, C., Eger, B.T., Okamoto, K., Nishino, T., Nishino, T., Pai, E. F. . Crystal Structures of Bovine Milk Xanthine Dehydrogenase and Xanthine Oxidase: Structure-Based Mechanism of Conversion. *PNAS* **2000**, *97* (20), 10723–10728. https://doi.org/10.1002/zaac.19040380133.

(63) Joshi, H. K.; Cooney, J. J. a; Inscore, F. E.; Gruhn, N. E.; Lichtenberger, D. L.; Enemark, J. H. Investigation of Metal-Dithiolate Fold Angle Effects: Implications for Molybdenum and Tungsten Enzymes. *Proceedings of the National Academy of Sciences of the United States of America* **2003**, *100* (7), 3719–3724. https://doi.org/10.1073/pnas.0636832100.

(64) Li, H. K.; Temple, C.; Rajagopalan, K. v.; Schindelin, H. The 1.3A Crystal Structure of Rhodobacter Sphaeroides Dimethyl Sulfoxide Reductase Reveals Two Distinct Molybdenum Coordination Environments. *Journal of the American Chemical Society* **2000**, *122* (32), 7673–7680. https://doi.org/10.1021/ja000643e.

(65) Schneider, F.; Löwe, J.; Huber, R.; Schindelin, H.; Kisker, C.; Knäblein, J. Crystal Structure of Dimethyl Sulfoxide Reductase from Rhodobacter Capsulatus at 1.88 Å Resolution. *Journal of Molecular Biology* **1996**, *263* (1), 53–69. https://doi.org/10.1006/jmbi.1996.0555.

(66) Czjzek, M.; dos Santos, J. P.; Pommier, J.; Giordano, G.; Méjean, V.; Haser, R. Crystal Structure of Oxidized Trimethylamine N-Oxide Reductase from Shewanella Massilia at 2.5 Å Resolution. *Journal of Molecular Biology* **1998**, *284* (2), 435–447. https://doi.org/10.1006/jmbi.1998.2156.

(67) Kubitza, C.; Bittner, F.; Ginsel, C.; Havemeyer, A.; Clement, B.; Scheidig, A. J. Crystal Structure of Human MARC1 Reveals Its Exceptional Position among Eukaryotic Molybdenum Enzymes. *Proceedings of the National Academy of Sciences of the United States of America* **2018**, *115* (47), 11958–11963. https://doi.org/10.1073/pnas.1808576115.

(68) Ellis, P. J.; Conrads, T.; Hille, R.; Kuhn, P. Crystal Structure of the 100 KDa Arsenite Oxidase from Alcaligenes Faecalis in Two Crystal Forms at 1.64 Å and 2.03 Å. *Structure* **2001**, *9* (2), 125–132. https://doi.org/10.1016/S0969-2126(01)00566-4.

(69) Dias, J. M.; Than, M. E.; Humm, A.; Huber, R.; Bourenkov, G. P.; Bartunik, H. D.; Bursakov, S.; Calvete, J.; Caldeira, J.; Carneiro, C.; Moura, J. J. G.; Moura, I.; Romão, M. J. Crystal Structure of the First Dissimilatory Nitrate Reductase at 1.9 Å Solved by MAD Methods. *Structure* **1999**, *7* (1), 65–79. https://doi.org/10.1016/S0969-2126(99)80010-0.

(70) Boyington, J. C.; Gladyshev, V. N.; Khangulov, S. v.; Stadtman, T. C.; Sun, P. D. Crystal Structure of Formate Dehydrogenase H: Catalysis Involving Mo, Molybdopterin, Selenocysteine, and an Fe4S4 Cluster. *Science* **1997**, *275* (5304), 1305–1308. https://doi.org/10.1126/science.275.5304.1305.

(71) Stein, B. W.; Yang, J.; Mtei, R.; Wiebelhaus, N. J.; Kersi, D. K.; Lepluart, J.; Lichtenberger, D. L.; Enemark, J. H.; Kirk, M. L. Vibrational Control of Covalency Effects Related to the Active Sites of Molybdenum Enzymes. *Journal of the American Chemical Society* **2018**, *140* (44), 14777–14788. https://doi.org/10.1021/jacs.8b08254.

(72) Wiebelhaus, N. J.; Cranswick, M. A.; Klein, E. L.; Lockett, L. T.; Lichtenberger, D. L.; Enemark, J. H. Metal-Sulfur Valence Orbital Interaction Energies in Metal-Dithiolene Complexes: Determination of Charge and Overlap Interaction Energies by Comparison of Core and Valence Ionization Energy Shifts. *Inorganic Chemistry* **2011**, *50* (21), 11021–11031. https://doi.org/10.1021/ic201566n.

(73) Cooney, J. J. A.; Cranswick, M. A.; Gruhn, N. E.; Joshi, H. K.; Enemark, J. H. Electronic Structure of Bent Titanocene Complexes with Chelated Dithiolate Ligands. *Inorganic Chemistry* **2004**, *43* (25), 8110–8118. https://doi.org/10.1021/ic049207+.

(74) Lauher, J. W.; Hoffmann, R. Structure and Chemistry of Bis(Cyclopentadienyl)-MLn Complexes. *Journal of the American Chemical Society* **1976**, *98* (7), 1729–1742. https://doi.org/10.1021/ja00423a017.

(75) Cranswick, M. A.; Dawson, A.; J. Cooney, J. A.; Gruhn, N. E.; Lichtenberger, D. L. ; E. J. Photoelectron Spectroscopy and Electronic Structure Calculations of D1 Vanadocene Compounds with Chelated Dithiolate Ligands: Implications for Pyranopterin Mo/W Enzymes. *Inorg Chem. 2007* **2007**, *46* (25), 10639–10646. https://doi.org/10.1038/jid.2014.371.

(76) Yang, J.; Mogesa, B.; Basu, P.; Kirk, M. L. Large Ligand Folding Distortion in an Oxomolybdenum Donor–Acceptor Complex. *Inorganic Chemistry* **2015**, *2*, acs.inorgchem.5b02252. https://doi.org/10.1021/acs.inorgchem.5b02252.

(77) Inscore, F. E.; Joshi, H. K.; McElhaney, A. E.; Enemark, J. H. Remote Ligand Substituent Effects on the Properties of Oxo-Mo(V) Centers with a Single Ene-1,2-Dithiolate Ligand. *Inorganica Chimica Acta* **2002**, *331* (1), 246–256. https://doi.org/10.1016/S0020-1693(01)00817-9.

(78) Johnson, J. L.; Rajagopalan, K. v. Structural and Metabolic Relationship between the Molybdenum Cofactor and Urothione. *Proceedings of the National Academy of Sciences of the United States of America* **1982**, *79* (22 I), 6856–6860. https://doi.org/10.1073/pnas.79.22.6856.

(79) Rajapakshe, A.; Tollin, G.; Enemark, J. H. Kinetic and Thermodynamic Effects of Mutations of Human Sulfite Oxidase. *Chemistry and Biodiversity*. September 2012, pp 1621–1634. https://doi.org/10.1002/cbdv.201200010.

(80) Li, H.; Robertson, A. D.; Jensen, J. H. Very Fast Empirical Prediction and Rationalization of Protein PK a Values. *Proteins: Structure, Function and Genetics* **2005**, *61* (4), 704–721. https://doi.org/10.1002/prot.20660.

(81) Raitsimring AM, Astashkin AV, F. C. et al. Studies of the Mo(V) Center of the Y343F Mutant of Human Sulfite Oxidase by Variable Frequency Pulsed EPR Spectroscopy. *Inorganica Chim Acta.* **2008**, *361* (4), 941–946. https://doi.org/10.1016/j.immuni.2010.12.017.Two-stage.

(82) Kappler, U.; Bailey, S.; Feng, C.; Honeychurch, M. J.; Hanson, G. R.; Bernhardt, P. v.; Tollin, G.; Enemark, J. H. Kinetic and Structural Evidence for the Importance of Tyr236 for the Integrity of the Mo Active Site in a Bacterial Sulfite Dehydrogenase. *Biochemistry* **2006**, *45* (32), 9696–9705. https://doi.org/10.1021/bi060058b.

(83) Feng, C.; Wilson, H. L.; Hurley, J. K.; Hazzard, J. T.; Tollin, G.; Rajagopalan, K. v.; Enemark, J. H. Role of Conserved Tyrosine 343 in Intramolecular Electron Transfer in Human Sulfite Oxidase. *Journal of Biological Chemistry* **2003**, *278* (5), 2913–2920. https://doi.org/10.1074/jbc.M210374200.

(84) Rothery, R. A.; Trieber, C. A.; Weiner, J. H. Interactions between the Molybdenum Cofactor and Iron-Sulfur Clusters of Escherichia Coli Dimethylsulfoxide Reductase. *Journal of Biological Chemistry* **1999**, *274* (19), 13002–13009. https://doi.org/10.1074/jbc.274.19.13002.

(85) Tang, H.; Rothery, R. A.; Voss, J. E.; Weiner, J. H. Correct Assembly of Iron-Sulfur Cluster FS0 into Escherichia Coli Dimethyl Sulfoxide Reductase (DmsABC) Is a Prerequisite for Molybdenum Cofactor Insertion. *Journal of Biological Chemistry* **2011**, *286* (17), 15147–15154. https://doi.org/10.1074/jbc.M110.213306.

(86) Jacques, J. G. J.; Fourmond, V.; Arnoux, P.; Sabaty, M.; Etienne, E.; Grosse, S.; Biaso, F.; Bertrand, P.; Pignol, D.; Léger, C.; Guigliarelli, B.; Burlat, B. Reductive Activation in Periplasmic Nitrate Reductase Involves Chemical Modifications of the Mo-Cofactor beyond the First Coordination Sphere of the Metal Ion. *Biochimica et Biophysica Acta - Bioenergetics* **2014**, *1837* (2), 277–286. https://doi.org/10.1016/j.bbabio.2013.10.013.

(87) Porras, A. G., and Palmer, G. The Room Temperature Potentiometry of Xanthine Oxidase. **1982**, *257* (19), 11617–11626.

(88) Dong, C.; Yang, J.; Leimkühler, S.; Kirk, M. L. Pyranopterin Dithiolene Distortions Relevant to Electron Transfer in Xanthine Oxidase/Dehydrogenase. *Inorganic Chemistry* **2014**, *53* (14), 7077–7079. https://doi.org/10.1021/ic500873y.

(89) Van Dyck, C.; Ratner, M. a. Molecular Rectifiers: A New Design Based on Asymmetric Anchoring Moieties. *Nano Letters* **2015**, *15* (3), 1577–1584. https://doi.org/10.1021/nl504091v.

(90) Kisker, C.; Schindelin, H.; Pacheco, A.; Wehbi, W. A.; Garrett, R. M.; Rajagopalan, K. v.; Enemark, J. H.; Rees, D. C. Molecular Basis of Sulfite Oxidase Deficiency from the Structure of Sulfite Oxidase. *Cell* **1997**, *91* (7), 973–983. https://doi.org/10.1016/S0092-8674(00)80488-2.

(91) Schneider, F.; Löwe, J.; Huber, R.; Schindelin, H.; Kisker, C.; Knäblein, J. Crystal Structure of Dimethyl Sulfoxide Reductase from Rhodobacter Capsulatus at 1.88 Å Resolution. *Journal of Molecular Biology* **1996**, *263* (1), 53–69. https://doi.org/10.1006/jmbi.1996.0555.

2. Chapter 2 - An Ancient Metallocofactor Exemplifies Molecular Rectifier Design Principles

Prior computational investigations into synthetic unimolecular rectifiers resulted in the Van Dyck/Ratner design 'rules', in which efficiency of rectification is modulated by manipulating the energy of frontier orbitals through which transmission occurs relative to the Fermi level (E_F) of metallic electrodes.[1] These rules are explained in depth in a later section (Section 2.3). In this study, we investigated the application of these 'rules' to a biological molecule postulated to function as an electron transfer conduit in molybdoenzymes: the pyranopterin dithiolene (PDT) ligand. This chapter serves as a general background with some of our results on unimolecular rectification.

2.1 Synthetic unimolecular rectifiers

Synthetic unimolecular rectifiers inspired by biological electron transfer processes have been of interest for decades in the quest to miniaturize electronic circuits.[2–4] The concept of continuously shrinking silicon semiconductor transistors so that every two years the number of transistors per chip doubles is known as "Moore's Law" and poses a serious issue as there is a physical limit that silicon transistors can shrink.[5] However, the development of single molecule circuits could allow the continuation of the quest to miniaturize electronics, which can increase computing speed by making the electronic components closer together.[6] While silicon transistors may not be able to be readily shrunk below ~50nm, molecules ranging

in size between 0.5 and 3 nm would permit electronics to be miniaturized beyond the limitations of silicon-based semiconductor devices.

A unimolecular rectifier permits the flow of current in one direction and acts as an insulator against current flow in the opposite direction.[7] For this to occur, the molecule must be asymmetric in nature; a highly efficient unimolecular rectifier will be capable of passing large currents in a single direction only with minimal current flow in the opposite direction. These molecules have historically been designed as an electron donor (D) fragment and an electron acceptor fragment (A) which are joined by a bridging fragment which is either saturated (σ) or conjugated (π).

2.2 Aviram and Ratner model of unimolecular rectification

This concept was first proposed by Aviram and Ratner in 1974, who proposed a D-σ-A molecule as a prototype for the design of a synthetic molecular rectifier based upon properties of p-n junctions, so that a unimolecular rectifier can have the same functionality as semiconductors.[8] The A portion of the molecule is relatively electron poor (p-type) and the D electron rich (n-type); this was achieved by adding electron withdrawing or electron donating substituents on the backbone of the A and D molecular fragments. The bridge fragment is necessary to separate these D and A fragments, for without this insulator group, the inherent D and A properties of the fragments would create a single donor level; in this case, a single molecular wavefunction spanning the entire molecule would change energetically under an applied bias, but rectification would be unlikely to occur particularly if this wavefunction mixes strongly with the metallic electrode states on both electrodes. The Aviram and Ratner prototype consisted of a tetrathiofulvalene (TTF) donor and

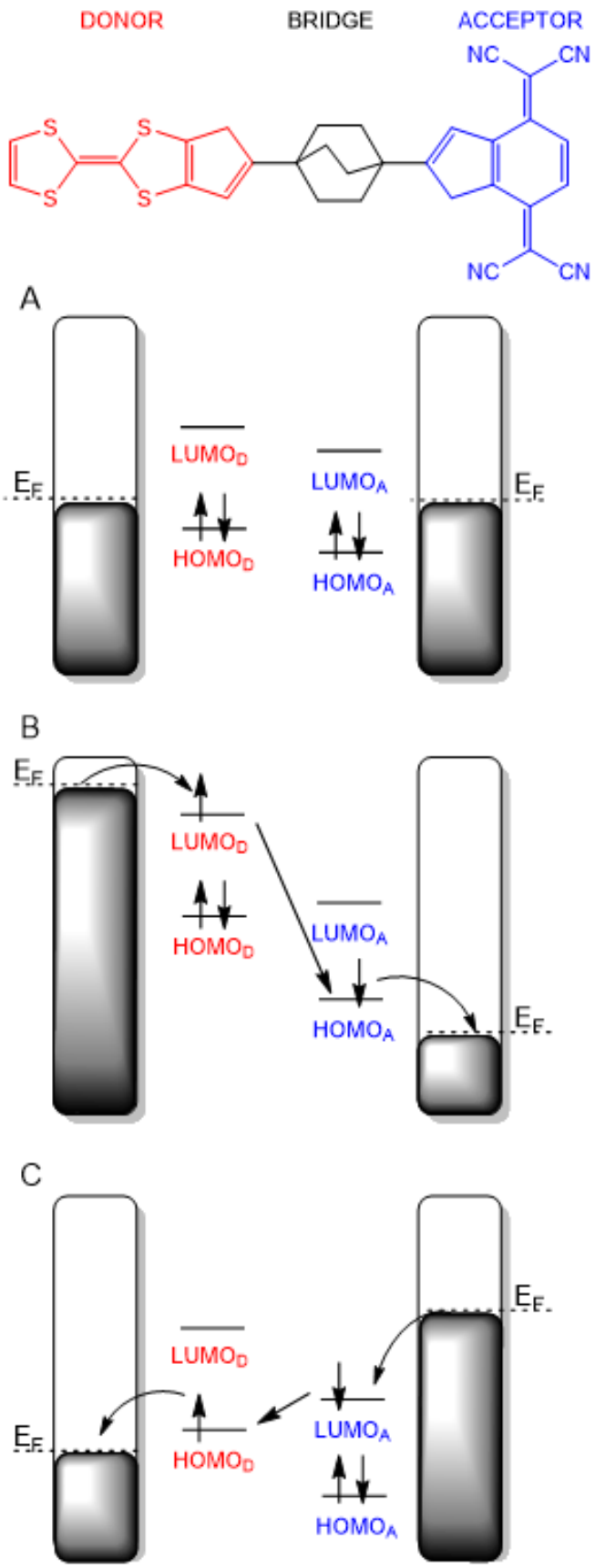

a tetracyanoquinodimethane (TCNQ) acceptor separated by a σ-bridging fragment consisting of three methylene (-CH2-) groups, chosen for its insulator properties as well as its contribution to the overall rigidity of the molecular construct; but their work was purely theoretically and this molecule was not actually synthesized.

Figure 2-1. Original proposed unimolecular rectifier and associated rectification mechanism by Aviram and Ratner.[8] Energy level diagrams under no applied bias (A), under negative bias (B), and positive bias (C) show the energies of the frontier molecular orbitals of the donor (D) and acceptor (A) fragments relative to that of the electrodes. Application of a bias voltage changes the electrochemical potentials of the left and right electrodes; the E_F of the electrodes shifts with the electrochemical potential. The difference between the E_F of the left and right electrodes under bias is known as the bias window, which is represented by the shaded region. Only orbitals within the bias window can

When the molecule is complexed to the electrodes the rectification behavior through the molecule is dependent upon the energies of the HOMO of the D and the LUMO of the A relative to the energy levels of the two electrodes; the HOMO and LUMO levels of the D are at higher energies than those of the A because of the lower oxidation potential and lower electron affinity of the D fragment (Figure 2-1A).[7] Furthermore, the Aviram/Ratner design makes it imperative that the HOMO(D) and LUMO(A) are localized on their respective fragments, which is why the presence of an insulating bridge between the two fragments is necessary.

When a bias is applied to the system, the energies of the orbitals and electrodes change (Figure 2-1B and C).[8] The E_F of the electrodes represents the electrochemical potential of the electrodes and lies between the filled and empty metallic states. [9] The relationship between bias voltage and the electrochemical potentials of the electrodes is written as

$$V = \frac{(\mu_R - \mu_L)}{e},$$

where V is the bias voltage and μ_R and μ_L are the electrochemical potentials of the right and left electrodes, respectively. The application of a bias voltage (V) shifts the electrochemical potentials of the right and left electrodes away from their zero-bias bulk E_F, which causes the opening of a bias window, which is defined as the electrochemical potential difference between the left and right electrodes. Therefore, at zero-bias, no bias window exists because the E_F of the right and left electrodes is the bulk value, and therefore equivalent. The bias window defines the energy range by which e- transport and current flow can occur.[10] Since the e-

transport takes place through the molecular orbitals (MOs) of the molecular bridge, only MOs within the bias window can contribute to conduction.

For the Aviram-Ratner model, upon the application of a positive bias (Figure 2-1C), the HOMO from the D fragment ($HOMO_D$) aligns energetically with the anode E_F and e- move from the HOMO to the anode, leaving a hole behind.[8] The hole is backfilled by the LUMO of the A fragment ($LUMO_A$), which draws e- from the cathode, to which it is energetically aligned. The e- transport from the cathode to $LUMO_A$ can only occur if $LUMO_A$ lies energetically below E_F of the cathode to which the A fragment is attached. Similarly, the $HOMO_D$ can only transport e- to the anode if the bias voltage applied exceeds the ionization potential of the D fragment. Aviram and Ratner proposed that upon the reversal of bias, a far greater bias would need to be applied to bring the E_F of the cathode energetically above the level of the LUMO of the D fragment ($LUMO_D$), since the $LUMO_D$ and $HOMO_D$ both lie at greater energies than those of the A fragment (Figure 2-1B). Thus, a rectifying effect would take place and the preferred direction of current flow would be from the A fragment to the D fragment.

2.3 Ellenbogen and Love model of unimolecular rectification

The proposed mechanism of electron transport from A to D in donor/bridge/acceptor molecules by Aviram and Ratner was contrasted by the proposed mechanism by Ellenbogen and Love in 2000, who hypothesized that electron transport from D to A in a donor/bridge/acceptor molecule would be more favorable due to the alignment of the $HOMO_D$ with the $LUMO_A$.[11] This alignment would create a conductive channel that spanned the length of the molecular bridge,

allowing conduction as long as the HOMO and LUMO are in resonance with each other within the bias window.

However, when a donor/saturated bridge/acceptor molecule of similar design to that proposed by Ellenbogen and Love was computationally assessed for its ability to be an effective rectifier by Stokbro *et al,* it was shown that it was ineffective.[12] This molecule consisted of two phenylene-ethynylene fragments, one substituted with an amino group (D fragment) and the other a nitro side group (A fragment); the D and A fragments were joined by a saturated dimethylene bridge. The molecule was anchored to gold electrodes via thiol groups. Upon the application of an external bias, the energetic alignment of the HOMO and LUMO shifted in energy until they aligned at the same energy at a specific applied voltage, forming a delocalized resonant state across the molecule to facilitate conduction. This HOMO/LUMO alignment occurred at both forward and reverse bias, which provided an excellent conducting channel through the molecule but made the proposed molecule a poor rectifier, as the conducting channel formed at both forward and reverse bias. The study by Ellenbogen and Love, and the later computational work by Stokbro *et al.*, demonstrated that the HOMO-LUMO gap decreases upon the application of an external bias and this property could potentially be exploited by designing rectifiers with small, intrinsic HOMO-LUMO gaps, such that an efficient delocalized resonant state can form under lower applied biases. These studies underscored the need to use computational work to screen promising candidates for unimolecular rectification, as well as highlighting

the importance of the energetic alignment of the frontier molecular orbitals in both facilitating conduction and improving rectification.

2.4 Orbital "rule" of molecular conduction

For effective e- transport using the molecular orbitals of D and A fragments, the orbitals must be within the bias window, which is formed by the difference in the electrochemical potentials of the filled levels of the left and right electrodes.[13–16] As a bias is applied and the orbital energies change, a former LUMO may become filled if it is energetically lower than the filled levels of the electrode connected to the corresponding molecular fragment, or a former HOMO may become empty if it is energetically higher than the filled levels of the electrode.

Computational studies on benzene, naphthalene, phenanthrene, and anthracene dithiolate derivatives complexed to gold electrodes have shown that the phase, amplitude and special distribution of the frontier molecular orbitals influences electron transport in electrode/molecule/electrode junctions.[17–19] These studies used Hückel MO theory to develop an orbital "rule" for electron transport through these π-conjugated molecules using a Green's function approach. The conductance increases with the zeroth Green's function that describes the propagation of a tunneling electron from sites r to s on the molecule. This can be written as

$$G_{rs}^{0}(E_F) = \frac{C_{rHOMO}C_{sHOMO}^{*}}{E_F - \varepsilon_{HOMO} \pm i\eta} + \frac{C_{rLUMO}C_{sLUMO}^{*}}{E_F - \varepsilon_{LUMO} \pm i\eta},$$

where C_{rHOMO} is the coefficient of the HOMO at position r, C^*_{sHOMO} is the coefficient of the HOMO at position s, C_{rLUMO} is the coefficient of the LUMO at position r, C^*_{sLUMO} is the coefficient of the LUMO at position s, E_F is the Fermi energy of the corresponding electrode, $i\eta$ is an infinitesimal number that is derived from the imaginary part of Green's function and the local density of states (LDOS). The stars ($*$) refer to the alternate carbons in π-conjugated molecules. This equation relates the offset in energy of the frontier molecular orbitals from the E_F of their adjacent electrode, which is the electrode that binds either the donor or

acceptor fragment. The closer the frontier MOs are to the E_F of the adjacent electrode, the more efficient the transport through the device. In this sense, orbitals that lie at energies far below, or far above, the E_F of the adjacent electrodes are not expected to contribute to conduction through the molecule. The coefficients in the numerator refer to the amplitude and phase (denoted by sign) of the orbital wavefunction at that position. The positions r and s refer to atoms at either end of the molecule and define the electron transport path. For efficient conduction, the product of the phase of the coefficients on r and s must be negative for the LUMO

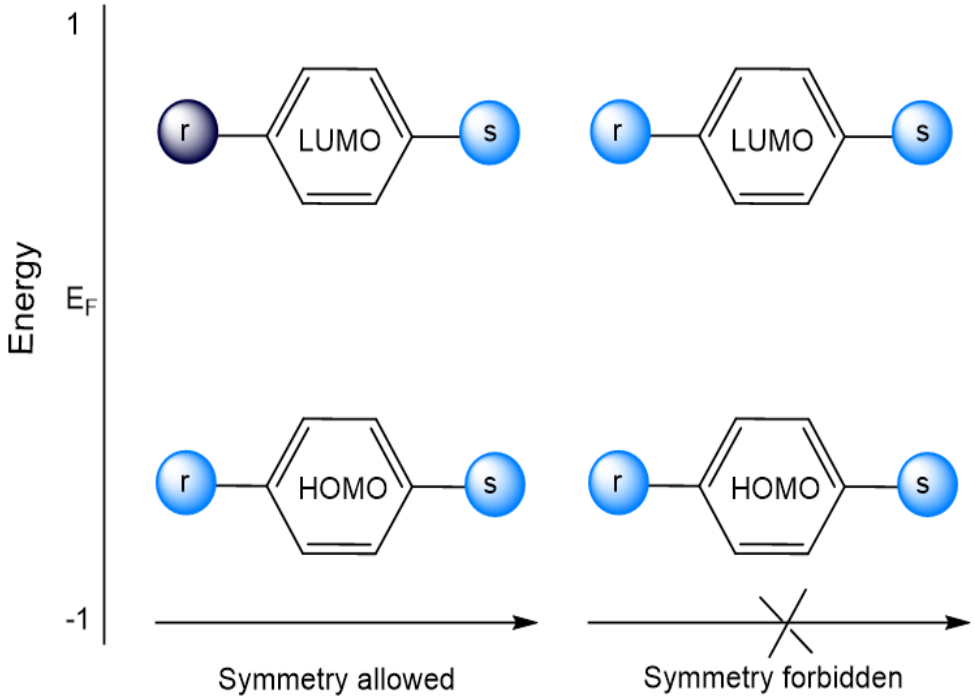

Figure 2-2. Scheme of orbital "rule" of molecular conduction. LUMO lies at energy above the E_F and the HOMO below; the E_F is located at the midpoint of the LUMO and HOMO energies in this system (this is not always the case). The phases and amplitudes of the frontier MOs are indicated on sites r and s of the molecule. When the sign of the product of the phases on sites r and s on the LUMO is different than that of the HOMO, symmetry allowed conduction through the molecule can occur, due to the additive effect on the zeroth Green's function. When the product of the phases on sites r and s are the same for the LUMO and HOMO, the value of the zeroth Green's function decreases and conduction through the molecule decreases. This scenario represents a symmetry forbidden pathway.

and positive for the HOMO. This is because the LUMO resides at positive energy relative to the E_F and the HOMO at negative energy so that when the product of the coefficients of the LUMO are negative and those of the HOMO are positive, the overall equation is positive and the conduction increases significantly with the zeroth Green's function, as shown in Figure 2-2. The amplitude of the wavefunction on r and s should be as large as possible in both the HOMO and LUMO to provide an efficient conduction channel. The geometry of how the molecule is anchored to the electrodes is also critically important in creating an efficient conduction channel; it was shown that the *para*-isomer of benzenedithiol had stronger contact with the gold electrodes, leading to broadening of the transmission peaks compared to the *meta*-isomer.[17]

It should be noted that this orbital "rule" is applicable only when the coupling between the electrodes and molecule is weak, the Fermi level (E_F) is at the midgap between HOMO and LUMO levels and there is electron-hole symmetry in both the orbital energies and MO expansion coefficients.[17] However, it can broadly be applied to other systems as a way to think about the creation of a delocalized resonance state across the molecule using HOMO-LUMO coupling to facilitate coherent electron transport, much like the model proposed by Ellenbogen and Love and Stokbro *et al.*, and how the coupling geometry between electrode and molecule can greatly impact the formation of a conducting molecular channel.[11,12]

2.5 Limitations of unimolecular electronics

The Aviram and Ratner unimolecular rectifier consisted of a donor and acceptor fragment that were separated by a saturated σ-bridge fragment.[8] However, it was

quickly realized that this design would not necessarily be the best for incorporating into molecular electronic devices, as conduction through the saturated component would be attenuated, which could lead to device overheating and long saturated σ-bridges would cause limitations to the ability to miniaturize circuits.[20] To circumvent these issues, other types of unimolecular rectification designs have been explored, particularly ones with different bridge fragment designs. One solution would be to achieve rectification using a shorter σ-bridge. A donor/bridge/acceptor unimolecular rectifier consisting of the weak donor and acceptor fragments of hemibiquinones (HBQs) decoupled by a bridge fragment consisting of a single σ bond was shown to achieve a surprisingly large RR of 160 at ±2.5V, due to the twist angle of the bridge that decoupled the frontier molecular orbitals and caused them to localize on the donor and acceptor fragments.[20]

Asymmetrical bridge fragments have also been explored as well, which can also influence the efficiency of rectification by the relative orientation of the bridge fragment with respect to the donor and acceptor fragments. One such example was the use of an amide bond as a bridging unit between a terpyridyl group bound to Mn and an acetylacetonate group bound to a TiO_2 surface; rectification of one isomer with the amide bond oriented one way was poor, while switching the orientation of the amide bond vastly increased molecular rectification.[21] This effect was attributed to the influence the amide orientation had on both the charge distribution and energetic alignment of the LUMO, which was the primary conducting MO.

Other unimolecular rectifiers are donor-acceptor types and do not contain a bridging fragment at all. One such example is a donor-acceptor molecule consisting of a 4-thio-phenalaza (4TPA) donor fragment directly bonded to a C_{60}-fullerence acceptor fragment, in which the decoupling between donor and acceptor fragments comes from a twist in the π system of the molecule.[22] This structure showed very effective rectification, with a rectification ratio of 145 at ±1V with a conductance that is over a magnitude greater than that of designs possessing saturated σ-bridges.

The efficiency of electron transport through an electrode/molecule/electrode junction is limited by decoherence and relaxation effects.[23] Relaxation is due to molecular vibronic coupling, which is an effect that does not influence electron transport in semiconductors, such as those made of silicon. Vibronic coupling is the interaction between electronic states and nuclear motion; as the excited state geometry of a molecule is usually different from that in the ground state, electronic transitions are often accompanied by nuclear motion.

Decoherence refers to the time-dependent phase shifting of the wave packet that propagates through the junction during electron transport.[23] Decoherence effects leads to the exponential decay of the electronic coupling between electrodes with increasing length of the molecular bridge. In proteins, dynamic fluctuations in the structure itself may impact the electron transfer rates, as these influence the electronic coupling (H_{DA}) between donor (D) and acceptor (A).[24] In an open quantum system, decoherence is represented as the reduction of the off-diagonal electronic coupling matrix element (H_{DA}) to zero due to interactions of the system

with the environment, reflected by the reorganization energy, which can decouple the electronic communication between donor and acceptor. Increasing the length of the molecular bridge in an electron/molecule/electrode junction will increase the range of nuclear motion in the molecule, which also impacts H_{DA} and can contribute to decoherence effects.[23,24]

Both decoherence and vibronic coupling are dependent upon both temperature and the length of the molecular bridge; as these factors increase, so to the effects of relaxation and decoherence on electron transport processes.[23] This can lead to changes in the mechanism of electron transport from coherent tunneling to incoherent hopping. Coherent tunneling occurs when an electron moves from one electrode to another by tunneling across the barriers created by complexation of molecule to electrode (as well as intramolecular barriers such as a saturated bridge fragment) through molecular states. Incoherent hopping occurs when electrons are excited into higher molecular orbitals, reducing the tunneling distance. The excitation of electrons that occurs in an incoherent hopping regime is usually accompanied by the excitation of a molecular vibration. This quality is exploited in inelastic electron tunneling spectroscopy (ITES), in which increasing the applied voltage can cause the switch from one mechanism to another. The switch to an inelastic tunneling mechanism causes the activation of molecular vibrations that increases the rate of current flow through the system, leading to a change in the slope of the I/V curve. The second derivative of the current to bias voltage gives a peak, which corresponds to the contribution of inelastic tunneling to the current.

While a mixture of both coherent tunneling and inelastic (incoherent) hopping are possible in an electrode/molecule/electrode junction, we expect tunneling to dominate the electron transport that we will see in our computations, as we are not using long molecular wires or elevated temperatures (the temperature for all computations in this study was kept at 300K). Tunneling is currently the most accepted mechanism for electron transfer in biological systems.[24]

2.6 Overview of different rectification mechanisms

Rectification mechanisms are classified in three categories.[1,22] Rectification can arise from the presence of asymmetric Schottky barriers, which is known as the S (Schottky)-type mechanism. Schottky barriers are potential energy barriers formed at the interface between metal electrodes and a semiconductor.[25] A (Asymmetric)-type rectification utilizes the asymmetric positioning of an electroactive group between two electrodes, such that it promotes the localization of conductive states nearer to one electrode in the junction.[1,22] There is also U (Unimolecular)-type rectification, which is considered to be true rectification through a single molecule. In this mechanism, rectification arises from the asymmetric spatial and energetic distribution of molecular orbitals, which move into and out of the bias window in a bias-dependent manner. Rectification through the PDT ligand is expected to be of the U-type and therefore we will assess the energetic and spatial distribution of the frontier molecular orbitals involved in electron transport.

2.7 Distinction between electron transfer and electron transport

As this study relates a biological molecule with the study of unimolecular rectification, it is necessary to make the distinction between e- transfer and e-

transport. Electron transport is a term that is used in the study of semiconductors to refer to the process by which electrons tunnel between electrodes in a voltage-dependent manner.[26] It is defined as a process in which the flow of electrons from a donor to acceptor which is not reliant on an electrolyte and utilizes electrodes which are not ion conductors.[27] For our study, since we are using a biological molecule, the PDT ligand, as a molecular bridge between electrodes to probe how electrons move through this system in a voltage-driven manner, without solvent or electrolytes included in the simulations, we will refer to this process as electron transport. The electron transport efficiency is given by conductance, G, given by the following equation,

$$G = \frac{I}{V}.$$

Where I is the current and V is the voltage.[26]

Non-equilibrium Green's function DFT (NEGF-DFT) is a standard method for computationally assessing the rectification of theoretical electrode/molecule/electrode systems.[28,29] It was first applied to describe the process of electron transfer between two electrodes through a molecular wire in 1994 by Ratner *et al*.[28] It utilizes the application of an external bias voltage (V) to the ground-state electron density to assess changes to the system under non-equilibrium conditions, such as when current flows from one electrode to the other through the molecular bridge. Thus, the NEGF formalism allows the assessment of phase-coherent e- transport when the electron density of the molecular bridge is polarized under the applied electric field, which allows the bias and energy-

dependent transmission function (T) to be calculated. Transmission (T) is the probability that at a given energy, an electron will be able to move from one electrode to the other through the molecular bridge.[26] The T within the bias window under different biases can be integrated using the Landauer formula to construct a current-voltage (I-V) curve, which can be used to assess bias-dependent rectification behavior through comparison of the current flow through the molecular bridge at forward and reverse bias.[10,30] The Landauer formula is given below as

$$I(V) = \frac{2e}{h}\int_{-\infty}^{\infty} T(E)[f_L(E) - f_R(E)]dE$$

where $I(V)$ is the voltage-dependent current, T is the transmission, and $f_L(E)$ and $f_R(E)$ are the Fermi distributions of the left and right electrodes, respectively.[31] The inclusion of the $f_L(E)$ and $f_R(E)$ terms ensures that only the transmission probability within the bias window is integrated to give the I(V) curve. Large transmission peaks may be present at energies that lie outside of the bias window, but they do not contribute to the flow of current through the system.

Of importance to us in this study is to relate the efficiency of rectification to a specific tautomeric form and oxidation state of the PDT. This is accomplished through the analysis of the I-V curves of each PDT, which allows us to measure the rectification ratio (RR). The rectification ratio (RR) is defined as

$$RR = \left|\frac{I(Vf)}{I(Vr)}\right|.$$

Here, *I* is the current, *Vf* is the voltage at forward bias, which is the direction that produces the greater current, and *Vr* is the voltage at reverse bias. The rectification ratio (RR) is the ratio of current that can flow at forward and reverse biases; high RRs are an indicator of high efficiency vectoral electron transfer.

Current flow through the device can be ohmic, where the current increases as voltage increases in a linear fashion, or non-ohmic, in which the current does not increase linearly with voltage. One such non-ohmic transport occurrence is negative differential resistance (NDR) in which the current decreases even as the applied bias voltage increases.[32] As voltage through the device increases, it can reach a critical value known as the "breakdown voltage", in which the electrode's electronic states delocalize along the length of the molecular bridge and electrons flow through the device via ballistic transport.[23] This effect can cause very large currents to flow through a unimolecular rectifier even when the bias direction is one in which the junction is normally insulating.[11] Therefore, the measure of RR is only useful at bias voltages that are below the breakdown voltage of a particular electrode/molecule/electrode junction.

The transmission probability through a molecular bridge is profoundly dependent upon the coupling between the molecule and electrodes, given by the formula

$$T = \Gamma_1^L \Gamma_N^R |G_{1N}|^2$$

where Γ_1^L and Γ_N^R are the coupling strengths between the molecule and L and R electrodes, respectively and $|G_{1N}|^2$ is the transmission probability through the molecule, based on the Green function, G_{1N}.[26,31]

Electron transfer, on the other hand is what is usually considered in biological redox reactions. It takes place in solution, in which electrolytes stabilize changes in the charges of donor and acceptor during the flow of electrons through the system.[27] Biological electron transfer processes commonly utilize the ions in solution to transfer the charge from donor to acceptor; therefore, the donor and acceptor do not have to be bonded to each other. The driving force for electron transfer is influenced by the differences in the redox potentials of the donor and acceptor entities.[33] It is given as a rate constant, $k_{D\text{-}A}$, that is described by the formula

$$k_{D-A} = \frac{1}{h}|V_{D1}V_{NA}|^2 F|G_{1N}|^2$$

which relates the rate of electron transfer to V_{D1} and V_{NA} which are the couplings between the bridging molecule to the donor and acceptor entities.[26] The term $|V_{D1}V_{NA}|^2$ has been also written as $|H_{DA}|^2$ by Nitzan; H_{DA} represents the electronic coupling matrix element which couples the donor fragment to the acceptor fragment.[34] The variable F is the thermally averaged and Franck-Condon (FC) weighted density of nuclear states that accounts for the structural changes

and solvent polarization effects that take place in redox reactions involving changes in the nuclear coordinates or charge of the molecule.[26,34] F also takes into account the energy gap that exists between the donor and acceptor states as well as the Boltzmann distribution over the donor states.[34] It can be expressed as the following expression

$$F(E_{AD}) = \frac{e^{-(\lambda+E_{AD})^2}/4\lambda k_B\ominus}{\sqrt{4\pi\lambda k_B\ominus}},$$

where k_B is the Boltzmann constant, $\ominus$ is the temperature, E_{AD} is the energy gap between the donor and acceptor states, and λ is the reorganisation energy of the nuclear coordinates of donor and acceptor fragments following electron transfer from donor to acceptor.

Transmission is related to the conductance G by the following formula,

$$G = \frac{2e^2}{h}T,$$

where h is Planck's constant, T is the total transmission probability, and e is the charge of an electron.[26] When T is 100%, as it approaches for several metals as single atoms, including Au, Cu, and Ag, the conductance is $\frac{2e^2}{h}$, but the T decreases for metal/molecule/metal junctions due to the contacts between the electrodes and molecular bridge. Electron transport and electron transfer can both be related to conductance by the following formula

$$G = \frac{2e^2}{h} \frac{\Gamma_1^L \Gamma_N^R}{|V_{D1} V_{NA}|^2 F} h k_{D-A}.$$

The above equation shows that the rate of electron transfer, k_{D-A}, is proportional to conductance, G, which we can computationally assess via the construction of I-V curves.[26] This allows us to use the NEGF-DFT method to relate our computational results to the rate of electron transfer (k_{ET}) in a biological system.

The rate of electron transfer (k_{ET}) is derived from Marcus theory, which originally was used to describe the process of through-space electron transfer from a donor to an acceptor, analogous to the process which occurs in molybdoenzymes, where the redox centers are not bonded.[24,27] It is described by the following

$$k_{ET} = \frac{2\pi}{\hbar} |H_{DA}|^2 \frac{1}{\sqrt{4\pi\lambda k_B \ominus}} exp\left(\frac{-(\lambda + \Delta G^\circ)^2}{4\pi\lambda k_B \ominus}\right),$$

where ΔG° is the Gibbs free energy of activation, H_{DA} is the electronic coupling matrix element which couples the donor and acceptor states, λ is the nuclear reorganization term that describes the changes to nuclear coordinates that occur during electron transfer, k_B is the Boltzmann constant, and $\ominus$ is the temperature.[24,27,34,35] The electronic coupling matrix element, H_{DA}, was first derived from Fermi's Golden Rule, which describes the probability for nonadiabatic electron transfer from donor to acceptor states given a perturbation to the system;

it is dependent upon the magnitude of H_{DA} as well as the density of states (DOS), which is the number of occupiable states at a given energy.[24,36] In our system, there is a continuum of states on the gold electrodes which mix with discrete molecular states. Transport of electrons through the molecule requires that occupiable states are available at specific energies and we will therefore use DOS later to describe the efficiency of this transport at a given energy. The magnitude of H_{DA} is dependent upon the distance between the donor and acceptor.[35] As it is a description of the degree of wavefunction overlap between donor and acceptor, as the distance (d) between the two increases, the overlap of the wavefunctions will decrease and H_{DA} will decrease.[35,37,38] This is expressed as

$$H_{DA}^2 = H_{DA}^{0\,2} exp(\beta d),$$

where β is the distance decay constant.[37] This expression indicates that the stronger the electronic coupling between donor and acceptor, the smaller the distance dependence between them. The mathematical expression

$$\beta = \frac{2}{\delta} ln\left(\frac{\Delta\varepsilon}{h_{bb}}\right),$$

shows the relationship between β and the tunneling-energy gap ($\Delta\varepsilon$), electronic coupling between the bridging fragments in a donor-bridge-acceptor system (h_{bb}) and the length of the bridging fragments (δ).[37,38] While the magnitude of

$\Delta\varepsilon$ cannot be measured experimentally, β can using techniques such as time-resolved fluorescence spectroscopy and transient absorption spectroscopy, and therefore serves as a sensitive experimental barometer of the tunneling-energy gap.[37] The distance is influenced by the barrier height of an electron tunneling between donor and acceptor.

The electronic coupling in a donor-bridge-acceptor system was mathematically described by McConnell in 1961 as

$$H_{DA} = \frac{h_{Db}}{\Delta\varepsilon}\left(\frac{h_{bb}}{\Delta\varepsilon}\right)^{n-1} h_{bA},$$

in which H_{DA} is dependent upon the individual couplings between donor and bridge (h_{Db}), the individual bridging units (h_{bb}), and the bridge and acceptor (h_{bA}).[37–39] The tunneling-energy gap ($\Delta\varepsilon$) represents the energy difference between the D-b-A transition state and the bridge transfer states, which can be the result of either hole or electron transport.[37] This is shown in Figure 2-3. It is also influenced by the relative redox potentials of each component of the donor-bridge-acceptor system.

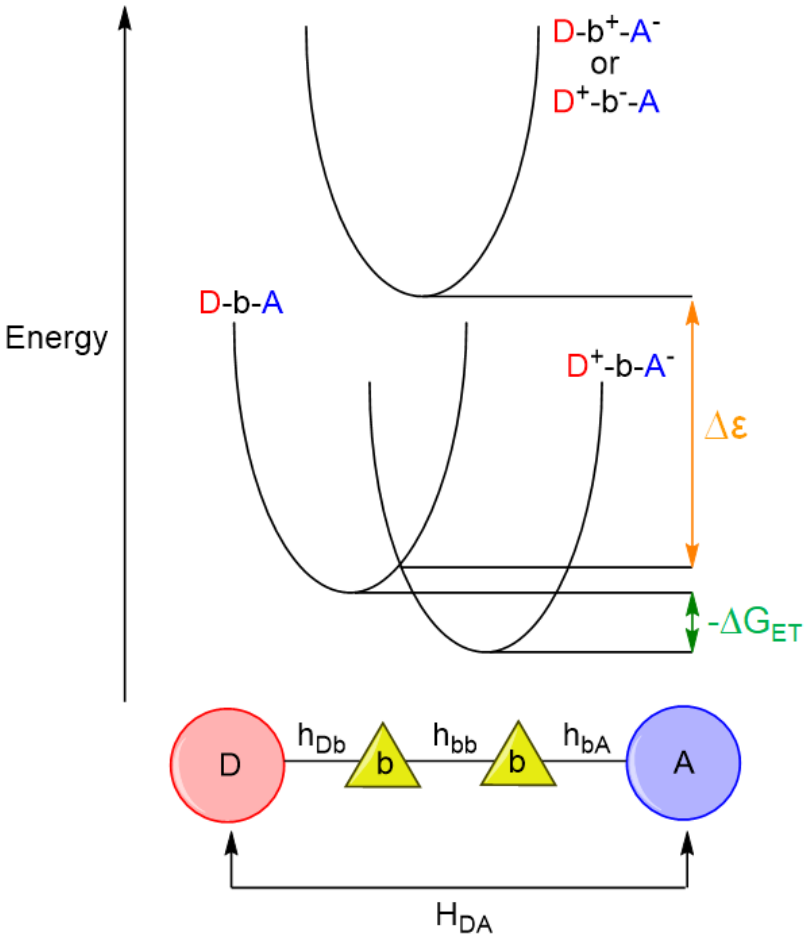

Figure 2-3. Superexchange model. The donor (D) and acceptor(A) fragments are separated by n bridge fragments (b). $-\Delta G_{ET}$ is the free energy of reaction and $\Delta\varepsilon$ is the tunneling-energy gap, which is unable to be measured directly from experiment as it is the vertical energy gap of the transition state configuration. Adapted from Wenger, O. S. How Donor - Bridge - Acceptor Energetics Influence Electron Tunneling Dynamics and Their Distance Dependences. Accounts of Chemical Research 2011, 44 (1), 25–35.

Of utmost importance to us is the identification of the frontier molecular orbitals that are involved in e-transport and rectification

behavior; this information can be used to understand the mechanisms of electron transfer in molybdoenzymes. This is accomplished by the projection of the molecular projected self-consistent Hamiltonian (MPSH) states, which are the molecular orbitals (MOs) that are perturbed energetically through the hybridization of the MOs and the electrode surface states.[29] The MPSH states are calculated by the diagonalization of the block matrix of the scattering region from the self-consistent non-equilibrium Hamiltonian described as

$$H = \begin{pmatrix} H_L & H_{LM} & 0 \\ H_{ML} & H_M & H_{MR} \\ 0 & H_{RM} & H_R \end{pmatrix},$$

where a molecule (M) is coupled to the left (L) and right (R) electrodes, but the electrodes themselves are decoupled so that $H_{RL} = H_{LR} = 0$.[31] The energies of the MPSH states may not be in full resonance with transmission peaks, due to the hybridization with the gold electrode states. The stronger the interaction between the electrodes and the MOs, the greater the energy shifts of the MPSH states relative to their corresponding MOs. Furthermore, the width of the transmission peaks in the spectra is proportional to the strength of this interaction, which results in a smearing of the energies of the states that are involved in transmission. As I(V) curves are constructed by integration of the transmission peaks within the bias window, strong coupling between MOs and the metallic electrodes leading to widening of the transmission peaks can lead to increased current flow through the molecule. The relative energies of the frontier MOs in relation to E_F has been shown to be dependent upon the molecular structure itself and its contact

geometry to the electrodes; this influences the zero-bias charge transfer between the molecule and electrodes and thus, the energetic alignment of the frontier MOs.[40] Therefore, the contacts between the molecule and electrodes is extremely influential on rectification and the efficiency of e- transport through the molecule.

2.8 Influence of HOMO-LUMO gap on molecular conduction

As e- transport through metal/molecule/metal junctions is a process in which electrons tunnel through the molecular bridge using MOs, the difference in energy between the E_F of the electrodes and the frontier MOs determines the efficiency of conductance.[26] Usually, there is a mismatch in the energetic alignment which prevents 100% T and therefore conductance, G, is far less than that of a single metal atom ($\frac{2e^2}{h}$). Therefore, the actual transmission probability is dependent upon the energy gap between the frontier MO(s) and the E_F, β, as well as the tunneling distance (length of the bridging molecule), L. The relationship between these values is given below as

$$T \propto e^{-\beta L}.$$

The closer in energy the MOs and the E_F of the adjacent electrode, the closer the T will be to 100% and the conductance will near that of a single metal atom.[23,26,41]

Because of the relationship between T and the energy gap between frontier MOs and the E_F of the electrode, there has been great interest in manipulating the energy levels of MOs to match the E_F of the corresponding electrode.

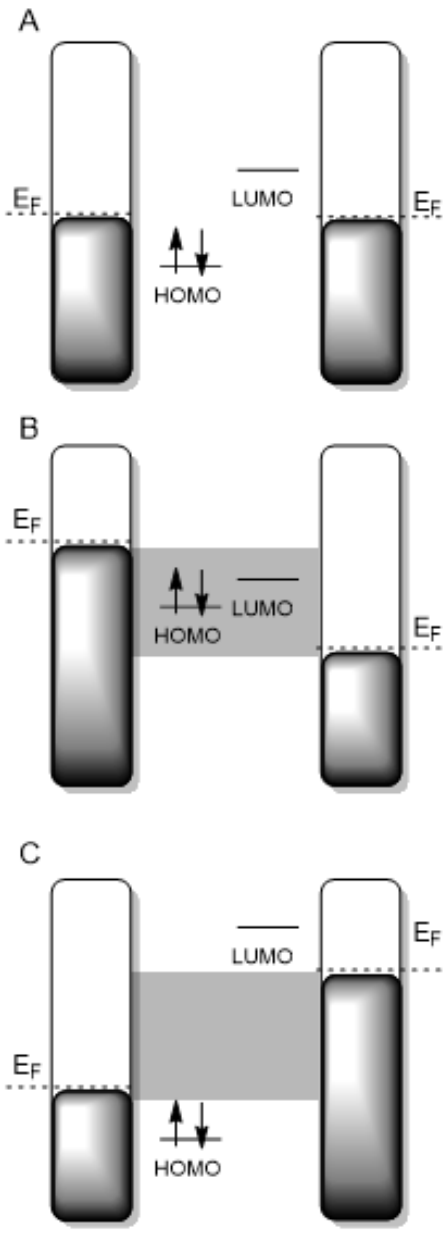

Figure 2-4. Fermi level pinning of molecular orbitals to the Fermi level (E_F) of the electrodes. Under zero-bias, the EF of the left and right electrodes is equivalent (A). Under forward bias, the HOMO and LUMO are pinned to the electrostatic potential of the left and right electrodes, respectively (B). This pulls both MOs into the bias window that is indicated by the shaded rectangle and decreases the HOMO-LUMO gap, allowing efficient e- transport through the molecule. Under reverse bias, the pinned HOMO and LUMO decrease and increase with the electrostatic potential of the left and right electrodes, respectively. This causes the HOMO-LUMO gap to increase and both orbitals to lie energetically outside of the bias window, preventing them from participating in e- transport. This creates an insulating environment.

The concept of a localized frontier molecular orbital shifting in energy when its corresponding electrode changes in electrostatic potential due to the increased application of bias voltage is known as a Fermi level pinning effect (Figure 2-4).[42,43] This effect is due to the formation of dipoles on the surface of the electrode as a result of the bonding between the molecular anchor and the electrode that as a result from charge transfer events at the interface. This has the net effect of changing the

electrostatic potential of the molecular orbital in a way that is modulated by the interfacial charge redistribution; thus, as the electrostatic potential of the electrode changes, the electrostatic potential of the MO changes in a similar manner.[42] The interactions between the frontier MOs of the molecule and the electrode states is also responsible for the energetic broadening of the frontier molecular orbitals that become hybridized with the gold states and the resultant broadening of peaks observed in the transmission spectra. If the MO broadening surpasses the energy difference between the Fermi levels of the electrodes (the bias window) and the

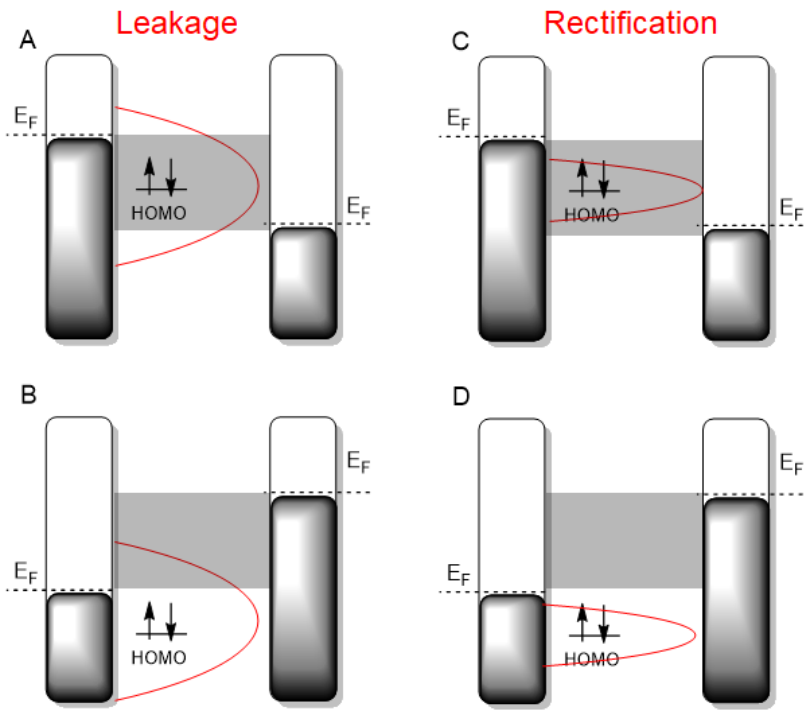

Figure 2-5. Broadening of a transmission peak (shown in red) in the transmission spectrum arises from the energetic broadening of the frontier molecular orbitals (i.e. the HOMO) that become hybridized with the gold states on the electrodes. Leakage occurs when the broadening allows the transmission peak to remain within the bias window (shaded region), even though the HOMO energetically moves with the changing potential of the adjacent electrode to which it is hybridized (A and B). If the transmission peak is less broad, due to lessened hybridization of the MO with the states of the gold electrode, rectification can occur through the asymmetric position of the transmission peak upon the reversal of bias (C and D). As the HOMO is pinned to the potential of the left electrode, the transmission peak associated with the HOMO will leave the bias window when the bias is reversed.

energy of the conducting MO, the rectification would become inefficient, as the MO would allow current flow in both bias directions; this is known as diode “leakage”.[44] This is shown in Figure 2-5.

Therefore, in the quest to design unimolecular rectifiers with frontier MOs that can be energetically aligned to the electrodes, the interaction between the anchoring groups and the electrodes cannot be neglected, as this interaction has profound effects on the broadening and energetic alignment of the MOs with respect to the E_F of the electrodes. It has been shown that only a single frontier molecular orbital is necessary for rectification through a molecular junction due to Fermi level pinning.[44–46] In one study, an asymmetrically coupled HOMO (spatially closer to a single electrode) pinned to the Fermi level of the adjacent electrode was responsible for a RR ratio of ~100 at ±1V bias.[44] Since rectification can occur through the differential energetic alignment of a single frontier MO at forward and reverse bias, which follows the potential of the adjacent electrode, the presence of distinct donor and acceptor molecular fragments is not necessarily required for rectification to occur.

The amplitudes of the induced surface dipoles are influenced by the change in the chemical potential (μ) of the molecule when it is complexed to the electrode; the value of μ for the molecule itself is assessed by the formula

$$\mu = \frac{-(IP+EA)}{2},$$

Where IP is the ionization potential (associated with the HOMO) and EA is the electron affinity (associated with the LUMO).[42]

As a result of this relationship, it has been demonstrated that changes in the IP and EA of the molecular fragments do not greatly influence the IV characteristics of an electrode/molecule/electrode junction, given a strong coupling between the molecular anchoring groups and the electrodes, as the system will compensate for these changes by the variation of the interface dipole amplitudes.[47] Therefore, a strong coupling or hybridization between a molecular orbital and the electrode is responsible for Fermi level pinning of the frontier molecular orbitals; the result of the formation of an interface dipole by transfer of electronic density between the molecule and electrode (i.e. electron transfer from the gold atoms to the sulfur anchoring group). The net effect of this strong coupling will be that the Fermi-level pinning of the HOMO will be largely unaffected by substituent changes in the parent molecule, such as the addition of electron-withdrawing substituents, as seen in a study of SAMs consisting of oligophenylene ethynylene (OPE) derivatives anchored to gold via thiol groups.[47] If the coupling between molecule and electrode is weak, the molecular frontier orbitals will more resemble the isolated molecule energetically and modifications to the structure that lead to changes in the IP and EA of the molecule will shift the HOMO and LUMO levels similarly what is observed in the isolated molecule.

The degree to which a frontier molecular orbital is pinned to the E_F of the corresponding electrode is quantified by the S-parameter, which represents the susceptibility of the orbital to be offset energetically from E_F due to changes in the energy orbital of the isolated molecule.[1] The S-parameter for the HOMO and LUMO is calculated by the following formulas,

$$S \equiv \frac{d(E_F - \varepsilon_{HOMO})}{d(IP)} \approx 0,$$

$$S \equiv \frac{d(E_F - \varepsilon_{LUMO})}{d(EA)} \approx 0,$$

where $\varepsilon_{HOMO/LUMO}$ is the energy of the HOMO or LUMO after the molecule is complexed to the electrodes, E_F is the Fermi energy of the electrode, IP is the ionization potential and EA is the electron affinity of the isolated molecule.[1,32] An S-parameter of zero indicates a perfect pinning scenario, where the HOMO or LUMO is always offset from the E_F of the electrode at a defined energy even as the applied bias is increased and the electrochemical potentials of the electrodes change.

The relative compression of the HOMO-LUMO gap upon complexation to the metallic electrodes has been shown to lead to effective electron transfer, which is intuitive in a tunneling regime.[12,48] The tunneling-energy gap depends on the energy difference between donor and bridge states involved in superexchange and the energy of the virtual bridge state is proportional to that of the LUMO.[37,49] By compressing the energy gap between the HOMO (donor) and LUMO (acceptor), tunneling becomes more favorable. For most organic molecules, the typical HOMO-LUMO gap is on the order of ~1eV.[46,47,50–52] Smaller HOMO-LUMO gaps for organometallic molecules occur due to metallic *d* states, which can increase the energy of the frontier MOs so that they lie closer to the Fermi level of the electrode.[46]

Van Dyck and Ratner related the pinning effect to the compression of the energy gap between the HOMO and LUMO that occurs when the molecule is complexed to the electrodes.[48] They found that if there is π-coupling between the donor and acceptor fragments, the IP and EA of the fragments are modified by the interaction between donor and acceptor, and the net effect is the widening of the HOMO-LUMO gap. However, a strong pinning effect of the HOMO and LUMO levels to the E_F of the electrodes leads to gap compression, which leads to a larger rectification, as seen in Figure 2-4. Therefore, to increase the efficiency of rectification, the decoupling of molecular fragments and a strong pinning effect that is largely unaffected by changes to the IP and EA of the molecular fragments is critical.[47] They found that a molecule consisting of two conjugated hydrocarbon fragments bridged by a saturated hydrocarbon fragment, anchored asymmetrically with SH and CN, fulfilled these criteria, giving a RR of 114 at ±1V bias.[48] When the saturated bridge fragment was removed, the HOMO-LUMO gap widened and the RR at ±1V bias dropped to 2.1.

HOMO-LUMO coupling was shown to be responsible for the high RR of 145 at ± 1V computationally obtained for a 4-thio-phenylaza-C60-fullerene (4TPA–C60).[22] A strong pinning effect of the HOMO to the left electrode was observed, but unexpectedly, the LUMO was observed to be pinned to the HOMO under forward bias, resulting in efficient current flow due to the formation of a conducting channel spanning the width of the molecule. The result of this was a decrease in the HOMO-LUMO gap as the forward bias increased; leading to a voltage drop at the interface of the molecule and electrode. When the bias was reversed, the LUMO

instead was pinned to the right electrode, which increased the HOMO-LUMO gap to increase and an insulating effect to occur. In this case, the voltage drop was observed to occur between the 4TPA and C_{60} fragments, due to the buildup of electrostatic charges as a result of poor charge transfer from the C_{60} to the 4TPA.

Fermi-level pinning of the HOMO and LUMO in a donor/σ-bridge/acceptor molecule complexed to one gold and one iron electrode was found to cause negative differential resistance (NDR).[32] A strong pinning effect of both MOs to their adjacent electrodes leads to the formation of a conducting channel across the molecule as the positive bias is increased and the HOMO/LUMO gap is compressed within the bias window, increasing the current. Further increase of the bias voltage causes HOMO-LUMO crossover, which causes the orbitals to again widen the HOMO/LUMO gap leading to a decrease of current flow with increasing bias voltage.

2.9 Importance of anchoring groups and identity of metallic electrodes

The choice of anchoring groups is highly important due to the effects of the electrode/molecule coupling on the special distribution and energy alignments of the frontier MOs.[19,53] Several different anchoring groups have been used to complex molecules to gold electrodes in past studies. In one study, the effects of three different anchoring groups (SH, NH_2, CN) used to bind the acceptor molecular fragment to a gold electrode (Au(111)) were explored.[54] The donor portion of the molecule was always anchored with a thiol group. It was observed that HOMO alignment to the E_F of the associated electrode (HOMO Fermi level pinning) was unaffected when the acceptor portion of the molecule was substituted

with different anchoring groups, but that the ionization potential (IP) of the molecule was sensitive to the substitutions. This change in IP profoundly affected the Au(111) work function, $\Phi_{Au(111)}$, which is defined as the difference between the electrostatic potential of the vacuum and the E_F of the electrode. The work function therefore is essentially a measure of the energy needed to remove an electron from the electrode to the vacuum. It was found that the ionization potentials of the molecule increased in the order of NH_2->SH->CN, which follows with the rationale that NH_2 is an electron donor group and CN is electron withdrawing. The change in $\Phi_{Au(111)}$, upon anchoring group substitution, was found to be a function of the induced dipole fluctuations at the interface of the electrode/molecule, which was sensitive to the identity of the anchoring group. This had the effect of lowering the $\Phi_{Au(111)}$ for the NH_2 and SH substituted molecules and raising it for the CN substituted molecule.[54] Therefore, the identity of the anchoring groups will have a profound effect on the efficiency of electron transport through the system, and this effect can be attributed to the changes in the induced bond dipoles at the electrode/molecule interface upon substitution of the anchoring groups.[55]

As was observed for changing the identity of the chemical anchoring groups, changing the identity of the metal electrode does not appear to greatly affect the Fermi level pinning of a system either. A study on oligoacene self-assembled monolayers (SAMs) on metallic substrates with metalized atomic force microscopy (AFM) tips using ultraviolet photoelectron spectroscopy (UPS), showed that changing the metal work function, Φ, by substituting Ag, Pt, or Au electrodes, had

little effect on the energetics of HOMO pinning, as the anchoring thiol sulfur acts as an electron donor to the metal and this causes a large bond dipole to form.[568] As the work function, Φ, increases from changing the electrode from Ag to Au to Pt, the magnitude of the S-metal bond dipole also increases, which prevents the perturbation of the HOMO energy level relative to that of the associated electrode, as the effects of this dipole are mainly localized to the molecule/metal interface and have very little effect on the HOMO itself. However, while Fermi level pinning is insensitive to changes in the metal work function, transport through the electrode/molecule/electrode junction is influenced by changing the identity of the electrode. This mainly derives from changes in the chemical contact barrier between molecule and electrode, which is sensitive to Φ. As Φ increases, the chemical contact barrier decreases, and this is a function of the magnitude of the S-metal bond dipole formed when the molecule is complexed to the electrode.

It has been demonstrated that asymmetric coupling of a symmetric molecule to electrodes alone is sufficient to induce rectification.[57,58] In one study, a Tour wire, which is an organic molecule comprised of phenyl rings with triply bonded carbon atoms as spacers, was bound to gold with either symmetric thiol contacts or a single thiol contact and H atom, which is unable to bond to gold.[59] The introduction of a vacuum-gap between the H atom and gold electrode changed the potential drop across the molecule, shifting the energetic alignment of the MOs from their relative position in the symmetrical contact junction and causing rectification to occur as the HOMO entered the bias window at forward bias but not at reverse bias in the asymmetrical junction.

As the PDT molecule in this study terminates in two dithiolene sulfurs and a NH_2 group on the pterin portion of the molecule, we will use these groups to anchor the molecule to the gold electrodes so that the molecule in its unmodified, biological form can be assessed. Substitution of these anchoring groups would be expected to change the native electron transport and rectification behavior of the PDT. By keeping the anchoring groups consistent, we can better assess the effect of the oxidation/tautomeric states of the PDT on these qualities.

2.10 Experimental techniques for assessing molecular rectification

Since the PDT ligand is unstable when displaced from the protective protein environment, we are unable to assess the rectification behavior of the native ligand directly from experimental techniques and therefore we will rely on computational methods.[60–62] Nonetheless, we will briefly touch upon a few experimental techniques for assessing the efficiency of unimolecular rectifiers in electrode/molecule/electrode junctions.

Recent progress on the creation of electrode/molecule/electrode junctions has facilitated the collection of experimental data. The single molecule break junction (STMBJ) technique, developed by Xu and Tao in 2003, uses a metallic STM tip as an electrode.[63] The tip is touched to a metallic substrate, which acts as the second electrode and is covered in the molecule of interest (Figure 2-6A). As the STM tip is withdrawn from the metallic surface, the tunneling current is monitored. Eventually, a single molecule will bridge the STM tip and metallic substrate as the tip is withdrawn to a certain distance (Figure 2-6B); as the tip is withdrawn further, the junction is broken (Figure 2-6C). The result of this experiment, which is

repeated thousands of times, is a conductance histogram, which represents the different contact geometries between the electrodes and molecule. The major drawback of this technique is that it is impossible to discern the geometries of contact that give the greatest conductance through the molecule. One advantage is that an I-V curve can be obtained from this technique by the application of a bias sweep to the electrode/molecule/electrode junction, which allows the rectification characteristics of the molecule to be assessed.[64]

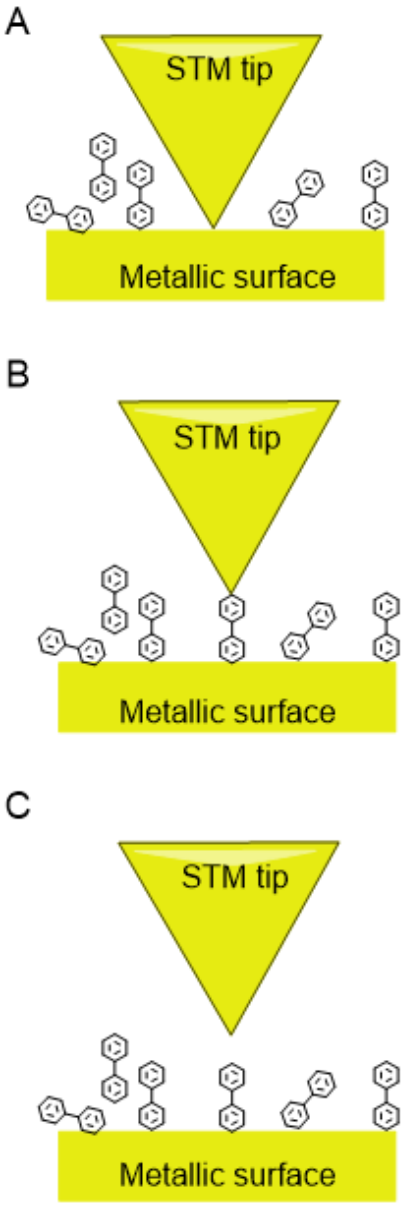

A similar technique that is commonly used is the conductive AFM break junction (C-AFMBJ) techniques, which is highly similar to that of STMBJ, except that a metallic AFM tip is used, allowing force measurements to also be performed.[64]

A variation on the original STMBJ technique, known as EC-STMBJ, was developed in 2013 by Zhou *et al*.[65] The STM tip is electrochemically deposited with metal until a metallic bridge forms

Figure 2-6. Single molecule break junction (STMBJ) technique. The STM tip and metallic surfaces act as electrodes for the molecular bridge. The STM tip is first brought in contact with the metallic surface, which is covered in the molecule of interest (A). As the tip is withdrawn, a single molecule forms an electrode/molecule/electrode junction (B). As the tip is further withdrawn, the junction is broken. The tunneling current is measured throughout this process, which is repeated thousands of times to generate conductance histograms.

between tip and substrate. As the tip is withdrawn from the substrate, the metallic bridge elongates and eventually breaks, which forms sharp nanowire tips as electrodes. Decreasing the surface area at the tip of the electrodes permits the formation of more well-defined molecular junctions, as fewer contact geometries will yield high conductance through the electrode/molecule/electrode junction.

Another variation is known as the mechanically controllable break-junction (MCB) technique, first developed by Krans *et al.* in 1996.[66] In this technique, the metallic electrodes consist of a notched wire that is mounted on a flexible substrate. This setup is cooled to liquid helium temperatures and the wire is broken by the application of force on the flexible substrate, this allows precise control over the distance between the two halves of the wire and a more predictable electrode/molecule/electrode junction. This experimental setup can be repeated hundreds of times to yield conductance histograms, similar to the other experimental techniques mentioned above.

2.11 The relationship between magnetic exchange, the electronic coupling matrix element, and molecular conductance

Note that the author of this dissertation directly contributed to the research in this section, which is published as Kirk, M. L.; Shultz, D. A.; Zhang, J.; Dangi, R.; Ingersol, L.; Yang, J.; Finney, N. S.; Sommer, R. D.; Wojtas, L. Heterospin Biradicals Provide Insight into Molecular Conductance and Rectification. Chem. Sci. 2017, 8 (8), 5408–5415. https://doi.org/10.1039/C7SC00073A.

One issue with experimental setups to measure rectification in a laboratory setting is that the exact contact geometry between molecule and electrodes is unknown and varies throughout multiple measurements, leading to the construction of conductance histograms which represent the compilation of many measurements

at many different contact geometries. Because of the ambiguity in the contact geometry that leads to rectification behavior in experiments, it is difficult to assess the exact mechanism controlling rectification behavior in these ensemble measurements.

However, theoretical methods for assessing the rectification behaviors of molecules do not adequately address the ambiguity of the geometry at the interface of molecule and electrode.[67] Many theoretical studies utilize a flat metallic surface and a static configuration for calculations, but metal surfaces used for electrodes in the laboratory are neither flat nor perfectly formed.[21,47,50,53,68–70] It is unknown whether the threefold hollow points (hcp and fcc) are the preferred attachment sites for a molecule, although this is sometimes assumed from the results of computational studies.[71–75] Forces applied to an electrode/molecule/electrode junction may affect the stability of different sites, and it is possible that attachment of the molecule may be sufficient to induce restructuring of the metallic atoms near the site of attachment.[67]

In previous work from our lab, a study in which the author of this dissertation

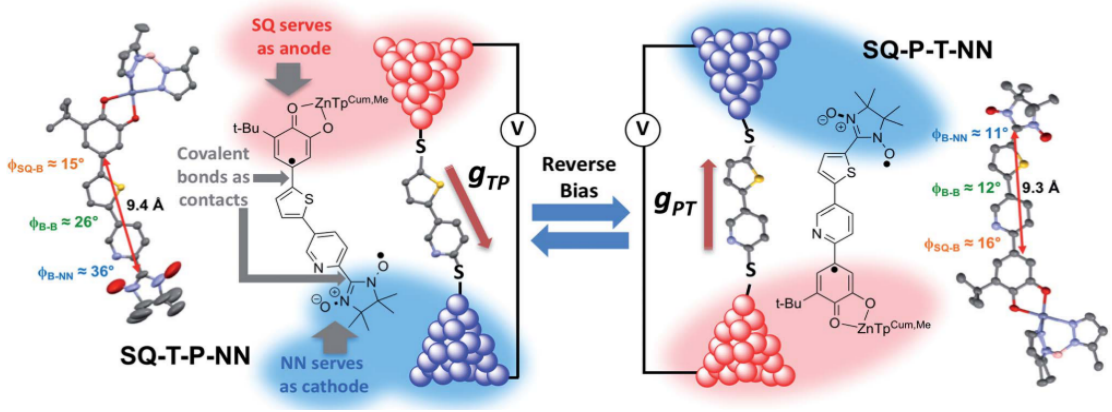

Figure 2-7. Scheme of the molecular constructs SQ-T-P-NN and SQ-P-T-NN, thermal ellipsoid plots and the corresponding electrode/molecular bridge/ electrode junctions with the T-P bridge. The bond torsion between the T and P fragments serve to partially decouple the π-system of the bridge fragment. The SQ and NN molecular groups are analogous to the electrodes in the junctions; the reversal of bias in the junctions is analogous to the different bridge orientations in the two constitutional isomers used in the experiments. Figure adapted from Kirk, M. L., Shultz, D. A., Zhang, J., Dangi, R., Ingersol, L., Yang, J., … Wojtas, L. (2017). Heterospin biradicals provide insight into molecular conductance and rectification. Chem. Sci., 8(8), 5408–5415.

participated in, this problem was addressed by replacement of the electrodes with analogous organic radical molecular fragments, bridged by a pyrimidine/thiophene (P/T) bridge component.[76] The organic radical fragments consisted of a semiquinone (SQ) donor and a nitronylnitroxide (NN) acceptor and the relative orientation of the bridging component was used to form two constitutional isomers, SQ-P-T-NN and SQ-T-P-NN, where the reversal of the orientation of the bridging fragment in these molecules mimicked the reversal of the bias in an electrode/molecular bridge/ electrode junction, as seen in Figure 2-7. The thiophene (T) itself acts as a donor and the pyrimidine (P) as an acceptor, decoupled by a torsionally rotated σ-bond, thus forming the analogous donor/bridge/acceptor unimolecular rectifier proposed by Aviram and Ratner.[8] In

this study, we related the magnetic exchange $J_{SQ-B-NN}$, obtained using magnetic susceptibility data (Figure 2-8) to the electronic coupling matrix elements $H_{SQ-B-NN}$, H_{SQ-B}, H_{B-NN}, and H_{BB} which represent the couplings between the various molecular fragments and molecular conductance g using the following relationship developed by the theoretical work of Anderson,[77] McConnell,[39] and Nitzan[78]

$$\sqrt{J_{SQ-B-NN}} \propto H_{SQ-B-NN} = \frac{H_{SQ-B} * H_{B-NN}}{\Delta}\left(\frac{H_{BB}}{\Delta}\right) = c\sqrt{g},$$

where c is a proportionality constant and Δ is the SQ -> B-NN intraligand charge transfer (ILCT) energy, obtained from electronic absorption spectra

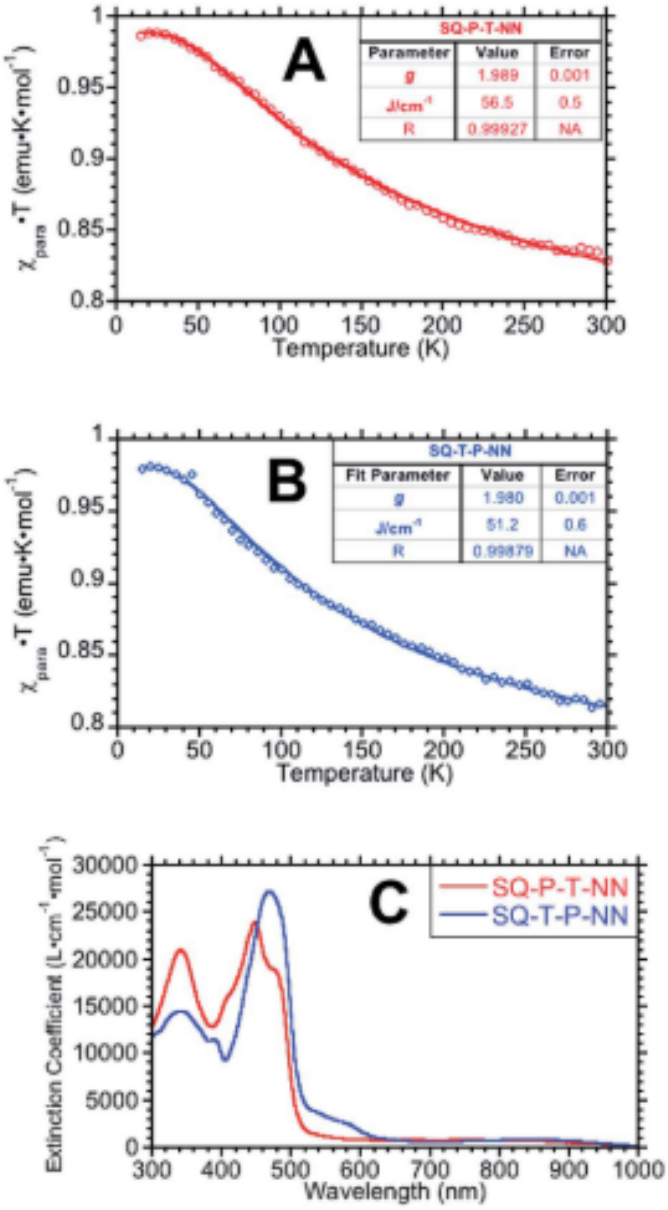

Figure 2-8. Magnetic susceptibility plots for SQ-P-T-NN (A) and SQ-T-P- NN (B). (C) Electronic absorption spectra for SQ-T-P-NN and SQ-P-T-NN. ILCT bands at ~475 nm assigned as an SQ->B-NN(LUMO) transition. Figure adapted from Kirk, M. L., Shultz, D. A., Zhang, J., Dangi, R., Ingersol, L., Yang, J., … Wojtas, L. (2017). Heterospin biradicals provide insight into molecular conductance and rectification. Chem. Sci., 8(8), 5408–5415.

(Figure 2-8) and TD-DFT calculations.[76] From the experimental data, we obtained an experimental RR via the following relationship,

$$\frac{J_{SQ-TP-NN}}{J_{SQ-PT-NN}} = \frac{51.2\ cm^{-1}}{56.5\ cm^{-1}} = \frac{g_{TP}}{g_{PT}} = 0.91 \equiv RR.$$

As the electronic coupling between the molecular fragments varies with the cosine of the torsion angles between the fragments, and thus varies $\sqrt{J_{SQ-B-NN}}$, the RR obtained is dependent upon the relative torsion angle of the two isomers. Computationally if the torsion angles between

SQ-B and B-NN result in a planer structure, and the cosine of these angles then equals 1, the RR above is calculated to be 1.58, indicating that the SQ-T-P-NN isomer provides a more favorable charge transfer path. This relationship is shown as

$$\sqrt{J_{SQ-B-NN}} \propto H_{SQ-B-NN} =$$

$$\frac{cos_{\Phi SQ-B} H_{SQ-B} * cos_{\Phi B-NN} H_{B-NN}}{\Delta} \left(\frac{cos_{\Phi BB} H_{BB}}{\Delta} \right) = c\sqrt{g}.$$

To further validate the experimental RR we obtained, we performed NEGF-DFT electron transport computations in which the T-P bridge fragment was attached to two gold electrodes via added thiol groups. For these calculations, we set the torsion angle between P and T to 20°, the value obtained from the X-ray crystal structure. The reversal of bias in the computations is analogous to the reversal of the orientation of the bridge fragment in the two experimental constitutional isomers SQ-P-T-NN and SQ-T-P-NN. The IV curve and corresponding transmission spectra under bias are shown in Figure 2-10.

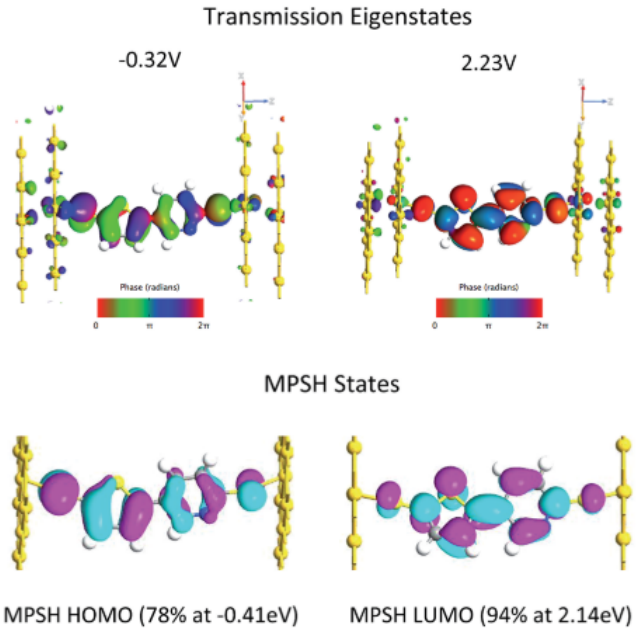

Figure 2-9. Transmission eigenstates at zero bias which represent the conduction channels through the molecule (top) and Molecular projected self-consistent Hamiltonian (MPSH) states corresponding to the frontier MOs of the free T-P bridge fragment that play a dominant role in conductance through the junction and the ILCT band in the molecular construct (bottom). The percentages of MPSH states that contribute to the transmission eigenstate at the indicated energy are shown. Figure adapted from Kirk, M. L., Shultz, D. A., Zhang, J., Dangi, R., Ingersol, L., Yang, J., … Wojtas, L. (2017). Heterospin biradicals provide insight into molecular conductance and rectification. Chem. Sci., 8(8), 5408–5415.

The computations revealed that the MPSH states corresponding to the HOMO and LUMO of the free molecule were responsible for conductance through the

molecule. The symmetric nature of the HOMO and LUMO, as seen in Figure 2-9, is responsible for the relatively poor RR obtained from our computational results as the ratio of the currents at forward and reverse bias, as asymmetry in the spatial or energetic distribution of molecular orbitals is necessary for unimolecular rectification. Energetically, the HOMO peak remains at approximately the same energy at both forward and reverse bias, as seen in the transmission spectra in Figure 2-10B, which also contributes to the poor RR for the bridging fragment and serves as the largest component of the delocalized conduction channel at low biases in both directions. As the bias is increased, the LUMO peak enters the bias window, as seen in Figure 2-10B, and conductance increases, but as the LUMO enters the bias window at the same voltage at both forward and reverse bias, there is not sufficient asymmetry in the energetic behavior of the LUMO to enhance rectification. The max RR was ~1.3 at ±2.56V

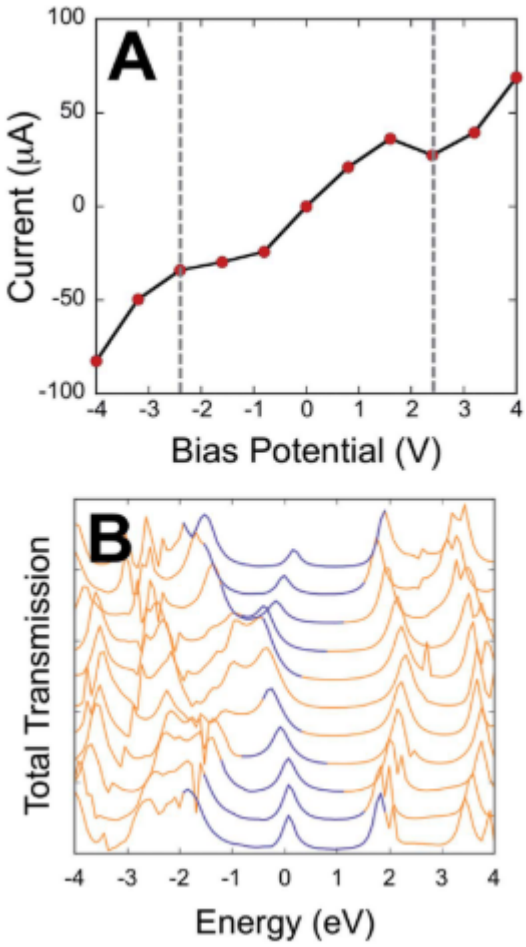

Figure 2-10. IV curve (A) and transmission spectra under bias (B) for the T-P bridge fragment. The bias window in the transmission spectra is represented by the blue region. The rectification ratio (RR) is 1.3 at ±2.56V. The transmission peak corresponding to the HOMO MPSH state remains at approximately the same energy within the bias window as the bias is increased in either direction. The LUMO peak, shown at positive energy, begins to enter the bias window at ±4V bias. Figure adapted from Kirk, M. L., Shultz, D. A., Zhang, J., Dangi, R., Ingersol, L., Yang, J., … Wojtas, L. (2017). Heterospin biradicals provide insight into molecular conductance and rectification. Chem. Sci., 8(8), 5408–5415.

bias and favored electron transport in the direction T->P, in good agreement with the experimental RR.

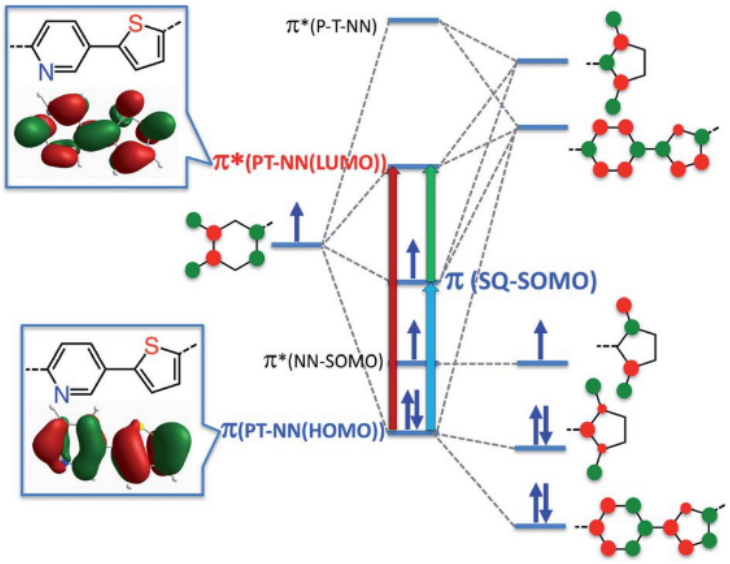

Figure 2-11. VCBI model for SQ-P-T-NN which depicts the symmetrical nature of the HOMO and LUMO of the bridge fragment, as seen in the DFT computed HOMO and LUMO in the insets. The symmetry in the frontier orbitals leads to ineffective rectification and exchange coupling. The red, blue, and green arrows depict the dominant one-electron contributions to the ILCT band. The red and blue arrows also show the major CT contributions to the magnetic superexchange pathways. Figure adapted from Kirk, M. L., Shultz, D. A., Zhang, J., Dangi, R., Ingersol, L., Yang, J., … Wojtas, L. (2017). Heterospin biradicals provide insight into molecular conductance and rectification. Chem. Sci., 8(8), 5408–5415.

Of particular interest was the observation of the LUMO MPSH state that enters the bias window when the potential nears the energy of the experimentally observed SQ(SOMO)->B-NN(LUMO) ILCT band, which further lends credibility to the robustness of computational results obtained from NEGF-DFT methods to provide valuable insight into experimental results. The ILCT band assignment was further quantified using the valence bond configuration interaction (VBCI) model, shown in Figure 2-11.

However, replacement of organic radical fragments with gold electrodes attached to the molecule via thiol groups does lead to some discrepancies in the data. For

instance, the T-P HOMO in computations plays a dominant role in conduction, comprising 78% of the transmission eigenstate that forms a delocalized conduction channel across the molecular bridge at even low bias voltages. But in TD-DFT calculations of the molecular construct, it has been shown that the HOMO only contributes ~14% to the ILCT band, which is a SQ(SOMO)->B-NN(LUMO) transition, which is a function of the differences in the energies and interactions between the bridge MOs and the electrodes, vs the interactions between MOs in the molecular construct.[76]

This study provided a link between NEGF-DFT electron transport calculations to computationally assess RR and conductance through frontier molecular orbitals and experimental data obtained using organic radical molecular constructs to obtain magnetic exchange couplings and electronic coupling matrix elements. The computations provide key information on the mechanisms by which rectification and directional charge transport can occur in molecules.

2.12 Limits of unimolecular rectification

In reality, the realization of a highly efficient unimolecular rectifier may be limited. A theoretical study performed by Armstrong *et al.* revealed that a unimolecular rectifier utilizing an asymmetric double barrier is limited to RRs that do not exceed ~22.[79] In this study, they related the ratio of the two tunneling barrier heights, U_{o1} and U_{o2}, and the lengths of the barriers d_1 and d_2, to the theoretical rectification ratio, as shown in Figure 2-12. They found that if the barrier heights are equal ($U_{o2}/U_{o1}=1$), no rectification occurs, as it forms a single barrier that is the same under both forward and reverse bias. As $U_{o2}/U_{o1}\rightarrow 0$ and $d_2/d_1\rightarrow 0$, no rectification

occurs due to the formation of a single, symmetrical barrier. The most efficient rectification occurs when $0.1<U_{o2}/U_{o1}<1$, but the RRs do not exceed ~22. When $U_{o2}/U_{o1}<0.1$, the RR can theoretically approach 40, but in a practical setting, the barrier height ratio is likely too high to be realized and the RR gain would likely be offset by other thermal and conductive effects. When one barrier height to tunneling becomes too high, the increase in rectification ratio due to the difference in the two barrier heights may be offset by a significant decrease in conductance, as seen in Figure 2-12B. The shape and size of the barriers in a practical setting would be defined by both the size and structure of the molecular bridge itself, while in this study, the theoretical barrier heights replaced the molecule.

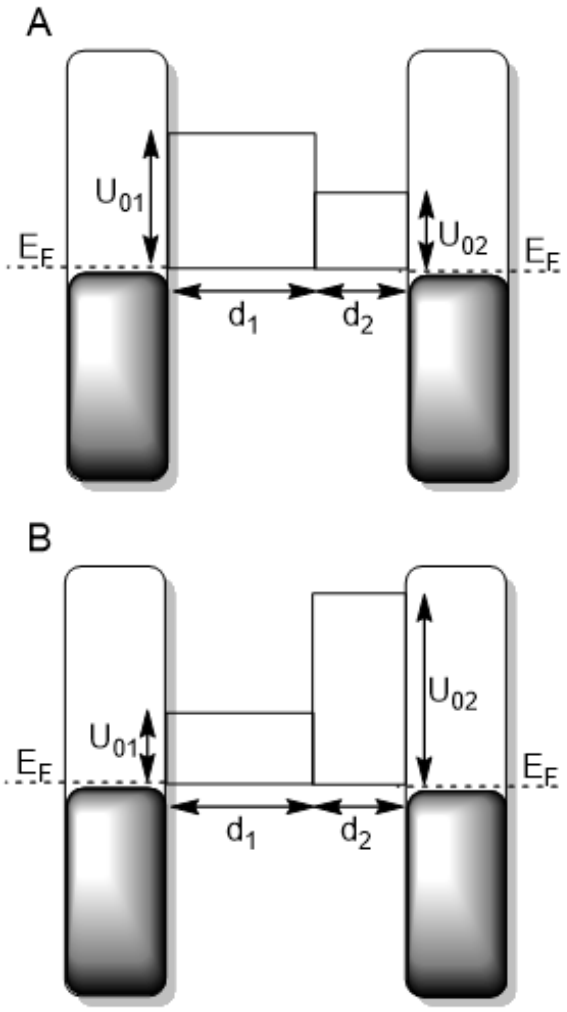

Figure 2-12. Model of double barrier rectification through a unimolecular bridge in an electrode/molecule/electrode junction. Asymmetry in the barrier heights ($U_{o2}/U_{o1}<1$) leads to efficient rectification (A). When $U_{o2}/U_{o1}>1$, rectification can occur, but the conductance decreases dramatically due to the formation of a significant tunneling barrier. Figure adapted from Armstrong, N., et al. (2007). Nano Letters, 7(10), 3018–3022.

The practical limit of RRs in electrode/molecule/electrode devices also was explored computationally using NEGF-DFT and AM1 by Stadler *et al.*[29] They found

both methods gave comparable results, and the RRs were low, on the order of ~1.2-2.3.

Unimolecular rectifiers with RRs of less than 10 are fairly common.[10,68,76,80–82] Conversely, RR of inorganic pn junctions have reported values of ~60-80.[4] Unimolecular rectifiers with a RR between 10-600 have also been observed, and obtaining higher RRs usually involves tuning the environment to promote MO alignment, which can be attained by such means as the use of an ionic solution, the presence of a third "gate" electrode, or addition of electron-donating groups to shift the HOMO energy to that of the Fermi level.[4,68,83–85] A shift in MO alignment can also be induced by application of a mechanical force to the junction; a study on 1,4'-benzenedithiol showed that stretching the molecular junction increased conductance by decreasing the hybridization between the molecular anchoring groups and the electrodes, shifting the energy of the conducting HOMO towards the Fermi level.[86]

However, an increase in RR is usually accompanied by a relative decrease in the maximum current that can flow through the junction.[44,85] Increases in RR by decreasing the electronic coupling matrix element between donor and acceptor MOs and decreasing the coupling between the molecule and electrodes leads to a decrease in the maximum current flow.[85]

2.13 Van Dyck/Ratner design "rules" for unimolecular rectifiers

Van Dyck and Ratner have recently refined the design criteria for molecular rectifiers and identify several critical components that contribute to efficient molecular rectification.[1] These include:

(1) The anchoring groups that connect the donor and acceptor components of the molecular rectifier to the electrodes should be asymmetrical. Electron accepting anchor groups promote LUMO alignment with the electrodes and electron donor groups promote HOMO alignment with the electrodes.

(2) The anchoring groups are chosen to promote the energetic alignment of the LUMO and HOMO with the Fermi level of the electrodes. This creates a Fermi pinning effect that results from the mixing of the molecular states with the states of the electrodes. This promotes rectification by ensuring that in one bias direction, the frontier molecular orbitals are within the bias window and upon bias reversal the frontier molecular orbitals are outside of the bias window. This derives from changes in the chemical potential of the electrodes upon application of a bias voltage.

(3) The molecule should consist of two π-conjugated molecular fragments that are connected via a saturated bridge that serves to decouple the π-systems of the two fragments.

The design proposed by Van Dyck and Ratner based upon this criteria showed a remarkable RR of 160 at ±1.2V and consisted of two π-conjugated hexene fragments separated by a saturated butane bridge; the anchoring groups consisted

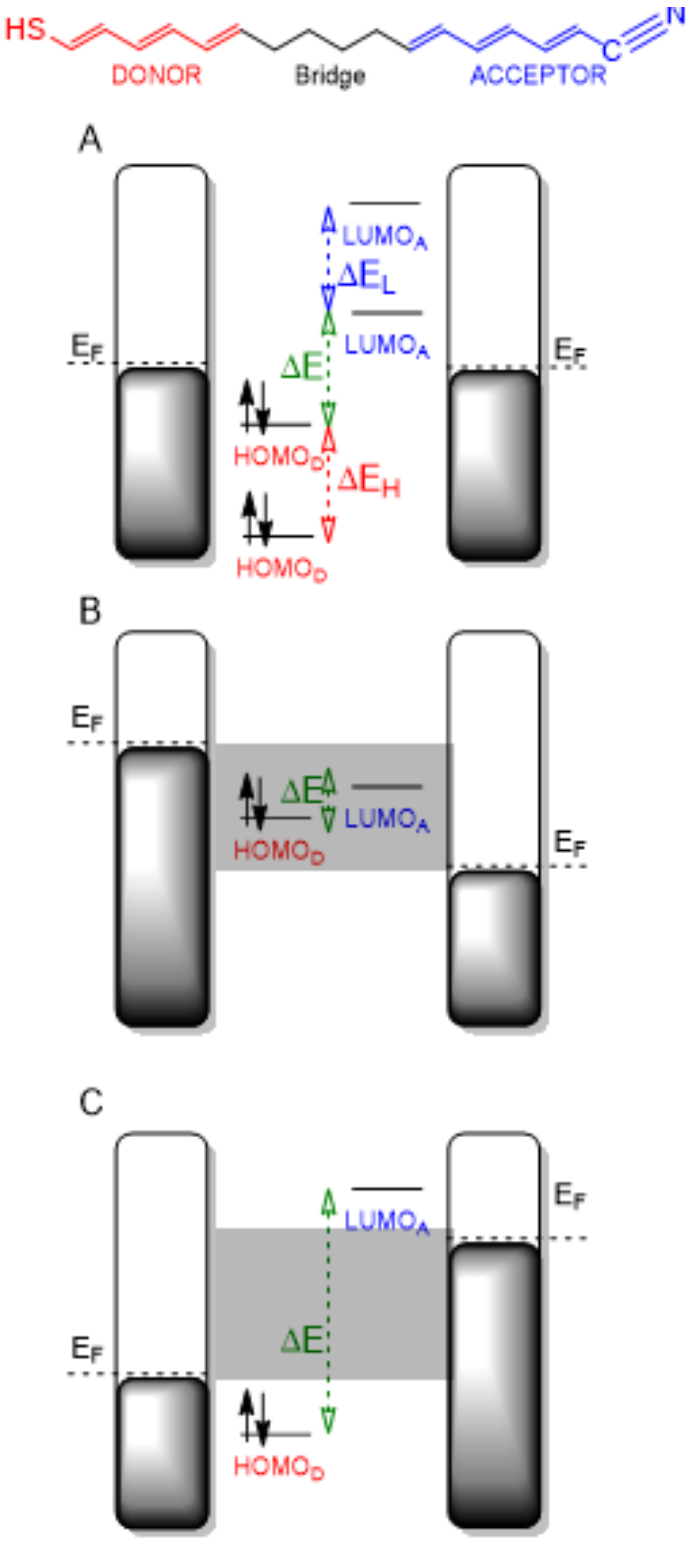

Figure 2-13. Proposed Van Dyck/Ratner rectifier based on their three design rules, consisting of a hexene fragment with thiol anchoring group (donor, shown in red) and hexene fragment with nitrile anchoring group (acceptor, shown in blue) separated by a saturated butane bridge (in black). At zero bias, the HOMO and LUMO of the donor and acceptor fragments change in energy following complexation to the electrodes and become pinned, as indicated by the red and blue dashed arrows (A). The green dashed arrow represents the HOMO/LUMO gap. This pinning causes the HOMO and LUMO to enter the bias window (shaded rectangle) at forward bias, compressing the HOMO-LUMO gap and permitting effective conduction through the molecule (B). When the bias is reversed, the pinning effect causes the HOMO/LUMO gap to increase and both orbitals move out of the bias window, causing an insulating effect in the device.

of a thiol to promote HOMO alignment and a nitrite group to promote LUMO alignment on the two hexene fragments (Figure 2-13).[1] The asymmetry of

the molecule that promotes rectification comes from the asymmetric anchoring groups to the gold electrodes, rather than asymmetry in the molecule itself. This was by design as well, as the Fermi pinning effect of the localized HOMO and LUMO has been shown to be controlled by the contacts between the electrodes and molecules, rather than a function of the properties of the molecule in isolation, as previously explained in Section 2.8. They found that by designing a molecule that promotes the pinning of the HOMO and LUMO to the E_F of their respective electrodes, the mechanism of efficient rectification comes from the compression of the HOMO-LUMO gap at forward bias, and the increase of the HOMO-LUMO gap at reverse bias, as shown in Figure 2-13B and C.

Examination of the structure of the PDT led us to postulate as to its possible role as a vectoral e- transfer conduit. The ligand itself is thought to be non-innocent in biological systems as explained in Chapter 1. The dithiolene portion of the ligand is part of a 6π electron system, in which 2e- on the dithiolene and 4 e- on the pterin ring are considered redox active. Therefore, the dithiolene can be thought as a potential e- donor fragment. The pterin portion of the molecule, which is bound to the enzymes via a series of hydrogen bonds, can potentially function as an e- acceptor, particularly in its more oxidized 10,10a dihydro and quinoid dihydro states. Interestingly, the fully reduced tetrahydro and the oxidized quinoid dihydro PDT both exemplify the Van Dyck/Ratner design rules for synthetic molecular rectifiers, indicating that nature may utilize molecular rectification in catalytic processes involving vectoral electron transfer. The 10,10a dihydro does not fulfill the Van Dyck/Ratner design rule 3 as it is fully conjugated, but this form was

included in this study as it is thought to exist in the SO family of molybdoenzymes and is therefore thought to be a biologically relevant form.[87] Furthermore, inclusion of the fully conjugated 10,10a dihydro helps determine how the nature of the bridging fragment influences the electronic communication between the donor and acceptor fragments, which could play a substantial role in both rectification behavior and the current carrying capacity of the molecule.

The relative difference in the protonation and conjugation of these three different oxidation/tautomeric states of the PDT ligand may also influence the relative directionality of the rectification, either favoring electron transfer from the Mo through the dithiolene to the pterin or in the reverse direction. Studies on the rectification behavior of a dipyrimidinyl-diphenyl molecular diode revealed a reversal of preferred electron transport direction when the dipyrimidinyl fragment was protonated; this was due to a reversal in the direction of the dipole moment of the molecule upon protonation which aligned the LUMO with the E_F of the gold electrode to promote resonant tunneling.[88,89] The RR was found to be modulated with the degree of protonation in these studies as well.

In this study, we computationally demonstrate how the RR can be modulated with changes in oxidation and tautomeric state of the PDT. Furthermore, we analyzed this rectification behavior by identifying the frontier molecular orbitals responsible for transmission. We evaluated the results of these computations in the context of the rational Van Dyck/Ratner design ‘rules’ for unimolecular rectifiers. This provides a basis for understanding how electron transfer processes occur in molybdoenzymes, via the evolutionarily conserved PDT ligand, as well as

informing further design criteria for novel biologically inspired synthetic molecular rectifiers.

2.14 References

(1) Van Dyck, C.; Ratner, M. a. Molecular Rectifiers: A New Design Based on Asymmetric Anchoring Moieties. *Nano Letters* **2015**, *15* (3), 1577–1584. https://doi.org/10.1021/nl504091v.

(2) Xiang, D.; Wang, X.; Jia, C.; Lee, T.; Guo, X. Molecular-Scale Electronics: From Concept to Function. *Chemical Reviews*. American Chemical Society April 27, 2016, pp 4318–4440. https://doi.org/10.1021/acs.chemrev.5b00680.

(3) Metzger, R. M. Unimolecular Electronics. *Chemical Reviews* **2015**, *115* (11), 5056–5115. https://doi.org/10.1021/cr500459d.

(4) Metzger, R. M. Unimolecular Rectifiers: Methods and Challenges. *Analytica Chimica Acta* **2006**, *568* (1–2), 146–155. https://doi.org/10.1016/j.aca.2006.01.051.

(5) Moore, G. M. Cramming More Components onto Integrated Circuits. *Electronics* **1965**, *38* (8), 114.

(6) Metzger, R. M. Unimolecular Electrical Rectifiers. *Chemical Reviews* **2003**, *103* (9), 3803–3834. https://doi.org/10.1021/cr020413d.

(7) Zhang, G. P.; Xie, Z.; Song, Y.; Hu, G. C.; Wang, C. K. Towards Rectifying Performance at the Molecular Scale. *Topics in Current Chemistry* **2017**, *375* (6), 1–36. https://doi.org/10.1007/s41061-017-0170-3.

(8) Aviram, A.; Ratner, M. Molecular Rectifiers. 1974, pp 277–283.

(9) Mujica, V.; Ratner, M. A.; Nitzan, A. Molecular Rectification: Why Is It so Rare? *Chemical Physics* **2002**, *281* (2–3), 147–150. https://doi.org/10.1016/S0301-0104(02)00494-9.

(10) Batra, A.; Darancet, P.; Chen, Q.; Meisner, J. S.; Widawsky, J. R.; Neaton, J. B.; Nuckolls, C.; Venkataraman, L. Tuning Rectification in Single-Molecular Diodes. *Nano Letters* **2013**, *13* (12), 6233–6237. https://doi.org/10.1021/nl403698m.

(11) Ellenbogen, J. C.; Love, J. C.; Christopher Love, J.; Love, J. C. Architectures for Molecular Electronic Computers: 1. Logic Structures and an Adder Designed from Molecular Electronic Diodes. *Proceedings of the IEEE* **2000**, *88* (3), 386–426. https://doi.org/10.1109/5.838115.

(12) Stokbro, K.; Taylor, J.; Brandbyge, M. Do Aviram - Ratner Diodes Rectify? *Journal of the American Chemical Society* **2003**, *125* (13), 3674–3675. https://doi.org/10.1021/ja028229x.

(13) Hu, G. C.; Zhang, G. P.; Li, Y.; Ren, J. F.; Wang, C. K. Proportion Effect in Diblock Co-Oligomer Molecular Diodes. *Chemical Physics Letters* **2014**, *614*, 207–213. https://doi.org/10.1016/j.cplett.2014.09.043.

(14) Hu, G. C.; Zhang, G. P.; Ren, J. F.; Wang, C. K.; Xie, S. J. Length-Dependent Inversion of Rectification in Diblock Co-Oligomer Diodes. *Applied Physics Letters* **2011**, *99* (8). https://doi.org/10.1063/1.3627169.

(15) Zhang, G. P.; Hu, G. C.; Song, Y.; Xie, Z.; Wang, C. K. Stretch or Contraction Induced Inversion of Rectification in Diblock Molecular Junctions. *Journal of Chemical Physics* **2013**, *139* (9). https://doi.org/10.1063/1.4820237.

(16) Bruot, C.; Hihath, J.; Tao, N. Mechanically Controlled Molecular Orbital Alignment in Single Molecule Junctions. *Nature Nanotechnology* **2012**, *7* (1), 35–40. https://doi.org/10.1038/nnano.2011.212.

(17) Tsuji, Y.; Staykov, A.; Yoshizawa, K. Orbital Views of Molecular Conductance Perturbed by Anchor Units. *Journal of the American Chemical Society* **2011**, *133* (15), 5955–5965. https://doi.org/10.1021/ja111021e.

(18) Yoshizawa, K. An Orbital Rule for Electron Transport in Molecules. *Accounts of Chemical Research* **2012**, *45* (9), 1612–1621. https://doi.org/10.1021/ar300075f.

(19) Yoshizawa, K.; Tada, T.; Staykov, A. Orbital Views of the Electron Transport in Molecular Devices. *Journal of the American Chemical Society* **2008**, *130* (29), 9406–9413. https://doi.org/10.1021/ja800638t.

(20) Meany, J. E.; Johnson, M. S.; Woski, S. A.; Metzger, R. M. Surprisingly Big Rectification Ratios for a Very Small Unimolecular Rectifier. *ChemPlusChem* **2016**, *81* (11), 1152–1155. https://doi.org/10.1002/cplu.201600383.

(21) Ding, W.; Negre, C. F. A.; Palma, J. L.; Durrell, A. C.; Allen, L. J.; Young, K. J.; Milot, R. L.; Schmuttenmaer, C. A.; Brudvig, G. W.; Crabtree, R. H.; Batista, V. S. Linker Rectifiers for Covalent Attachment of Transition-Metal Catalysts to Metal-Oxide Surfaces. *ChemPhysChem* **2014**, *15* (6), 1138–1147. https://doi.org/10.1002/cphc.201400063.

(22) Thong, A. Z.; Shaffer, M. S. P.; Horsfield, A. P. HOMO-LUMO Coupling: The Fourth Rule for Highly Effective Molecular Rectifiers. *Nanoscale* **2017**, *9* (24), 8119–8125. https://doi.org/10.1039/c7nr01680h.

(23) Joachim, C.; Ratner, M. a. Molecular Electronics: Some Views on Transport Junctions and Beyond. *Proceedings of the National Academy of Sciences of the United States of America* **2005**, *102* (25), 8801–8808. https://doi.org/10.1073/pnas.0500075102.
(24) Narth, C.; Gillet, N.; Cailliez, F.; Lévy, B.; de La Lande, A. Electron Transfer, Decoherence, and Protein Dynamics: Insights from Atomistic Simulations. *Accounts of Chemical Research* **2015**, *48* (4), 1090–1097. https://doi.org/10.1021/ar5002796.
(25) Tung, R. T. The Physics and Chemistry of the Schottky Barrier Height. *Applied Physics Reviews* **2014**, *1* (1). https://doi.org/10.1063/1.4858400.
(26) Chen, F.; Tao, N. J. Electron Transport in Single Molecules: From Benzene to Graphene. *Accounts of Chemical Research* **2009**, *42* (3), 429–438. https://doi.org/10.1021/ar800199a.
(27) Bostick, C. D.; Mukhopadhyay, S.; Sheves, M.; Cahen, D.; Lederman, D. Protein Bioelectronics : A Review of What We Do and Do Not Know. *Reports of Progress in Physics* **2017**, 1–158.
(28) Mujica, V.; Kemp, M.; Ratner, M. A. Electron Conduction in Molecular Wires. I. A Scattering Formalism. *The Journal of Chemical Physics* **1994**, *101* (8), 6849–6855. https://doi.org/10.1063/1.468314.
(29) Stadler, R.; Geskin, V.; Cornil, J. A Theoretical View of Unimolecular Rectification. *Journal of Physics Condensed Matter* **2008**, *20* (37), 374105. https://doi.org/10.1088/0953-8984/20/37/374105.
(30) Fisher, D. S.; Lee, P. A. Relation between Conductivity and Transmission Matrix. *Phys. Rev. B* **1981**, *23* (12), 15.
(31) Coto, P. B.; Hofmeister, C.; Prucker, V.; Weckbecker, D.; Thoss, M.; Binder, K.; M, M.; Kremer, M.; Editors, A. S.; Coto, P. B.; Hofmeister, C.; Prucker, V. Simulation of Electron Transfer and Electron Transport in Molecular Systems at Surfaces. *NIC Symposium* **2016**, *48*, 133–140.
(32) Koley, S.; Chakrabarti, S. Large Negative Differential Resistance and Rectification from a Donor–σ–Acceptor Molecule in the Presence of Dissimilar Electrodes. *Chemistry - A European Journal* **2018**, *24* (22), 5876–5882. https://doi.org/10.1002/chem.201705683.
(33) Regan, J. J.; Ramirez, B. E.; Winkler, J. R.; Gray, H. B.; Malmström, B. G.; Malmstrom, B. G. Pathways for Electron Tunneling in Cytochrome c Oxidase. *Journal of Bioenergetics and Biomembranes* **1998**, *30* (1), 35–39. https://doi.org/10.1023/A:1020551326307.
(34) Nitzan, A. Electron Transmission through Molecules and Molecular Interfaces. *Annu. Rev. Phys. Chem* **2001**, *52*, 681–750.
(35) Hopfield, J. J. Electron Transfer between Biological Molecules by Thermally Activated Tunneling. *Proceedings of the National Academy of Sciences of the United States of America* **1974**, *71* (9), 3640–3644. https://doi.org/10.1073/pnas.71.9.3640.
(36) Traub, M. C.; Brunschwig, B. S.; Lewis, N. S. Relationships between Nonadiabatic Bridged Intramolecular, Electrochemical, and Electrical Electron-Transfer Processes. *Journal of Physical Chemistry B* **2007**, *111* (24), 6676–6683. https://doi.org/10.1021/jp065520g.
(37) Wenger, O. S. How Donor - Bridge - Acceptor Energetics Influence Electron Tunneling Dynamics and Their Distance Dependences. *Accounts of Chemical Research* **2011**, *44* (1), 25–35. https://doi.org/10.1021/ar100092v.
(38) Gray, H. B.; Winkler, J. R. Long-Range Electron Transfer. *Proceedings of the National Academy of Sciences of the United States of America* **2005**, *102* (10), 3534–3539. https://doi.org/10.1073/pnas.0408029102.
(39) McConnell, H. M. Intramolecular Charge Transfer in Aromatic Free Radicals. *The Journal of Chemical Physics* **1961**, *35* (2), 508–515. https://doi.org/10.1063/1.1731961.
(40) Stadler, R.; Jacobsen, K. W. Fermi Level Alignment in Molecular Nanojunctions and Its Relation to Charge Transfer. *Physical Review B - Condensed Matter and Materials Physics* **2006**, *74* (16), 1–4. https://doi.org/10.1103/PhysRevB.74.161405.
(41) Tomfohr, J. K.; Sankey, O. F. Simple Estimates of the Electron Transport Properties of Molecules. *Physica Status Solidi (B) Basic Research* **2002**, *233* (1), 59–69. https://doi.org/10.1002/1521-3951(200209)233:1<59::AID-PSSB59>3.0.CO;2-6.
(42) van Dyck, C.; Geskin, V.; Cornil, J. Fermi Level Pinning and Orbital Polarization Effects in Molecular Junctions: The Role of Metal Induced Gap States. *Advanced Functional Materials* **2014**, *24* (39), 6154–6165. https://doi.org/10.1002/adfm.201400809.
(43) van Dyck, C.; Geskin, V.; Kronemeijer, A. J.; de Leeuw, D. M.; Cornil, J. Impact of Derivatization on Electron Transmission through Dithienylethene-Based Photoswitches in Molecular Junctions. *Physical Chemistry Chemical Physics* **2013**, *15* (12), 4392–4404. https://doi.org/10.1039/c3cp44132f.
(44) Nijhuis, C. A.; Reus, W. F.; Whitesides, G. M. Mechanism of Rectification in Tunneling Junctions Based on Molecules with Asymmetric Potential Drops. *Journal of the American Chemical Society* **2010**, *132* (51), 18386–18401. https://doi.org/10.1021/ja108311j.

(45) Kornilovitch, P. E.; Bratkovsky, A. M.; Stanley Williams, R. Current Rectification by Molecules with Asymmetric Tunneling Barriers. *Physical Review B - Condensed Matter and Materials Physics* **2002**, *66* (16), 1–11. https://doi.org/10.1103/PhysRevB.66.165436.

(46) Liu, R.; Ke, S. H.; Yang, W.; Baranger, H. U. Organometallic Molecular Rectification. *Journal of Chemical Physics* **2006**, *124* (2). https://doi.org/10.1063/1.2141955.

(47) Rodriguez-Gonzalez, S.; Xie, Z.; Galangau, O.; Selvanathan, P.; Norel, L.; van Dyck, C.; Costuas, K.; Frisbie, C. D.; Rigaut, S.; Cornil, J. HOMO Level Pinning in Molecular Junctions: Joint Theoretical and Experimental Evidence. *Journal of Physical Chemistry Letters* **2018**, *9* (9), 2394–2403. https://doi.org/10.1021/acs.jpclett.8b00575.

(48) van Dyck, C.; Ratner, M. a. Molecular Junctions: Control of the Energy Gap Achieved by a Pinning Effect. *The Journal of Physical Chemistry C* **2017**, acs.jpcc.6b07855. https://doi.org/10.1021/acs.jpcc.6b07855.

(49) Kilså, K.; Kajanus, J.; Macpherson, A. N.; Mårtensson, J.; Albinsson, B. Bridge-Dependent Electron Transfer in Porphyrin-Based Donor-Bridge-Acceptor Systems. *Journal of the American Chemical Society* **2001**, *123* (13), 3069–3080. https://doi.org/10.1021/ja003820k.

(50) Getty, S. A.; Engtrakul, C.; Wang, L.; Liu, R.; Ke, S. H.; Baranger, H. U.; Yang, W.; Fuhrer, M. S.; Sita, L. R. Near-Perfect Conduction through a Ferrocene-Based Molecular Wire. *Physical Review B - Condensed Matter and Materials Physics* **2005**, *71* (24), 2–5. https://doi.org/10.1103/PhysRevB.71.241401.

(51) Reichert, J.; Ochs, R.; Beckmann, D.; Weber, H. B.; Mayor, M.; Löhneysen, H. v. Driving Current through Single Organic Molecules. *Physical Review Letters* **2002**, *88* (17), 4. https://doi.org/10.1103/PhysRevLett.88.176804.

(52) Kubatkin, S.; Danilov, A.; Hjort, M.; Cornil, J.; Brédas, J. L.; Stuhr-Hansen, N.; Hedegård, P.; Bjørnholm, T. Single-Electron Transistor of a Single Organic Molecule with Access to Several Redox States. *Nature* **2003**, *425* (6959), 698–701. https://doi.org/10.1038/nature02010.

(53) Zhang, G. P.; Hu, G. C.; Song, Y.; Li, Z. L.; Wang, C. K. Modulation of Rectification in Diblock Co-Oligomer Diodes by Adjusting Anchoring Groups for Both Symmetric and Asymmetric Electrodes. *Journal of Physical Chemistry C* **2012**, *116* (41), 22009–22014. https://doi.org/10.1021/jp304890p.

(54) Heimel, G.; Romaner, L.; Brédas, J. L.; Zojer, E. Interface Energetics and Level Alignment at Covalent Metal-Molecule Junctions: π-Conjugated Thiols on Gold. *Physical Review Letters* **2006**, *96* (19), 2–5. https://doi.org/10.1103/PhysRevLett.96.196806.

(55) Lee, Y.; Carsten, B.; Yu, L. Understanding the Anchoring Group Effect of Molecular Diodes on Rectification. *Langmuir* **2009**, *25* (3), 1495–1499. https://doi.org/10.1021/la802923a.

(56) Kim, B.; Choi, S. H.; Zhu, X. Y.; Frisbie, C. D. Molecular Tunnel Junctions Based on π-Conjugated Oligoacene Thiols and Dithiols between Ag, Au, and Pt Contacts: Effect of Surface Linking Group and Metal Work Function. *Journal of the American Chemical Society* **2011**, *133* (49), 19864–19877. https://doi.org/10.1021/ja207751w.

(57) Dhirani, A.; Lin, P.-H. H.; Guyot-Sionnest, P.; Zehner, R. W.; Sita, L. R. Self-Assembled Molecular Rectifiers. *Journal of Chemical Physics* **1997**, *106* (12), 5249–5253. https://doi.org/10.1063/1.473523.

(58) Fu, X. X.; Zhang, R. Q.; Zhang, G. P.; Li, Z. L. Rectifying Properties of Oligo(Phenylene Ethynylene) Heterometallic Molecular Junctions: Molecular Length and Side Group Effects. *Scientific Reports* **2014**, *4*, 1–7. https://doi.org/10.1038/srep06357.

(59) Taylor, J.; Brandbyge, M.; Stokbro, K. Theory of Rectification in Tour Wires: The Role of Electrode Coupling. *Physical Review Letters* **2002**, *89* (13), 1–4. https://doi.org/10.1103/PhysRevLett.89.138301.

(60) Hille, R. The Mononuclear Molybdenum Enzymes. *Chemical Reviews* **1996**, *96*, 2757–2816. https://doi.org/10.1021/cr950061t.

(61) Basu, P.; Burgmayer, S. J. N.; Basu, Partha, Burgmeyer, S. Pterin Chemistry and Its Relationship to the Molybdenum Cofactor. *Coordination chemistry reviews* **2011**, *255* (9–10), 1016–1038. https://doi.org/10.1037/a0030561.Striving.

(62) Johnson, J. L.; Rajagopalan, K. v. Structural and Metabolic Relationship between the Molybdenum Cofactor and Urothione. *Proceedings of the National Academy of Sciences of the United States of America* **1982**, *79* (22 I), 6856–6860. https://doi.org/10.1073/pnas.79.22.6856.

(63) Xu, B., Tao, N. Measurement of Single-Molecule Resistance by Repeated Formation of Molecular Junctions. *Science* **2003**, *301*, 1221–1223. https://doi.org/10.1557/mrs2003.223.

(64) Wang, K.; Xu, B. Modulation and Control of Charge Transport Through Single-Molecule Junctions. *Topics in Current Chemistry* **2017**, *375* (1), 1–43. https://doi.org/10.1007/s41061-017-0105-z.

(65) Zhou, X. Y.; Peng, Z. L.; Sun, Y. Y.; Wang, L. N.; Niu, Z. J.; Zhou, X. S. Conductance Measurement of Pyridyl-Based Single Molecule Junctions with Cu and Au Contacts. *Nanotechnology* **2013**, *24* (46). https://doi.org/10.1088/0957-4484/24/46/465204.

(66) Krans, J. M.; van Ruitenbeek, J. M.; de Jongh, L. J. Atomic Structure and Quantized Conductance in Metal Point Contacts. *Physica B: Condensed Matter* **1996**, *218* (1–4), 228–233. https://doi.org/10.1016/0921-4526(95)00601-X.

(67) Basch, H.; Ratner, M. a. Binding at Molecule/Gold Transport Interfaces. II. Orbitals and Density of States. *The Journal of Chemical Physics* **2003**, *119* (22), 11943–11950. https://doi.org/10.1063/1.1613942.

(68) Ding, W.; Koepf, M.; Koenigsmann, C.; Batra, A.; Venkataraman, L.; Negre, C. F. A. a; Brudvig, G. W.; Crabtree, R. H.; Schmuttenmaer, C. a.; Batista, V. S. Computational Design of Intrinsic Molecular Rectifiers Based on Asymmetric Functionalization of N-Phenylbenzamide. *Journal of Chemical Theory and Computation* **2015**, *11* (12), 5888–5896. https://doi.org/10.1021/acs.jctc.5b00823.

(69) Sikri, G.; Sawhney, R. S. First Principle Approach to Elucidate Transport Properties through L-Glutamic Acid-Based Molecular Devices Using Symmetrical Electrodes. *Journal of Molecular Modeling* **2020**, *26* (4). https://doi.org/10.1007/s00894-020-4323-x.

(70) Strange, M.; Rostgaard, C.; Häkkinen, H.; Thygesen, K. S. Self-Consistent GW Calculations of Electronic Transport in Thiol- and Amine-Linked Molecular Junctions. *Physical Review B - Condensed Matter and Materials Physics* **2011**, *83* (11), 1–12. https://doi.org/10.1103/PhysRevB.83.115108.

(71) Kryachko, E. S.; Remade, F. Complexes of DNA Bases and Watson-Crick Base Pairs with Small Neutral Gold Clusters. *Journal of Physical Chemistry B* **2005**, *109* (48), 22746–22757. https://doi.org/10.1021/jp054708h.

(72) Li, Z.; Kosov, D. S. Dithiocarbamate Anchoring in Molecular Wire Junctions: A First Principles Study. *Journal of Physical Chemistry B* **2006**, *110* (20), 9893–9898. https://doi.org/10.1021/jp0610665.

(73) Zhou, J. G.; Hagelberg, F. Do Methanethiol Adsorbates on the Au(111) Surface Dissociate? *Physical Review Letters* **2006**, *97* (4), 12–15. https://doi.org/10.1103/PhysRevLett.97.045505.

(74) Cometto, F. P.; Paredes-Olivera, P.; Macagno, V. A.; Patrito, E. M. Density Functional Theory Study of the Adsorption of Alkanethiols on Cu(111), Ag(111), and Au(111) in the Low and High Coverage Regimes. *Journal of Physical Chemistry B* **2005**, *109* (46), 21737–21748. https://doi.org/10.1021/jp053273v.

(75) Rodriguez, J. A.; Dvorak, J.; Jirsak, T.; Liu, G.; Hrbek, J.; Aray, Y.; González, C. Coverage Effects and the Nature of the Metal-Sulfur Bond in S/Au(111): High-Resolution Photoemission and Density-Functional Studies. *Journal of the American Chemical Society* **2003**, *125* (1), 276–285. https://doi.org/10.1021/ja021007e.

(76) Kirk, M. L.; Shultz, D. A.; Zhang, J.; Dangi, R.; Ingersol, L.; Yang, J.; Finney, N. S.; Sommer, R. D.; Wojtas, L. Heterospin Biradicals Provide Insight into Molecular Conductance and Rectification. *Chemical Science* **2017**, *8* (8), 5408–5415. https://doi.org/10.1039/C7SC00073A.

(77) Anderson, P. W. New Approach to the Theory of Superexchange. *Physical Review* **1959**, *115* (1).

(78) Nitzan, A. A Relationship between Electron-Transfer Rates and Molecular Conduction. *Journal of Physical Chemistry A* **2001**, *105* (12), 2677–2679. https://doi.org/10.1021/jp003884h.

(79) Armstrong, N.; Hoft, R. C.; McDonagh, A.; Cortie, M. B.; Ford, M. J. Exploring the Performance of Molecular Rectifiers: Limitations and Factors Affecting Molecular Rectification. *Nano Letters* **2007**, *7* (10), 3018–3022. https://doi.org/10.1021/nl0714435.

(80) Díez-Pérez, I.; Hihath, J.; Lee, Y.; Yu, L.; Adamska, L.; Kozhushner, M. A.; Oleynik, I. I.; Tao, N. Rectification and Stability of a Single Molecular Diode with Controlled Orientation. *Nature Chemistry* **2009**, *1* (8), 635–641. https://doi.org/10.1038/nchem.392.

(81) Fujii, S.; Tada, T.; Komoto, Y.; Osuga, T.; Murase, T.; Fujita, M.; Kiguchi, M. Rectifying Electron-Transport Properties through Stacks of Aromatic Molecules Inserted into a Self-Assembled Cage. *Journal of the American Chemical Society* **2015**, *137* (18), 5939–5947. https://doi.org/10.1021/jacs.5b00086.

(82) Weigend, F.; Elbing, M.; Ochs, R.; Koentopp, M.; Fischer, M.; Ha, C. von; Evers, F.; Weber, H. B.; Mayor, M. A Single-Molecule Diode. **2005**.

(83) Capozzi, B.; Xia, J.; Adak, O.; Dell, E. J.; Liu, Z. F.; Taylor, J. C.; Neaton, J. B.; Campos, L. M.; Venkataraman, L. Single-Molecule Diodes with High Rectification Ratios through Environmental Control. *Nature Nanotechnology* **2015**, *10* (6), 522–527. https://doi.org/10.1038/nnano.2015.97.

(84) Perrin, M. L.; Galán, E.; Eelkema, R.; Thijssen, J. M.; Grozema, F.; van der Zant, H. S. J. J. A Gate-Tunable Single-Molecule Diode. *Nanoscale* **2016**, *8* (16), 8919–8923. https://doi.org/10.1039/C6NR00735J.

(85) Perrin, M. L.; Galan, E.; Eelkema, R.; Grozema, F.; Thijssen, J. M.; van der Zant, H. S. J. Single-Molecule Resonant Tunneling Diode. *Journal of Physical Chemistry C* **2015**, *119* (10), 5697–5702. https://doi.org/10.1021/jp512803s.

(86) Bruot, C.; Hihath, J.; Tao, N. Mechanically Controlled Molecular Orbital Alignment in Single Molecule Junctions. *Nature Nanotechnology* **2012**, *7* (1), 35–40. https://doi.org/10.1038/nnano.2011.212.

(87) Rothery, R. a.; Stein, B.; Solomonson, M.; Kirk, M. L.; Weiner, J. H. Pyranopterin Conformation Defines the Function of Molybdenum and Tungsten Enzymes. *Proceedings of the National Academy of Sciences* **2012**, *109* (37), 14773–14778. https://doi.org/10.1073/pnas.1200671109.

(88) Morales, G. M.; Jiang, P.; Yuan, S.; Lee, Y.; Sanchez, A.; You, W.; Yu, L. Inversion of the Rectifying Effect in Diblock Molecular Diodes by Protonation. *Journal of the American Chemical Society* **2005**, *127* (30), 10456–10457. https://doi.org/10.1021/ja051332c.

(89) Zhang, G. P.; Hu, G. C.; Li, Z. L.; Wang, C. K. Theoretical Studies on Protonation-Induced Inversion of the Rectifying Direction in Dipyrimidinyl-Diphenyl Diblock Molecular Junctions. *Journal of Physical Chemistry C* **2012**, *116* (5), 3773–3778. https://doi.org/10.1021/jp211021t.

3. Chapter 3- Rectification behavior of the evolutionarily ancient pyranopterin dithiolene ligand of molybdoenzymes

3.1 Methods

To assess the rectification behavior of the pyranopterin dithiolene ligand (PDT), we utilized a computational approach in which the PDT is anchored to two gold electrodes as a molecular bridge to allow us to compute the electron transport properties of the three molecules under positive and negative bias (Figure 3-1). The molecular junctions were constructed in Atomistix ToolKit (ATK 2016.0 v16.3).[1] Each molecular junction consists of a central scattering region and a left and right semi-infinite Au (111) electrode with periodic boundary condition in the z direction, the direction of transport in these calculations. Each electrode consists of nine layers, each layer consisting of a 3 x 3 array of Au (111) atoms, totaling 81 gold atoms per electrode. Within the central region, each construct used in this study was oriented with the dithiolene sulfurs anchored to the left electrode and the amine anchoring group on the pterin attached to the right electrode. That was to ensure that the direction of bias-dependent e- transport through the molecules remained consistent during analysis. It should be noted that the direction of e- transport is always opposite the direction of current flow through the device, as is the convention in electronics.[2]

Prior to complexation to the electrodes, each molecule was first optimized in Gaussian 09 with 6-311g(d,p) basis set and a B3LYP functional. Following complexation to the gold electrodes, the construct is optimized again by first

optimizing the electrodes, attaching the previously optimized molecule, then rigidly constraining the position of the gold atoms while allowing the distance between the

Figure 3-1. Schematic of the orientation of the tetrahydro form of PDT, complexed to the flat gold electrodes with respect to electron flow under bias. The direction of electron transport is in the Z direction, as indicated.

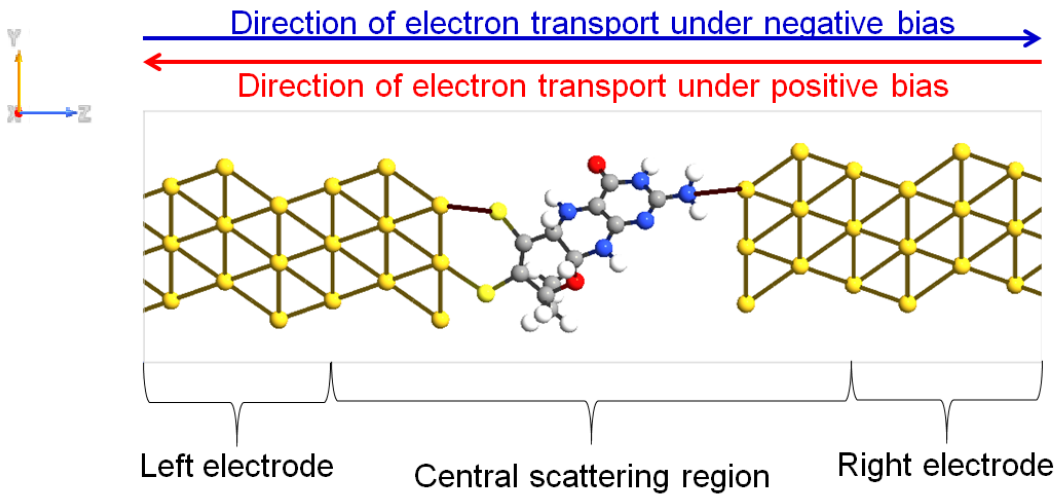

molecule and electrodes to optimize. The bulk optimization was performed using ATK-DFT with a Perdew Zunger local density approximation (LDA-PZ) exchange correlation, with a single zeta basis set on all gold atoms and a double zeta basis set on all other atoms. The density mesh cut-off for the real space grid was set to 75 Hartrees and a k-point sampling of 5 x 5 was used in the x and y directions, both chosen after extensive convergence analysis. Following optimization, the bulk configuration was converted into the final device geometry for use in all transport calculations. In the device configuration, the k-point sampling in the x, y, and z directions was 5 x 5 x 51, respectively.

In the z direction, which is the direction of transport, Dirichlet fixed boundary conditions were used. The x and y boundary conditions are defined by the program; the default parameterization is periodic for the x and y directions. The

non-equilibrium Green's function (NEGF) method, in conjunction with ATK DFT methods, was employed to assess the electron transport properties of the device. The temperature for all calculations was kept at 300K.

3.2 Overview of electrode/molecule/electrode device

For assessing the rectification behavior of the PDT, the molecule was attached to the left electrode via the two dithiolene sulfur atoms and to the right electrode via the terminal amine group on the pyrimidine ring of the pterin. Both sulfur and amine groups have been used as anchoring groups to gold in prior computational work.[3,4] Sulfur electronically couples more strongly to gold than amine, which helps further draw the analogy between the gold electrodes and the active site in XO family enzymes, where the PDT coordinates to the Mo through the dithiolene sulfurs and the pterin component is more weakly coupled to the first iron sulfur cluster in the electron transfer chain because it lacks direct covalent bonds to that structure.[5–9] Thus, we can expect the stronger coupling of the dithiolene sulfurs to the left gold electrode to be analogous to the covalent bonding between Mo and the dithiolene sulfurs in the enzyme. Furthermore, the weaker coupling between the terminal amine on the pyrimidine ring and the right gold electrode mimics the weaker, through-space interaction between the PDT ligand and the first iron sulfur cluster in XO family enzymes.

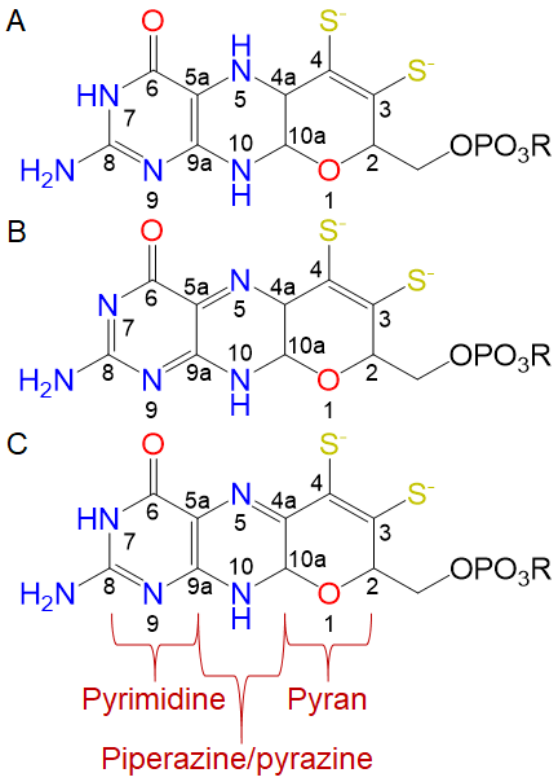

Figure 3-2. Structure of the pyranopterin dithiolene (PDT). Tetrahydro (A), quinoid dihydro (B), and 10,10a dihydro (C) forms are shown. The dithiolene sulfurs coordinate to Mo/W in the active site of the enzymes. The pterin component of the PDT is comprised of the pyrimidine and piperazine/pyrazine rings and will be referred to as the pterin component in the text.

As the anchoring groups for each of the three PDT forms in this study are identical; the primary difference in the rectification behavior of these molecules arises from the degree of oxidation and conjugation present in the different oxidation/tautomeric states. Therefore, we assessed rectification behavior in terms of Van Dyck/Ratner design rule 3.[10] The fully reduced tetrahydro has two π-conjugated molecular fragments that are decoupled by the presence of hydrogen atoms at N5, N10 and C4a (Figure 3-2A). Oxidation of the tetrahydro to 10,10a dihydro allows π-coupling between the two fragments that were previously decoupled through removal of the N5 and C4a hydrogens (Figure 3-2C). Quinoid 4a,10a-dihydro, which will henceforth be referred to as quinoid (Figure 3-2B) is a tautomer of the two-electron oxidized 10,10a dihydro, but like tetrahydro contains a saturated component separating the two π-conjugated fragments, due to the presence of a hydrogen at C4a. By utilizing these three different forms of the PDT, we can assess how e- transport is influenced by

the relative oxidation state of the molecule (i.e. reduced tetrahydro vs. the oxidized 10,10a dihydro and quinoid forms) as well as the degree of conjugation across the molecule (i.e. fully conjugated 10,10a dihydro vs. tetrahydro and quinoid forms).

Based upon examination of the structures of each of the PDT forms, shown in Figure 3-2, we were able to make some preliminary hypotheses. We expected that the fully conjugated 10,10a dihydro would be an excellent e- transport conduit as it is fully π-conjugated. The tetrahydro and quinoid forms have saturated components that interrupt the π-conjugation in the middle of the molecule and would hinder efficient e- transport. However, we would expect that based on the Van Dyke-Ratner Design Rule 3, the 10,10a dihydro PDT would make an inefficient rectifier based upon its more conjugated nature.[10] The tetrahydro and quinoid dihydro forms fulfill this design criteria by possessing two molecular fragments which are conjugated that are separated by a saturated component in the middle of the two fragments.

3.3 Analysis of the I(V) curves

The voltage dependent current I(V) was calculated using the Landauer- Buttiker formula, which relates the transmission probability to conductance through a molecular junction by integration of the transmission function.[11]

As the bias is applied in the positive and negative directions, a bias window opens about the Fermi level (E_F) of the gold electrodes. Only the transmission peaks that lie within the bias window are integrated to produce the I(V) curves; the I(V) curve is thus constructed using a series of transmission spectra obtained at different

positive and negative bias voltages. Thus, the bias windows indicated by the dashed lines in Figure 3-3, represent the positive and negative bias voltages that were applied to obtain the maximum rectification ratio (RR_{max}), which is a ratio of the relative current recorded at a negative bias voltage (I_-) over the current recorded at positive bias voltage (I_+). The bias voltages that are used to obtain a RR are the same in magnitude, only the direction of electron transport changes with the application of a positive and negative bias, as indicated in Figure 3-1. To obtain the RR_{max} for each molecule, the RR was plotted as a function of absolute bias voltage, as shown in Figure 3-4. The bias at which the RR_{max} was achieved for each molecule was subsequently used for further analysis of the mechanisms by which rectification occurs in these molecules.

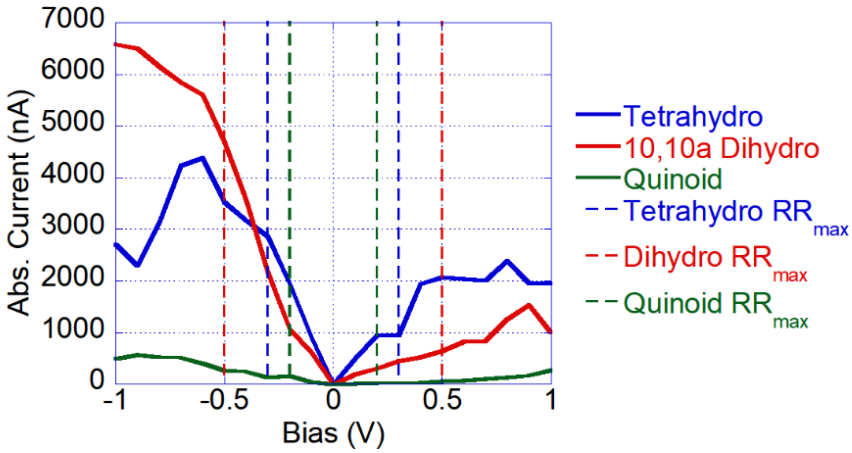

Figure 3-3. IV curve plotted as bias voltage vs. the absolute value of the current. The bias windows at which the maximum rectification ratio occurs (RR_{max}) is indicated by the dashed lines. The Fermi level (E_F) of the electrodes is represented as 0V bias.

Our electron transport computations show that the current carrying capacity of the three PDT forms follow the order 10,10a dihydro > tetrahydro > quinoid dihydro as shown in the IV curve (Figure 3-3). Tetrahydro has a RR_{max} of 3.03 at 0.3V, which makes it the poorest rectifier out of the three forms, an unexpected result based

upon our preliminary examination of its structure. Quinoid has the greatest RR_{max} of the three forms, 10.00 at 0.2V bias, which is comparable to the rectification ratios of many synthetic rectifiers. 10,10a dihydro has a RR_{max} of 7.14 at 0.5V making this form a surprisingly effective rectifier despite its violation of the Van Dyke/Ratner Design Rule 3 by its more conjugated structure.[10]

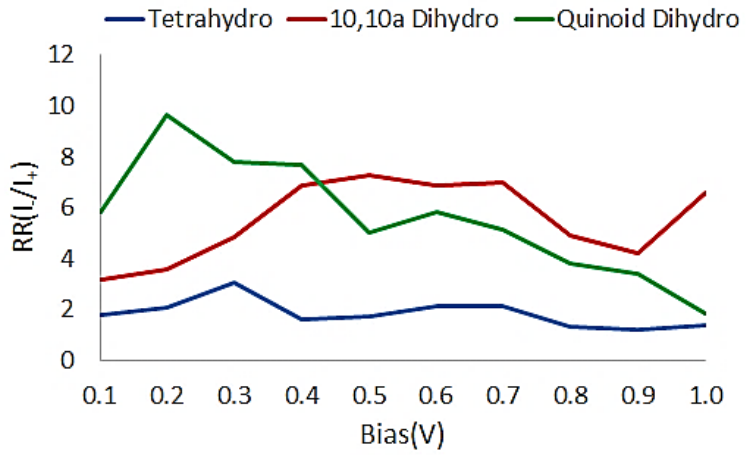

Figure 3-4. RR vs. bias voltage. The indicated bias voltage is the absolute value of the positive and negative biases applied to obtain the RR. The higher RR obtained for each molecule is RR_{max}; the bias at which this occurs was used for subsequent analysis.

Based on the results of the IV curve analysis, we can speculate that the modest current carrying capacity of the quinoid would indicate that it would be a poor electron transfer conduit in a biological setting and its electronic contribution to the active site may serve to modulate the reduction potential on Mo. Interestingly, all three forms preferentially transport electrons from the dithiolene (donor) to pterin (acceptor). This provides supporting evidence that XO family enzymes, which are thought to contain a tetrahydro PDT, utilize the ligand for electron transfer in the direction Mo->dithiolene->pterin->iron-sulfur cluster.[12] The preferred electron transport direction we observe in our computational results is

also identical to the ILCT observed for the Mo(IV) quinoxalyl-dithiolene ligand model of a 10,10a dihydro PDT.[13,14]

3.3 Rectification Ratios

When the average current at a given bias is plotted as a function of its RR_{max} at the same bias, as shown in Figure 3-5, we observe that in the tetrahydro and quinoid forms the current carrying capacity of the PDT ligand is decreased as the rectifying behavior of the molecule is enhanced.[15] This effect is attributed to the interruption of π conjugation across the molecule by the addition of hydrogens at strategic positions, which decouples the electron donor, the dithiolene, from the electron acceptor, the pterin. Surprisingly, the 10,10a dihydro is a 'rule-breaker' in that it has the highest current carrying capacity of the three forms while retaining a RR_{max} of ~7, remarkable when considering many synthetic rectifiers have a RR_{max} of 10 or less.[16–21] The efficiency of the 10,10a dihydro as a conductor is evident due to its more conjugated structure but examination of the structure alone does not explain the high RR observed.

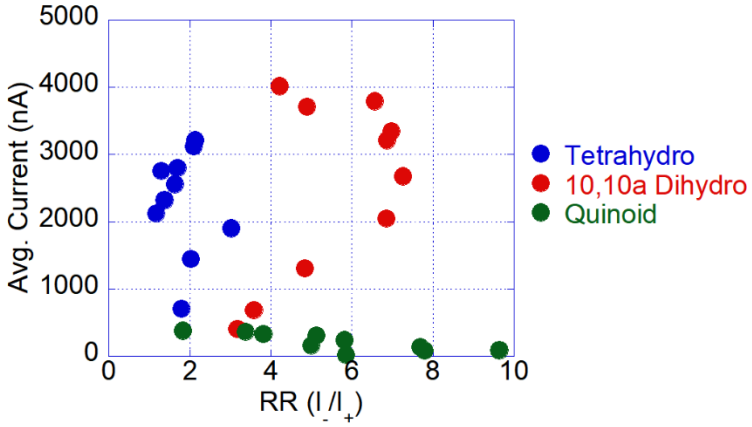

Figure 3-5. RR vs. average current plot. Each data point represents the values taken at +/- the bias voltage. The average current is the average of the currents produced at forward (I_-) and reverse (I_+) biases of the same magnitude.

3.4 Relationship between transmission, transmission eigenchannels, and MPSH states

For greater clarity of the mechanisms by which rectification occurs, we chose the forward and reverse bias that gave the greatest RR for each molecule for the remainder of our analysis. To explain the rectification behavior observed in the IV curve analysis, particularly the unusual rectification behavior of the 10,10a dihydro PDT, we explored the mechanism by which each molecule functions in electron transport by analyzing the changes in the transmission spectra under bias and the molecular orbitals contributing to conduction. The diagonalization of the block matrix of the scattering region from the self-consistent non-equilibrium Hamiltonian results in the molecular projected self-consistent Hamiltonian (MPSH). The MPSH states correspond to molecular orbitals that are energetically perturbed upon complexation to the left and right electrodes, where they both shift in energy and broaden, and allow us to identify the resonant molecular orbitals contributing to transmission.[22]

However, as the MOs hybridize with the states of the gold electrodes, it is more useful to analyze transmission through the molecular bridge using transmission eigenchannels, which correspond to the scattering state from one electrode to the other electrode which arise from molecular orbitals and are the result of the diagonalization of the transmission matrix.[23,24] Transmission eigenchannels represent defined scattering states with a transmission probability between 0 and 1; at a particular energy, several transmission eigenchannels may contribute to the total transmission at that energy.[24] For our purposes, we selected the transmission

eigenchannel with the greatest contribution to the transmission peak for analysis, as the other transmission eigenchannels often contribute to the peak by orders of magnitude less than the primary transmission eigenchannel. The transmission eigenchannel complex wave function can be visualized, and aid identification of the molecular orbitals involved in transport. This is critical to our analysis as transmission peaks typically have contributions from more than one molecular orbital, so even though a particular MPSH state is energetically resonant with a transmission peak, the transmission peak may not fully arise due to the sole contribution of that particular MPSH state. The mixing of frontier orbitals contributes to formation of transmission eigenstates that lie within the bias window, which creates channels for e- transport through the molecule.

As the IV curves are obtained by integration of the transmission peaks within the bias window at different bias voltages, we can expect that the rectification behavior of the different PDT forms can be observed by the presence of transmission peaks within the bias window at forward bias, and the absence or attenuation of transmission peaks within the bias window upon bias reversal. The MPSH states that are expected to contribute to transmission will be energetically near the Fermi level (E_F); identification of the MPSH states that contribute to the transmission peaks within the bias window will allow us to identify the molecular orbitals essential for e- transport through the molecule. Sharp peaks in the transmission spectra indicate a resonance tunneling effect taking place at that energy through MPSH states.[25] The relative contribution of these MPSH states to peaks in the transmission spectra were calculated by assessing the projected weight of each

MPSH state to the transmission eigenchannel at a given energy (Tables 3-1-through 3-3).

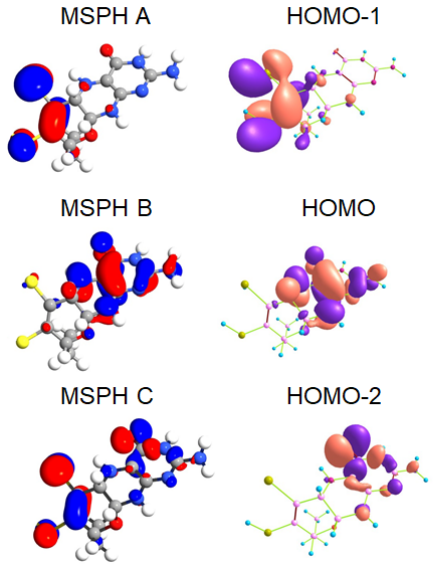

Figure 3-6. The tetrahydro PDT MPSH states A, B, and C are compared on the right to their corresponding molecular frontier orbitals.

Bias(V)	+0.3		-0.3		
MPSH	-0.18eV	-0.34eV	-0.04eV	-0.16eV	-0.46eV
A	-	0.25	-	0.06	0.10
B	0.95	-	0.54	0.92	0.08
C	-	0.60	0.27	-	0.75

Table 3-1. Projected weight of tetrahydro MPSH states for the primary transmission eigenchannel at the energies where peaks occur in the transmission spectra. The dashes (-) refer to a calculated projected weight value of <0.05 indicating <5% contribution to transmission peak at energy indicated in table.

The tetrahydro PDT has a maximum rectification ratio (RR_{max}) of ~3.03 at ±0.3V bias. At -0.3V bias the transmission peak within the bias window at -0.04eV (Figure 3-8B), is calculated to contain 54% MPSH B and 27% MPSH C (Table 3-1). MPSH B is a filled orbital (HOMO) localized on the pterin (Figure 3-6) but mixing with MPSH C (HOMO-2), which is a delocalized state that contains dithiolene character permits formation of a delocalized state. However, the transmission eigenchannel (Figure 3-8B, inset) occurring at this energy is a localized state on the dithiolene, resembling MPSH A (HOMO-1). As transmission eigenchannels include an incident state and a reflective state, the two states can destructively interfere, causing the amplitude of the transmission eigenchannel wavefunction to approach zero on the pterin portion of the molecule.[23]

MPSH A (HOMO-1), a dithiolene state, remains energetically pinned to the left electrode to which the dithiolene sulfurs are anchored. The peak at -0.16eV that occurs at -0.3V bias is 92% MPSH B (HOMO) with 6% MPSH A (HOMO-1). Again, the mixing of a pterin state, MPSH B, with a dithiolene state, MPSH A, contributes to a delocalized state which accounts for a large peak in transmission at this energy.

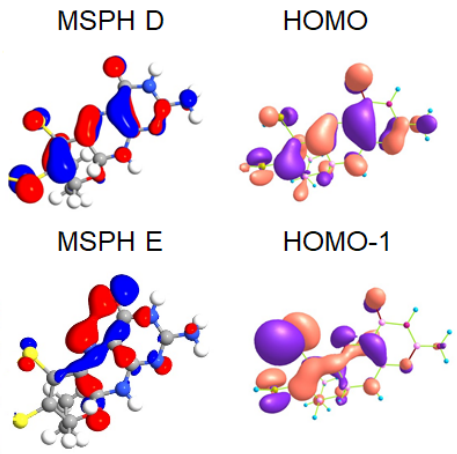

Figure 3-7. The 10,10a dihydro PDT MPSH states D and E are compared on the right to their corresponding molecular frontier orbitals.

Bias(V)	+0.5		-0.5	
MPSH	-0.32eV	-0.54eV	-0.16eV	-0.78eV
D	0.88	0.79	0.92	-
E	-	-	-	0.21

Table 3-2. Projected weight of the 10,10a dihydro MPSH states for the primary transmission eigenchannel at the energies where peaks occur in the transmission spectra. The dashes (-) refer to a calculated projected weight value of <0.05 indicating <5% contribution to transmission peak at energy indicated in table.

Examination of the transmission spectra for 10,10a dihydro allows for rationalization of its surprising rectification behavior (Figure 3-8C and D). A large transmission peak enters the bias window at -0.5V bias, occurring at -0.16eV, is 92% MPSH D (Table 3-2). MPSH D is a π orbital delocalized over the dithiolene and pterin (Figure 3-7), resembling the molecular HOMO (Figure 3-7) that accounts for 10,10a dihydro's large current carrying capacity; the primary transmission eigenchannel that contributes to the transmission peak strongly resembles MPSH D (HOMO) (Figure 3-8D, inset). The absence of appreciable transmission peaks within the bias window at +0.5V bias accounts for the diminished current flow at this bias as seen in Figure 3-3. This

indicates that the rectification mechanism of 10,10a dihydro is dependent upon the presence or absence of peaks within the bias window which are resonant with delocalized molecular states and implies that rectification can occur even in a highly conjugated molecule. A pinning effect of MPSH D to the left electrode is evident, as shown in Figure 3-8C and D, indicating that the interaction between the anchoring dithiolene sulfurs and the left electrode is a critical component 10,10a dihydro's rectifying behavior. The rectification behavior that is primarily attributed to MPSH D is supported by the study by Burgmeyer *et al.* in which an analogue of 10,10a dihydro is shown to have a ILCT from dithiolene to pterin that is mediated by out-of-plane dithiolene orbitals.[13] MPSH D is comprised of out-of-plane dithiolene and pterin orbitals.

Figure 3-8. Transmission spectra for tetrahydro at +0.3V (A) and -0.3V bias (B), 10,10a dihydro at +0.5V (C) and -0.5V bias (D), and quinoid at +0.2V (E) and -0.2V bias (F). The MPSH state energies are indicated to demonstrate Fermi level pinning of the tetrahydro and 10,10a dihydro PDT forms. The primary transmission eigenchannel of the largest peak within the bias window for each PDT are shown in the insets.

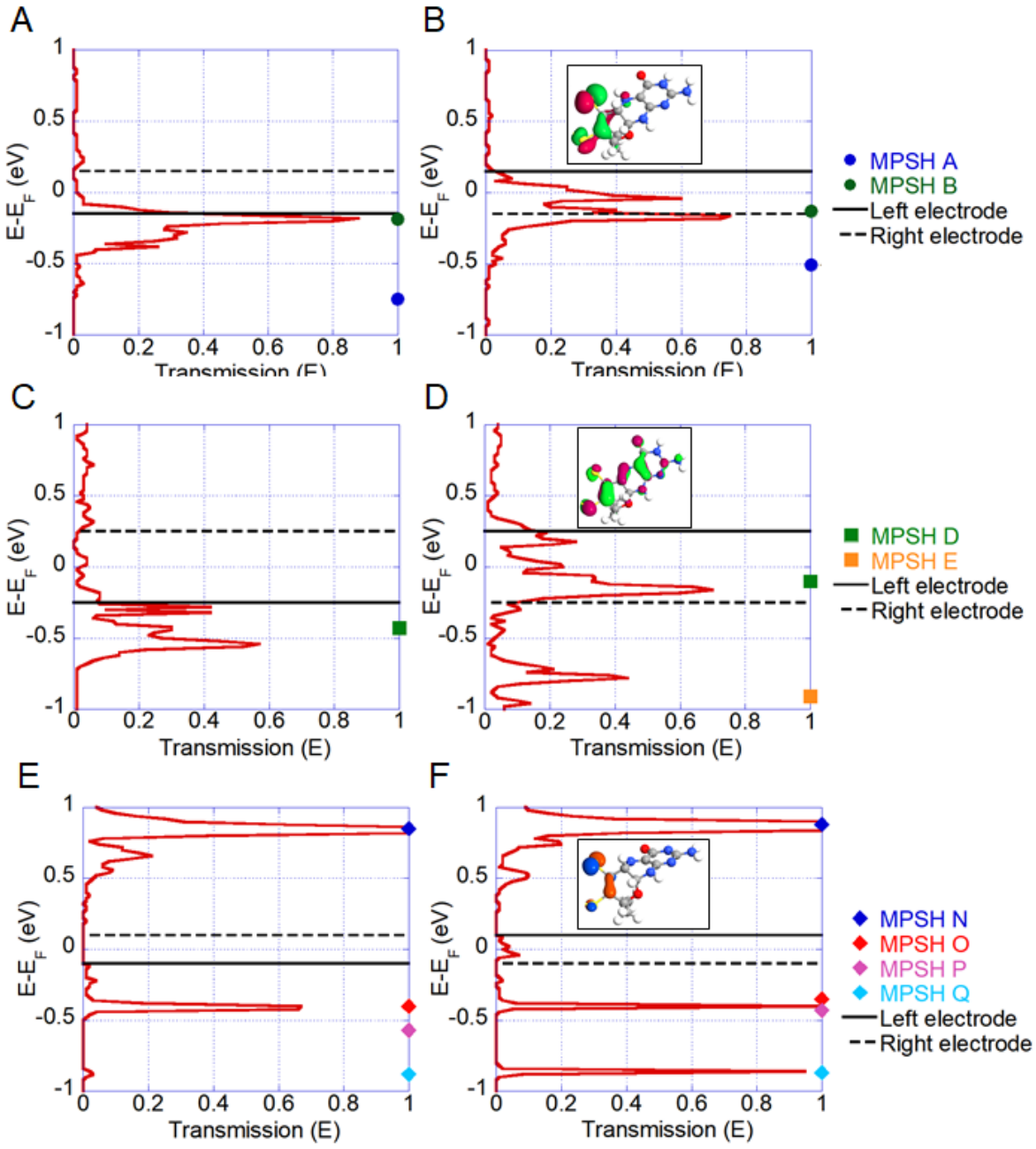

The transmission spectra of the quinoid shows a very weak transmission peak that is present in the bias window at -0.2V bias and is absent upon bias reversal (Figure

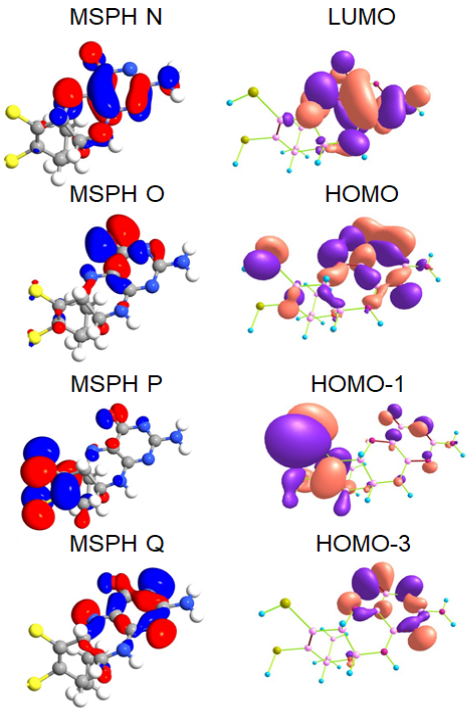

Figure 3-9. The quinoid PDT MPSH states N, O, P, and Q are compared on the right to their corresponding molecular frontier orbitals.

3-8E and F). Unlike the tetrahydro and 10,10a dihydro, the quinoid has a large transmission peak that is resonant with MPSH N, which corresponds to the LUMO of the free molecule (Figure 3-9). The LUMO of the quinoid is analogous to the HOMO of the reduced tetrahydro, which becomes empty when the tetrahydro is oxidized to the quinoid. However, once the free quinoid is complexed to the gold electrodes, the LUMO level becomes filled and electron transport through the quinoid is a hole transfer process.[26] At -0.2V bias, the primary transmission eigenchannel contributing to the transmission peak at -0.02eV is comprised of 43% MPSH O and 17% MPSH P (Table 3-3); both MPSH states contain dithiolene and pterin character (Figure 3-9). As seen with the tetrahydro PDT, the transmission eigenchannel displays destructive interference with an incident state and a reflective state, which again causes the amplitude of the transmission eigenchannel wavefunction to approach zero on the pterin portion of the molecule (Figure 3-8F, inset).[23]

3.5 Analysis of the density of states

To further understand the differences in rectifying behavior between the three PDT forms we assessed the contributions of individual parts of the molecules to the

density of states. In Figure 3-11, the projected device density of states (PDDOS) is broken down by molecular fragments consisting of the dithiolene (sulfur atoms, C3 and C4), the pterin (which consists of the pyrimidine and piperazine rings), and the terminal amine group that anchors the molecule to the right electrode (Figure 3-10).

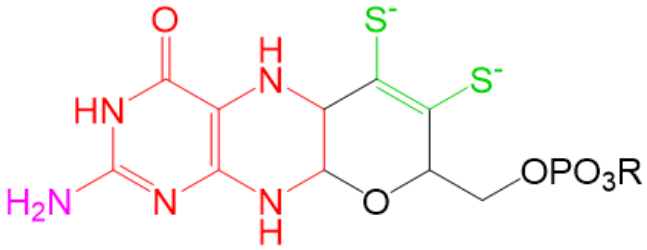

Figure 3-10. Color coded structure of tetrahydro PDT that indicates how the PDDOS is broken down by molecular fragments consisting of the dithiolene (sulfur atoms, C3 and C4) in green, the pterin (which consists of the pyrimidine and piperazine rings) in red, and the terminal amine group that anchors the molecule to the right electrode in pink.

The resultant PDDOS broken down by molecular fragment is plotted as a function of energy relative to the average Fermi level (E_F) of the two electrodes (Figure 3-11). The local device density of states (LDDOS) is projected onto the molecule and shown in the insets (Figure 3-11). This provides a visual representation of the individual contributions from each fragment to the DOS at the energy indicated. At +0.3V, the DOS peaks for tetrahydro within the bias window are less than half the amplitude of the peaks occurring at -0.3V but remain attributable to an out-of-plane dithiolene state localized on the anchoring sulfur atoms (Figure 3-11A and B). At +0.3V, the peaks occurring in the energy

Bias(V)	+0.2		-0.2			
MPSH	0.84eV	-0.42eV	0.88eV	-0.02eV	-0.40eV	-0.86eV
N	0.97	-	0.97	-	-	-
O	-	0.69	-	0.43	-	-
P	-	0.27	-	0.17	0.64	-
Q	-	-	-	-	0.35	0.99

Table 3-3. Projected weight of the quinoid MPSH states for the primary transmission eigenchannel at the energies where peaks occur in the transmission spectra. The dashes (-) refer to a calculated projected weight value of <0.05 indicating <5% contribution to transmission peak at energy indicated in table.

range of -0.15 to -0.26eV are a mixture of dithiolene and pterin states; the projection of these states onto the molecule resembles a linear combination of MPSH A and B, the HOMO-1 and HOMO (Figure 3-6), respectively.

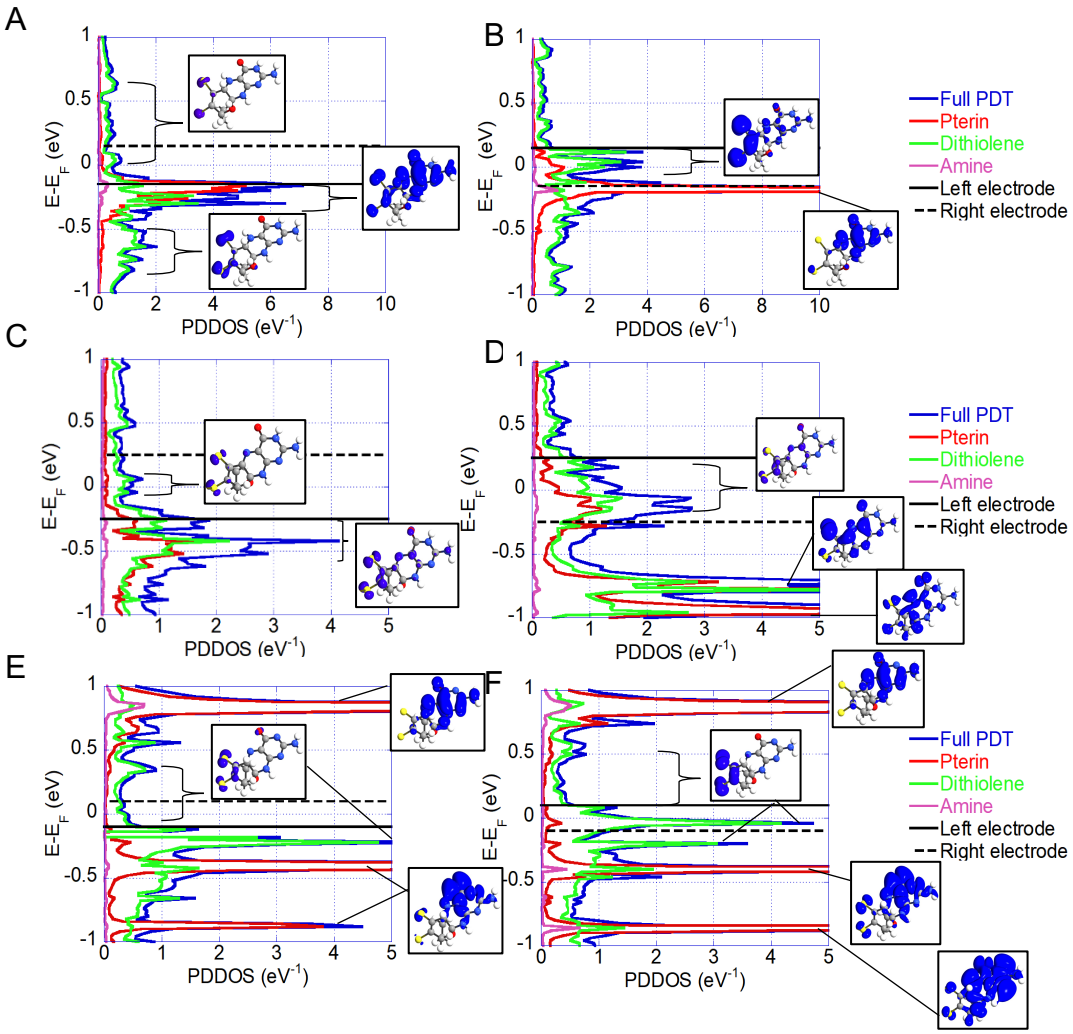

Figure 3-11. Projected device density of states (PDDOS) for tetrahydro at +0.3V (A) and -0.3V (B), for 10,10a dihydro at +0.5V (C) and -0.5V (D), and for quinoid at +0.2V (E) and -0.2V (F). The PDDOS is broken down by molecular fragments consisting of the dithiolene (sulfur atoms, C3 and C4), the pterin (which consists of the pyrimidine and piperazine rings), and the terminal amine group that anchors the molecule to the right electrode and plotted as a function of energy relative to the average Fermi level of the two electrodes. The PDDOS of the full PDT is indicated by the blue line. Insets show the local device density of states (LDDOS) at a particular energy projected onto the molecule; all are shown at the same isovalue for comparison purposes. The color code corresponds to the fragments shown in Figure 3-10.

At -0.3V, the tetrahydro form shows a high DOS within the bias window that is attributable to a state that is mostly localized on the dithiolene but shows some delocalization onto the pterin (Figure 3-11B); this again resembles a linear combination of MPSH A and B, the HOMO-1 and HOMO (Figure 3-6). The presence of a delocalized state within the bias window at -0.3V bias provides an efficient channel for current flow and the absence of such a state upon bias reversal causes a loss of this current carrying efficiency, leading to an asymmetric IV curve. Also, at -0.3 bias, the tetrahydro form shows a large DOS peak arising from a pterin state occurs at the same energy as the previously observed transmission peak, -0.15eV, and resembles MPSH B (HOMO) when projected onto the molecule (Figure 3-6). The tail of this peak enters the bias window and mixes with the dithiolene states; the molecular projection of the states resembles MPSH A, corresponding to the HOMO-1, with some amplitude on the pterin.

The DOS plots of 10,10a dihydro form further reveal the origin of its remarkable rectification behavior (Figure 3-11C and D). At +0.5V, the DOS peaks within the bias window are reduced in amplitude compared to the bias occurring at the energy range of 0.06 to -0.04eV, upon bias reversal. Examination of the molecular composition of these peaks show that they contain mostly dithiolene character, and when projected onto the molecule resemble an in-plane dithiolene orbital localized on the anchoring sulfur atoms. In contrast, the DOS peaks occurring at this energy range under -0.5V bias contain an appreciable amount of pterin character mixed into the dithiolene states. Projection of these states onto the molecule reveal an out-of-plane dithiolene orbital mixed with an out-of-plane pterin

orbital, resembling MPSH D, the molecular HOMO (Figure 3-7). Consistent with the transmission spectra and MPSH analysis, the rectification behavior of 10,10a dihydro can be attributed to the presence of a delocalized state within the bias window at negative bias voltage that is absent at positive bias voltage; this delocalized state also provides a highly efficient current carrying channel at negative bias voltage.

At +0.2V bias, the DOS plot for quinoid shows a region of low DOS within the bias window that is almost entirely out-of-plane dithiolene states observable in the molecular projection (Figure 3-11E and F). A large peak located at 0.84eV is attributable to a pterin state which resembles the molecular LUMO/MPSH N (Figure 3-9). As observed in the corresponding peaks occurring at this energy in the transmission spectra (Figure 3-8E and F), this DOS peak does not alter much in energy upon reversal of bias to -0.2V (Figure 3-11E and F). Within the bias window at -0.2V, there is a DOS peak that occurs at -0.04eV that is mainly dithiolene in origin but contains about 8% contribution from the pterin (Figure 3-11F). When this state is projected onto the molecule it appears as an out-of-plane state localized on the dithiolene. This accounts for the poor current-carrying capacity of the quinoid, as the states available within the bias window at -0.2V bias are localized almost entirely on the dithiolene. The small pterin contribution is thought to provide enough delocalization to allow some current flow at this bias, but when the bias is reversed to +0.2V, the pterin component of the DOS within the bias window becomes negligible. The absence of any delocalization of the DOS creates an insulating effect within the device.

3.6 Relationship between density of states and transmission

To further examine the relationship between delocalization of the DOS and transmission spectra peaks at corresponding energies, we plotted the DOS of the pterin component multiplied by the DOS of the dithiolene component of the PDT as a function of energy and overlaid this plot with the corresponding transmission spectra at the biases at which maximum RR was observed (Figure 3-12). An observable peak in the DOS in these plots indicate a delocalized state that possesses both dithiolene and pterin character. We observed that the DOS peaks energetically corresponded to the peaks in the transmission spectra, indicating that transmission is dependent upon a delocalized state that contains both dithiolene and pterin character at that particular energy.

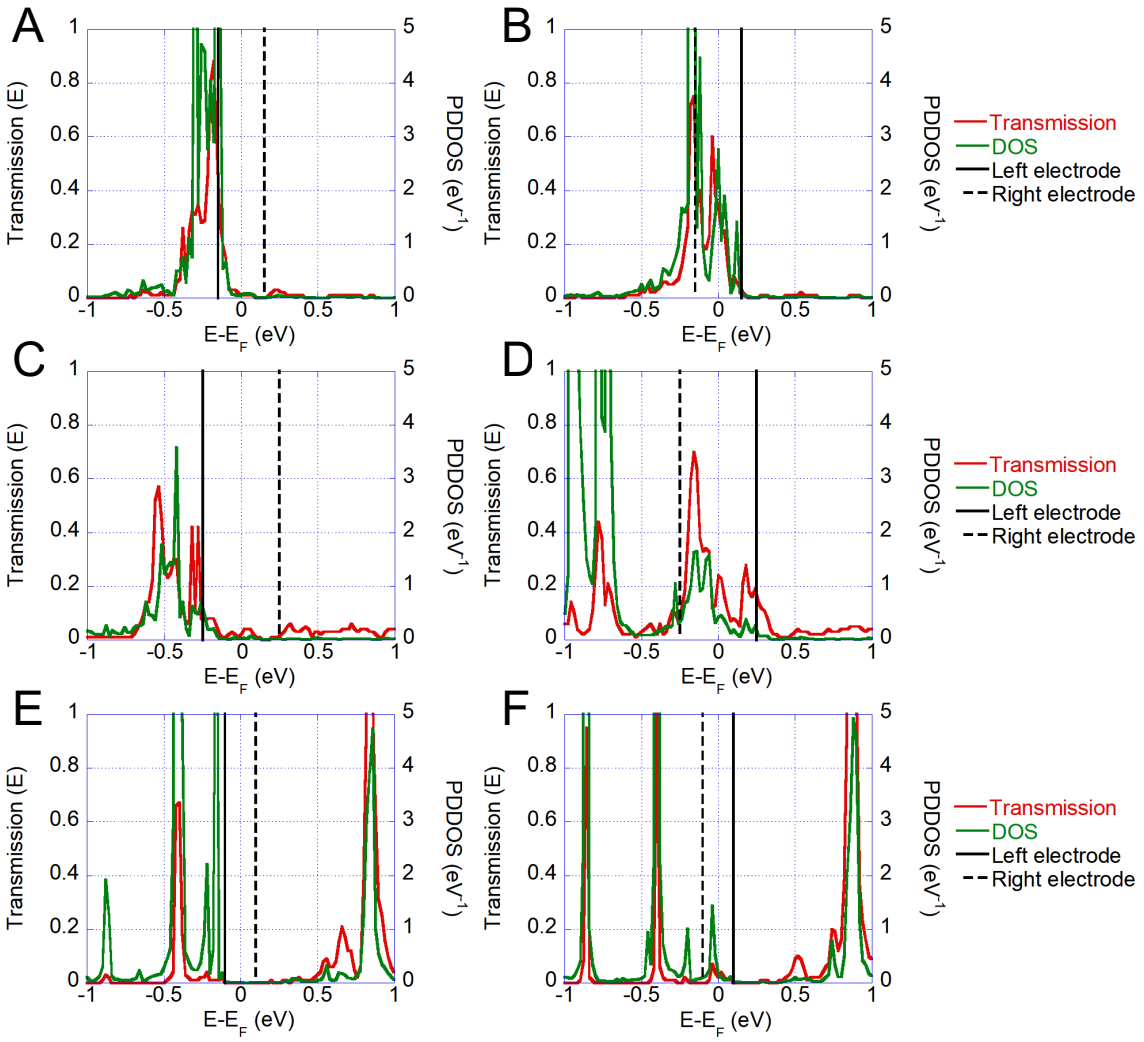

*Figure 3-12. Combined transmission and (pterin*dithiolene) projected device density of states (PDDOS) spectra for tetrahydro at +0.3V (A) and -0.3V (B), for 10,10a dihydro at +0.5V (C) and -0.5V (D), for quinoid at +0.2V (E) and -0.2V (F). The figure shows that the amplitude of the transmission peaks corresponds to the energies at which a high DOS that is delocalized across the molecule occurs. This indicates that transmission is dependent upon the presence of a delocalized state across the molecule at a particular energy, which provides a channel for the movement of e- through the molecule.*

For tetrahydro PDT at +0.3V bias, the high DOS peak at -0.16eV lies just beyond the bias window and corresponds with a transmission peak that occurs at -0.18eV, indicating that delocalized states are contributing to the enhancement of transmission at this energy (Figure 3-12A). Both the DOS and transmission peaks

have tails that enter the bias window, but the tail of the DOS peak precipitously drops off in intensity as it approaches -0.12eV and the transmission peak also shows a corresponding drop in amplitude. In contrast, at -0.3V bias the DOS shows several peaks within the bias window, occurring at -0.12, 0.04, 0.06 and 0.12eV that indicate the presence of delocalized states creating efficient current-carrying channels which contribute to a broadened transmission peak at -0.04eV (Figure 3-12B).

Under -0.5V bias, 10,10a dihydro has two DOS peaks occurring within the bias window at -0.14 and -0.06eV (Figure 3-12D). The presence of delocalized states at these energies is predicted by the presence of MPSH D, the molecular HOMO, which lies at -0.10eV at this bias and give rises to two broadened and robust transmission peaks within the bias window, as seen in Figures 3-8D and 3-11D. Three additional transmission peaks at -0.04, 0.18 and 0.24eV are attributed to the presence of other delocalized states indicated by a series of small DOS peaks at corresponding energies. At +0.5V, some transmission and DOS peaks of low amplitude occur within the bias window at -0.18, -0.04 and 0.04eV, but the larger DOS and transmission peaks remain outside of the bias window (Figure 3-12C). This implies that the absence of delocalized states within the bias window creates an insulating effect, supported by the previous observation that MPSH D, the molecular HOMO, lies outside of the bias window at +0.5V (Figure 3-8C). This supports the conclusion that rectification can occur in the presence of extended molecular conjugation, as long as a delocalized state is present within the bias window at forward bias, and absent under reverse bias. This also indicates that

the Van Dyke/Ratner Design Rule 3 is not necessary for designing an efficient molecular rectifier.[10]

At +0.2V bias, the quinoid pterin*dithiolene DOS within the bias window is negligible and predictably there are no transmission peaks within the bias window (Figure 3-12E). A large DOS peak lies outside of the bias window at -0.16eV, but surprisingly does not give rise to a robust transmission peak at this energy. At -0.2V bias, there is a DOS peak within the bias window at -0.06eV that corresponds with several small amplitude transmission peaks occurring at -0.02, 0.06 and 0.10eV (Figure 3-12F). This agrees with the previously mentioned projected weight analysis, which showed that the major transmission peak within the bias window at -0.02eV had a mixture of MPSH O and MPSH P with amplitude on both the pterin and dithiolene portions of the molecule (Figure 3-8F, Table 3-3, and Figure 3-9). However, both MPSH states O and P are nodal on the saturated carbons separating the dithiolene and pterin components of a molecule. This prevents the full delocalization of the transmitting states, as seen in the fully conjugated 10,10a dihydro and leads to the dampening of current-carrying capacity in the quinoid tautomer. This explains the efficient rectification behavior of the quinoid PDT, as it fulfills the Van Dyke/Ratner Design Rule 3 in which two conjugated molecular fragments are decoupled by a saturated fragment in the middle of the molecule.[10] However, this comes at the expense of the current-carrying capacity of the quinoid, as seen in Figure 3-3.

3.7 Conclusions

The unique geometric and electronic structure of the PDT, coupled with its potential role as an ET conduit, illustrates the importance of further defining its role in catalysis and for investigating this structure as a molecular electronics component. Here, we employed a series of electron transport computations to understand the mechanism by which electron transport through the PDT occurs and how the oxidation/tautomeric state of the PDT influences directional electron transport. We have computed the current that can be passed through the PDT and identified the frontier orbitals that are responsible for transmission. We have found that the energetics of the frontier orbitals relative to the Fermi level of the system informs rectification behavior and this is highly dependent upon the oxidation and tautomeric state of the molecule. Furthermore, we have shown that for effective transmission to occur, a delocalized DOS located within the bias window that has both dithiolene and pterin character is critical.

The role of the PDT component of Moco in catalysis is supported by the observation that the non-planer geometric distortions of the PDT observed in enzyme crystal structures may be implicated in enzyme function.[12,27–37] We present the first evidence that the PDT can function as a biological molecular rectifier to aid in vectoral electron transport. The tetrahydro and quinoid dihydro PDT forms fulfill all three Van Dyke/Ratner design 'rules' for molecular rectifiers.[10] The oxidized quinoid dihydro, with a RR_{max}~10, is a more efficient rectifier than the reduced tetrahydro, with a RR_{max}~3; this is likely due to the increased electron withdrawing capacity of the pterin when oxidized, which makes it less favorable for

electrons to flow from pterin to dithiolene and more favorable for electron flow from the dithiolene to the pterin.

We have demonstrated that for efficient transmission to occur, the presence of a state with both pterin and dithiolene character within the bias window is critical. Yoshizawa, Tada and Staykov have addressed the importance of the phase and amplitude of the conducing frontier orbitals in transmission efficiency, placing particular importance on the orbital nature of the HOMO and LUMO localized on atoms directly connected to the electrodes in a metal-molecule-metal device.[38] They found that to have an effective transmission channel, the orbital amplitude on the two connecting atoms must be opposite in phase, so that the sign of the product of the orbital phases on the two connecting atoms in the HOMO is opposite that of the LUMO, and the orbital amplitude of both the HOMO and LUMO on the connecting sites must be large. In this study, we found that the delocalized spatial distribution of the conducting state(s) within the bias window is essential to providing an efficient transmission channel through the molecular bridge. This implies that a molecule can act as a rectifier without impeding current flow if delocalized conducting state(s) are present in the bias window at forward bias and absent upon bias reversal. This creates an insulating effect at reverse bias while allowing efficient current flow through the delocalized conducting state(s) at forward bias.

This effect is observed in the 10,10a dihydro, which while in violation of the decoupling 'rule' can function as a surprisingly effective rectifier, with a RR_{max}~7.[10] Furthermore, the conjugated structure makes 10,10a dihydro a more efficient

conductor than either the tetrahydro or quinoid dihydro forms, indicating that the efficiency of rectification need not necessarily be achieved at the expense of molecular current-carrying capacity.

In long-range ET pathways, such as the ones utilized in molybdoenzymes, the electron donor and ultimate electron acceptor are separated spatially and there is no direct interaction through covalent bonding. Considering the PDT analogous to a molecular bridge between donor and acceptor moieties in an enzyme, the ET reaction between donor and acceptor can occur either via electron transfer through reduced bridge states, or hole transfer through oxidized bridge states.[39] In the case of the reduced tetrahydro, we observe that the electron transport calculations support a hole-transfer mechanism through filled MPSH states corresponding to the HOMO and HOMO-1 of the free molecule. Similarly, 10,10a dihydro, although an oxidized form of the PDT, also utilizes a hole-transfer mechanism that is primarily mediated by an out-of-plane π-orbital resembling the molecular HOMO. The quinoid mediates electron transport utilizing its LUMO, which is analogous to the oxidized HOMO of the tetrahydro. Although this LUMO level becomes reduced when the quinoid complexed to the electrodes and therefore in our calculations ET is occurring via a hole transfer process, ET in the enzymes utilizing the quinoid LUMO may occur via an electron transfer mechanism in which electrons must first fill the LUMO level from the donor.

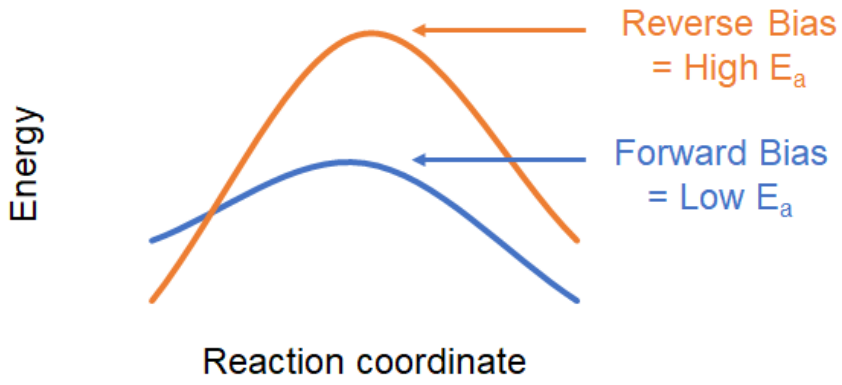

Figure 3-13. Diagram of a sample reaction coordinate illustrating that forward bias promotes efficient ET by lowering the activation energy of the reaction (blue curve). Upon bias reversal, ET becomes less favorable due to increasing activation energy.

Directional biological electron transfer processes occur in nature; one notable example is photosystem II, which couples several one-electron transfer events to create a pH gradient for the synthesis of ATP.[40,41] Photosystem II utilizes a series of redox cofactors to promote the kinetically favored directional electron transfer pathway over the thermodynamically favored recombination pathway. In xanthine oxidase, sequential one-electron transfer events from the reduced Mo active site to the two 2Fe2S clusters and eventually to FAD permits the regeneration of the catalytically active Mo site.[8] It has been demonstrated that the reduction potentials of chemically modified flavins influence the rate of reaction (V_{max}) which indicates that the relative reduction potentials of Mo and its redox active partners influences V_{max}.[42]

This implies a critical role for the PDT in influencing directional electron transfer between two redox active centers using rectification mechanisms; this could help prevent back electron transfer which would impede catalysis by preventing

regeneration of the catalytically competent active site and promote the kinetically favorable pathway of electron transfer away from Mo through the 2Fe2S clusters.

The preference for electron transport in a specific direction under bias, which we observed in our rectification computational work on the PDT ligand, can be extrapolated as possibly relating to the promotion of directional electron transfer in a biological system. In a biological system, the activation energy (E_a) may be lower for one direction because of the relative reduction potentials of the redox active centers, as seen in Figure 3-13.

The PDT ligand in xanthine oxidase is likely a tetrahydro PDT; the preferred direction of electron transport in our computational work is from dithiolene to pterin for the tetrahydro.[12] This supports a model in which the electrons are shuttled from Mo to the first 2Fe2S cluster through the PDT ligand, in the direction of dithiolene to pterin. This indicates that one of the possible functions of the PDT ligand in molybdoenzymes is to serve as a directional electron transfer conduit, to favor the egress of electrons from the reduced Mo(IV) active site.

3.8 References

(1) Smidstrup, S.; Markussen, T.; Vancraeyveld, P.; Wellendorff, J.; Schneider, J.; Gunst, T.; Verstichel, B.; Stradi, D.; Khomyakov, P. A.; Vej-Hansen, U. G.; Lee, M. E.; Chill, S. T.; Rasmussen, F.; Penazzi, G.; Corsetti, F.; Ojanperä, A.; Jensen, K.; Palsgaard, M. L. N.; Martinez, U.; Blom, A.; Brandbyge, M.; Stokbro, K. QuantumATK: An Integrated Platform of Electronic and Atomic-Scale Modelling Tools. *Journal of Physics Condensed Matter* **2020**, *32* (1). https://doi.org/10.1088/1361-648X/ab4007.

(2) Ellenbogen, J. C.; Love, J. C.; Christopher Love, J.; Love, J. C. Architectures for Molecular Electronic Computers: 1. Logic Structures and an Adder Designed from Molecular Electronic Diodes. *Proceedings of the IEEE* **2000**, *88* (3), 386–426. https://doi.org/10.1109/5.838115.

(3) Strange, M.; Rostgaard, C.; Häkkinen, H.; Thygesen, K. S. Self-Consistent GW Calculations of Electronic Transport in Thiol- and Amine-Linked Molecular Junctions. *Physical Review B - Condensed Matter and Materials Physics* **2011**, *83* (11), 1–12. https://doi.org/10.1103/PhysRevB.83.115108.

(4) Heimel, G.; Romaner, L.; Brédas, J. L.; Zojer, E. Interface Energetics and Level Alignment at Covalent Metal-Molecule Junctions: π-Conjugated Thiols on Gold. *Physical Review Letters* **2006**, *96* (19), 2–5. https://doi.org/10.1103/PhysRevLett.96.196806.

(5) Chen, F.; Li, X.; Hihath, J.; Huang, Z.; Tao, N. Effect of Anchoring Groups on Single-Molecule Conductance: Comparative Study of Thiol-, Amine-, and Carboxylic-Acid-Terminated Molecules. *Journal of the American Chemical Society* **2006**, *128* (49), 15874–15881. https://doi.org/10.1021/ja065864k.

(6) Zotti, L. A.; Kirchner, T.; Cuevas, J.; Pauly, F.; Huhn, T.; Scheer, E.; Erbe, A. Revealing the Role of Anchoring Groups in the Electrical Conduction Through Single-Molecule Junctions. **2010**, 1529–1535. https://doi.org/10.1002/smll.200902227.

(7) Kirk, M. L.; Stein, B. *Molybdenum Enzymes*; Elsevier Ltd., 2013. https://doi.org/10.1016/B978-0-08-097774-4.00316-8.

(8) Hille, R. The Mononuclear Molybdenum Enzymes. *Chemical Reviews* **1996**, *96*, 2757–2816. https://doi.org/10.1021/cr950061t.

(9) Cao, H.; Pauff, J. M.; Hille, R. Substrate Orientation and Catalytic Specificity in the Action of Xanthine Oxidase: The Sequential Hydroxylation of Hypoxanthine to Uric Acid. *Journal of Biological Chemistry* **2010**, *285* (36), 28044–28053. https://doi.org/10.1074/jbc.M110.128561.

(10) van Dyck, C.; Ratner, M. a. Molecular Rectifiers: A New Design Based on Asymmetric Anchoring Moieties. *Nano Letters* **2015**, *15* (3), 1577–1584. https://doi.org/10.1021/nl504091v.

(11) Coto, P. B.; Hofmeister, C.; Prucker, V.; Weckbecker, D.; Thoss, M.; Binder, K.; M, M.; Kremer, M.; Editors, A. S.; Coto, P. B.; Hofmeister, C.; Prucker, V. Simulation of Electron Transfer and Electron Transport in Molecular Systems at Surfaces. *NIC Symposium* **2016**, *48*, 133–140.

(12) Rothery, R. a.; Stein, B.; Solomonson, M.; Kirk, M. L.; Weiner, J. H. Pyranopterin Conformation Defines the Function of Molybdenum and Tungsten Enzymes. *Proceedings of the National Academy of Sciences* **2012**, *109* (37), 14773–14778. https://doi.org/10.1073/pnas.1200671109.

(13) Matz, K. G.; Mtei, R. P.; Rothstein, R.; Kirk, M. L.; Burgmayer, S. J. N. Study of Molybdenum(4+) Quinoxalyldithiolenes as Models for the Noninnocent Pyranopterin in the Molybdenum Cofactor. *Inorganic Chemistry* **2011**, *50* (20), 9804–9815. https://doi.org/10.1021/ic200783a.

(14) Matz, K. G.; Mtei, R. P.; Leung, B.; Burgmayer, S. J. N.; Kirk, M. L.; Al, E. Noninnocent Dithiolene Ligands: A New Oxomolybdenum Complex Possessing a Donor-Acceptor Dithiolene Ligand. *Journal of the American Chemical Society* **2010**, *132* (23), 7830–7831. https://doi.org/10.1016/j.surg.2006.10.010.Use.

(15) Armstrong, N.; Hoft, R. C.; McDonagh, A.; Cortie, M. B.; Ford, M. J. Exploring the Performance of Molecular Rectifiers: Limitations and Factors Affecting Molecular Rectification. *Nano Letters* **2007**, *7* (10), 3018–3022. https://doi.org/10.1021/nl0714435.

(16) Batra, A.; Darancet, P.; Chen, Q.; Meisner, J. S.; Widawsky, J. R.; Neaton, J. B.; Nuckolls, C.; Venkataraman, L. Tuning Rectification in Single-Molecular Diodes. *Nano Letters* **2013**, *13* (12), 6233–6237. https://doi.org/10.1021/nl403698m.

(17) Ding, W.; Koepf, M.; Koenigsmann, C.; Batra, A.; Venkataraman, L.; Negre, C. F. A. a; Brudvig, G. W.; Crabtree, R. H.; Schmuttenmaer, C. a.; Batista, V. S. Computational Design of Intrinsic Molecular Rectifiers Based on Asymmetric Functionalization of N-Phenylbenzamide. *Journal of Chemical Theory and Computation* **2015**, *11* (12), 5888–5896. https://doi.org/10.1021/acs.jctc.5b00823.

(18) Kirk, M. L.; Shultz, D. A.; Zhang, J.; Dangi, R.; Ingersol, L.; Yang, J.; Finney, N. S.; Sommer, R. D.; Wojtas, L. Heterospin Biradicals Provide Insight into Molecular Conductance and Rectification. *Chemical Science* **2017**, *8* (8), 5408–5415. https://doi.org/10.1039/C7SC00073A.

(19) Díez-Pérez, I.; Hihath, J.; Lee, Y.; Yu, L.; Adamska, L.; Kozhushner, M. A.; Oleynik, I. I.; Tao, N. Rectification and Stability of a Single Molecular Diode with Controlled Orientation. *Nature Chemistry* **2009**, *1* (8), 635–641. https://doi.org/10.1038/nchem.392.

(20) Fujii, S.; Tada, T.; Komoto, Y.; Osuga, T.; Murase, T.; Fujita, M.; Kiguchi, M. Rectifying Electron-Transport Properties through Stacks of Aromatic Molecules Inserted into a Self-Assembled Cage. *Journal of the American Chemical Society* **2015**, *137* (18), 5939–5947. https://doi.org/10.1021/jacs.5b00086.

(21) Weigend, F.; Elbing, M.; Ochs, R.; Koentopp, M.; Fischer, M.; Ha, C. von; Evers, F.; Weber, H. B.; Mayor, M. A Single-Molecule Diode. **2005**.

(22) Aviram, A.; Ratner, M. Molecular Rectifiers. 1974, pp 277–283.

(23) Huang, B.; Zhang, F.; Yang, Y.; Zhang, Z. Length-Dependent Electronic Transport Properties of the ZnO Nanorod. *Micromachines* **2018**, *10* (1). https://doi.org/10.3390/mi10010026.

(24) Paulsson, M.; Brandbyge, M. Transmission Eigenchannels from Nonequilibrium Green's Functions. *Physical Review B - Condensed Matter and Materials Physics* **2007**, *76* (11). https://doi.org/10.1103/PhysRevB.76.115117.

(25) Yoshizawa, K. An Orbital Rule for Electron Transport in Molecules. *Accounts of Chemical Research* **2012**, *45* (9), 1612–1621. https://doi.org/10.1021/ar300075f.

(26) Beratan, D. N. Why Are DNA and Protein Electron Transfer So Different ? **2019**, 71–97.

(27) Rothery, R. a.; Weiner, J. H. Shifting the Metallocentric Molybdoenzyme Paradigm: The Importance of Pyranopterin Coordination. *JBIC Journal of Biological Inorganic Chemistry* **2015**, *20* (2), 349–372. https://doi.org/10.1007/s00775-014-1194-6.

(28) Wu, S. Y.; Rothery, R. a.; Weiner, J. H. Pyranopterin Coordination Controls Molybdenum Electrochemistry in Escherichia Coli Nitrate Reductase. *Journal of Biological Chemistry* **2015**, *290* (41), 25164–25173. https://doi.org/10.1074/jbc.M115.665422.

(29) Bertero, M. G.; Rothery, R. A.; Palak, M.; Hou, C.; Lim, D.; Blasco, F.; Weiner, J. H.; Strynadka, N. C. J. J. Insights into the Respiratory Electron Transfer Pathway from the Structure of Nitrate Reductase A. *Nature Structural Biology* **2003**, *10* (9), 681–687. https://doi.org/10.1038/nsb969.

(30) Rajapakshe, A.; Tollin, G.; Enemark, J. H. Kinetic and Thermodynamic Effects of Mutations of Human Sulfite Oxidase. *Chemistry and Biodiversity* **2012**, *9* (9), 1621–1634. https://doi.org/10.1002/cbdv.201200010.

(31) Raitsimring AM, Astashkin AV, F. C. et al. Studies of the Mo(V) Center of the Y343F Mutant of Human Sulfite Oxidase by Variable Frequency Pulsed EPR Spectroscopy. *Inorganica Chim Acta.* **2008**, *361* (4), 941–946. https://doi.org/10.1016/j.immuni.2010.12.017.Two-stage.

(32) Feng, C.; Wilson, H. L.; Hurley, J. K.; Hazzard, J. T.; Tollin, G.; Rajagopalan, K. v.; Enemark, J. H. Role of Conserved Tyrosine 343 in Intramolecular Electron Transfer in Human Sulfite Oxidase. *Journal of Biological Chemistry* **2003**, *278* (5), 2913–2920. https://doi.org/10.1074/jbc.M210374200.

(33) Kappler, U.; Bailey, S.; Feng, C.; Honeychurch, M. J.; Hanson, G. R.; Bernhardt, P. v.; Tollin, G.; Enemark, J. H. Kinetic and Structural Evidence for the Importance of Tyr236 for the Integrity of the Mo Active Site in a Bacterial Sulfite Dehydrogenase. *Biochemistry* **2006**, *45* (32), 9696–9705. https://doi.org/10.1021/bi060058b.

(34) Rothery, R. A.; Trieber, C. A.; Weiner, J. H. Interactions between the Molybdenum Cofactor and Iron-Sulfur Clusters of Escherichia Coli Dimethylsulfoxide Reductase. *Journal of Biological Chemistry* **1999**, *274* (19), 13002–13009. https://doi.org/10.1074/jbc.274.19.13002.

(35) Tang, H.; Rothery, R. A.; Voss, J. E.; Weiner, J. H. Correct Assembly of Iron-Sulfur Cluster FS0 into Escherichia Coli Dimethyl Sulfoxide Reductase (DmsABC) Is a Prerequisite for Molybdenum Cofactor Insertion. *Journal of Biological Chemistry* **2011**, *286* (17), 15147–15154. https://doi.org/10.1074/jbc.M110.213306.

(36) Jacques, J. G. J.; Fourmond, V.; Arnoux, P.; Sabaty, M.; Etienne, E.; Grosse, S.; Biaso, F.; Bertrand, P.; Pignol, D.; Léger, C.; Guigliarelli, B.; Burlat, B. Reductive Activation in Periplasmic Nitrate Reductase Involves Chemical Modifications of the Mo-Cofactor beyond the First Coordination Sphere of the Metal Ion. *Biochimica et Biophysica Acta - Bioenergetics* **2014**, *1837* (2), 277–286. https://doi.org/10.1016/j.bbabio.2013.10.013.

(37) Dong, C.; Yang, J.; Leimku, S.; Kirk, M. L.; Leimkühler, S.; Kirk, M. L. Pyranopterin Dithiolene Distortions Relevant to Electron Transfer in Xanthine Oxidase/Dehydrogenase. *Inorganic Chemistry* **2014**, *53* (14), 7077–7079. https://doi.org/10.1021/ic500873y.

(38) Tsuji, Y.; Staykov, A.; Yoshizawa, K. Orbital Views of Molecular Conductance Perturbed by Anchor Units. *Journal of the American Chemical Society* **2011**, *133* (15), 5955–5965. https://doi.org/10.1021/ja111021e.

(39) Gray, H. B.; Winkler, J. R. Electron Transfer in Proteins. *Annual review of biochemistry* **1996**, *65*, 537–561. https://doi.org/10.1146/annurev.bi.65.070196.002541.

(40) Sproviero, E. M.; Gascón, J. A.; McEvoy, J. P.; Brudvig, G. W.; Batista, V. S. Computational Studies of the O2-Evolving Complex of Photosystem II and Biomimetic Oxomanganese Complexes. *Coordination Chemistry Reviews* **2008**, *252* (3–4), 395–415. https://doi.org/10.1016/j.ccr.2007.09.006.

(41) Sproviero, E. M.; Gascón, J. A.; McEvoy, J. P.; Brudvig, G. W.; Batista, V. S. Quantum Mechanics/Molecular Mechanics Structural Models of the Oxygen-Evolving Complex of Photosystem II. *Current Opinion in Structural Biology* **2007**, *17* (2), 173–180. https://doi.org/10.1016/j.sbi.2007.03.015.

(42) Hille, R.; Massey, V. The Kinetic Behavior of Xanthine Oxidase Containing Chemically Modified Flavins. *Journal of Biological Chemistry* **1991**, *266* (26), 17401–17408.

4. Chapter 4 - Background information on the unusual E. coli molybdoenzyme MsrP

4.1 Introduction to MsrP

MsrP, formerly known in the literature as YedY, was first discovered in a bioinformatics screen of the *E. coli* genome; MsrP has now been identified in most Gram negative bacteria.[1] MsrP from *R. sphaeroides* shares ~50% of sequence identity with the *E. coli* enzyme, indicating a high degree of conservation between the two.[2] It is a soluble, 33.6kDa, twin-arginine signal-containing protein found in the periplasm. It functions as a methionine sulfoxide reductase and is reported to be capable of repairing oxidized methionine (MetO) residues in protein.[3] Its membrane-anchored redox partner MsrQ, formerly known as YedZ, is thought to pass reducing equivalents to MsrP from the membrane quinone pool.[1,3]

4.2 X-ray crystal structure of MsrP

Loshi *et al.* crystallized *E. coli* MsrP at a resolution of 2.5Å; the shared fold and the overall similarity of the active site structure led them to classify MsrP as a member of the SO family of molybdoenzymes, as it does not structurally resemble members of the DMSOR and XO families (Figure 4-1A and B).[1] The MsrP/Q system is analogous to that of the two subunits of CSO. Subunit II of CSO contains the molybdenum cofactor, and shares similarities to the protein fold of MsrP, despite the low 18% shared sequence identity between the two proteins (Figure 4-1A).

MsrQ is analogous to subunit I of CSO, in that both contain hemes that act as redox partners for their respective Moco-containing counterparts.

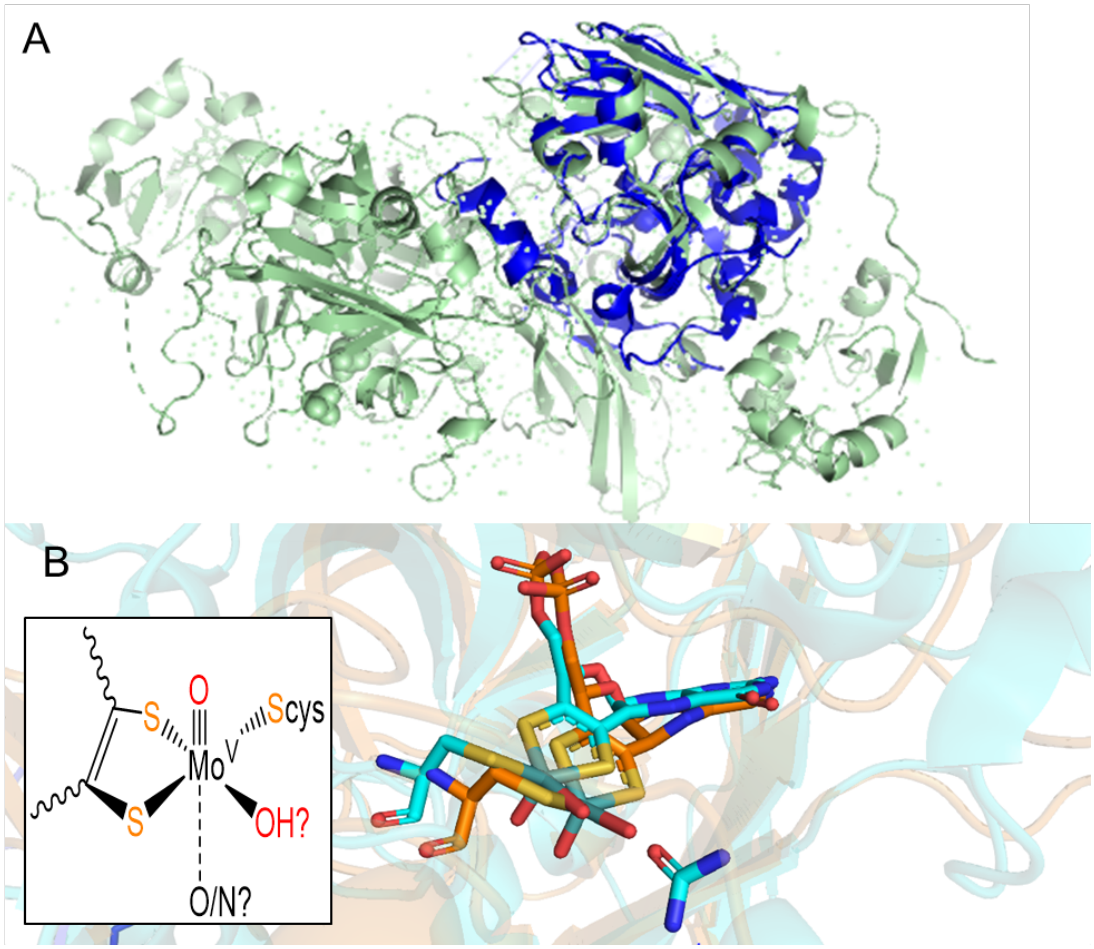

Figure 4-1. Overlay of MsrP (blue, PDB 1XDQ)[1] and subunit II of CSO (sage, PDB 1SOX)[6] (A). Closeup of an overlay of the active sites of MsrP (blue) and CSO (orange) (B). Urea from the crystallization buffer is in the substrate binding pocket of MsrP, oriented towards the putative equatorial -OH group. Insert shows the originally proposed active site structure of MsrP, with Mo ligated by a single PDT ligand, a sulfur from Cys, an axial oxo group, and a putative -OH ligand in the equatorial position at the entrance of the binding pocket. A long bond to the O/N of Asn-45 has been suggested.[52] Structural overlay created using Pymol version 2.0.7.

The structure of MsrP is comprised of 12 α-helices and two β-sheets, which are formed by the interactions of 10 β-strands. It is crystallized as a homopentameric structure but is likely dispersed as a monomer in a physiological setting. MsrP surprisingly contains a molybdopterin-type (MPT) cofactor, meaning that it is not conjugated to a nucleotide via its phosphate group. The recently discovered YdhV protein in *E. coli* is the only other known prokaryotic molybdoenzyme found to possess two MPT cofactors that are unmodified by a nucleotide.[41]

The original assignment of the groups coordinated to Mo in MsrP by Loschi *et al.* is similar to other members of the SO family. The active site of the enzyme consists of Mo coordinated by an axial oxo, and in the equatorial plane, a single pyranopterin dithiolene, a sulfur from Cys-102, and a putative O(H) group (Figure 4-1B and inset). The poor resolution of the electron density in the area of the putative O(H) made the actual assignment of this group ambiguous. The assignment of the equatorial atom at this position as O was largely based upon the similarity of the crystal structure to CSO, as members of the SO family of molybdoenzymes all share a common active site configuration about Mo.[1]

The active site itself is somewhat buried in the protein structure, located roughly 16Å from the protein surface. The substrate channel leading to the active site opens directly to the position of the equatorial, putative O(H) group, which is consistent with the known catalytic mechanisms of SO family members, where this coordination position is the one to which substrate binds.[5]

There are striking differences in the substrate binding pocket of MsrP, compared to other eukaryotic sulfite oxidases. In CSO, three conserved arginine residues

(Arg-138, Arg-190, and Arg-450), Trp-204, Tyr-322, and Lys-200 form a positively charged substrate binding pocket which electrostatically favors the negatively charged sulfite/sulfate substrate.[6] Two of the three arginine residues (Arg-190 and Arg-138) are conserved in nitrate reductases. A methionine residue, conserved in the nitrate reductases, is in the position corresponding to the third arginine in CSO.[7]

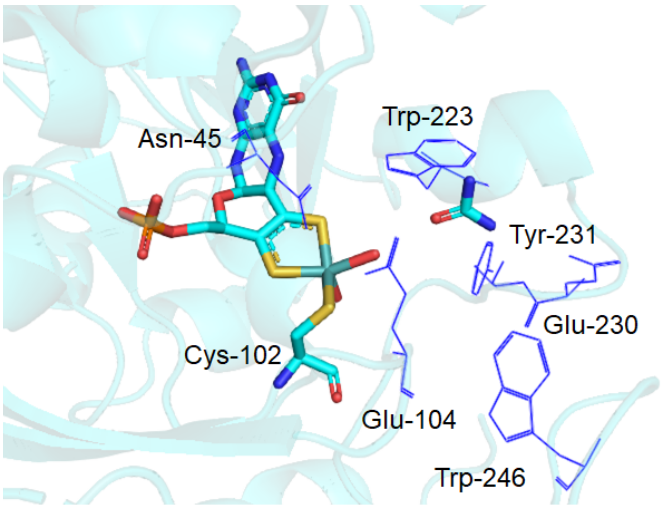

Figure 4-2. Hydrophobic binding pocket of MsrP (PDB 1XDQ).[1] Figure created using Pymol version 2.0.7.

In contrast, the substrate binding pocket of MsrP is hydrophobic, due to the presence of four aromatic residues (Tyr-47, Tyr-231, Trp-223, and Trp-246) at the entrance of the cavity (Figure 4-2).[1] Arg-138 in CSO is replaced by Asn-45 in MsrP, *trans* to the axial oxo group bound to Mo. MsrP also possesses two hydrophobic residues located ~5Å from Mo itself: Phe-203 and Val-103. Glu-104 is positioned next to the putative O(H) at the end of the substrate binding pocket. The carboxylate form of Glu-104 would electrostatically repel a negatively charged substrate, such as sulfite or sulfate. Therefore, the hydrophobic environment of the substrate binding pocket is perfectly designed to support molecules with hydrophobic regions, such as the side chain of MetO.

MsrQ has not been crystallized but is predicted to consist of six segments which transverse the inner membrane of bacterial cells via analysis of its sequence.[1,8] The membrane-spanning domain of MsrQ is referred to as a ferric reductase domain (FRD); this domain is present in the eukaryotic NADPH oxidase (NOX/DUOX) family of proteins that produce ROS.[9,10] Both MsrQ and NOX bind heme groups and are integral to electron transfer pathways. MsrQ contains two *b*-type hemes which are bound via three histidines which are conserved in all FRD containing proteins. One of these histidines (His-91) is present in in the transmembrane domain 3 (TM3) and two are found in TM5 (His-151 and His-164) and mutation of these residues causes loss of the bound heme groups.[9]

4.3 Tungsten-substituted MsrP crystal structure

Loschi *et al.* also crystallized tungsten-substituted MsrP (W-MsrP) by adding $Na_2O_4W \cdot 2H_2O$ to the culture media.[1] There were striking differences between W-MsrP and Mo-MsrP. W-MsrP has no observable W(V) EPR signal.[11] Although W-MsrP was also coordinated by the two dithiolene sulfurs and a sulfur from Cys-102, there was no atom coordinated to W in the corresponding position of the putative O(H) in Mo-MsrP. Furthermore, unlike Mo-MsrP, the substrate binding pocket was filled with water molecules, which formed hydrogen bonding interactions with Glu-104, Tyr-47, and Tyr-431. W-MsrP was not observed to be coordinated by an axial oxo group.

Substitution of Mo for W in DMSOR from *R. capsulatus* and trimethylamine N-oxide reductase from E. coli, caused both enzymes to show increases in their catalytic efficiencies.[12,13] Unlike other molybdoenzymes, which retain their activity upon W-

substitution, W-MsrP is not catalytically active; although this difference may be attributed to the presence of a single PDT ligand in W-MsrP versus a doubly PDT-ligated active site in the other enzymes.[1,11] This is further supported by the observation that W-substituted SO from rat liver is not catalytically active; like MsrP, SO is ligated by a single PDT.[14] While Mo-MsrP is described in the literature as a pink protein, attributed to an absorption at 503nm, the tungsten form of the enzyme is colorless and has no reported absorption peaks in the visible range.[1,11,15]

4.4 Ability to function as a protein repair enzyme

MsrP/Q appears to be an oxidative-damage response system that Gram-negative bacteria activate when exposed to reactive chloride species (RCS), such as from exposure to bleach or other household cleaning products or produced by the innate immune system to defend against infection by microorganisms.[16] MsrP is classified as a methionine sulfoxide reductase as a result of its ability to reduce oxidized Met on proteins in the periplasm which occur as a result of RCS.[3,16]

Met contains a thioether on its side chain which can be oxidized to a sulfoxide or further oxidized to a sulfone, although methionine sulfone is not thought of as biologically significant, due to the rareness of this species and the irreversibility of this oxidation event (Figure 4-3).[17,18] Methionine oxidation can cause structural changes to a protein. Though rare, it has been demonstrated that oxidized methionine can cause fragmentation of Ser and Thr residues when they are located on the N-term of proteins. This occurs when a hydroxyl radical adds to the

methionine sulfur to create a hydroxyl sulfuranyl radical and a subsequent proton transfer from Thr or Ser causes Met to eliminate water.[19] As methionine is hydrophobic and therefore can be often be found buried within the protein structure, oxidation of this residue increases its polarity and can change the structural integrity of the protein.[18] The oxidation of methionine residues can also alter the function of proteins. For example, the *E. coli* ribosomal protein L12 shows inhibition of its ability to bind to ribosomes upon oxidation of three of its methionine residues.[20]

Figure 4-3. Scheme of the formation of methionine sulfoxides and sulfones on proteins. Methionine-S-sulfoxide can be reduced by MsrP and MsrA, while the R diastereomer can be reduced by MsrP and MsrB. MsrA and MsrB reside in the cytoplasm, while MsrP is located in the periplasm. Formation of methionine sulfone is rare but irreversible.

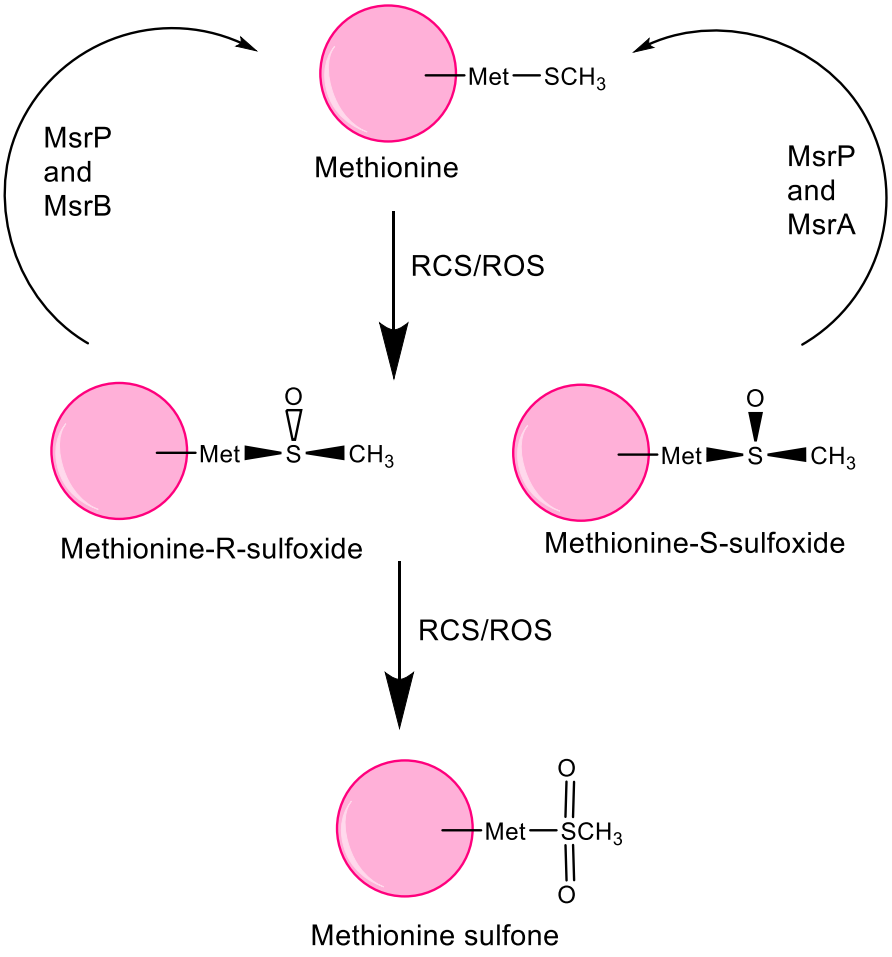

RCS are capable of rapidly oxidizing methionine residues, forming R- and S-diastereomers of MetO (Figure 4-3). Hypochloride (HOCl) reacts with methionine at a rate of 3.8 x 10^7 $M^{-1}s^{-1}$ and is far more reactive to methionine than it is with cysteine (3.0 x 10^7 $M^{-1}s^{-1}$) or histidine (1.0 x 10^5 $M^{-1}s^{-1}$).[21] HOCl is released when phagocytes, in a defensive response to invading bacteria, produce myeloperoxidase (MPO). Myeloperoxidase catalyzes formation of HOCl using peroxide and Cl- ions.[21] The rapid oxidation of methionine residues in proteins cause structural destabilization, protein aggregation, and loss of activity and can ultimately lead to cell death.[3,16,21]

Methionine can be used as a methyl donor, which is prevented by methionine oxidation due to the respiratory burst of monocytes.[22] In *E. coli*, S-adenosylmethionine (SAM) is synthesized from methionine and ATP; the conversion to SAM causes the activation of the methyl group and allows it to be easily donated to other entities within the cell.[23] SAM is the most active methyl donor in both eukaryotes and prokaryotes. In both prokaryotes and eukaryotes, methylation is a highly important post-translational modification, especially in the control of differential gene expression through the modification of translation factors (TFs) and other elements of the translational machinery within the cell.[24] Addition of a methyl group can potentially lower the pKa of the attached group, due to its electron-donating abilities, change the structure of a protein, thus affecting its function, or neutralize charges on free carbonyl groups; these post-translational modifications can influence both the activity and targeting of methylated proteins.[24,25]

A study by Rosen *et al.* assessed the viability of bacteria in response to methionine oxidation caused by either MPO released by neutrophils or HOCl.[26] They found that viability declined as the percentage of periplasmic and outer membrane proteins that had oxidized methionine residues approached 30-40%. However, out of the oxidized methionines 55-60% were found on outer membrane proteins, while 25-25% were found on proteins in the periplasm when the bacterial cells were still at 95% of their maximum viability. This indicates the oxidation of methionine residues on outer membrane proteins may serve to help shield the cell from the oxidation of more critical proteins in compartments located farther within the cell. They also found that two Msrs, MsrA and MsrB, were able to mitigate the detrimental effect of the oxidative stress on the bacterial viability.

MsrP is notable in that it is the only known Msr protein that is capable of acting upon both R- and S- diastereomers of $MetO^2$; other known Msr proteins are stereospecific (Figure 4-3). Gennaris *et al.* found that a mutant deficient in the genes necessary for the synthesis of quinones in the inner membrane pool was not able to reduce MetO using MsrP/Q, indicating that the quinone pool is the source of reducing equivalents for the MsrP/Q system.[3] This is consistent with MsrQ possessing a b-type heme, which is a common electron transfer redox partner found in SO family enzymes.[11] MsrQ has also been shown to be able to be reduced *in vitro* by menadiol and other analogues of common quinols, further supporting that the inner membrane quinone pool is the source of reducing equivalents.[11] It has also been demonstrated that the heme groups on MsrQ can

be reduced by the transfer of electrons from the soluble cytoplasmic protein Fre, an NADPH flavin-dependent oxidoreductase (Figure 4-4).[9]

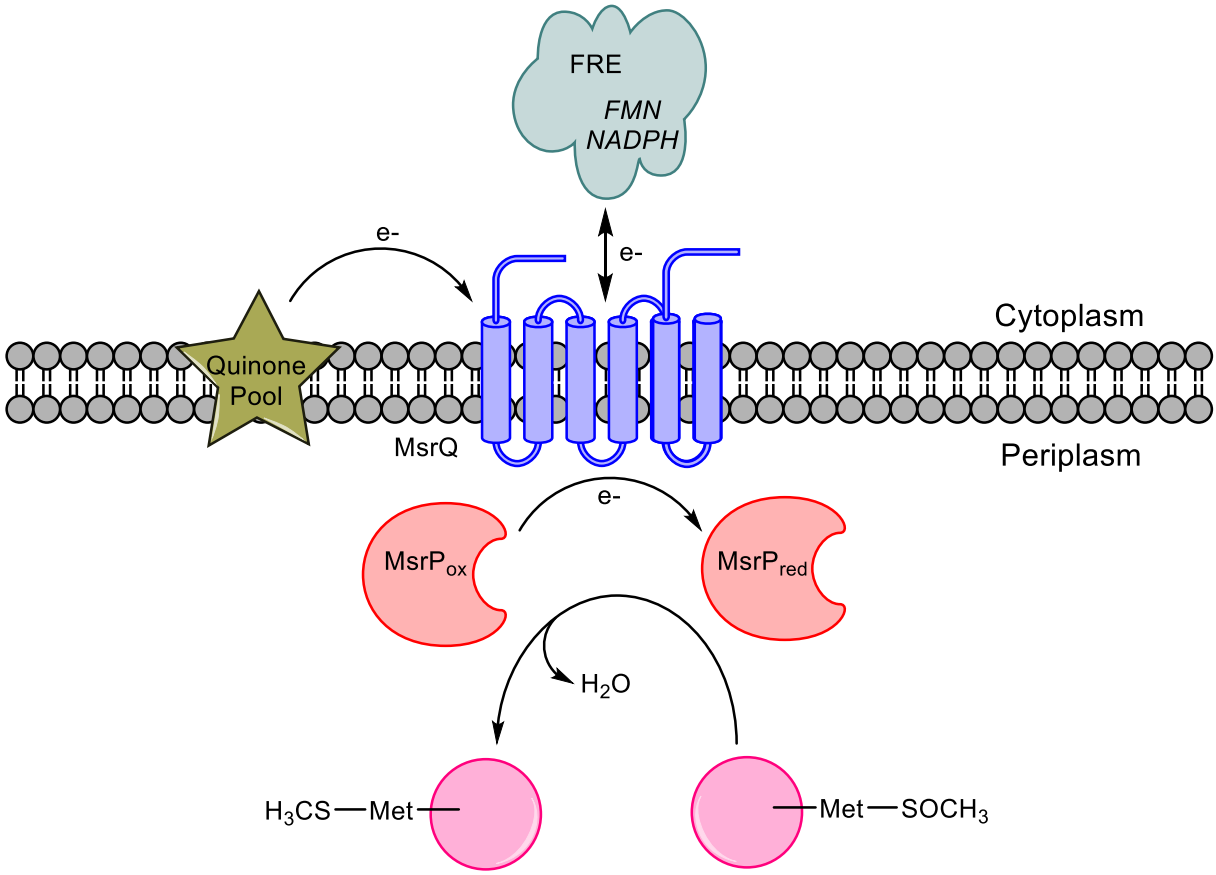

Figure 4-4. Scheme of electron flow from MsrQ in the inner membrane to soluble MsrP in the periplasm. MsrQ can obtain reducing equivalents from the inner membrane pool of quinones or the soluble cytoplasmic protein FRE. It then can reduce MsrP via an unknown mechanism. MsrP is then catalytically active and can reduce MetO on periplasmic proteins, restoring the structure and function of the oxidized proteins.

4.5 Other Msr enzymes

Msr proteins are expressed in all three domains of life; thought to have evolutionary origins that were a response to the Great Oxidation Event which occurred ~2.4

billion years ago.[27] It is speculated that bacterial need for protective measures against oxygen-induced damage towards methionine residues led to the evolution of Msrs, which could reduce damaged methionine residues and restore protein function.

The first isolation of an Msr protein from *E.coli* was achieved by Brot *et al.* in 1981, who demonstrated the ability of MsrA to reduce MetO in a protein.[28] The discovery of MsrB in *E. coli* occurred in 2001; it was found to be a highly conserved protein in bacteria, eukaryotes and some archaea.[29] The opposing stereospecificity of MsrA and MsrB was evidenced by the partial reduction of oxidized calmodulin by either enzyme, but the complete reduction of all MetO on calmodulin when incubated with both Msrs. MsrA exclusively reduces the S- diastereomer of MetO**[32],** while MsrB exclusively reduces the R- diastereomer. MsrA is also able to more efficiently reduce free MetO than MsrB by a factor of ~1000. In 2007, a Msr (MsrC) which could reduce the R-diastereomer of free MetO was discovered in *E. coli*; this enzyme was found to also be 1000-fold more active than MsrB at reducing free MetO.[30]

MsrA and MsrB have no homology and are the result of a convergent evolutionary event.[27] Yet, despite this, MsrA and MsrB have a similar catalytic mechanism in which a catalytic Cys residue abstracts the oxygen from MetO to form a sulfenic acid (-SOH) on Cys. A second Cys residue on the Msr then forms an intramolecular disulfide bond with the first Cys and releases the oxygen as a water. A thioredoxin (Trx) protein reduces the disulfide bond to create the catalytically competent Msr (Figure 4-5).[31–34] *E. coli* have two Trx proteins, Trx1 and Trx2. It has been shown

that Trx1, which is known to be essential for the reduction of disulfide bonds in various proteins, has been shown to be critical for MetO reduction.[31,33] Trx is reduced through the action of thioredoxin reductase (TrxR), which oxidizes NADPH to provide reducing equivalents to Trx.[35]

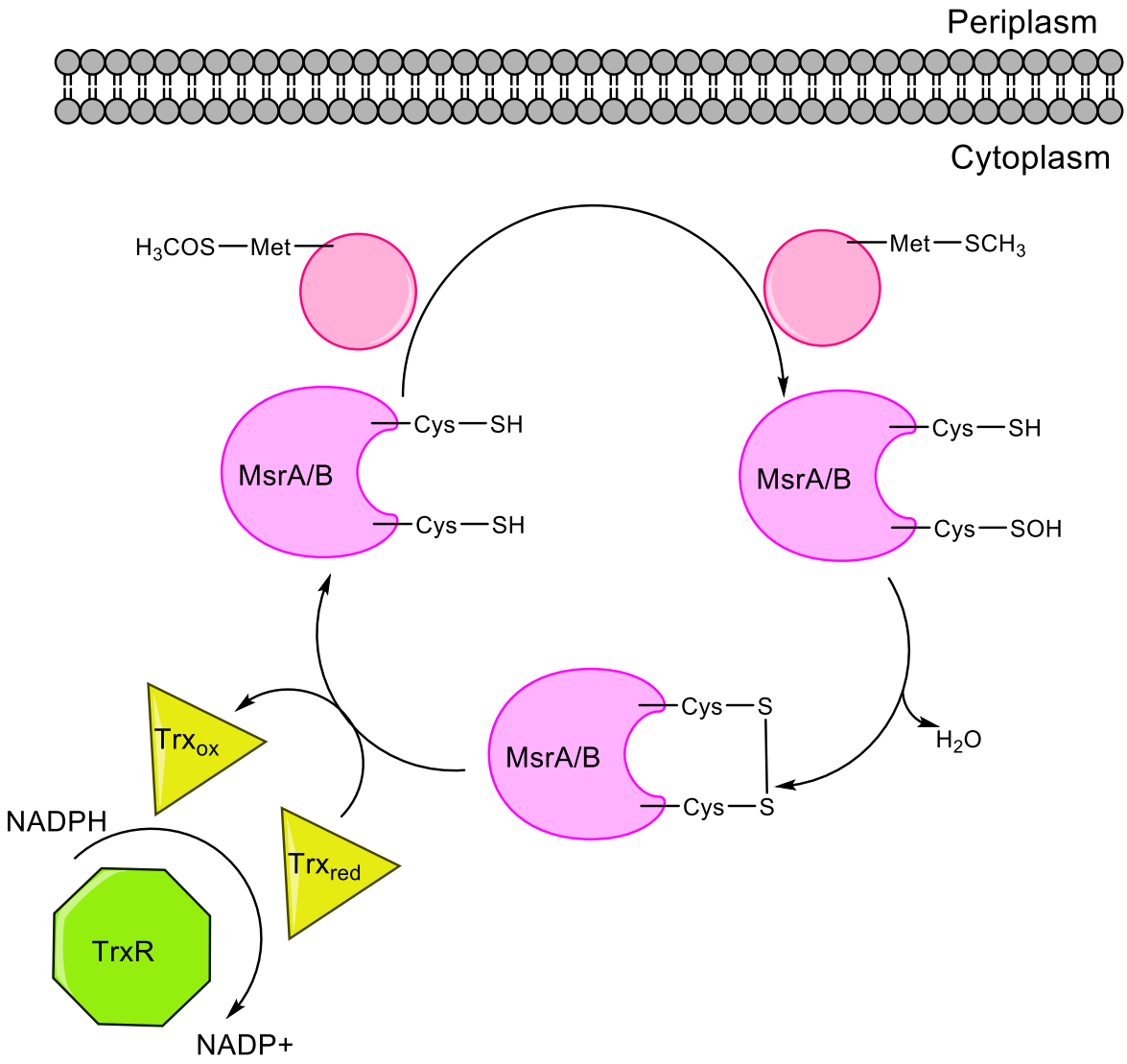

Figure 4-5. Scheme of mechanism by which MsrA/B reduce protein bound MetO in bacteria.

The opposing stereospecificity of MsrA and B is explained by the active sites of the enzymes, which are mirror images of each other.[36] The opposing orientation of a tryptophan within the binding pockets prevents the binding of the non-favored diastereomer of MetO by specific interactions with the terminal methyl group. [31,37–39]

Another bacterial, cytoplasmic molybdoenzyme, BisC, has been shown to be specific for reducing the free S-diastereomer of MetO.[40] However, it was shown that unlike MsrP, BisC cannot reduce MetO in proteins. Therefore, although BisC likely cannot rescue oxidized proteins, it could mitigate oxidative damage on free methionine pools within the cytoplasm, which are essential for protein synthesis.

All four of these bacterial Msrs are responsible for the reduction of MetO found in the cytoplasm and bacterial cell envelope. MsrP, found in the periplasm, helps to fulfill a necessary niche role as a protein repair enzyme for proteins damaged by methionine oxidation within this cellular compartment. In contrast to the other known cytoplasmic Msrs which use the Trx system as a source of reducing equivalents, MsrP uses electrons from the inner membrane quinone pool, or from the soluble cytoplasmic oxidoreductase Fre, which are shuttled to MsrP by membrane bound MsrQ.[3,9,11]

4.6 Transcriptional regulation of MsrP

MsrP transcription is found to be induced upon exposure of bacterial cells to HOCl.[3] Melnyk *et al.* investigated the mechanism by which this transcriptional regulation occurs in *Azospira sillum*.[16] They found that a transcription factor, SigF

induces transcription from the SigF regulon containing MsrP, MsrQ and a protein called MrpX in response to RCS stress. SigF is normally sequestered by a membrane-bound protein NrsF; this is known as a sigma factor/anti-sigma factor system and is known to be a sensitive responder to environmental factors. SigF has been implicated in the transcriptional regulation of genes involved in stress responses to heavy metals and oxidative stress that occurs when bacterial cells are in stationary phase, though Melnyk *et al.* provided evidence that SigF responds primarily to RCS-induced oxidative stress and not that caused by ROS.[16,41,42]

The discovery of MrpX by Melnyk *et al.* on the same operon as MsrP/Q provides further evidence of MsrP as a protein-repair enzyme.[16] MrpX has a large percentage of methionine residues (20%) and a TAT-signal peptide to export it to the periplasm. It is upregulated by 20 to 60-fold following RCS stress and the evidence supports that the methionine residues on MrpX become oxidized following RCS exposure; it is likely that this protein acts as a sink for RCS in the periplasm as MrpX is particularly sensitive to methionine oxidation by HOCl.

4.7 Possible function as a virulence factor

The transcriptional response of upregulating the MsrP/Q system specifically induced by RCS exposure, but not ROS exposure, implies that this system may have evolved as a virulence factor to promote cell survival in response to exposure to phagocytes of the innate immune system.[16,21] The upregulation of the operon encoding MsrP was observed in a pathogenic E. coli O157:H7 strain upon exposure to chlorine, implicating that pathogenic bacteria may have intrinsic resistance to household cleaning products.[43] The transcriptional upregulation of

MsrP/Q was also observed for *Shewanella algae* when the cells were undergoing chlorate-respiration.[44] Melnyk *et al.* also observed that a “housekeeping” MsrP is expressed in several pathogenic bacteria, including a uropathogenic *E. coli,* which suggests that organisms that are in regular contact with host immune cells may regularly utilize the MsrP/Q system for survival.[16]

An analogue of MsrP found in the human pathogen *Campylobacter jejuni*, was found to be unimportant for growth of the cell.[45] However, a mutant strain of *C. jejuni* deficient in MsrP was found to be less virulent in a chicken colonization model, in addition to having a reduced survival towards nitrosating and NO-producing agents.

Another newly discovered methionine sulfoxide reductase molybdoenzyme in *H. influenzae*, MtsZ, has been implicated as a possible virulence factor, aiding the intracellular survival of the bacterial cells and playing a role in their ability to adhere and invade human epithelial cells, as well as to promoting the survival of *H. influenzae* in a murine infection model.[46] It does not appear to be critical to survival for oxidative stress by RCS, although it does seem to play a role in the promotion of biofilm formation.

MtsZ shares many similarities with MsrP. Like MsrP it is a soluble protein which contains a twin-arginine signal peptide; it also has a membrane bound redox partner MtsY, which analogous to the proposed role of MsrQ, also utilizes the quinone pool to provide reducing equivalents to MtsZ.[46] In addition to showing activity towards TMAO, BSO, and DMSO, it is able to utilize both diastereomers of free MetO. However, a key difference between MsrP and MtsZ is that the latter

does not seem capable of reducing MetO on calmodulin, although free MetO seems to be its favored substrate.[3,46] It is suggested that MstZ may be important for energy generation and the redox balance of the cell.

4.8 Originally proposed catalytic mechanism of MsrP

Moco-containing molybdoenzymes ubiquitously utilize catalytic cycles that involve Mo(IV)/Mo(V)/Mo(VI) oxidation state cycling.[47] However, MsrP has been observed to be unable to reach the Mo(VI) oxidation state, even under highly oxidizing conditions using ferricyanide at potentials of greater than +350mV, or when electrochemically poised at highly oxidizing potentials of +600mV.[11,48] Brokx *et al.* used EPR redox titrations to determine a midpoint potential of the Mo(V)/Mo(IV) couple of approximately 134mV at pH 7, with an n~1.63.[11] This is an unusually positive reduction potential[49–51], and the n-value greater than 1.0 is attributed to the weak coupling of this redox transition on Mo to a 2-electron redox event occurring in close proximity to the metal. This was suggested to be due to a redox event occurring on the PDT.

The inability of Mo to be oxidized to Mo(VI), coupled with evidence of a redox event occurring on the pyranopterin ligand, was mystifying as to how MsrP was able to catalyze reduction of a vast number of substrates, given that it appeared to be unable to utilize the commonly known reaction mechanisms of other molybdoenzymes. Adamson *et al.* proposed an unusual catalytic cycle based upon their results of dcV and FTacV electrochemical experiments, which suggested that redox changes on the pyranopterin dithiolene provided the reducing equivalents to the substrate.[48] They measured a midpoint potential of the Mo(V)/Mo(IV) couple

as 174mV at pH 7; this transition was linked to the loss of the 503nm absorbance band that is assigned as a LMCT event[15], indicating a change in the oxidation state of Mo. Furthermore, the slow rate of the electron transfer for this redox event, measured as 3-6 s^{-1}, also indicates that the species undergoes structural changes upon reduction. This geometric change is supported by the XAS data reported by Pushie *et al.*, in which the Mo(V) species is thought to be six-coordinated via the interaction of Asn-45 with Mo *trans* to the oxo group, but upon reduction to Mo(IV) becomes a five coordinate species with Asn-45 dissociated completely from the metal.[52]

Adamson *et al.* also observed redox transitions at -239mV and -261mV, which they ascribed to a pyranopterin redox event transforming the oxidized dihydro form to a reduced tetrahydro form of the cofactor.[48] This redox event was suggested to occur via two sequential e- transfer events that occurred rapidly, exceeding $2 \cdot 10^4$ s^{-1}. As this was deemed to be too rapid to be a metal-centered redox event, the non-innocent PDT ligand seemed to be a likely source of the observed transition.

Given the repeated observation that the Mo(VI) oxidation state was inaccessible, combined with the electrochemical evidence of a PDT centered redox event, and evidence that the fully reduced form of MsrP is responsible for reduction of DMSO, Adamson *et al.* proposed an unusual catalytic mechanism (Figure 4-6).[48] They proposed that *as-isolated* MsrP is a Mo(V)/dihydro-PDT species (semi-oxidized metal/oxidized ligand), which undergoes a 1e-/1H+ metal-based reduction to form the Mo(IV)/dihydro-PDT species (reduced metal/oxidized ligand). The Mo(IV)/dihydro-PDT species can then undergo a 2e-/2H+ reduction to form a

Mo(IV)/tetrahydro-PDT (reduced metal/reduced ligand), which is the species thought to be able to bind the DMSO substrate. It is unclear how the substrate coordinates MsrP, but following substrate turnover, MsrP is thought to be in a Mo(IV)/dihydro-PDT state (reduced metal/oxidized ligand), with the PDT poised to be reduced to continue the catalytic cycle.

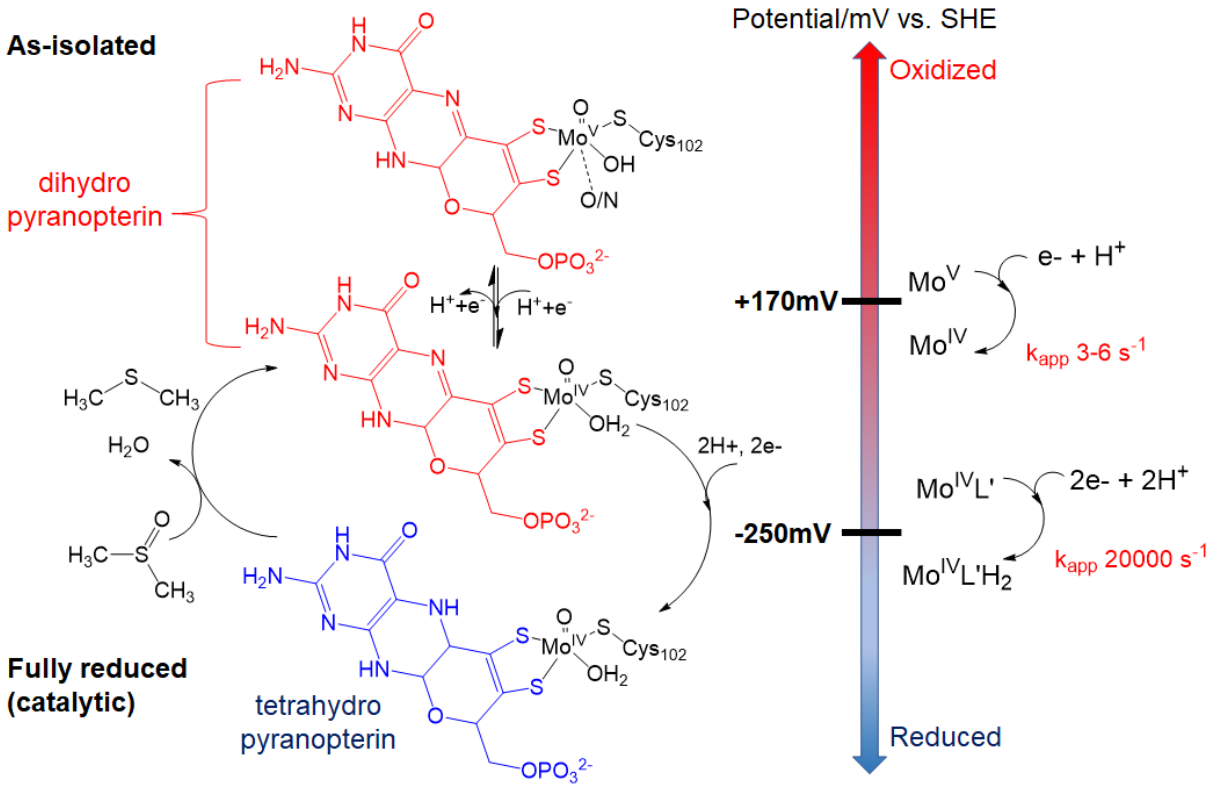

Figure 4-6. Proposed catalytic cycle by Adamson, H. et al. Proc. Natl. Acad. Sci. ***112,*** *1–6 (2015).*[48] *As-isolated MsrP is in the Mo(V) oxidation state and undergoes a 1e-/1H+ reduction to form a Mo(IV) species with an oxidized 10,10a dihydro PDT. The PDT undergoes a 2e-/2H+ reduction to form a Mo(VI) species with a reduced tetrahydro PDT, which is the presumed catalytically active form of the enzyme. Substrate turnover occurs via an unknown mechanism which involves oxidation state changes on the PDT ligand while the metal remains in the Mo(IV) oxidation state throughout the catalytic cycle. Figure adapted from Lee, C. C., Sickerman, N. S., Hu, Y., & Ribbe, M. W. (2016). ChemBioChem, 17(6), 453–455.*[68]

The striking contrast of this proposed mechanism to all accepted molybdoenzyme mechanisms is evidenced by Mo remaining in the reduced Mo(IV) oxidation state throughout the catalytic cycle, whereas other molybdoenzymes ubiquitously utilize the common Mo(IV)/(V)/(VI) oxidation state cycling to oxidize or reduce substrates.[47] The binding pocket of MsrP leads directly to the coordination position occupied by the putative O(H) ligand on Mo, which makes it a likely location for substrate binding following the labilization of the O(H) by a protonation event to make a water.[1] Given that the substrate likely binds to Mo in an analogous way to the substrate binding in other molybdoenzymes, Mo remaining in the Mo(IV) oxidation state throughout catalytic turnover seems unlikely, as reducing equivalents would probably need to be shuttled to the substrate through the metal even if redox changes occurred on the PDT ligand during catalysis.[5,53]

4.9 Kinetics and substrate specificities

MsrP, unlike the structurally similar SO, does not function as a sulfite oxidase, but instead is reported as having reductase activity towards TMAO, DMSO, MetO and various sulfoxides.[1]

Loschi *et al.* first assessed the kinetic activity of *as-isolated* MsrP from *E. coli* by observing the change in absorption at 570nm, signaling the substrate-dependent oxidation of reduced benzyl viologen, which was used as an electron donor during catalysis.[1] *As-isolated* MsrP showed reductase activity towards DMSO, TMAO, and various sulfoxides, but did not show any activity towards cyclic N-oxides, chlorate or hydroxylamine. They also monitored changes in absorbance of two distinct electron acceptors, ferricyanide and *S. cerevisiae* cytochrome c, to assess

the ability of *as-isolated* MsrP to oxidize sulfite and demonstrated that the enzyme displayed no activity towards this substrate.

As-isolated E. coli MsrP yields remarkably poor kinetic parameters. Loschi *et al.* reported a k_{cat}/K_M of 0.403 $s^{-1}mM^{-1}$ when DMSO was used as a substrate.[1] In contrast, the structurally similar CSO has a reported k_{cat}/K_M of 5200 $s^{-1}mM^{-1}$.[54] DMSO reductase from *E. coli* has a reported k_{cat}/K_M of 4.55 $s^{-1}mM^{-1}$, an 11-fold increase over MsrP.[55]

The relatively poor kinetics of MsrP is also observable when the enzyme is isolated from species other than *E. coli*. Hitchcock *et al.* reported that the kinetic parameters of an MsrP analogue from *C. jejuni* were poor towards all substrates tested, including DMSO, TMAO, TMSO and MetO.[45] MsrP from *R. sphaeroides* had a reported k_{cat}/K_M of 1.00 $s^{-1}mM^{-1}$towards free racemic MetO[56], whereas MsrA from *E. coli* has a reported k_{cat}/K_M of 2000 $s^{-1}mM^{-1}$ towards S-MetO.[35] The kinetic behavior of MsrP compared to other Msrs and select molybdoenzymes is shown in Table 4-1.

The poor kinetic activity of MsrP greatly contrasts *in vitro* with its apparent importance *in vivo.* One suggested reason for the observed poor kinetics of *as-isolated* MsrP was that the original construct was a recombinant enzyme which contained a C-term His tag, which was thought to destabilize the protein and cause alterations in activity.[2] Sequence alignment analysis of over 1800 MsrP proteins revealed a highly conserved hydrophobic residue at the end of the C-term, which was usually a tyrosine or phenylalanine; addition of a hydrophobic His tag could lead to unfavorable interactions with this conserved residue, causing structural

alterations to the enzyme. A study conducted by Sabaty *et al.* on MsrP from *R. sphaeroides*, using DMSO as a substrate, demonstrated a K_M of ~261mM for the C-term His tag MsrP. Enzyme containing the N-term-His tag had a K_M of ~43mM and following TEV cleavage of the N-term His tag, a K_M of ~61mM.[2] It was also suggested that the true physiological substrate of MsrP was yet to be found, which could explain the poor kinetic values obtained from the substrates that have been tested.

Enzyme	Substrate	k_{cat} (s^{-1})	K_M (mM)	k_{cat}/K_M ($s^{-1}mM^{-1}$)
MsrP (E. coli)	DMSO[1,48]	4.2-4.8	12-35	0.12 -0.403
	R-MetO[3]	-	25.7	-
	S-MetO[3]	-	8.0	-
MsrA (E. coli)	S-MetO[35]	3.7	1.900	2.000
MsrB (E. coli)	R-MetO[35]	6.9	3.9	1.7
CSO (Chicken Liver)	Sulfite[54]	59.6	0.0113	5200
DmsABC (E. coli)	DMSO[55]	79	18	4.55
TorZ (H. influenzae)	DMSO[46]	85.4	0.14	610
	S-BSO[46]	182.6	1.2	152
	Racemic-MetO[46]	91.7	0.41	224
MsrP (R. sphaeroides)	DMSO[56]	28	61	0.465
	Free L-Met-*R,S*-O[56]	122	115	1.06
	Ser-MetO-Ser[56]	108	130	8.30
	Oxidized β-casein[56]	100	0.093	10.75
BisC (E.coli)	S-MetO[40]	0.053	0.017	3.12
	R-MetO[40]	No activity	No activity	No activity

Table 4-1. Kinetic parameters of as-isolated MsrP from E. coli vs. other known bacterial Msr proteins and molybdoenzymes.

4.10 X-ray Absorption Spectroscopy of MsrP

The Mo K-edge near-edge spectra (XANES) of *as-isolated* Mo(V) MsrP and dithionite-reduced Mo(IV) MsrP are sensitive to the oxidation state of the

metal.[52,57,58] The rising edge of the Mo(IV) species occurs at approximately 1eV lower energy relative to the Mo(V) species. This is consistent with the energies expected of these formal oxidation states and supports the reported EPR data that *as*-isolated MsrP is primarily in the Mo(V) oxidation state.[11,15,57] Pushie *et al.* also observed that although addition of 20mM ferricyanide was not able to oxidize *as-isolated* MsrP to Mo(VI), as evidenced by no observable change in the energy of the rising edge of the sample, addition of 20mM hexachlorioiridate(IV) did shift the rising edge energy by nearly 2eV, although unfortunately, this spectrum was not published.[52] No change in the energy of the rising edge of MsrP was detected upon the addition of 5mM DMSO, indicating no oxidation state change to the metal.[52,57]

A pre-edge peak in the XANES of the Mo(IV) and Mo(V) species occurs at ~20,007.0 and ~20,006.2eV, respectively.[52,57] This peak is a sensitive barometer of the number of Mo=O bonds present in the structure; it arises as a result of a Mo 1s→4d (Mo=O) π* transition.[57–59] This transition, though formally dipole-forbidden, is made allowed due to p-d orbital mixing arising from the distortion of the active site from octahedral. Pushie *et al.* compared the Mo(IV) and Mo(V) species of MsrP with that of Mo(VI) SO, which is fully oxidized and possesses two Mo=O bonds, and found that the pre-edge feature of both MsrP species is less intense than that of SO, indicating that MsrP likely contains a single Mo=O bond.[52] Havelius *et al.* compared the intensity of the pre-edge feature of *as-isolated* Mo(V) MsrP with that of reduced Mo(IV), which has a single M=O bond, and oxidized Mo(VI) hSO, which has two Mo=O bonds, and found that the intensity of the pre-edge peak of MsrP was between that observed for the two hSO species.[57] They concluded that this

likely meant that there was between one and two Mo=O bonds in the MsrP structure, which could possibly indicate a mixture of species in the *as-isolated* MsrP sample. The possible mixture of species is also supported by the Q-band EPR data collected by Havelius *et al.*, which they believed was responsible for the two slightly different g_1 values they observed. A more detailed explanation of the Q-band EPR data is discussed in section 4-12.

The EXAFS region of the Mo K-edge XAS spectra consists of oscillations that correlate to the photo ejected electron originating from the Mo 1s orbital interacting with the electron clouds of the first coordination sphere atoms; these oscillations are Fourier transformed to help elucidate the number and identity of atoms forming the first coordination sphere of Mo, as well as the relative distances of these atoms from the metal.[60] Previously collected EXAFS of *as-isolated* MsrP, reported by Pushie *et al.* is consistent with the original interpretation of the crystal structure; consisting of a single 1.71Å Mo=O bond, three 2.37Å Mo-S bonds, and a longer 2.08Å Mo-O(H) bond, as well as a long Mo-N/O bond that they neither observed in the reduced Mo(IV) species nor identified in the crystal structure.[1,52] They suggested that this interaction was not observed in the crystal structure due to photoreduction of the active site, which caused Asn-45 to dissociate from Mo. They also reported that the Mo(IV) species likely possessed an OH_2 in the equatorial position. The group in this position was identified to be an O(H) in the *as-isolated* Mo(V) species, which is consistent with the reaction mechanism proposed by Adamson *et al.,* as discussed in section 4-8.[48,52]

Havelius *et al.* reported a similar active site structure as Pushie *et al*. and found that the fit improved with the addition of a long 2.6Å O/N bond that they speculated arose from an interaction between Mo and Asn-45.[57] Consistent with their XANES and Q-band observations that supported the presence of two species in their protein sample, approximately 50% of the EXAFS sample was interpreted to possess two short Mo-O bonds and 50% to possess both a long and a short Mo-O bond. They hypothesized that it was possible that the equatorial oxygen atom had a pK_a of ~8, which matched the pH of the sample; therefore, half of the sample contained a protonated oxygen and half was deprotonated, shortening the observed Mo-O^- bond.

4.11 UV-Vis and Magnetic Circular Dichroism (MCD) spectroscopies

As-isolated MsrP is reported to be pink.[1,11,15] The UV/Vis of the prepared enzyme has a broad peak at 503nm and another at 360nm, which are not present in the spectrum of the reduced Mo(IV) form of MsrP.[11] Reduction of the *as-isolated* enzyme by addition of 2mM sodium dithionite concurrently results in the loss of the characteristic pink color of the Mo(V) enzyme. The loss of these peaks has also been observed as an electrochemically induced, metal-based reduction event.[48]

Yang *et al.* assigned the transitions observed in the UV/Vis and MCD spectra of *as-isolated* MsrP as LMCT bands.[15] The origins of the two lowest bands are LMCT transitions from the dithiolene sulfur out-of-plane orbital (S'^{op}) to the Mo(x^2-y^2) singly occupied orbital and the cysteine thiolate sulfur (S^V_{Cys}) to the Mo(x^2-y^2) orbital. The (S'^{op}) to Mo(x^2-y^2) transition is low intensity, indicating that there is little overlap between the two orbitals. This indicates that electronic communication

between the Mo(x^2-y^2) redox orbital and the PDT via the S'^{op} is minimal, and likely the PDT would not be highly involved in electron transfer during catalysis. A geometric change due to a redox event during catalysis might allow orbital mixing and thus, improved electronic communication between Mo and the PDT ligand, but there is no current evidence of this occurring in the enzyme.

The O_{oxo}-Mo-S_{Cys}-C dihedral angle obtained from the crystal structure is 65°. It has been previously demonstrated that the covalency between Mo-S_{cys}, in oxomolybdenum thiolate models of the active site of SO, is dependent upon the O_{oxo}-Mo-$S_{thiolate}$-C dihedral angle.[61–63] The percentage of sulfur character in the wavefunction has a $\cos^2$ dependence upon the dihedral angle, which indicates that if the dihedral angle is ~90°, the sulfur p-orbital is completely orthogonal to the metal redox orbital in the equatorial plane and the overlap between the two orbitals is minimal. However, as this dihedral angle becomes more acute, the overlap between the two orbitals increases until the covalency between Mo-S is maximized. Based upon the dihedral angle found in MsrP, there is an estimated 4.5% S^{V}_{Cys} character in the β-LUMO wavefunction, which agrees with the 5.9% that was calculated via DFT.[15]

The crystal structure of CSO shows an 84° O_{oxo}-Mo-S_{Cys}-C dihedral angle.[6] When this value is compared to the more acute 65° O_{oxo}-Mo-S_{Cys}-C dihedral angle in MsrP, the covalency in the Mo-S_{cys} bond in MsrP is estimated to be 6-fold greater than that of CSO.[15] It is speculated that charge donation from S_{cys} to Mo may serve to reduce the effective nuclear charge on the metal in SO, favoring the Mo(VI) state

and facilitating ET to restore the active site to a catalytically competent form.[63] Due to this, it was speculated that the 6-fold increase in the S_{cys}-Mo covalency may energetically favor adoption of the Mo(V) oxidation state in *as-isolated* MsrP.[15]

4.12 EPR of WT MsrP

Given the presumed structural similarities between MsrP and CSO, it would be expected that the EPR spectra of *as-isolated* MsrP would resemble that of CSO, but that is not the case (Figure 4-7 and Table 4-2). The EPR parameters of both enzymes are summarized in Table 4-2.

	g values				A values (10^{-4} cm^{-1})			
	1	2	3	av.	1	2	3	av
MsrP[15]	2.030	1.974	1.969	1.991	54.5	23.5	22.5	33.5
CSO (low pH form)[64]	2.004	1.972	1.966	1.981	0.85	0.80	1.30	0.98
CSO (high pH form)[64]	1.987	1.964	1.953	1.968	-	-	-	-

Table 4-2. EPR parameters of as-isolated MsrP and the low and high pH forms of CSO.

The X-band EPR of *as-isolated* MsrP from *E. coli* is consistent with reports that the enzyme is purified in exclusively the Mo(V) state.[11,15,52,57] The EPR spectra of CSO are decidedly more rhombic than that of MsrP (Figure 4.7).[64] The g and A tensors of the reported spectra of MsrP are surprisingly axial, with an unusually high g_1 value of 2.031 and $g_{2,3}$ of 1.976. The g_1 is higher than that of even the very rapid xanthine oxidase intermediate species (XO_{vr}), with a g_1 of 2.025[14].[15,65] XO_{vr} possesses a terminal sulfido in the equatorial plane; there is a significant amount of electron delocalization on the sulfido. Furthermore, XAS shows that the Mo(d)-S(p) π covalency is ~2-3 fold greater than that due to the Mo(d)-S(p) σ bonding, and the LUMO contains ~35% S(p) character.[66] This increased covalency is responsible for the relatively high g_1 value in XO_{vr}.

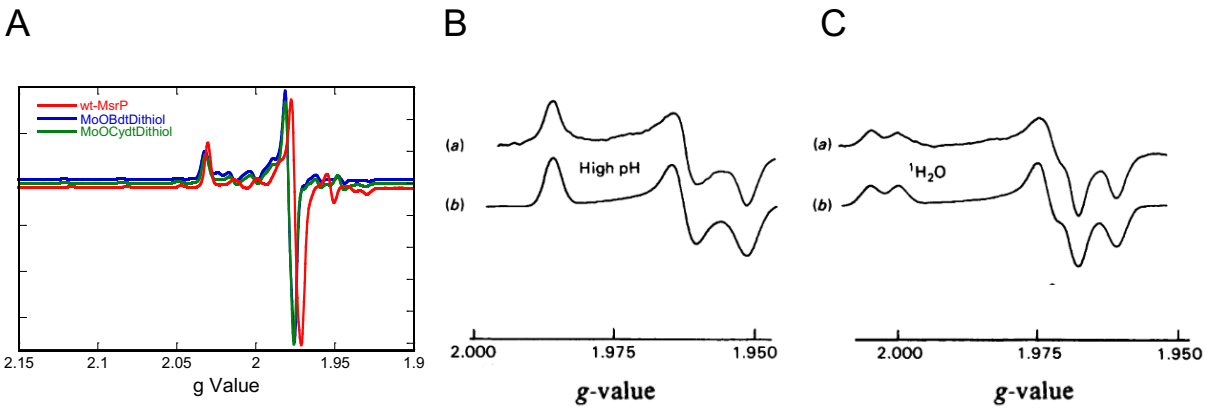

Figure 4-7. X band EPR spectra of as-isolated MsrP and synthetic analogues of the active site (A). The experimental data is in red and the simulation is in blue. The high pH form of CSO[64] (B); the experimental data (a) and simulation (b) is shown. The low pH form of CSO[64] (C); the experimental data (a) and simulation (b) is shown. Figure A is modified from Ingersol, L. J.; et al. Addressing Ligand-Based Redox in Molybdenum-Dependent Methionine Sulfoxide Reductase. J. Am. Chem. Soc. 2020, 142 (6), 2721–2725. https://doi.org/10.1021/jacs.9b11762.

Increases in Mo-S covalency in MsrP would increase the g_1 value, but as discussed in Section 4.11, the lack of substantial overlap between the dithiolene

S^{op} orbital and the Mo(x^2-y^2) orbital results in minimal Mo-$S_{dithiolene}$ covalency, and therefore cannot be the source of the high g_1 value.[15] The β-LUMO of MsrP contains ~4.5% S^{V}_{Cys} character, which is far less than the ~35% S(p) character in the LUMO of XO_{vr}.[15,66] Yet, despite the overall decrease in Mo-S covalency in MsrP compared to XO_{vr}, it has a greater g_1 value, indicating that the source of the high g_1 is unexplained by the covalency between Mo-S_{cys} or Mo-$S_{dithiolene}$.

Furthermore, the g-tensor of XO_{vr} is also more anisotropic than that observed for MsrP; the degree of anisotropy is indicative of increased asymmetry in the equatorial ligands around Mo.[11,15,65] However, given that the first coordination sphere of MsrP and XO are originally assigned as three S and one O, the highly axial g and A tensors of MsrP are an unlikely observation for the originally accepted active site structure.[1]

There is no proton hyperfine in the EPR spectra of *as-isolated* MsrP, which would be expected for a Mo active site with an equatorial -OH group.[11,15,52,57] This could be explained by the relative orientation of the putative -OH group with respect to the Mo, as this would influence the amount of overlap the proton would have with the SOMO centered on Mo. This is seen in the case of the low pH form of SO, in which the hydrogen on the -OH group forms a hydrogen bonding interaction with the S_{Cys}, which brings the proton into the equatorial plane aligned with the Mo d_{xy} orbital.[67] The high pH form of SO does not show the same proton hyperfine in the EPR spectra because the proton no longer resides in the equatorial plane, making its interaction with the Mo d_{xy} orbital minimal.

To further resolve the g-tensor of *as-isolated* MsrP from *E. coli*, Havelius *et al*. performed Q-band EPR.[57] The spectrum showed a slight rhombicity in $g_{2,3}$, but the simulated parameters of the Q-band data agree with those obtained at X-band.[11,15,52,57]

Sabaty *et al*. performed low-temperature X-band EPR on MsrP from *R.sphaeroides* and found evidence of two different Mo(V) species, with slight differences in their g- and A-tensors.[2] The observation of two slightly different electronic structures suggesting a mixture of two different Mo(V) species in the sample is similar to the XAS data observed by Havelius *et al*.[57] However, the EPR simulations of the *R.sphaeroides* MsrP was highly similar to that obtained for the *E. coli* enzyme, with a high g_1 of ~2.030 and an axial g_2,g_3.[2]

4.13 Conflicting spectroscopic and structural data of MsrP

There are several puzzling characteristics of *as-isolated* MsrP which differentiate it from other known molybdoenzymes. It is the only molybdoenzyme that is isolated in the Mo(V) oxidation state and reportedly cannot not achieve the Mo(VI) oxidation state.[11,15,48,57] This led to the proposal of the unusual catalytic cycle by Adamson *et al.* in which the Mo remains in the Mo(IV) oxidation state while the PDT ligand undergoes redox changes to catalyze the reduction of the substrate.[48] This mechanism contrasts with the accepted mechanism of every other known molybdoenzyme, in which the metal utilizes the Mo(IV)/Mo(V)/Mo(VI) oxidation states to drive the oxidation or reduction of substrates, and is entirely based upon the assumption that the Mo(VI) oxidation state is inaccessible.[53]

Furthermore, it is unclear how a Mo coordinated by an axial oxo group, and four inequivalent atoms in the first coordination sphere in the equatorial plane can produce an unusually high g_1 value and an axial X- and Q-band EPR spectra.[11,15,52,57] If the proposed active site structure of *as-isolated* MsrP resembles that of CSO, it would follow that their EPR spectra would be comparable, but they are not.[1] The reported EPR spectra for *as-isolated* MsrP is incongruent with the active site structure proposed by the original interpretation of the crystal structure and the XAS data.[1,52,57]

It is also indeterminate how MsrP seems essential for rescuing periplasmic proteins damaged by RCS by reducing MetO, *in vivo*, yet displays poor kinetic parameters *in vitro.*[1,3,48]

In this study, we used a combination of site-directed mutagenesis, spectroscopies such as EPR and XAS, computational work, and docking studies to elucidate the answers to these questions. We provide strong evidence that *as-isolated* MsrP represents a thiol-inhibited species that likely forms upon lysis of the cells for protein purification. This explains the incongruency between the original proposed structure of the active site and the EPR data, the inability of *as-isolated* MsrP to be oxidized to the Mo(VI) oxidation state, and the poor kinetic parameters observed *in vitro*.

4.14 References

(1) Loschi, L.; Brokx, S. J.; Hills, T. L.; Zhang, G.; Bertero, M. G.; Lovering, A. L.; Weiner, J. H.; Strynadka, N. C. J. Structural and Biochemical Identification of a Novel Bacterial Oxidoreductase. *The Journal of biological chemistry* **2004**, *279* (48), 50391–50400. https://doi.org/10.1074/jbc.M408876200.

(2) Sabaty, M.; Grosse, S.; Adryanczyk, G.; Boiry, S. S.; Biaso, F. F.; Arnoux, P.; Pignol, D. Detrimental Effect of the 6 His C-Terminal Tag on YedY Enzymatic Activity and Influence of the TAT Signal Sequence on YedY Synthesis. *BMC Biochemistry* **2013**, *14* (1), 1–12. https://doi.org/10.1186/1471-2091-14-28.

(3) Gennaris, A.; Ezraty, B.; Henry, C.; Agrebi, R.; Vergnes, A.; Oheix, E.; Bos, J.; Leverrier, P.; Espinosa, L.; Szewczyk, J.; Vertommen, D.; Iranzo, O.; Collet, J.-F.; Barras, F. Repairing Oxidized Proteins in the Bacterial Envelope Using Respiratory Chain Electrons. *Nature* **2015**, *528* (7582), 409–412. https://doi.org/10.1038/nature15764.

(4) Reschke, S.; Duffus, B. R.; Schrapers, P.; Mebs, S.; Teutloff, C.; Dau, H.; Haumann, M.; Leimkühler, S. Identification of YdhV as the First Molybdoenzyme Binding a Bis-Mo-MPT Cofactor in Escherichia Coli. *Biochemistry* **2019**, *58* (17), 2228–2242. https://doi.org/10.1021/acs.biochem.9b00078.

(5) Hille, R.; Hall, J.; Basu, P. The Mononuclear Molybdenum Enzymes. *Chemical Reviews* **2014**, *114* (7), 3963–4038. https://doi.org/10.1021/cr400443z.

(6) Kisker, C.; Schindelin, H.; Pacheco, A.; Wehbi, W. A.; Garrett, R. M.; Rajagopalan, K. v.; Enemark, J. H.; Rees, D. C. Molecular Basis of Sulfite Oxidase Deficiency from the Structure of Sulfite Oxidase. *Cell* **1997**, *91* (7), 973–983. https://doi.org/10.1016/S0092-8674(00)80488-2.

(7) Fischer, K. Structural Basis of Eukaryotic Nitrate Reduction: Crystal Structures of the Nitrate Reductase Active Site. *the Plant Cell Online* **2005**, *17* (4), 1167–1179. https://doi.org/10.1105/tpc.104.029694.

(8) von Rozycki, T.; Yen, M. R.; Lende, E. E.; Saier, M. H. The YedZ Family: Possible Heme Binding Proteins That Can Be Fused to Transporters and Electron Carriers. *Journal of Molecular Microbiology and Biotechnology* **2005**, *8* (3), 129–140. https://doi.org/10.1159/000085786.

(9) Juillan-Binard, C. C. C.; Picciocchi, A.; Andrieu, J.-P. P.; Dupuy, J.; Petit-Hartlein, I.; Caux-Thang, C.; Vivès, C.; Nivière, V.; Fieschi, F.; Vivï¿½s, C.; Niviï¿½re, V.; Fieschi, F. A Two-Component NADPH Oxidase (NOX)-like System in Bacteria Is Involved in the Electron Transfer Chain to the Methionine Sulfoxide Reductase MsrP. *Journal of Biological Chemistry* **2017**, *292* (6), 2485–2494. https://doi.org/10.1074/jbc.M116.752014.

(10) Sanchez-Pulido, L.; Rojas, A. M.; Valencia, A.; Martinez-A, C.; Andrade, M. A. ACRATA: A Novel Electron Transfer Domain Associated to Apoptosis and Cancer. *BMC Cancer* **2004**, *4*, 1–6. https://doi.org/10.1186/1471-2407-4-98.

(11) Brokx, S. J.; Rothery, R. a; Zhang, G.; Ng, D. P.; Weiner, J. H. Characterization of an Escherichia ColiSulfite Oxidase Homologue Reveals the Role of a Conserved Active Site Cysteine in Assembly and Function †. *Biochemistry* **2005**, *44* (30), 10339–10348.

(12) Stewart, L. J.; Bailey, S.; Bennett, B.; Charnock, J. M.; Garner, C. D.; McAlpine, A. S. Dimethylsulfoxide Reductase: An Enzyme Capable of Catalysis with Either Molybdenum or Tungsten at the Active Site. *Journal of molecular biology* **2000**, *299* (3), 593–600. https://doi.org/10.1006/jmbi.2000.3702.

(13) Buc, J.; Santini, C.-L.; Giordani, R.; Czjzek, M.; Wu, L.-F.; Giordano, G. Enzymatic and Physiological Properties of the Tungsten-Substituted Molybdenum TMAO Reductase from Escherichia Coli. *Molecular Microbiology* **1999**, *32* (1), 159–168. https://doi.org/10.1046/j.1365-2958.1999.01340.x.

(14) Johnson, J. L.; Rajagopalan, K. v. Electron Paramagnetic Resonance of the Tungsten Derivative of Rat Liver Sulfite Oxidase. *Journal of Biological Chemistry* **1976**, *251* (18), 5505–5511.

(15) Yang, J.; Rothery, R.; Sempombe, J.; Weiner, J. H.; Kirk, M. L. Spectroscopic Characterization of YedY: The Role of Sulfur Coordination in a Mo(V) Sulfite Oxidase Family Enzyme Form. *Journal of the American Chemical Society* **2009**, *131* (43), 15612–15614. https://doi.org/10.1021/ja903087k.

(16) Melnyk, R. a; Youngblut, M. D.; Clark, I. C.; Carlson, H. K.; Wetmore, K. M.; Price, M. N.; Iavarone, A. T.; Deutschbauer, A. M.; Arkin, A. P.; Coates, J. D. Novel Mechanism for Scavenging of Hypochlorite Involving a Periplasmic Methionine-Rich Peptide and Methionine Sulfoxide Reductase. *mBio* **2015**, *6* (3), 1–8. https://doi.org/10.1128/mBio.00233-15.Editor.

(17) Vogt, W. Oxidation of Methionyl Residues in Proteins: Tools, Targets, and Reversal. *Free Radical Biology and Medicine* **1995**, *18* (1), 93–105. https://doi.org/10.1016/0891-5849(94)00158-G.

(18) Davies, M. J. The Oxidative Environment and Protein Damage. *Biochimica et Biophysica Acta - Proteins and Proteomics* **2005**, *1703* (2), 93–109. https://doi.org/10.1016/j.bbapap.2004.08.007.

(19) Schóneich, C., Zhao, F., Madden, K., Bobrowski, K. Side Chain Fragmentation of N-Terminal Threonine or Serine Residue Induced through Intramolecular Proton Transfer to Hydroxy Sulfuranyl Radical Formed at Neighboring Methionine in Dipeptides. *J. Am. Chem. Soc.* **1994**, No. 116, 4641–4652.

(20) Caldwell, P.; Luk, D. C.; Weissbach, H.; Brot, N. Oxidation of the Methionine Residues of Escherichia Coli Ribosomal Protein L12 Decreases the Protein's Biological Activity. *Proceedings of the National Academy of Sciences of the United States of America* **1978**, *75* (11), 5349–5352. https://doi.org/10.1073/pnas.75.11.5349.

(21) Pattison, D. I.; Davies, M. J. Absolute Rate Constants for the Reaction of Hypochlorous Acid with Protein Side Chains and Peptide Bonds. *Chemical Research in Toxicology* **2001**, *14* (10), 1453–1464. https://doi.org/10.1021/tx0155451.

(22) Bonvini, E.; Bougnoux, P.; Stevenson, H. C.; Miller, P. Activation of the Oxidative Burst in Human Monocytes Is Associated with Inhibition of Methionine- Dependent Methylation of Neutral Lipids and Phospholipids

Functions Thought to Require Methylation Reaction (s) for Their Expression . The Present Study In. *J Clin Invest* **1983**, *73* (14), 1629–1637.

(23) Cantoni, G. L. Biological Methylation: Selected Aspects. *Annual Review of Biochemistry* **1975**, *44* (1), 435–451. https://doi.org/10.1146/annurev.bi.44.070175.002251.

(24) Polevoda, B.; Sherman, F. Methylation of Proteins Involved in Translation. *Molecular Microbiology* **2007**, *65* (3), 590–606. https://doi.org/10.1111/j.1365-2958.2007.05831.x.

(25) Paik, Woon, Kim, S. Protein Methylation: Chemical, Enzymological, and Biological Significance. *Adv. Enzymol* **1975**, *42*, 227–286.

(26) Rosen, H.; Klebanoff, S. J.; Wang, Y.; Brot, N.; Heinecke, J. W.; Fu, X. Methionine Oxidation Contributes to Bacterial Killing by the Myeloperoxidase System of Neutrophils. *Proceedings of the National Academy of Sciences of the United States of America* **2009**, *106* (44), 18686–18691. https://doi.org/10.1073/pnas.0909464106.

(27) Delaye, L.; Becerra, A.; Orgel, L.; Lazcano, A. Molecular Evolution of Peptide Methionine Sulfoxide Reductases (MsrA and MsrB): On the Early Development of a Mechanism That Protects against Oxidative Damage. *Journal of Molecular Evolution* **2007**, *64* (1), 15–32. https://doi.org/10.1007/s00239-005-0281-2.

(28) Brot, N.; Weissbach, L.; Werth, J.; Weissbach, H. Enzymatic Reduction of Protein-Bound Methionine Sulfoxide. *Proceedings of the National Academy of Sciences of the United States of America* **1981**, *78* (4), 2155–2158. https://doi.org/10.1073/pnas.78.4.2155.

(29) Grimaud, R.; Ezraty, B.; Mitchell, J. K.; Lafitte, D.; Briand, C.; Derrick, P. J.; Barras, F. Repair of Oxidized Proteins: Identification of a New Methionine Sulfoxide Reductase. *Journal of Biological Chemistry* **2001**, *276* (52), 48915–48920. https://doi.org/10.1074/jbc.M105509200.

(30) Lin, Z.; Johnson, L. C.; Weissbach, H.; Brot, N.; Lively, M. O.; Lowther, W. T. Free Methionine-(R)-Sulfoxide Reductase from Escherichia Coli Reveals a New GAF Domain Function. *Proceedings of the National Academy of Sciences of the United States of America* **2007**, *104* (23), 9597–9602. https://doi.org/10.1073/pnas.0703774104.

(31) Ezraty, B.; Gennaris, A.; Barras, F.; Collet, J.-F. Oxidative Stress, Protein Damage and Repair in Bacteria. *Nature Reviews Microbiology* **2017**, *15* (7), 385–396. https://doi.org/10.1038/nrmicro.2017.26.

(32) Gonzalez Porqué, P.; Baldesten, A.; Reichard, P. The Involvement of the Thioredoxin System in the Reduction of Methionine Sulfoxide and Sulfate. *Journal of Biological Chemistry* **1970**, *245* (9), 2371–2374.

(33) Stewart, E. J.; Åslund, F.; Beckwith, J. Disulfide Bond Formation in the Escherichia Coli Cytoplasm: An in Vivo Role Reversal for the Thioredoxins. *EMBO Journal* **1998**, *17* (19), 5543–5550. https://doi.org/10.1093/emboj/17.19.5543.

(34) Boschi-Muller, S.; Azza, S.; Branlant, G. E. Coli Methionine Sulfoxide Reductase with a Truncated N Terminus or C Terminus, or Both, Retains the Ability to Reduce Methionine Sulfoxide. *Protein Science* **2008**, *10* (11), 2272–2279. https://doi.org/10.1110/ps.10701.

(35) Kappler, U.; Nasreen, M.; McEwan, A. New Insights into the Molecular Physiology of Sulfoxide Reduction in Bacteria. *Advances in Microbial Physiology* **2019**, *75*. https://doi.org/10.1016/bs.ampbs.2019.05.001.

(36) Lowther, W. T.; Weissbach, H.; Etienne, F.; Brot, N.; Matthews, B. W. The Mirrored Methionine Sulfoxide Reductases of Neisseria Gonorrhoeae Pilb. *Nature Structural Biology* **2002**, *9* (5), 348–352. https://doi.org/10.1038/nsb783.

(37) Lowther, W. T.; Brot, N.; Weissbach, H.; Matthews, B. W. Structure and Mechanism of Peptide Methionine Sulfoxide Reductase, an “anti-Oxidation” Enzyme. *Biochemistry* **2000**, *39* (44), 13307–13312. https://doi.org/10.1021/bi0020269.

(38) Ranaivoson, F. M.; Neiers, F.; Kauffmann, B.; Boschi-Muller, S.; Branlant, G.; Favier, F. Methionine Sulfoxide Reductase B Displays a High Level of Flexibility. *Journal of Molecular Biology* **2009**, *394* (1), 83–93. https://doi.org/10.1016/j.jmb.2009.08.073.

(39) Boschi-Muller, S.; Gand, A.; Branlant, G. The Methionine Sulfoxide Reductases: Catalysis and Substrate Specificities. *Archives of Biochemistry and Biophysics* **2008**, *474* (2), 266–273. https://doi.org/10.1016/j.abb.2008.02.007.

(40) Ezraty, B.; Bos, J.; Barras, F.; Aussel, L. Methionine Sulfoxide Reduction and Assimilation in Escherichia Coli: New Role for the Biotin Sulfoxide Reductase BisC. *Journal of Bacteriology* **2005**, *187* (1), 231–237. https://doi.org/10.1128/JB.187.1.231-237.2005.

(41) Kohler, C.; Lourenço, R. F.; Avelar, G. M.; Gomes, S. L. Extracytoplasmic Function (ECF) Sigma Factor F Is Involved in Caulobacter Crescentus Response to Heavy Metal Stress. *BMC Microbiology* **2012**, *12*. https://doi.org/10.1186/1471-2180-12-210.

(42) Masloboeva, N.; Reutimann, L.; Stiefel, P.; Follador, R.; Leimer, N.; Hennecke, H.; Mesa, S.; Fischer, H. M. Reactive Oxygen Species-Inducible Ecf σ Factors of Bradyrhizobium Japonicum. *PLoS ONE* **2012**, *7* (8). https://doi.org/10.1371/journal.pone.0043421.

(43) Wang, S.; Deng, K.; Zaremba, S.; Deng, X.; Lin, C.; Wang, Q.; Tortorello, M. lou; Zhang, W. Transcriptomic Response of Escherichia Coli O157:H7 to Oxidative Stress. *Applied and Environmental Microbiology* **2009**, *75* (19), 6110–6123. https://doi.org/10.1128/AEM.00914-09.

(44) Clark, I. C.; Melnyk, R. A.; Iavarone, A. T.; Novichkov, P. S.; Coates, J. D. Chlorate Reduction in Shewanella AlgaeACDC Is a Recently Acquired Metabolism Characterized by Gene Loss, Suboptimal Regulation and Oxidative Stress. *Molecular Microbiology* **2014**, *94* (1), 107–125. https://doi.org/10.1111/mmi.12746.

(45) Hitchcock, A.; Hall, S. J.; Myers, J. D.; Mulholland, F.; Jones, M. A.; Kelly, D. J. Roles of the Twin-Arginine Translocase and Associated Chaperones in the Biogenesis of the Electron Transport Chains of the Human Pathogen Campylobacter Jejuni. *Microbiology* **2010**, *156* (10), 2994–3010. https://doi.org/10.1099/mic.0.042788-0.

(46) Dhouib, R.; Othman, D. S. M. P.; Lin, V.; Lai, X. J.; Wijesinghe, H. G. S.; Essilfie, A. T.; Davis, A.; Nasreen, M.; Bernhardt, P. v.; Hansbro, P. M.; McEwan, A. G.; Kappler, U. A Novel, Molybdenum-Containing Methionine Sulfoxide Reductase Supports Survival of Haemophilus Influenzae in an in Vivo Model of Infection. *Frontiers in Microbiology* **2016**, *7* (NOV), 1–16. https://doi.org/10.3389/fmicb.2016.01743.

(47) Hille, R. The Mononuclear Molybdenum Enzymes. *Chemical Reviews* **1996**, *96*, 2757–2816. https://doi.org/10.1021/cr950061t.

(48) Adamson, H.; Simonov, a. N.; Kierzek, M.; Rothery, R. a.; Weiner, J. H.; Bond, a. M.; Parkin, a. Electrochemical Evidence That Pyranopterin Redox Chemistry Controls the Catalysis of YedY, a Mononuclear Mo Enzyme. *Proceedings of the National Academy of Sciences* **2015**, *112* (47), 1–6. https://doi.org/10.1073/pnas.1516869112.

(49) Spence, J. T.; Kipke, C. A.; Enemark, J. H.; Kipke, C. A.; Sunde, R. A.; Sunde, R. A. Stoichiometry of Electron Uptake and the Effect of Anions and PH on the Molybdenum and Heme Reduction Potentials of Sulfite Oxidase. *Inorganic Chemistry* **1991**, *30* (15), 3011–3015. https://doi.org/10.1021/ic00015a014.

(50) Kay, C. J.; Barber, M. J.; Notton, B. A.; Solomonson, L. P. Oxidation--Reduction Midpoint Potentials of the Flavin, Haem and Mo-Pterin Centres in Spinach (Spinacia Oleracea L.) Nitrate Reductase. *The Biochemical journal* **1989**, *263* (1), 285–287. https://doi.org/10.1042/bj2630285.

(51) Kay, C. J.; Barber, M. J.; Solomonson, L. P. Circular Dichroism and Potentiometry of FAD, Heme and Mo—Pterin Prosthetic Groups of Assimilatory Nitrate Reductase. *Biochemistry* **1988**, *27* (16), 6142–6149. https://doi.org/10.1021/bi00416a047.

(52) Pushie, M. J.; Doonan, C. J.; Moquin, K.; Weiner, J. H.; Rothery, R.; George, G. N. Molybdenum Site Structure of Escherichia Coli YedY, a Novel Bacterial Oxidoreductase. *Inorganic Chemistry* **2011**, *50* (3), 732–740. https://doi.org/10.1021/ic101280m.

(53) Kirk, M. L.; Stein, B. *Molybdenum Enzymes*; Elsevier Ltd., 2013. https://doi.org/10.1016/B978-0-08-097774-4.00316-8.

(54) Brody, M. S.; Hille, R. The Kinetic Behavior of Chicken Liver Sulfite Oxidase. *Biochemistry* **1999**, *38* (20), 6668–6677. https://doi.org/10.1021/bi9902539.

(55) Simala-Grant, J. L. C.; Weiner, J. H. Kinetic Analysis and Substrate Specificity of Escherichia Coli Dimethyl Sulfoxide Reductase. *Microbiology* **1996**, *142* (11), 3231–3239. https://doi.org/10.1099/13500872-142-11-3231.

(56) Tarrago, L.; Grosse, S.; Siponen, M. I.; Lemaire, D.; Alonso, B.; Miotello, G.; Armengaud, J.; Arnoux, P.; Pignol, D.; Sabaty, M. Rhodobacter Sphaeroides Methionine Sulfoxide Reductase P Reduces R- and S-Diastereomers of Methionine Sulfoxide from a Broad-Spectrum of Protein Substrates. *Biochemical Journal* **2018**, *475* (23), 3779–3795. https://doi.org/10.1042/BCJ20180706.

(57) Havelius, K. G. v; Reschke, S.; Horn, S.; Döring, A.; Niks, D.; Hille, R.; Schulzke, C.; Leimkühler, S.; Haumann, M. Structure of the Molybdenum Site in YedY, a Sulfite Oxidase Homologue from Escherichia Coli. *Inorganic Chemistry* **2011**, *50* (3), 741–748. https://doi.org/10.1021/ic101291j.

(58) Cramer, S. P.; Eccles, T. K.; Kutzler, F. W.; Hodgson, K. O.; Mortenson, L. E. Molybdenum X-Ray Absorption Edge Spectra. The Chemical State of Molybdenum in Nitrogenase. *Journal of the American Chemical Society* **1976**, *98* (5), 1287–1288. https://doi.org/10.1021/ja00421a053.

(59) Kutzler, F. W.; Natoli, C. R.; Misemer, D. K.; Doniach, S.; Hodgson, K. O. Use of One-Electron Theory for the Interpretation of near Edge Structure in K-Shell x-Ray Absorption Spectra of Transition Metal Complexes. *The Journal of Chemical Physics* **1980**, *73* (7), 3274–3288. https://doi.org/10.1063/1.440523.

(60) Cramer, S. P.; Wahl, R.; Rajagopalan, K. v. Molybdenum Sites of Sulfite Oxidase and Xanthine Dehydrogenase. A Comparison by EXAFS. *Journal of the American Chemical Society* **1981**, *103* (26), 7721–7727. https://doi.org/10.1021/ja00416a005.

(61) Peariso, K.; Helton, M. E.; Duesler, E. N.; Shadle, S. E.; Kirk, M. L. Sulfur K-Edge Spectroscopic Investigation of Second Coordination Sphere Effects in Oxomolybdenum-Thiolates: Relationship to Molybdenum-Cysteine

Covalency and Electron Transfer in Sulfite Oxidase. *Inorganic Chemistry* **2007**, *46* (4), 1259–1267. https://doi.org/10.1021/ic061150z.

(62) McNaughton, R. L.; Helton, M. E.; Cosper, M. M.; Enemark, J. H.; Kirk, M. L. Nature of the Oxomolybdenum-Thiolate ??-Bond: Implications for Mo-S Bonding in Sulfite Oxidase and Xanthine Oxidase. *Inorganic Chemistry* **2004**, *43* (5), 1625–1637. https://doi.org/10.1021/ic034206n.

(63) McNaughton, R. L.; Tipton, A. A.; Rubie, N. D.; Conry, R. R.; Kirk, M. L. Electronic Structure Studies of Oxomolybdenum Tetrathiolate Complexes: Origin of Reduction Potential Differences and Relationship to Cysteine - Molybdenum Bonding in Sulfite Oxidase. *Inorganic Chemistry* **2000**, *39* (25), 5697–5706. https://doi.org/10.1021/ic0003729.

(64) Lamy, M. T.; Gutteridge, S.; Bary, R. C. Electron-Paramagnetic-Resonance Parameters of Molybdenum(V) in Sulphite Oxidase from Chicken Liver. *The Biochemical journal* **1980**, *185* (2), 397–403. https://doi.org/10.1042/bj1850397.

(65) George, G. N.; Bray, R. C. Studies by Electron Paramagnetic Resonance Spectroscopy of Xanthine Oxidase Enriched with Molybdenum-95 and with Molybdenum-97. *Biochemistry* **1988**, *27* (10), 3603–3609. https://doi.org/10.1021/bi00410a011.

(66) Doonan, C. J.; Rubie, N. D.; Peariso, K.; Harris, H. H.; Knottenbelt, S. Z.; George, G. N.; Young, C. G.; Kirk, M. L. Electronic Structure Description of the Cis-MoOS Unit in Models for Molybdenum Hydroxylases. *Journal of the American Chemical Society* **2008**, *130* (1), 55–65. https://doi.org/10.1021/ja068512m.

(67) Astashkin, A. v.; Mader, M. L.; Pacheco, A.; Enemark, J. H.; Raitsimring, A. M. Direct Detection of the Proton-Containing Group Coordinated to Mo(V) in the High PH Form of Chicken Liver Sulfite Oxidase by Refocused Primary ESEEM Spectroscopy: Structural and Mechanistic Implications. *Journal of the American Chemical Society* **2000**, *122* (22), 5294–5302. https://doi.org/10.1021/ja9916761.

(68) Lee, C. C.; Sickerman, N. S.; Hu, Y.; Ribbe, M. W. YedY: A Mononuclear Molybdenum Enzyme with a Redox-Active Ligand? *ChemBioChem* **2016**, *17* (6), 453–455. https://doi.org/10.1002/cbic.201600004.

5. Chapter 5 - Elucidating the conflicting spectroscopic and crystallographic data of MsrP

Note: This chapter contains previously published data from the paper: Ingersol, L. J.; Yang, J.; Kc, K.; Pokhrel, A.; Astashkin, A. V.; Weiner, J. H.; Johnston, C. A.; Kirk, M. L. Addressing Ligand-Based Redox in Molybdenum-Dependent Methionine Sulfoxide Reductase. J. Am. Chem. Soc. ***2020****, 142 (6), 2721–2725. https://doi.org/10.1021/jacs.9b11762.*

5.1 Methods

Expression, isolation, and purification of as-isolated MsrP and variants

For the following studies, we used MsrP from *E. coli* exclusively. Therefore, the terminology of *as-isolated* MsrP refers to *E. coli* MsrP that is expressed and isolated from *E. coli* and is unaltered by any redox cycling. *As-isolated* WT MsrP, and the N45R and E104G variants, were previously cloned into plasmid pMSYZ3 possessing an ampicillin resistance gene; expression from this construct yielded protein containing a C-term His_6 tag.[1,2] For the following studies, we expressed the plasmid in *E. coli* BL21 cells. The bacteria were grown in LB Auto Induction media (Formedium LB Broth Base including Trace elements) with 1.44mM added Na2MoO4 and 200mg/L Ampicillin for 72h at room temperature with continuous shaking at 300rpm. The cells were then spun down at 5000rpm for 10 minutes, the media was discarded, and the cell pellets were frozen at -80C for storage.

The protein isolation began by thawing the frozen cell pellets on ice and resuspending them in 50mM Bis-Tris propane + 300mM NaCl + 10mM imidazole

(pH 8.0). The cells were then lysed using sonication consisting of two 45s cycles of 0.5s on and 0.5s off bursts. The lysed cell debris was spun at 9000rpm for 20 minutes and the soluble fraction containing the target protein was incubated with preequilibrated His60 Ni Superflow Resin (Clontech) for 2h at 4C. The beads were then washed twice with aliquots of 50mM Bis-Tris propane + 30mM imidazole (pH 8.0) and the protein was then eluted from the resin with 50mM Bis-Tris propane + 300mM imidazole (pH 8.0). A final buffer exchange into 50mM Bis-Tris propane (pH 8.0) was performed to remove the excess imidazole and the protein was concentrated and stored at -80C in ~150uL aliquots.

Site-directed mutagenesis of MsrP

A C102S variant of MsrP was created using primers containing the single point mutation (Table 5-1) and the plasmid pMSYZ3 containing WT MsrP. This deletion was confirmed via PCR. This plasmid was then transformed into *E. coli* BL21 cells and expressed, isolated, and purified as described above.

C102S Primer	***Sequence (from 5' to 3')***
Forward	GAGCGTATTTATCGTATGCGCTCCGTGGAAGCGTGGTC GATGGTG
Reverse	CACCATCGACCACGCTTCCACGGAGCGCATACGATAAAT ACGCTC

Table 5-1 Primers for site-directed mutagenesis to generate C102S variant of MsrP

DFT calculations

Transition state calculations and geometry optimizations were performed using Orca 4.1.0.[3] Geometry optimization were performed using the B3LYP functional with a def2-TZVP basis set for Mo and a def2-SVP basis set for all other atoms. Transition state was located using a relaxed surface scan followed by an Intrinsic Reaction Coordinate (IRC) method to confirm the identified transition state. Solvation was simulated using the conductor-like polarizable continuum model, CPCM, in Orca, with a dielectric constant (ε) of 4.

Docking studies

Docking studies were performed using the computational docking program (Autodock 4.2.6.).[4] The published crystal structure (PDB 1XDQ) was used for all docking studies.[1] The substrates used to dock with the crystal structure were first optimized in Orca 4.1.0 with a B3LYP functional with a def2-SVP basis set for all atoms.

EPR data collection

The samples *as*-isolated WT MsrP and N45R MsrP were suspended in 50 mM Bis-Tris propane buffer (pH=8.0) and complexes 1 and 2 in n-butylnitrile for EPR spectra collection. CW EPR spectra were recorded on a X-band (9.4GHz) and Q-band (34 GHz) Bruker ESP 300 spectrometer with associated Bruker magnet control electronics and microwave bridges. Low temperature (77K) EPR spectra were collected using an Oxford Instrument ESR 910 liquid helium low cryostat. EasySpin5 (version:5.2.13) was used to perform EPR spectral simulations with using a Matlab (version R2015b) platform.

XAS data collection

Samples of *as-isolated* WT-MsrP (in 50 mM Bis-Tris propane buffer (pH=8.0)) and whole cells (*E. coli* BL21 cells induced to express MsrP) were used for XAS data collection. Mo K-edge X-ray absorption spectroscopic data were collected on beamline 7-3 at the Stanford Synchrotron Radiation Lightsource (SSRL) with the SPEAR storage ring containing 200− 300 mA at 3.0 GeV. Beamline 7-3 is equipped with rhodium-coated mirrors upstream and downstream of the Si (220) double-crystal monochromator. The incident and transmitted X-ray intensities (I0, I1, and I2) were monitored with three nitrogen-filled ionization chambers. The sample temperature was maintained at 10 K using an Oxford Instruments CF1208 continuous flow liquid helium cryostat. The *as-isolated* WT-MsrP sample (in 50 mM Bis-Tris propane buffer (pH=8.0)) was injected into the Delrine liquid sample holder and subsequently frozen in the liquid nitrogen. Data was collected in florescence mode (Mo Ka) using a 30-element Ge solid-state detector. A Zr-3 filter and a Soller slit were used before the detector to reject the scattered radiation. The internal energy was calibrated using a Mo foil reference with the first inflection point set to 20,000 eV. XAS data were processed using the Demeter software suite (version .9.025).[5] The XANES spectra was calibrated and normalized in Athena with the threshold energy assigned as 20,010 eV. The data showing here are four-sweep averaged spectra. The EXAFS simulations were performed using Artemis. Backscattering paths were calculated from the embedded IFEFF (version IFEFF6) program using the DFT gas-phase optimized geometries. All Fourier transforms were phase corrected using Mo-oxo backscattering. The data was fitted in k-space with the k range of 2.5–14Å-1.

5.2 X-band and Q-band EPR of *as-isolated* WT MsrP

X-band and Q-band EPR of *as-isolated* WT MsrP yielded spectra with virtually identical g- and A-tensors as those previously obtained (Figures 5-1 and 5-2).[2,6,7] The unusually high g_1 value of 2.030 and the highly axial g- and A- tensor values is consistent with reported values. This confirms that the protein expressed and isolated in our lab is present as a previously observed Mo(V) species, despite differences in the strain of *E. coli* used to express the protein and the change in the choice of buffers used during lysis and isolation of the protein.[1,2,6–9] This provides evidence that changing these variables does not have an effect on the electronic structure of *as-isolated* WT MsrP

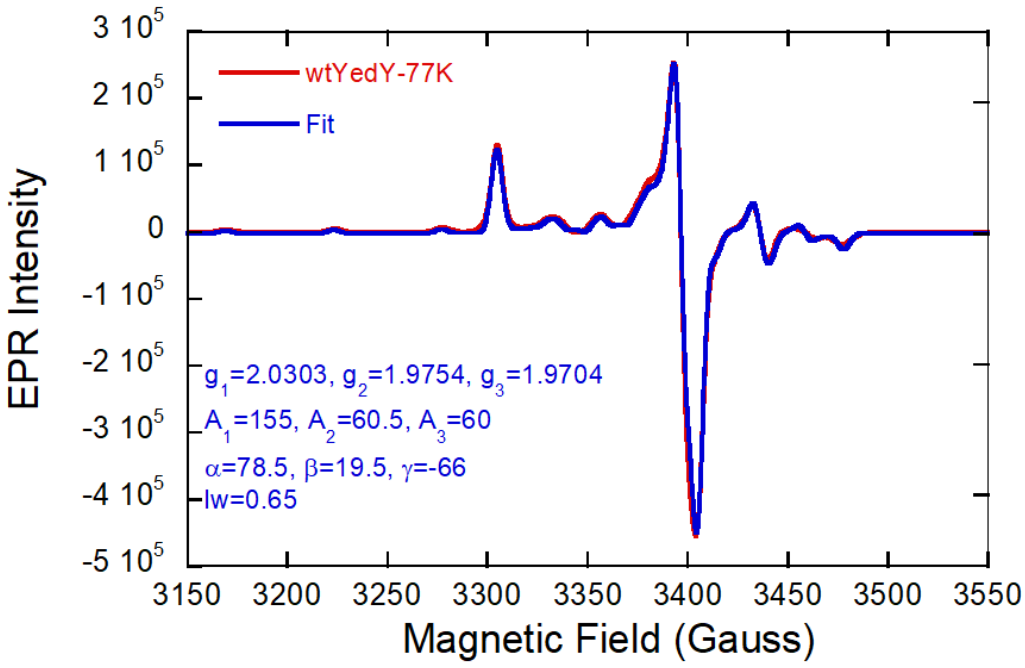

Figure 5-1. 77K X-band EPR spectrum of as-isolated WT MsrP (red) and the fit (blue).

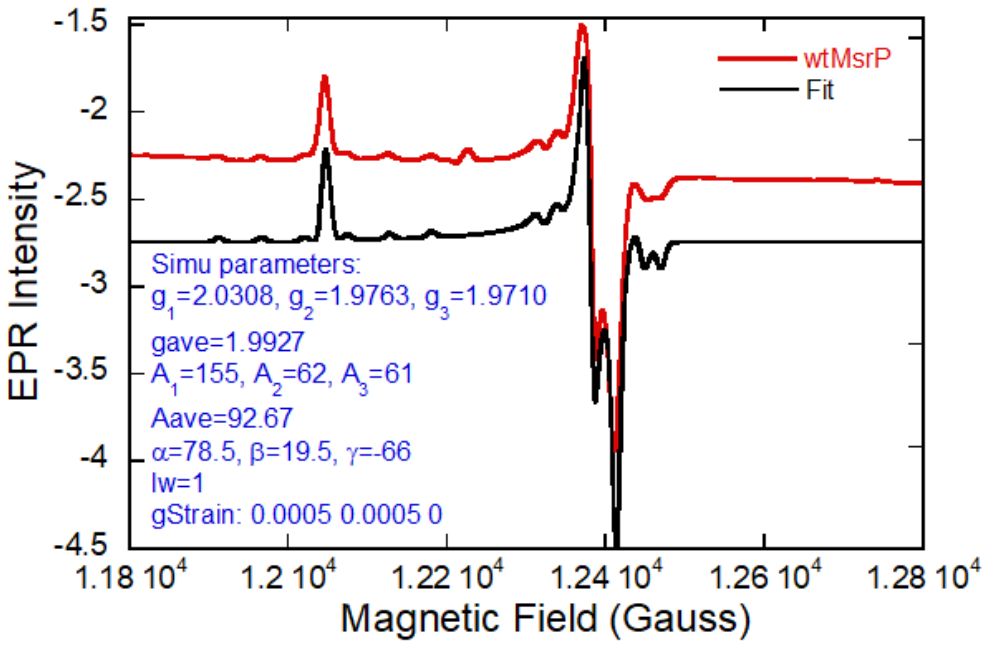

Figure 5-2. 77K Q-band EPR spectrum of as-isolated WT MsrP (red) and the fit (black).

5.3 X-band and Q-band EPR of N45R MsrP

Following verification that our cell growth and protein isolation procedure can produce WT MsrP which gives an identical X-band EPR spectrum as that previously reported, we turned our attention to expressing select variants which differ in key active site residues. We selected residues in close proximity to the Mo active site which could potentially contribute to the unusually high g_1 value or axial X-band EPR spectrum, or provide a clue as to why *as-isolated* MsrP cannot achieve the Mo(VI) oxidation state.

Asn-45 is oriented *trans* to the axial oxo group which is directly coordinated to Mo (Figure 5-3); it has been speculated to coordinate to Mo via a long ~2.64Å Oδ bond in the interpretation of a DFT optimized structure.[9] The position of Asn-45 is analogous to that of a conserved arginine residue in both human (Arg-160) and chicken (Arg-138) SO, which is also found conserved in the assimilatory nitrate reductases.[1,10,11] This positively charged Arg forms a critical electrostatic interaction with the negatively charged sulfate substrate during catalysis. The importance of an Arg in this position was discovered by investigating the cause of a SO deficiency in a five-year-old girl, which is now attributed to an identified Arg-160 to Gln mutation.[12] Analysis of this variant of recombinant hSO revealed that while the variant still loaded the molybdenum cofactor efficiently, the loss of the critical Arg-160 raised the K_M value, indicating that the Arg plays a role in attracting and positioning the substrate within the active site. In addition, this residue is critical for efficient intramolecular electron transfer (IET) in hSO; mutation of Arg-160 to a Gln caused a decrease in the IET rate by 3 orders of magnitude while mutation to a Lys caused the rate to decrease to a quarter of that observed for the WT enzyme.[10]

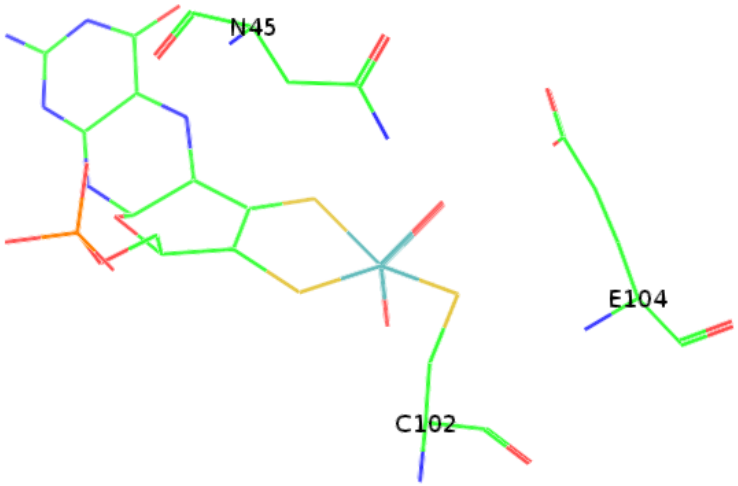

Figure 5-3. Active site of MsrP showing positions of Asn-45 and Glu-104 relative to Moco.

Given the critical importance of this position in SO family enzymes, it is reasonable to expect that Asn-45 may play a critical role in MsrP catalysis. It has been speculated that this residue is responsible for the high g_1 value observed in *as-isolated* MsrP. A pseudo-octahedral geometry was first suggested from an interpretation of XAS data fitting indicating the presence of a long O/N bond to Mo, located *trans* to the axial oxo group.[9] Asn-45 seemed to be the most likely origin of this observed long bond, which was thought to occur in the *as-isolated* Mo(V) species but not observed in the reduced Mo(IV) form of MsrP. This distortion into a pseudo-octahedral geometry could potentially raise the g_1 value by pulling the Mo into the same plane as the equatorial S ligands, facilitating an increase in the covalency between Mo-S through increased spin-orbit coupling.

To test this hypothesis, we expressed an N45R variant of MsrP in *E. coli*. This variant was also isolated in the Mo(V) oxidation state and the successful assembly of the cofactor within the variant was readily evident by the deep pink/red color of the isolated protein. *As-isolated* N45R MsrP was EPR active and X- and Q- band spectra is shown in Figure 5-1. The variant shows a slight splitting in the g_2 and g_3 EPR values, which indicates that compared to the WT enzyme, the N45R variant possesses a slight anisotropy in the equatorial plane. This rhombic splitting of $g_{2,3}$ is more evident in the Q-band spectrum (Figure 5-4B). However, the g_1 value of the N45R variant is essentially identical to that of the WT MsrP enzyme at both X- and Q-band, indicating that the speculated coordination of this residue to Mo is not the origin of the high g_1 value. Asn-45 may still interact with the active site in a way

that causes the slight structural change evident at Q-band and this variant should therefore be tested for any kinetic effects in the future.

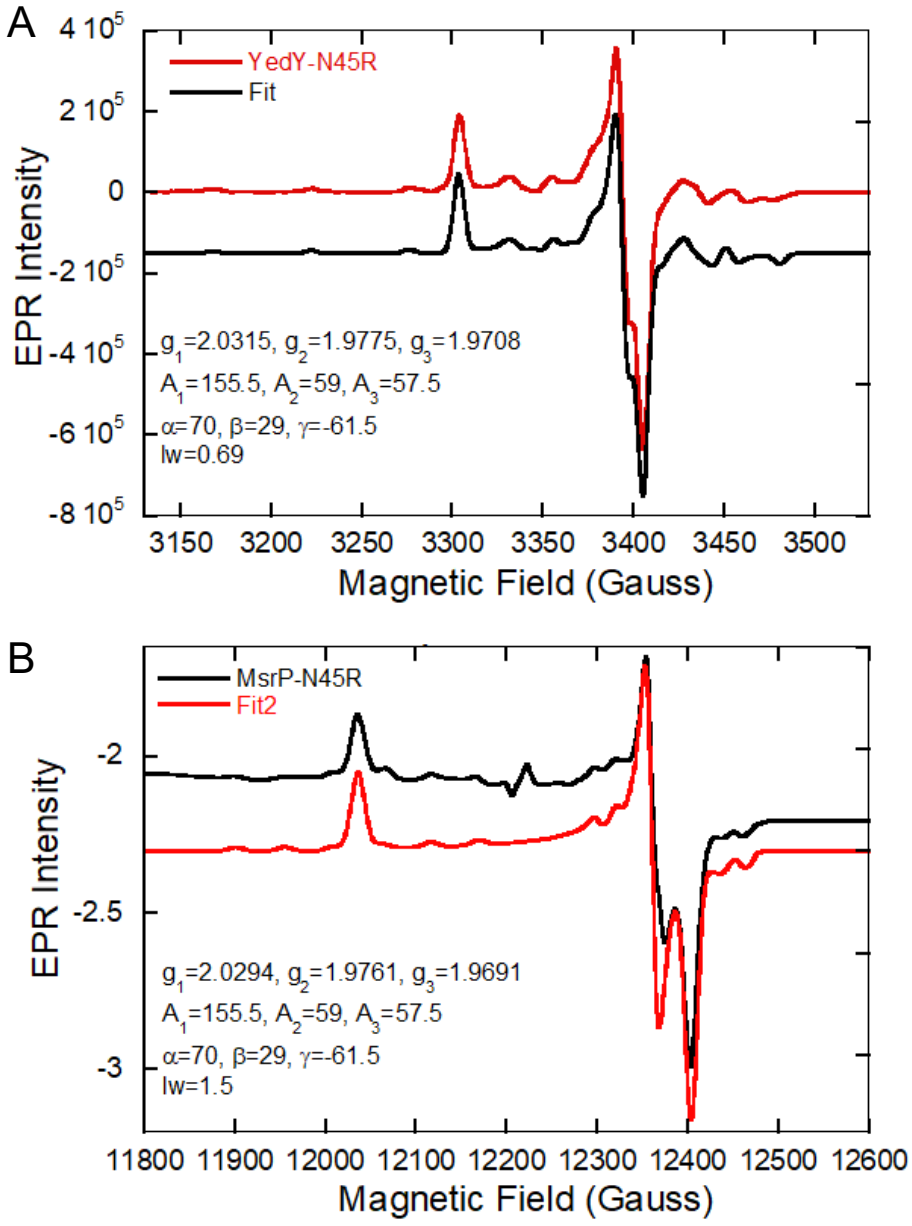

Figure 5-4. 77K EPR spectra of N45R variant of MsrP taken at X-band (A) and Q-band (B). The splitting on $g_{2,3}$ indicates a slight anisotropy in the equatorial plane of the N45R variant which is not present in WT as-isolated MsrP. The g_1 values of the N45R variant are comparable to that of WT as-isolated MsrP.

However, the importance of this position in SO family enzymes and the slight splitting in the $g_{2,3}$ values of the N45R variant may imply that this residue still plays an important role in the catalytic cycle of MsrP and should be investigated in more detail in the future.

5.4 X-band EPR of E104G MsrP

Another residue of interest in MsrP is a glutamate at position 104, which is oriented near the putative water ligand to Mo within the substrate binding pocket. Analogous to Glu-104 in MsrP is an arginine (Arg-161) in rCSO; glutamate in this position prevents the binding of anionic substrates, such as sulfite, to Mo in MsrP, as the carboxylate would electrostatically clash with a negatively charged molecule.[1,13]

Glutamate residues located near the active sites of certain molybdoenzymes often play critical roles in catalysis. A key glutamate is implicated in the catalytic cycle of members of the XO family molybdoenzymes; Glu-232 in xanthine dehydrogenase from *R. capsulatus* is suggested to expedite proton transfer between N3 and N9 of xanthine during catalysis.[14] And in recombinant *R. capsulatus* xanthine oxidase, Glu-730 is in an analogous position to Glu-104 in MsrP and plays an essential role as a proton acceptor in the reductive half-reaction of XO.[14] One proposed mechanism for tungsten-dependent formaldehyde ferredoxin oxidoreductase from *Pyrococcus furiosus* features a catalytic glutamate that activates a water molecule for nucleophilic attack on the aldehyde substrate.[15,16] DFT calculations for the molybdoenzyme aldehyde oxidoreductase from *Desulfovibrio gigas* supports a

mechanism by which Glu-864 acts as a base to activate a coordinated water molecule; facilitating hydride transfer to the sulfido group on Mo.[17]

The position occupied by Glu-104 in MsrP is analogous to Asp-147 in DMSO reductase and Asp-145 in TMAO reductase.[18,19] Though in both enzymes, the Asp residues are oriented with their side chains pointing away from Mo, it has been suggested that conformational flexibility may allow the side chains to dynamically function as proton donors or acceptors during substrate turnover.[19]

In MsrP, Glu-104 was identified as a possible culprit in why *as-isolated* MsrP was not able to be oxidized to the Mo(VI) oxidation state. It was hypothesized that the proximity of Glu-104 to the putative O(H) ligand could form a hydrogen-bonded network, possibly raising the Em value of Mo and accounting for both the inability of the enzyme to be oxidized to Mo(IV) as well as its unusual property of being the only known molybdoenzyme isolated in the Mo(V) oxidation state.[7]

To test whether the proximity of this glutamate to the active site influenced the unusually high g_1 value of the EPR spectra, as well as the propensity for *as-isolated* MsrP to adopt a Mo(V) oxidation state, we expressed an E104G variant of Mo in *E. coli*. The isolated protein had an identical dark red/pink color as the *as-isolated* WT MsrP, and it was found to be isolated in a Mo(V), EPR-active form. The EPR spectrum of the E104G variant was virtually identical to that of WT MsrP, indicating that the overall geometry of the active site was unchanged (Figure 5-5).

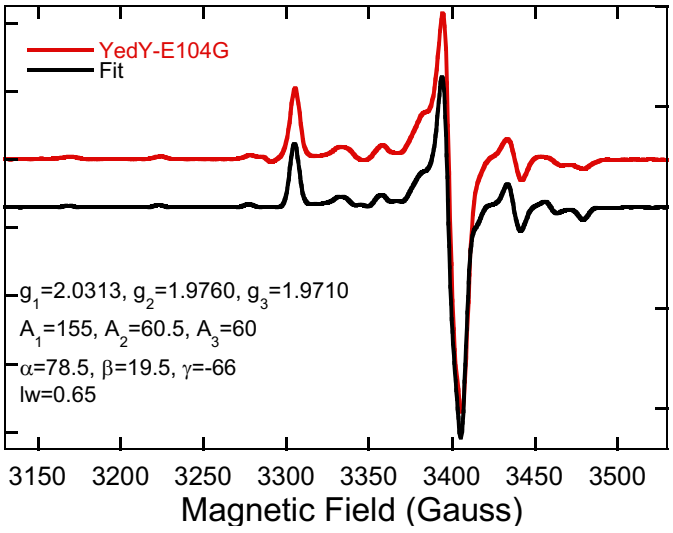

Figure 5-5. 77K EPR spectra of E104G variant of MsrP taken at X-band. The g_1 values of the E104G variant are comparable to that of WT as-isolated MsrP.

However, Glu-104 may still play a critical role in catalysis and future investigation into the kinetic properties of this variant should be pursued. It is possible, given its position near the entrance of the active site in close proximity to the location of substrate coordination to Mo, that it can serve as a source of hydrogen to be donated to the oxygen atom following OAT from a MetO substrate to Mo, thus allowing the regeneration of the active site through a protonation event creating a labile water.

5.5 Reanalysis of the electron density of the crystal structure of *as-isolated* WT MsrP

Given that the source of the high g_1 value for *as-isolated* WT MsrP was not explained by the proximity of either Asn-45 or Glu-104 to the active site, we again turned our attention back to the original crystal structure of *as-isolated* WT MsrP obtained by Loschi *et al.*[1] At 2.5Å resolution the electron density surrounding the Mo itself was poorly resolved. Although the axial oxo group was able to be fit well at a distance of 1.6-1.8Å from Mo, the atom in the equatorial substrate binding position was not able to be unambiguously assigned. Based upon the similarity of

MsrP to SO, it was assumed to be an O, and was able to be fit either as an oxo group at 1.6-1.8Å, or a water at 2.1-2.4Å.

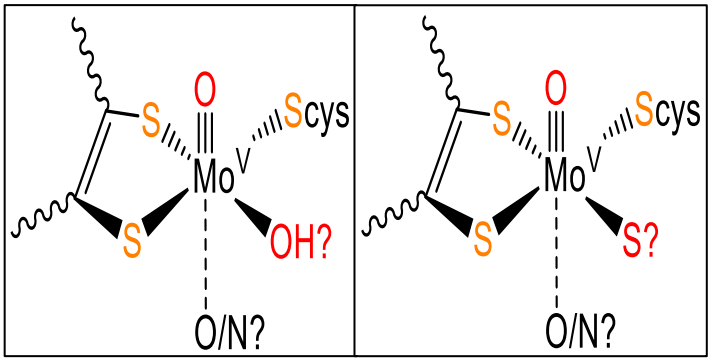

Figure 5-6. The original proposed structure of as-isolated MsrP (A) and the revised structure with a sulfur atom in the position of the putative -OH in the equatorial plane (B).[1]

Based upon the axial nature of the EPR spectrum of *as-isolated* WT MsrP and the variants, and the nearly identical $g_{2,3}$ values, the equatorial plane should be symmetrical about Mo. Given that the Mo is known to be coordinated by two dithiolene sulfurs and a cysteine sulfur in the equatorial plane, coordination by a fourth sulfur atom in the position of the putative O(H) would fulfill the requirements for generating an axial EPR spectrum (Figure 5-6). The increased covalency between Mo-S, as opposed to Mo-O, would also account for the unusually high g_1 value.

To test whether a sulfur atom could be reasonably modeled in the electron density of the equatorial position Refmac5 was used to reanalyze the previously published crystal structure of *as-isolated* MsrP (PDB 1XDQ).[1,20] The electron-density map of MsrP was used as the basis for the reanalysis. The electron-density map is created from the intensities of the reflections of the raw diffraction data.[21] The agreement between the model and the map is assessed using an R-factor (R_{work}), which relates the experimental reflection amplitudes (*Fo*) with those that are calculated by the model of the protein structure (*Fc*) via the equation:

$$Rwork = \frac{\Sigma|Fo-Fc|}{\Sigma Fo}.$$

In addition to R_{work}, another R-factor (R_{free}) is calculated to further validate the fit of the protein structure to the electron density map. R_{free} is calculated by using 5-10% of random reflections from the data which are excluded from refinement. Good agreement between the model and experimental data is indicated by a low R_{free}. The difference between the R_{free} and R_{work} values should be ~5% for structures between 3-4Å resolution and this value can decrease to less than 2% for structural resolutions of greater than 1Å. A high value of R_{free} that exceeds R_{work} by greater than 7% is interpreted as an over-fitting of the data.[22]

Both the R_{work} and R_{free} obtained with sulfur in this position are comparable to those obtained with oxygen (Table 5-2). From these results, we can conclude that the identity of the equatorial atom cannot be conclusively identified as oxygen.

The crystal structure also had a region of electron density within the substrate cavity which was originally modeled as a urea from the crystallization buffer.[1] However, given that the identity of the equatorial atom near the putative urea could not be conclusively assigned, it is possible that the electron density in the binding pocket was erroneously assigned as urea. Speculating that the source of the electron density in this region may be due to the binding of a physiological thiol to the active site, we fit methionine, homocysteine, and alanine (with the equatorial oxygen atom assigned as a sulfur) to the electron density within the binding pocket using the program Refmac5.[20] The results are shown in Table 5-2. The fits for the

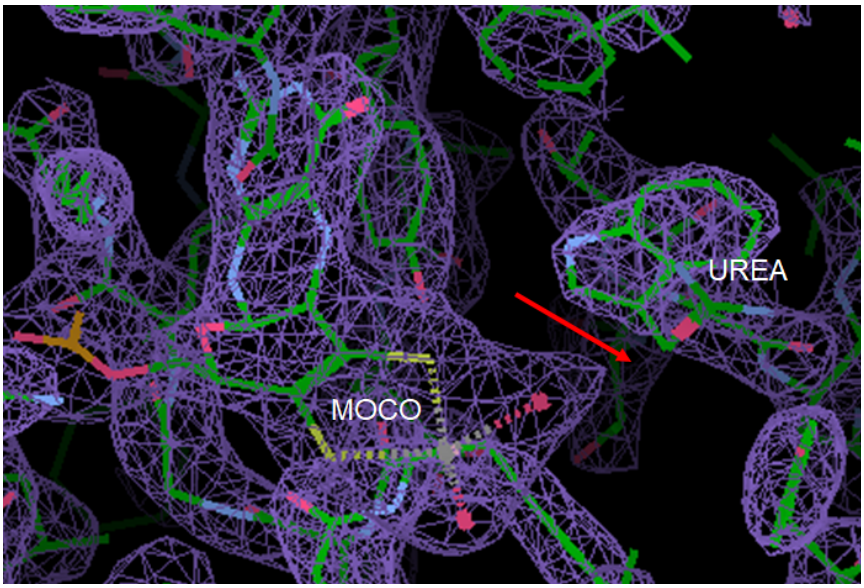

Figure 5-7. Electron density map of MsrP overlay with the structural model originally proposed by Loschi et al.[1] The positions of the molybdenum active site (Moco) and urea are labeled. The red arrow indicates the position between the putative urea and equatorial oxygen that is devoid of appreciable electron density.

physiological thiols are considerably worse than the fits obtained for the urea model, as evidenced by the increases in R_{free} and R_{work}. We attribute the worsening of the fits to a region with less electron density between the equatorial position and the area of higher electron density in the substrate cavity (Figure 5-7).

From this data, we cannot conclude the source of the electron density in the binding pocket is a physiological sulfur-containing molecule. There is simply not high enough resolution in the existing crystal structure. However, that a sulfur can be modeled well in the equatorial position lends more weight to the original identity of the equatorial atom being erroneously assigned, which would account for the discrepancies between the accepted active site structure for MsrP based on crystallographic data and the electronic structure data which does not support the existence of the proposed crystal structure.

Model	R_{work}	R_{free}
Original	0.226	0.266
O→S	0.230	0.267
With Met	0.247	0.281
With Homocysteine	0.246	0.280
O→S, Urea→Ala	0.237	0.274

Table 5-2. Summary of results of refitting the electron density of the crystal structure with new models of the MsrP active site. Arrow indicates replacement of the original atom or group with the new atom or group.

5.6 Synthetic models of the proposed active site

Given the preponderance of evidence that to explain the unusually high g_1 value and axial g-tensor, *as-isolated* MsrP would need to possess a highly symmetrical environment in the equatorial plane, achievable only if the identity of the fourth equatorial atom is a sulfur, we compared enzymatic EPR data to that of synthetic models of an active site that would fulfill these criteria. Two synthetic models were used for this comparison: $[Mo^{V}O(SC_6H_2\text{-}2,4,6\text{-}Pr^{i}_3)_2(cydt)]^{1-}$ (1) (cydt = cyclohexene-1,2-dithiolate) and $[Mo^{V}O(SC_6H_2\text{-}2,4,6\text{-}Pr^{i}_3)_2(bdt)]^{1-}$ (2)[9] (bdt = benzene-1,2-dithiolate). Both models possess an axial oxo group and four sulfur atoms bound to Mo in the equatorial plane. Low temperature EPR taken at both X-band (Figure 5-8) and Q-band (data not shown) for the models provided strong evidence that the fourth atom in the equatorial plane of the enzyme is a sulfur. The

g-values obtained from both models are nearly identical to that of the enzyme, including the high g_1 and axial g-tensor (Figure 5-8). Holm *et al.* made a series of synthetic molecules for the active sites of both xanthine oxidase and sulfite oxidase.[23] One of the models, $[MoO(2\text{-}AdS)2(S2C2Me2)]^{1-}$, which also possesses an axial oxo group and four sulfurs coordinated to Mo in the equatorial plane, has

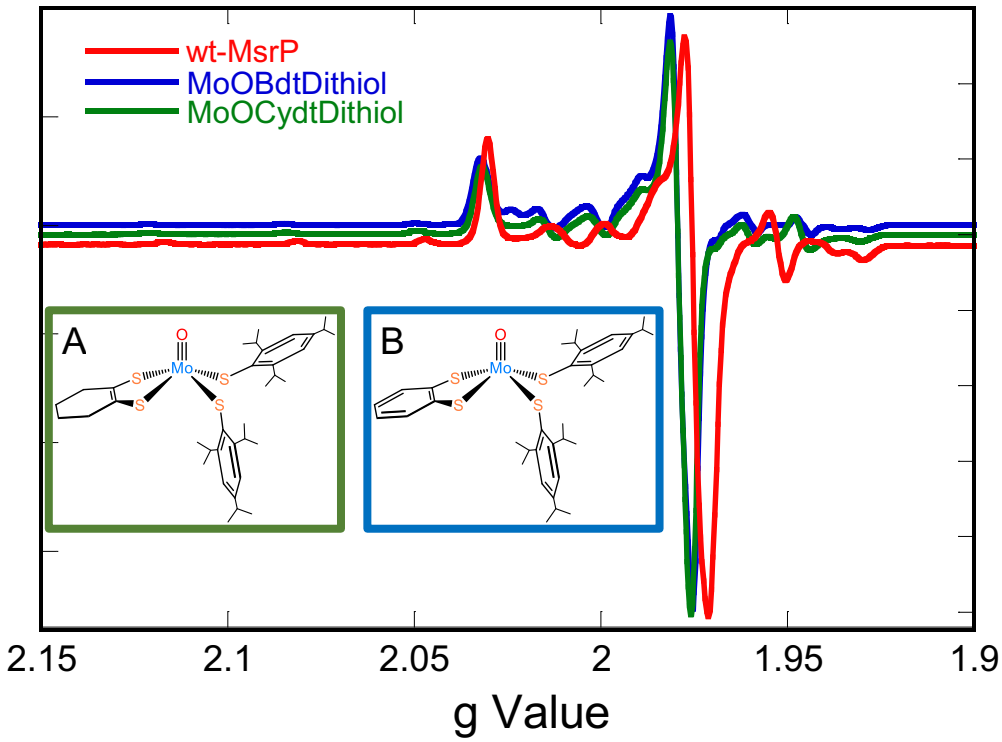

Figure 5-8. 77K X-band EPR overlay spectra of as-isolated MsrP and model compounds. Inset shows structures of $[Mo^{V}O(SC_6H_2\text{-}2,4,6\text{-}Pr^{i}_3)_2(cydt)]^{1-}$ (A) and $[Mo^{V}O(SC_6H_2\text{-}2,4,6\text{-}Pr^{i}_3)_2(bdt)]^{1-}$ (B): (cydt = cyclohexene-1,2-dithiolate) and (bdt = benzene-1,2-dithiolate).

nearly identical spin-Hamiltonian parameters to that of *as-isolated* MsrP. Thus, three distinct synthetic models of a square-pyramidal active site with a highly symmetrical equatorial plane consisting of four S-containing ligands and an axial oxo produce nearly identical EPR parameters to *as-isolated* MsrP.

5.7 XAS studies of MsrP

Mo K-edge EXAFS data was obtained for MsrP previously.[7,9] The conclusions were in support of the original interpretation of the MsrP crystal structure, which assigned the fourth equatorial atom bound to Mo as an oxygen.[1] However, in light of the reanalysis of the crystallographic data and EPR comparisons of synthetic models to the enzyme, we decided to reanalyze previously obtained XAS data as well. The best fit for the XAS data indicates that *as-isolated* MsrP possesses an oxo group at 1.719Å and four S atoms at an average 2.390Å distance from Mo. The previously modeled O/N, presumably from Asn-45, gave negative values for the Debye-Waller factor during the reanalysis. From this, it was concluded that it was unlikely that Asn-45 had an appreciable interaction with Mo, which was supported by the nearly identical EPR spectra obtained for the N45R variant.

5.8 Whole cell EPR of MsrP

MsrP is isolated in the Mo(V) oxidation state, a characteristic that is unobserved in any other known molybdoenzyme.[24,25] Given this unusual property, we decided to perform whole cell EPR to determine whether MsrP is detectable in the cells as a Mo(V) species or whether this species is specifically formed during isolation of the protein. The whole cell sample was EPR silent at room temperature X-band, indicating that MsrP is not primarily in the Mo(V) oxidation state within the cell (data not shown).

5.9 Whole cell XAS of MsrP

To further determine the oxidation state of MsrP prior to isolation, we performed whole cell XANES. Mo(IV), Mo(V), and Mo(VI) species have characteristic pre-edge energies that allow the unambiguous assignment of the enzyme oxidation state.[26,27] The energy of the pre-edge peak in the whole cell XANES spectra (Figure 5-9A) provides compelling evidence that the oxidation state is Mo(VI) in MsrP prior to lysis. Furthermore, the peak on the rising edge indicates the likely presence of two oxo groups bound to Mo.

The EXAFS region of the whole cell spectra was fit with both a water (Figure 5-9B) and S_{Cys} (Figure 5-9C) in the equatorial position; both models included the two dithiolene sulfurs from the PDT ligand and two oxo groups, one in the axial and one in the equatorial position. Neither fit provided conclusive evidence of the identity of the atom in the fourth equatorial position. One possibility is that the endogenous expression of DMSO reductase is competing with the expression of MsrP and competing for the molybdenum cofactor, which would explain the poor fit as this technique might be detecting two different molybdoenzymes at two different ratios.[28] However, from the results we can conclude that there are two oxo groups and two sulfur atoms bound to Mo, and that the enzyme is primarily in the Mo(VI) oxidation state within the cell.

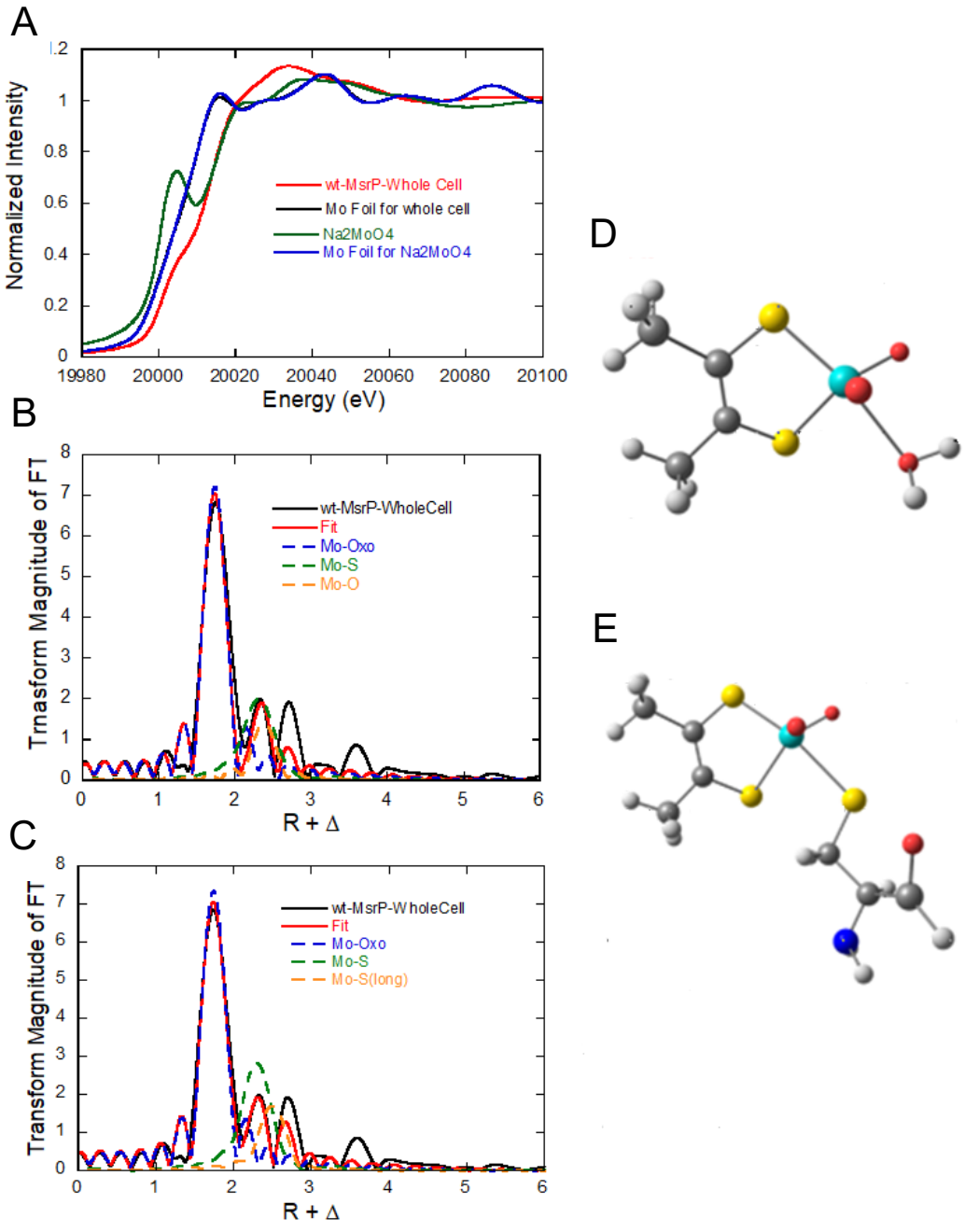

Figure 5-9. Whole-cell Mo K-edge XANES of as-isolated WT MsrP shows that the protein is in the Mo(VI) oxidation state within the cell (A). Fits of the EXAFS Fourier transformed data with two Mo=O, two Mo-S, and one longer Mo-O bond (B) and two Mo=O, two Mo-S, and one longer Mo-S_{cys} bond (C). Optimized structures depicting models of a Mo(O2S2H2O) (D) and Mo(O2S2SCys) (E) active site.

5.10 Identifying the source of the exogenous inhibitory thiol

As we found compelling evidence that the source of the inhibitory thiol is endogenous to the lysed *E. coli*, we turned our attention to attempting to identify the possible inhibitory molecule(s). The hydrophobicity of the binding pocket of MsrP, coupled with its relatively buried active site indicated that binding would favor thiols with a hydrophobic group or chain that would interact with the hydrophobic binding pocket and a terminal thiol group which could bind to the empty coordination sphere of Mo, assuming that like CSO, this position is occupied by an -O(H) in the cell which could be labialized by a protonation to create a water.[1,29]

The short list of possible culprits which fulfil these criteria include homocysteine (hCys) and cysteine (Cys). HCys is an intermediate in the metabolic pathway for the synthesis of methionine (Met) in *E. coli*.[30] It differs from cysteine only in that it possesses two carbons on its side chain, whereas cysteine only has a single side chain. In this sense, hCys is perfect for fitting into a binding pocket that utilizes Met as a physiological substrate, as their structures differ only by the absence of a terminal methyl group on hCys that is present on the sulfur atom of the side chain of Met.

Cysteine is imported into *E. coli* as cystine via the cystine importer TcyP.[31] However, once inside the cell, the disulfide bond of cystine needs to be reduced via a glutaredoxin system to prevent the transfer of disulfide bonds to other protein

thiols.[32] This mechanism allows the cells to maintain a pool of free intracellular cysteine, which is likely released into the buffer following cell lysis.

Glutathione (GSH) is the most predominate thiol in the intracellular thiol pool in *E. coli.*[32] It is a tripeptide consisting of a glycine, cysteine, and glutamate present in large quantities in eukaryotes and Gram-negative bacteria.[33] It functions as an antioxidant by removing free radicals via electron donation by the sulfhydryl group of cysteine; this reaction causes GSH to form a radical species (GS·) which can react with another thiyl radical on a second glutathione (GS·) to form glutathione disulfide (GSSG). The ability of GSH to form disulfide species also plays key roles in regulation of other proteins by modifying structures through the formation/reduction of disulfides on proteins. Its overall abundance in *E. coli* makes this a possible inhibitory molecule for *as-isolated* MsrP.

MOPS (3-[N-morpholine]propanesulfonic acid) is a buffer that was first developed in 1981 by Thomas and Hodes for polyacrylamide gel electrophoresis.[34] The original protein isolation procedure described by Loschi *et al.* for *as-isolated* MsrP utilized a 100mM MOPS buffer during the lysis step.[1] MsrP samples isolated and/or prepared in MOPS buffer have been used in obtaining a crystal structure, kinetic studies, and spectroscopic studies.[1,2,6,35] The structure of MOPS, shown in Figure 5-10, shows that it possesses a hydrophobic chain terminating in a sulfonic acid, which makes it likely that it could fit into the hydrophobic binding pocket of MsrP.

The identity(ies) of the inhibitory thiol(s) is currently unknown. However, to begin to identify which endogenous sulfur-containing molecules in *E. coli* could bind to

the active site, we used the crystal structure (PDB 1XDQ) of *as-isolated* MsrP and a computational docking program (Autodock 4.2.6.) to test the docking of several physiological thiols.[1,4] For the docking studies, a Lamarckian genetic algorithm was used. The docking procedure entails the development of an initial set of conformations which evolve over time, as the ligand samples the docking space to find conformations of minimal energy and this information is passed to the next generation of sampling conformations.

We found that free Met, Cys, hCys, glutathione and MOPS were all able to dock favorably to the binding pocket. The docking of hCys to the crystal structure of MsrP is shown in Figure 5-11. In the minimized energy conformation of the docking, the terminal sulfur atom of hCys is positioned in the empty equatorial coordination position at a distance of 3.4Å away from Mo. The tripeptide, glutathione was able to dock with the binding pocket, but the terminal sulfur on the cysteine was positioned 4.1Å away from Mo. This was due to the presence of the other two amino acids on either side of the cysteine, which interacted with the residues surrounding the binding pocket and prevented the cysteine from venturing far enough into the pocket to bind to Mo via the terminal thiol. However, the overall orientation of the cysteine in glutathione was favorable to thiol binding and as docking utilizes a static model of the crystal structure of MsrP, it is possible that the dynamic motion of the enzyme in a physiological setting could permit a thiol-Mo interaction by bringing the S and Mo in close proximity. The docking of free Met showed that the binding pocket highly favored this ligand; like hCys, the sulfur of Met was oriented 3.5Å away from Mo. Free Cys was able to bind to Mo, but the

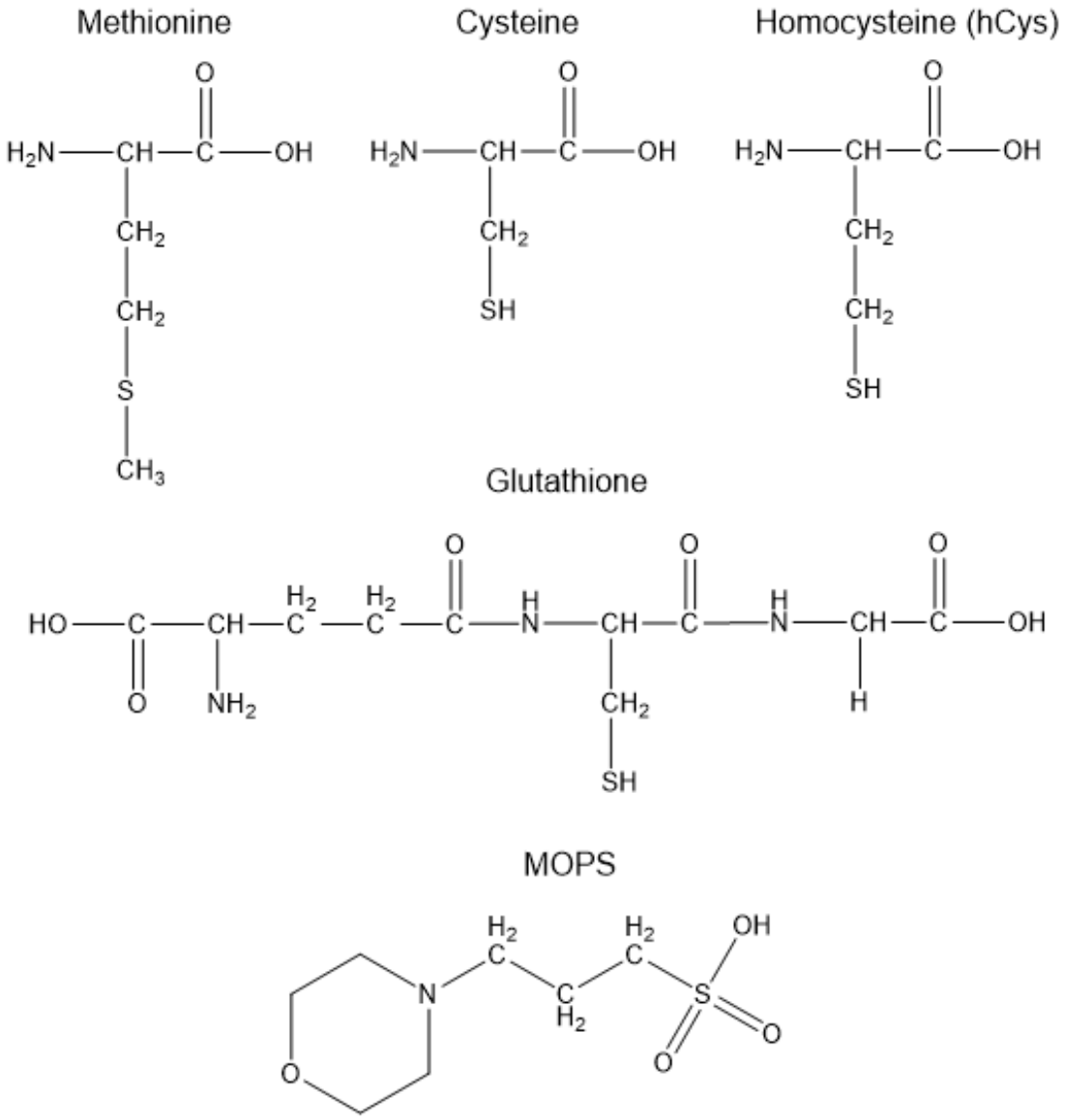

Figure 5-10. Structures of possible inhibitory thiols used for docking studies.

binding favored the terminal -OH, which was located 2.5Å away from Mo, with the thiol oriented towards the entrance of the binding pocket.

Interestingly, MOPS docked very favorably within the binding pocket, with the sulfur located 3.0Å away from Mo, the -OH 3.3Å away, one of the terminal oxo groups 2.3Å away, and the other terminal oxo 3.2 Å away from Mo. This leads to

the surprising discovery that the very buffer used in most of the prior MsrP studies may function as a competitive inhibitor in the binding pocket. For this reason, we chose to use a Bis-Tris propane buffer instead of MOPS in all of our studies of MsrP.

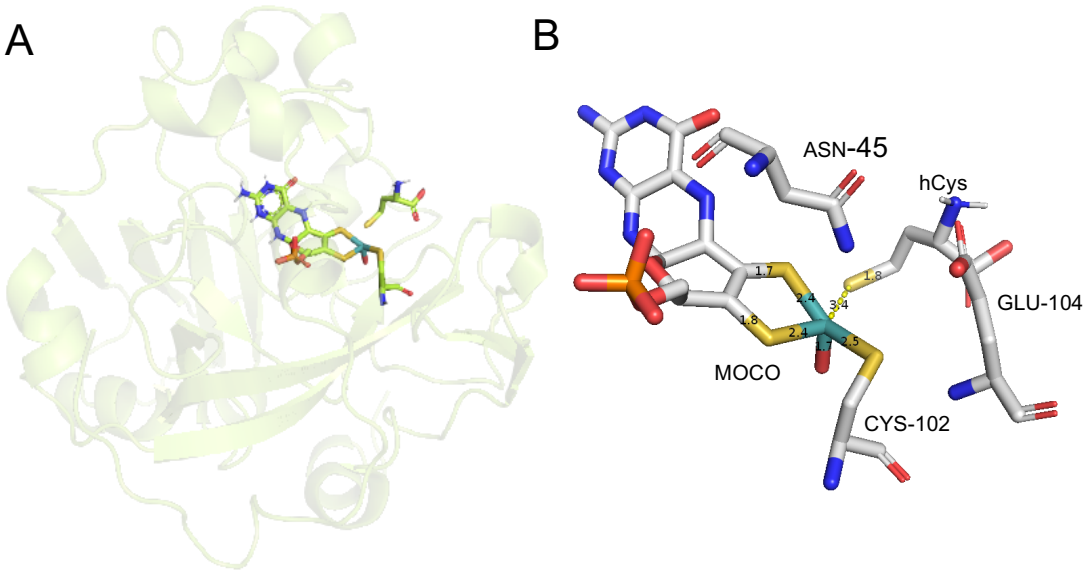

Figure 5-11. Pymol (version 2.0.7.) rendering of docking of homocysteine (hCys) to the active site of MsrP (PDB 1XDQ) (A). Closeup of the docking with selected residues and atomic distances in Å (B).

To further validate the role of MsrP as a methionine sulfoxide reductase for Met residues on the surface of proteins, we also docked a tripeptide consisting of Ala-MetO-Ala. We found that the most favorable conformation was with MetO oriented within the binding pocket, with the sulfoxide oxygen oriented 2.5Å away from Mo in the equatorial position formerly occupied by the putative -OH (Figure 5-12). This provides support that the binding pocket can accommodate an oxidized Met on a peptide chain and that the binding favors orientation of the sulfoxide oxygen which

allows it to bind to Mo. This is also the first evidence of how the substrate might coordinate to Mo within the binding pocket.

Figure 5-12. Pymol (version 2.0.7.) rendering of docking of a tripeptide consisting of Ala-MetO-Ala to the active site of MsrP (PDB 1XDQ).

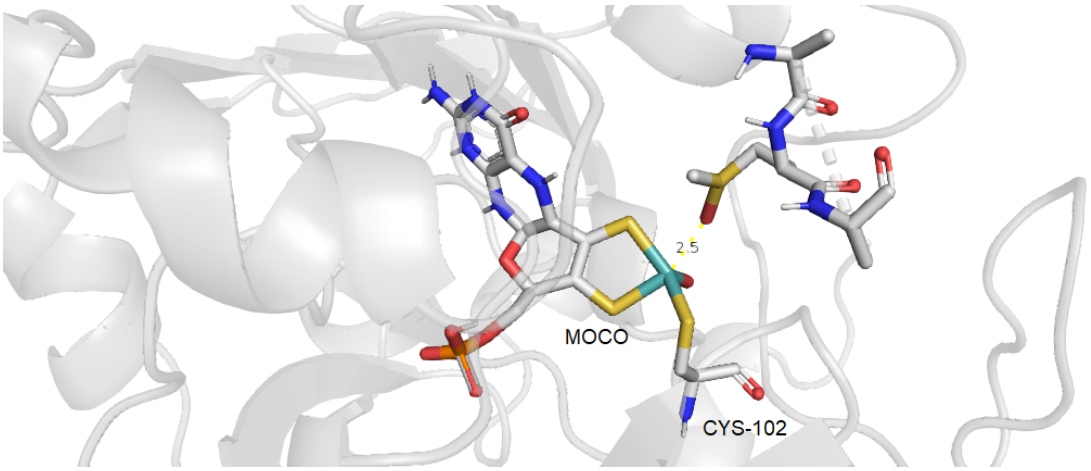

5.11 Prevention of thiol inhibition during isolation of MsrP

The difference in the oxidation states of *as-isolated* MsrP and MsrP found in whole cell samples indicates that the thiol inhibition likely occurs upon cell lysis. To attempt to prevent this thiol inhibition from occurring, and to facilitate the isolation of uninhibited MsrP, we added excess 2-iodoacetamide to the lysis buffer (Figure 5-13). Iodoacetamide is commonly used in cell biology as a thiol-reactive probe, particularly for the labeling of cysteine residues on proteins.[36] However, iodoacetamide will react with all free thiols to form thioethers, and can form sometimes stable bonds with methionine, histidine, or tyrosine as well as the free base form of amines. These “off-target” interactions generally occur when

iodoacetamide is added in excess and there is a shortage of cysteines or free thiols to react with. When iodoacetamide reacts with free thiols, it forms highly water-soluble thioether adducts. The rationale of this experimental design was that an addition of excess 2-iodoacetamide to the lysis buffer would bind to the free thiols which are released after cell lysis, preventing them from binding to and inhibiting MsrP. Following isolation of MsrP by binding it to a nickel resin via its His-tag, a series of buffer exchanges could then remove the thioether adducts and facilitate the isolation of purified, uninhibited protein.

As both the identity(-ies) of the inhibitory thiols and their relative concentrations following cell lysis is unknown, the amount of iodoacetamide to be added was not easily determined. Loshi *et al.* originally obtained 15mg/mL, or 0.45mM, of *as-isolated* MsrP.[1] To ensure that the amount of iodoacetamide exceeded the amount of protein we could expect to isolate, iodoacetamide was added at a final concentration of 100mM, far exceeding the concentration of over-expressed protein we could expect to isolate. Furthermore, since the inhibition likely occurs upon cell lysis, the iodoacetamide was added to the lysis buffer that the cells were resuspended in prior to being lysed. Iodoacetamides are unstable in light, particularly in solution, so cell lysis and subsequent isolation steps were carried out in the dark or in opaque centrifugation tubes.[36]

Following concentration, a room temperature X-band EPR was taken of the sample. The spectrum showed a strong Mo(V) signal, and an identical spectrum to previously obtained *as-isolated* MsrP, indicating that it was likely still a thiol-inhibited species (data not shown).

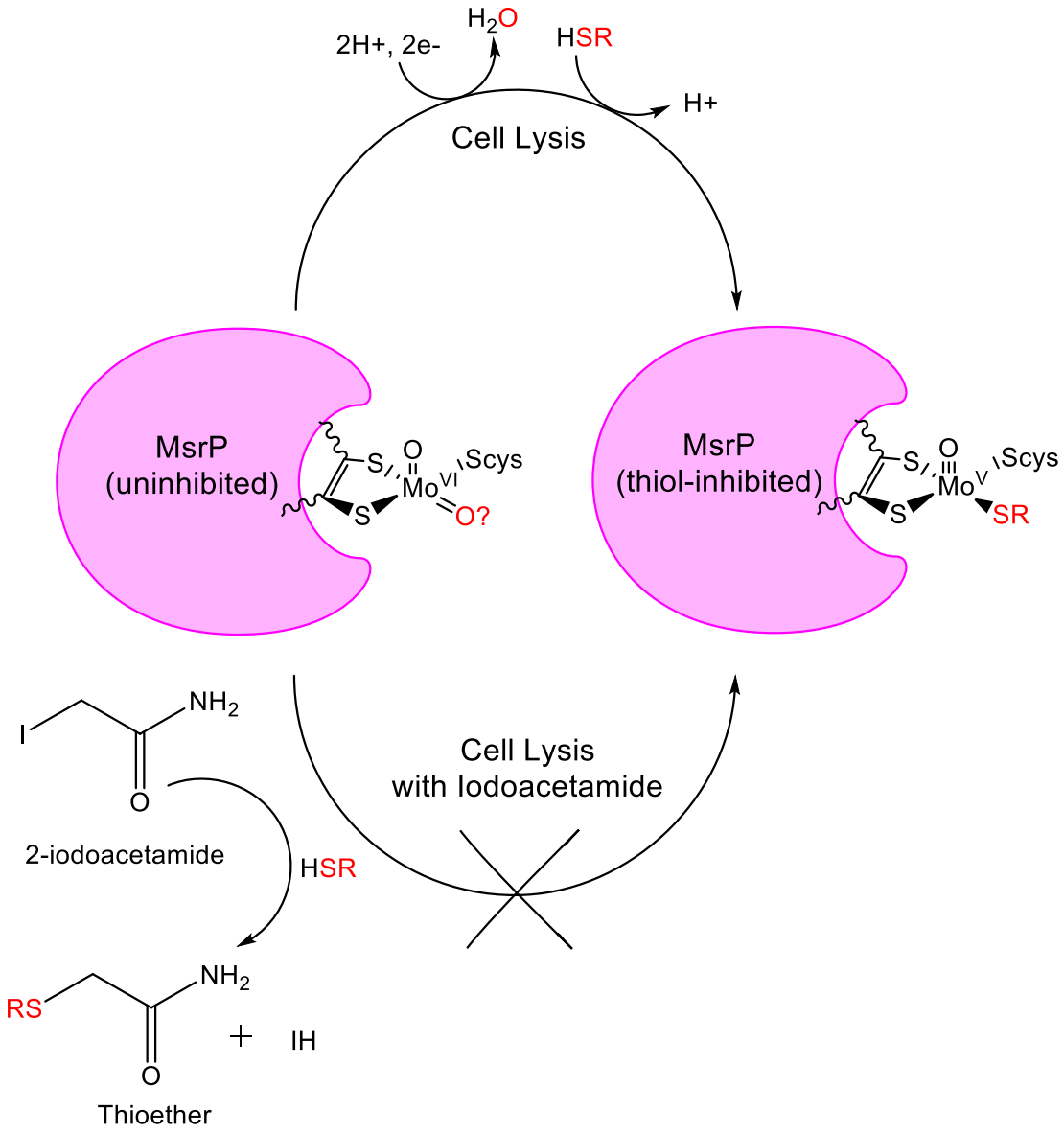

Figure 5-13. Scheme depicting thiol-inhibition of WT MsrP by endogenous thiols present in the lysate following cell lysis. Addition of 2-iodoacetamide binds to the free thiols and forms a water-soluble thioether adduct that is removable via a series of buffer exchanges.

XAS was subsequently performed on this sample; it verified that the sample contained a Mo(V), thiol-inhibited species, highly similar to what was previously observed (data not shown).[7,9] We concluded that 100mM iodoacetamide was likely

too low a concentration to prevent thiol inhibition by binding to the free thiols in the lysis buffer following cell lysis.

To test whether this effect was indeed due to a low concentration of iodocetamide in the lysis buffer, we doubled the concentration of iodoacetamide added to the cells prior to lysis to a final concentration of 200mM.

The isolated protein was then assessed by room temperature X-band EPR, and the Mo(V) EPR signal was found to be nearly non-existent (data not shown).

Mo K-edge XAS was then performed to assess the oxidation state of the metal and coordination environment around Mo. The sample was a yellowish color, unlike the deep reddish-pink color of the *as-isolated* Mo(V) thiol-blocked species that was previously isolated. An overlay of the Mo K-edge XANES with that of several other Mo(VI) dioxo molybdoenzymes shows the similarity of the rising edge energy, providing evidence that the MsrP sample is primarily in the Mo(VI) oxidation state (Figure 5-14). The similarities in the intensity of the rising edge peaks suggest that MsrP also has two Mo-O_{oxo} bonds.

The EXAFS analysis supported an active site structure with two 1.760Å Mo-Oxo bonds and two 2.400Å Mo-S bonds. The data could not be conclusively fit to a two Mo-Oxo, three Mo-S model of the active site, due to the overall noise in the data (Figure 5-15), but the data overall confirms that the primary species in the sample prepared with 200mM iodoacetamide is not the same species as *as-isolated,* thiol-blocked MsrP.

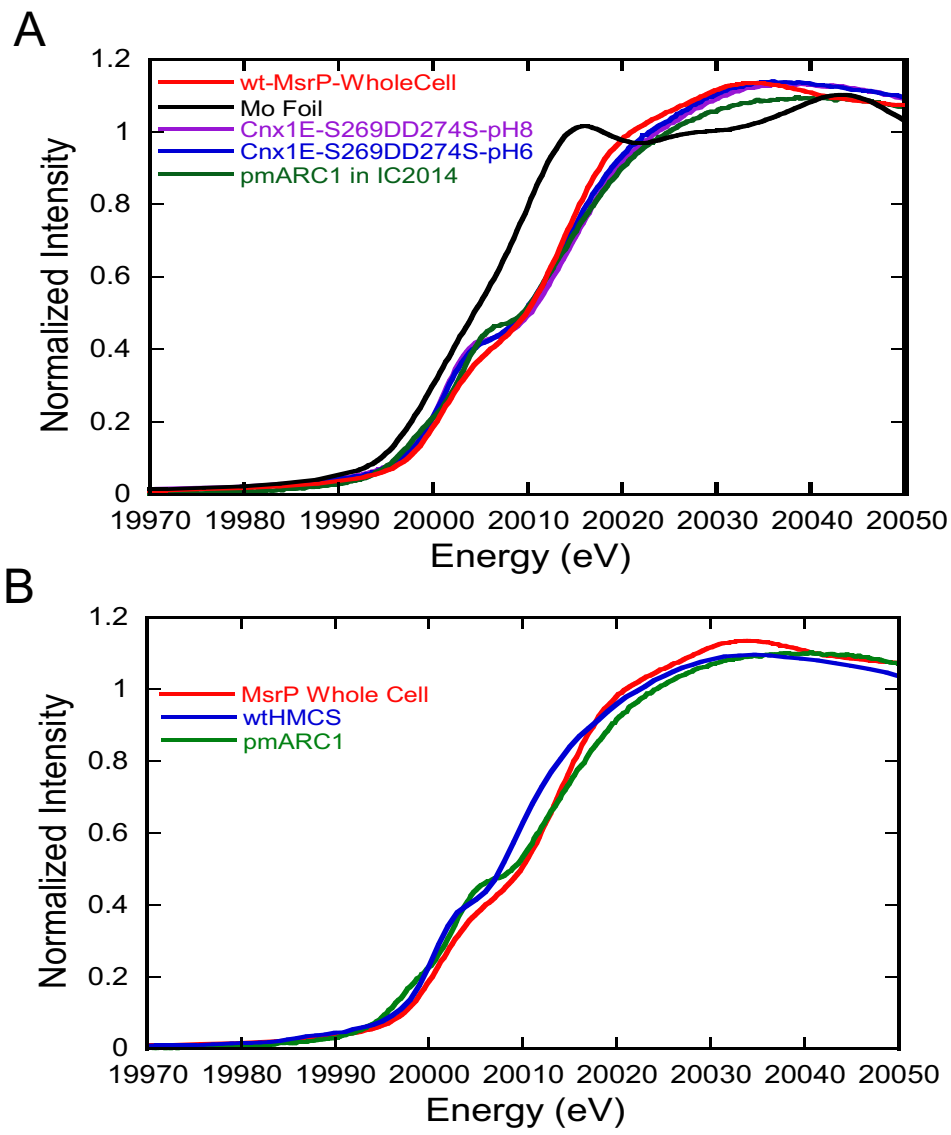

Figure 5-14. Overlay of Mo K-edge XAS of WT MsrP with 200mM of 2-iodoacetamide added to the lysis buffer (red) with that of other molybdoenzymes that are in the Mo(VI) oxidation state and possess two oxo ligands, mARC (green), and plant molybdenum insertase, Cnx1E at pH 8 (purple) and pH 6 (blue) (A). Overlay of Mo K-edge XAS of WT MsrP with 200mM of 2-iodoacetamide added to the lysis buffer (red) with that of other molybdoenzymes that are in the Mo(VI) oxidation state and possess two oxo ligands, mARC (green), and molybdenum cofactor sulfurase, wtHMCS (blue) (B). The similarity of the intensity of the rising edge peak suggests that WT MsrP has two Mo=O_{oxo} bonds and the energy of the rising edge suggests a Mo(VI) species, which is an oxidation state previously thought inaccessible for WT MsrP.

This provides compelling evidence that the Mo(VI) oxidation state can be achieved

by *as-isolated* MsrP, which implies that a more kinetically-active form of the enzyme may be isolatable in a laboratory setting and should be actively pursued in the future.

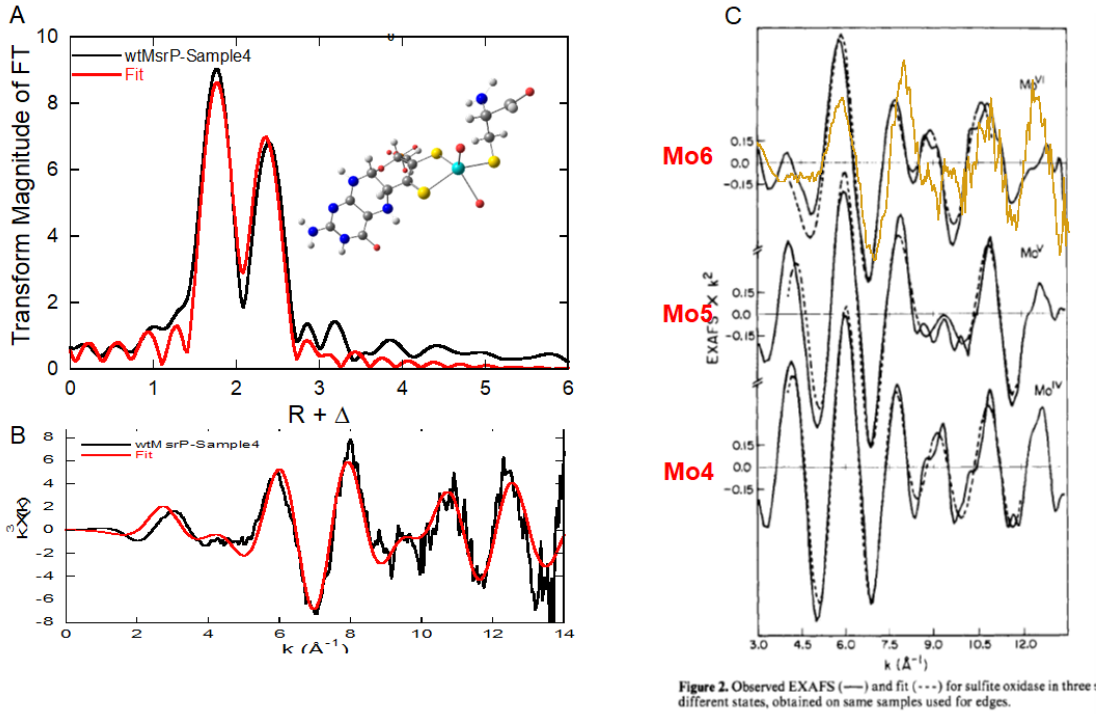

Figure 2. Observed EXAFS (——) and fit (- - -) for sulfite oxidase in three different states, obtained on same samples used for edges.

Figure 5-15. EXAFS data from Mo K-edge XAS of WT MsrP with 200mM iodoacetamide added to the lysis buffer. The fit of the Fourier transformed EXAFS data with a model of the MsrP active site that resembles that of CSO, with two sulfurs from the PDT, one sulfur from Cys-102 and two oxo groups (A, B and inset). Overlay of the k-space EXAFS spectrum for MsrP (k=3-13.5) in gold with published data from Gray, H. B. The Molybdenum Site of Sulfite Oxidase, Structural Information from X-Ray Absorption Spectroscopy. JACS 1979, 101 (10), 2772–2774 (C).

5.12 Computational evidence of a metal-based redox mechanism

Although substrates for MsrP have been identified, there is no published information on how the substrate coordinates to Mo, nor any information about the reaction mechanism. To address this gap in the knowledge, we calculated the reaction coordinate for the reduction of DMSO, shown in Figure 5-16. We found that the reaction had an energy of activation (E_A) of approximately 0.37 kJ/mol, a small activation barrier. As the water ligand in the fourth equatorial position dissociates from Mo, the binding of the substrate becomes extremely favorable. This further supports the hypothesis that a thiol binding in the position of the labile water represents a catalytically inactive form of the enzyme, which explains the poor kinetics of *as-isolated* MsrP.

The unusual catalytic mechanism proposed by Adamson *et al.* was based upon the idea that MsrP cannot achieve a Mo(VI) oxidation state and instead the metal remains in the Mo(IV) oxidation state throughout the catalytic cycle while the PDT redox cycles to provide reducing equivalents necessary for reduction of substrates. [8] However, as shown in Figure 5-16, the reduction of DMSO to DMS can occur without any oxidation state changes taking place on the fully reduced tetrahydro PDT ligand. To compare the relative stability of a Mo(VI) active site with a tetrahydro PDT (oxidized metal, reduced PDT) with that of a species possessing a Mo(IV) active site with an oxidized 10,10a dihydro PDT (reduced metal, oxidized PDT) we used DFT computations in both the gas phase and when solvated. We found that the Mo(VI)-tetrahydro species was more stable by 0.9eV in the gas phase and 0.5eV when solvated (Figure 5-17). This provides further support for a

mechanism in which the metal redox cycles during catalysis. As we have provided the first experimental evidence that MsrP can achieve a Mo(VI) oxidation state and the *as-isolated* WT MsrP represents a thiol-blocked species, the relative stability of the Mo(VI) species with a reduced tetrahydro PDT in calculations supports a mechanism in which the redox changes during catalysis are metal-based.

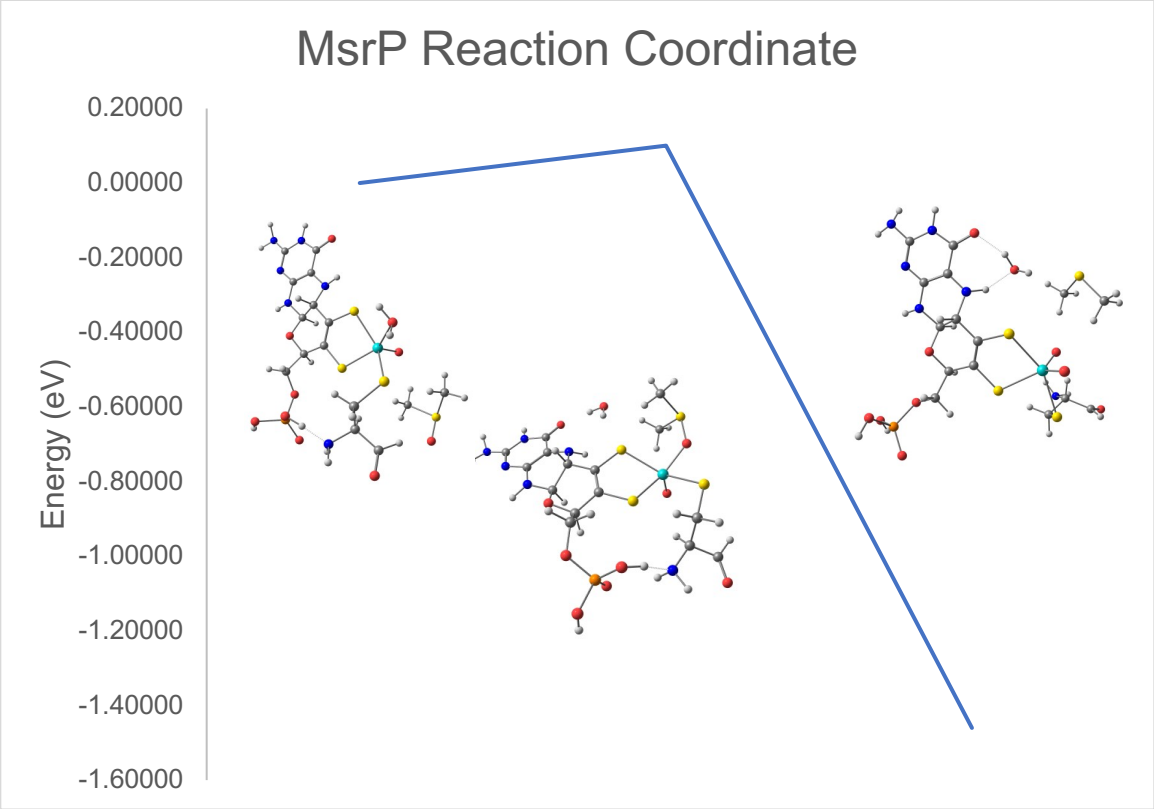

Figure 5-16. Reaction coordinate diagram of the reduction of DMSO to DMS by MsrP with a fully reduced tetrahydro PDT in gas phase. The oxidation state of the PDT ligand remains the same throughout the catalytic cycle. The oxidation state of the metal cycles from Mo(IV) to Mo(VI) during the catalytic cycle. The activation energy is 0.1006 eV or 2.320 kcal/mol.

Figure 5-17. The relative stability of the active site of MsrP with a reduced Mo(IV) and oxidized 10,10a dihydro PDT (left) was compared using DFT to an oxidized Mo(VI) active site with a reduced tetrahydro PDT (right).

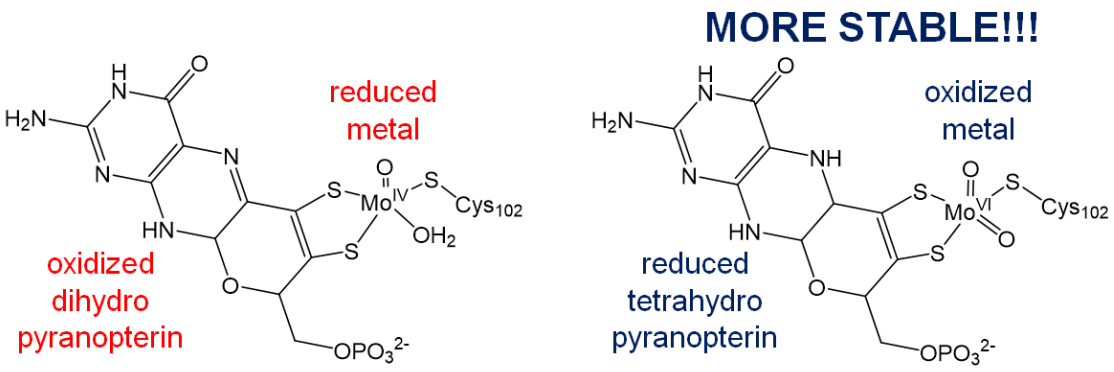

5.13 Preliminary studies on the C102S variant of MsrP

The molybdenum of MsrP is bound by a cysteine in the equatorial plane (Cys-102) is a strictly conserved residue in SO family enzymes; the equivalent cysteine in rat and human SO (Cys-207) were found to display marked impairments in enzymatic function and significant differences in the spectroscopic data compared to the WT enzymes.[37] Mutation of the equivalent cysteine in chicken liver SO to either a serine or an alanine resulted in a Mo(VI) species in which the Ser and Ala were completely dissociated from the metal. Instead, an additional oxygen was found coordinated to the metal at the position usually occupied by the Cys sulfur; this generated a trioxo-dithiolene active site.[38] The C207S mutant of human SO was also found to possess a fully oxidized Mo trioxo active site, but some evidence was presented that indicated that the Ser may be labile upon oxidation and may ligate

to Mo when the metal is fully reduced.[39] It is thought that this mutation yields a fully oxidized, trioxo species which is not catalytically active.

A C102S variant of MsrP was previously made by Brokx *et al.*; they did not perform any spectroscopy on this variant. [2] However, it was reported that mutation of Cys-102 resulted in the localization of MsrP in the cytoplasmic fraction, rather than the periplasm where MsrP is typically localized. Furthermore, while it appeared that the cofactor loading was successful in this variant, it was deemed to be catalytically inactive.

In order to further investigate the active site of the C102S variant spectroscopically, we generated our own plasmid containing the C102S gene variant and expressed it in *E. coli.* The *as-isolated* WT MsrP, the N45R, and the E104G variants are isolated in the Mo(V) oxidation, which allows direct collection of EPR from samples without redox cycling the enzymes. The *as-isolated* C102S variant was EPR silent, indicating that this variant is not isolated in the Mo(V) oxidation state.

	Mo-Oxo			ΔE_0	R_f (%)
	N	R_{fit} (R_{guess})	σ^2		
Fit1. Trioxo model, S_0^2=1, only use Oxo path, allow N to vary					
Fit1	3.263	1.768/1.716	0.0026	-11.19	40.19

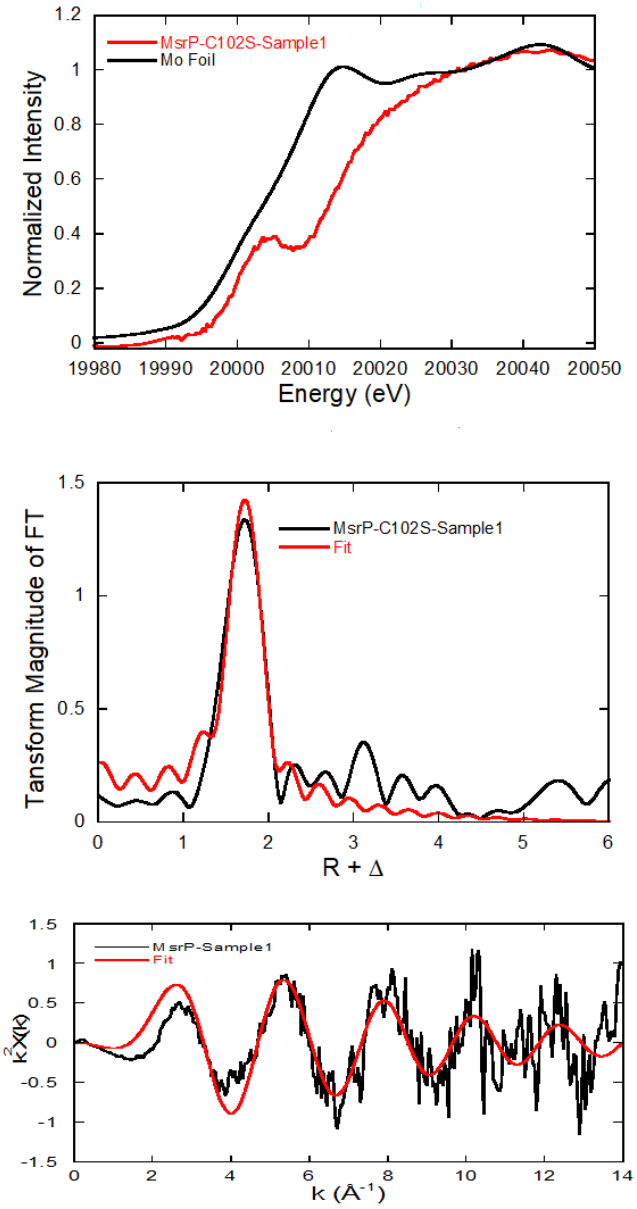

Figure 5-18. XAS data of C102S variant of MsrP.

We attempted to collect EXAFS data on two samples of the C102S variant, but the

data proved to be too noisy to be conclusive (Figure 5-18). We are currently working on obtaining a higher quality sample of this variant for XAS and X-ray crystallography to obtain more conclusive evidence as to the oxidation state of Mo and the nature of the atoms occupying the first coordination sphere.

5.14 Conclusions

The evidence presented in this work strongly suggests that previous interpretation of the crystal structure erroneously identified the fourth equatorial ligand as an O(H) and that the correct assignment of the fourth equatorial atom bound to Mo is a S. Reanalysis of the crystal structure and XAS data, comparing EPR data of active site models to the enzyme, and obtaining whole cell XAS provides conclusive evidence that the active site of *as-isolated* MsrP is a $[(PDT)Mo^{V}O(S_{Cys})(thiolate)]^{1-}$.

Given that the reported kinetic data of MsrP indicates the enzyme is highly inefficient, it is likely that the $[(PDT)Mo^{V}O(S_{Cys})(thiolate)]^{1-}$ structure represents a *thiol-blocked* species that represents a catalytic dead-end on the reaction coordinate.[1,8,35] Our whole cell EPR and XAS data provide evidence that the enzyme is not primarily in a Mo(V) oxidation state but found in a Mo(VI) oxidation state.

The results of this study underscore the critical importance of preventing the over-reliance on the interpretation of X-ray crystal structures when analyzing other data that provides structural information. The proposed active site based on the crystal structure homology to that of CSO led to the erroneous conclusion that the inability

of *as-isolated* MsrP to obtain a Mo(VI) oxidation state was a unique quirk of this particular molybdoenzyme and led to the proposal of a ligand-based redox mechanism which represented a massive paradigm shift from the generally accepted catalytic mechanism of other known molybdoenzymes, which rely on metal-based redox events to provide/abstract reducing equivalents to/from the substrate.[8,24,25,40] In light of the new evidence, we would like to propose the alternative mechanism shown in Figure 5-19, which features a metal-based redox mechanism.

For future work, we plan on further exploring this mechanism via QM/MM computations, which will help us better determine which residues within the active site contribute to catalysis. We also plan to generate more uninhibited MsrP using 2-iodoacetamide added to the lysis buffer in order to obtain better quality XAS data on this species, perform kinetic studies, and obtain a crystal structure of the uninhibited WT enzyme, as well as the C102S variant. We also plan to pursue improved spectroscopic data on the C102S variant to help provide further confirmation of the oxidation state of Mo, as well as the coordination environment around the metal.

Figure 5-19. Newly proposed mechanism for MsrP.

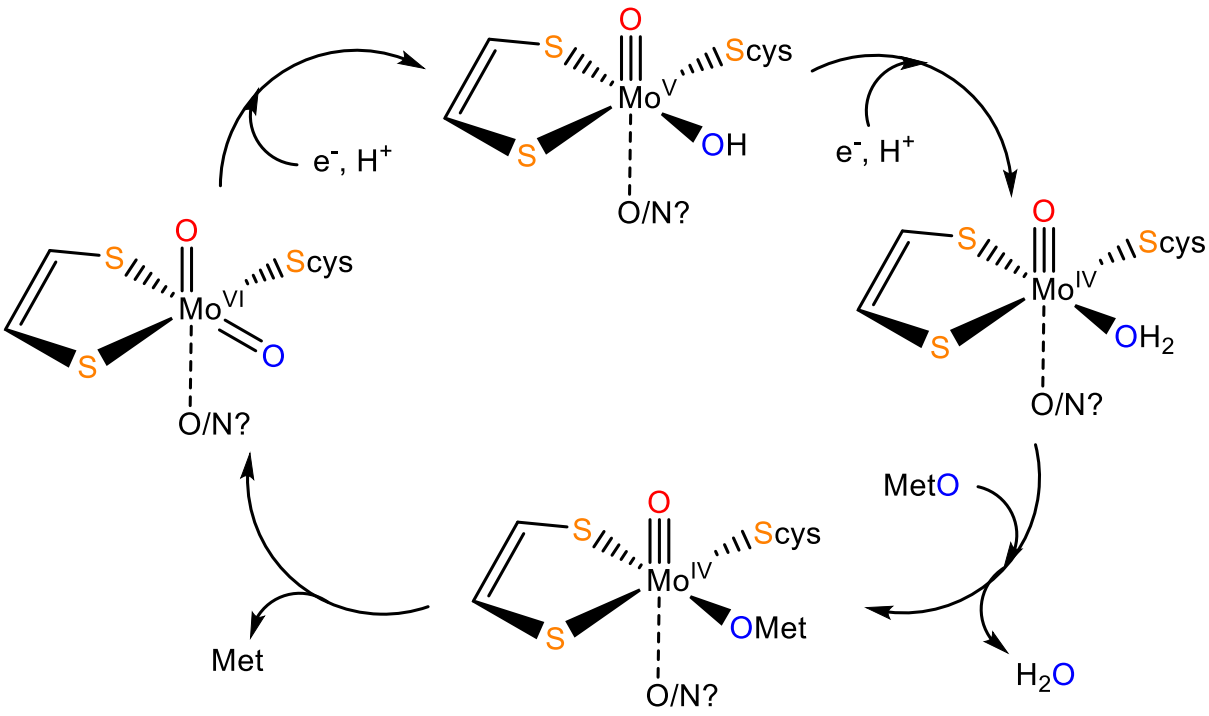

5.15 References

(1) Loschi, L.; Brokx, S. J.; Hills, T. L.; Zhang, G.; Bertero, M. G.; Lovering, A. L.; Weiner, J. H.; Strynadka, N. C. J. Structural and Biochemical Identification of a Novel Bacterial Oxidoreductase. *The Journal of biological chemistry* **2004**, *279* (48), 50391–50400. https://doi.org/10.1074/jbc.M408876200.

(2) Brokx, S. J.; Rothery, R. a; Zhang, G.; Ng, D. P.; Weiner, J. H. Characterization of an Escherichia ColiSulfite Oxidase Homologue Reveals the Role of a Conserved Active Site Cysteine in Assembly and Function †. *Biochemistry* **2005**, *44* (30), 10339–10348.

(3) Neese, F. The ORCA Program System. *Wiley Interdisciplinary Reviews: Computational Molecular Science* **2012**, *2* (1), 73–78. https://doi.org/10.1002/wcms.81.

(4) Morris, G. M., Huey, R., Lindstrom, W., Sanner, M. F., Belew, R. K., Goodsell, D. S. and Olson, A. J. AutoDock4 and AutoDockTools4: Automated Docking With. *Journal of computational chemistry* **2009**, *16*, 2785–2791. https://doi.org/10.1002/jcc.

(5) Ravel, B.; Newville, M. ATHENA, ARTEMIS, HEPHAESTUS: Data Analysis for X-Ray Absorption Spectroscopy Using IFEFFIT. *Journal of Synchrotron Radiation* **2005**, *12* (4), 537–541. https://doi.org/10.1107/S0909049505012719.

(6) Yang, J.; Rothery, R.; Sempombe, J.; Weiner, J. H.; Kirk, M. L. Spectroscopic Characterization of YedY: The Role of Sulfur Coordination in a Mo(V) Sulfite Oxidase Family Enzyme Form. *Journal of the American Chemical Society* **2009**, *131* (43), 15612–15614. https://doi.org/10.1021/ja903087k.

(7) Havelius, K. G. v; Reschke, S.; Horn, S.; Döring, A.; Niks, D.; Hille, R.; Schulzke, C.; Leimkühler, S.; Haumann, M. Structure of the Molybdenum Site in YedY, a Sulfite Oxidase Homologue from Escherichia Coli. *Inorganic Chemistry* **2011**, *50* (3), 741–748. https://doi.org/10.1021/ic101291j.

(8) Adamson, H.; Simonov, a. N.; Kierzek, M.; Rothery, R. a.; Weiner, J. H.; Bond, a. M.; Parkin, a. Electrochemical Evidence That Pyranopterin Redox Chemistry Controls the Catalysis of YedY, a Mononuclear Mo Enzyme. *Proceedings of the National Academy of Sciences* **2015**, *112* (47), 1–6. https://doi.org/10.1073/pnas.1516869112.

(9) Pushie, M. J.; Doonan, C. J.; Moquin, K.; Weiner, J. H.; Rothery, R.; George, G. N. Molybdenum Site Structure of Escherichia Coli YedY, a Novel Bacterial Oxidoreductase. *Inorganic Chemistry* **2011**, *50* (3), 732–740. https://doi.org/10.1021/ic101280m.

(10) Feng, C.; Wilson, H. L.; Hurley, J. K.; Hazzard, J. T.; Tollin, G.; Rajagopalan, K. v.; Enemark, J. H.; Oxidase, H. S.; Feng, C.; Wilson, H. L.; Hurley, J. K.; Hazzard, J. T.; Tollin, G.; Rajagopalan, K. v.; Enemark, J. H. Essential Role of Conserved Arginine 160 in Intramolecular Electron Transfer in Human Sulfite Oxidase? *Biochemistry* **2003**, *42* (42), 12235–12242. https://doi.org/10.1021/bi0350194.

(11) Meyer, C.; Gonneau, M.; Caboche, M.; Rouzé, P. Identification by Mutational Analysis of Four Critical Residues in the Molybdenum Cofactor Domain of Eukaryotic Nitrate Reductase. *FEBS Letters* **1995**, *370* (3), 197–202. https://doi.org/10.1016/0014-5793(95)00827-V.

(12) Garrett, R. M.; Johnson, J. L.; Graf, T. N.; Feigenbaum, A.; Rajagopalan, K. v. Human Sulfite Oxidase R160Q: Identification of the Mutation in a Sulfite Oxidase-Deficient Patient and Expression and Characterization of the Mutant Enzyme. *Proceedings of the National Academy of Sciences* **2002**, *95* (11), 6394–6398. https://doi.org/10.1073/pnas.95.11.6394.

(13) Karakas, E.; Wilson, H. L.; Graf, T. N.; Xiang, S.; Jaramillo-Busquets, S.; Rajagopalan, K. v.; Kisker, C. Structural Insights into Sulfite Oxidase Deficiency. *Journal of Biological Chemistry* **2005**, *280* (39), 33506–33515. https://doi.org/10.1074/jbc.M505035200.

(14) Hall, J.; Reschke, S.; Cao, H.; Leimkühler, S.; Hille, R. The Reductive Half-Reaction of Xanthine Dehydrogenase from Rhodobacter Capsulatus the Role of GLU232 in Catalysis. *Journal of Biological Chemistry* **2014**, *289* (46), 32121–32130. https://doi.org/10.1074/jbc.M114.603456.

(15) Hu, Y.; Faham, S.; Rees, D. C. Formaldehyde Ferredoxin Oxidoreductase from Pyrococcus Furiosus: The 1.85. *Journal of Molecular Biology* **1999**, *286* (3), 899.

(16) Liao, R. Z.; Yu, J. G.; Himo, F. Tungsten-Dependent Formaldehyde Ferredoxin Oxidoreductase: Reaction Mechanism from Quantum Chemical Calculations. *Journal of Inorganic Biochemistry* **2011**, *105* (7), 927–936. https://doi.org/10.1016/j.jinorgbio.2011.03.020.

(17) Romão, M. J.; Rösch, N.; Huber, R. The Molybdenum Site in the Xanthine Oxidase-Related Aldehyde Oxidoreductase from Desulfovibrio Gigas and a Catalytic Mechanism for This Class of Enzymes. *Journal of Biological Inorganic Chemistry* **1997**, *2* (6), 782–785. https://doi.org/10.1007/s007750050195.

(18) Czjzek, M.; dos Santos, J. P.; Pommier, J.; Giordano, G.; Méjean, V.; Haser, R. Crystal Structure of Oxidized Trimethylamine N-Oxide Reductase from Shewanella Massilia at 2.5 Å Resolution. *Journal of Molecular Biology* **1998**, *284* (2), 435–447. https://doi.org/10.1006/jmbi.1998.2156.

(19) Schneider, F.; Löwe, J.; Huber, R.; Schindelin, H.; Kisker, C.; Knäblein, J. Crystal Structure of Dimethyl Sulfoxide Reductase from Rhodobacter Capsulatus at 1.88 Å Resolution. *Journal of Molecular Biology* **1996**, *263* (1), 53–69. https://doi.org/10.1006/jmbi.1996.0555.

(20) Murshudov, G. N.; Skubák, P.; Lebedev, A. A.; Pannu, N. S.; Steiner, R. A.; Nicholls, R. A.; Winn, M. D.; Long, F.; Vagin, A. A. REFMAC5 for the Refinement of Macromolecular Crystal Structures. *Acta Crystallographica Section D: Biological Crystallography* **2011**, *67* (4), 355–367. https://doi.org/10.1107/S0907444911001314.

(21) Arkhipova, V.; Guskov, A.; Slotboom, D.-J. Analysis of the Quality of Crystallographic Data and the Limitations of Structural Models. *The Journal of General Physiology* **2017**, *149* (12), 1091–1103. https://doi.org/10.1085/jgp.201711852.

(22) Wlodawer, A.; Minor, W.; Dauter, Z.; Jaskolski, M.; Physics, B. Protein Crystallography for Non-Crystallographers, or How to Get the Best (but Not More) from Published Macromolecular Structures. *Febs J.* **2008**, *275* (1), 1–21. https://doi.org/10.1111/j.1742-4658.2007.06178.x.Protein.

(23) Lim, B. S.; Willer, M. W.; Miao, M.; Holm, R. H. Monodithiolene Molybdenum(V,VI) Complexes: A Structural Analogue of the Oxidized Active Site of the Sulfite Oxidase Enzyme Family. *Journal of the American Chemical Society* **2001**, *123* (34), 8343–8349. https://doi.org/10.1021/ja010786g.

(24) Hille, R. The Mononuclear Molybdenum Enzymes. *Chemical Reviews* **1996**, *96*, 2757–2816. https://doi.org/10.1021/cr950061t.

(25) Kirk, M. L.; Stein, B. *Molybdenum Enzymes*; Elsevier Ltd., 2013. https://doi.org/10.1016/B978-0-08-097774-4.00316-8.

(26) Cramer, S. P.; Eccles, T. K.; Kutzler, F. W.; Hodgson, K. O.; Mortenson, L. E. Molybdenum X-Ray Absorption Edge Spectra. The Chemical State of Molybdenum in Nitrogenase. *Journal of the American Chemical Society* **1976**, *98* (5), 1287–1288. https://doi.org/10.1021/ja00421a053.

(27) Kutzler, F. W.; Natoli, C. R.; Misemer, D. K.; Doniach, S.; Hodgson, K. O. Use of One-Electron Theory for the Interpretation of near Edge Structure in K-Shell x-Ray Absorption Spectra of Transition Metal Complexes. *The Journal of Chemical Physics* **1980**, *73* (7), 3274–3288. https://doi.org/10.1063/1.440523.

(28) Stewart, L. J.; Bailey, S.; Bennett, B.; Charnock, J. M.; Garner, C. D.; McAlpine, A. S. Dimethylsulfoxide Reductase: An Enzyme Capable of Catalysis with Either Molybdenum or Tungsten at the Active Site. *Journal of molecular biology* **2000**, *299* (3), 593–600. https://doi.org/10.1006/jmbi.2000.3702.

(29) Kisker, C.; Schindelin, H.; Pacheco, A.; Wehbi, W. A.; Garrett, R. M.; Rajagopalan, K. v.; Enemark, J. H.; Rees, D. C. Molecular Basis of Sulfite Oxidase Deficiency from the Structure of Sulfite Oxidase. *Cell* **1997**, *91* (7), 973–983. https://doi.org/10.1016/S0092-8674(00)80488-2.

(30) Tuite, N. L.; Fraser, K. R.; Byrne, C. P. O. Homocysteine Toxicity in Escherichia Coli Is Caused by a Perturbation of Branched-Chain Amino Acid Biosynthesis. **2005**, *187* (13), 4362–4371. https://doi.org/10.1128/JB.187.13.4362.

(31) Nagornykh, M.; Shakulov, R.; Nudler, E.; Zavilgelsky, G.; Korolkova, N.; Seregina, T.; Mironov, A.; Shatalin, K.; Lopes, L. E.; Kotova, V.; Luhachack, L. G. Mechanism of H 2 S-Mediated Protection against Oxidative Stress in Escherichia Coli . *Proceedings of the National Academy of Sciences* **2017**, *114* (23), 6022–6027. https://doi.org/10.1073/pnas.1703576114.

(32) Park, S.; Imlay, J. A. High Levels of Intracellular Cysteine Promote Oxidative DNA Damage by Driving the Fenton Reaction. *Journal of Bacteriology* **2003**, *185* (6), 1942–1950. https://doi.org/10.1128/JB.185.6.1942-1950.2003.

(33) Smirnova, G. v.; Oktyabrsky, O. N. Glutathione in Bacteria. *Biokhimiya* **2005**, *70* (11), 1459–1473.

(34) Thomas, J. M.; Hodes, M. E. A New Discontinuous Buffer System for the Electrophoresis of Cationic Proteins at Near-Neutral PH. *Analytical Biochemistry* **1981**, *118* (1), 194–196. https://doi.org/10.1016/0003-2697(81)90178-0.

(35) Gennaris, A.; Ezraty, B.; Henry, C.; Agrebi, R.; Vergnes, A.; Oheix, E.; Bos, J.; Leverrier, P.; Espinosa, L.; Szewczyk, J.; Vertommen, D.; Iranzo, O.; Collet, J.-F.; Barras, F. Repairing Oxidized Proteins in the Bacterial Envelope Using Respiratory Chain Electrons. *Nature* **2015**, *528* (7582), 409–412. https://doi.org/10.1038/nature15764.

(36) Thermo Fisher Scientific. CHAPTER 2 Fluorophores and Thiol-Reactive Probes Their Amine-Reactive. *Molecular Probes(TM) Handbook* **2010**, 96–121. https://doi.org/10.3390/s121115907.

(37) Rajagopalan, K. v. Site-Directed Mutagenesis of Recombinant Sulfite Oxidase. *Journal of Biological Chemistry* **1996**, *271* (13), 7387–7391. https://doi.org/10.1074/jbc.271.13.7387.

(38) Qiu, J. A.; Wilson, H. L.; Pushie, M. J.; Kisker, C.; George, G. N.; Rajagopalan, K. v. The Structures of the C185S and C185A Mutants of Sulfite Oxidase Reveal Rearrangement of the Active Site. *Biochemistry* **2010**, *49* (18), 3989–4000. https://doi.org/10.1021/bi1001954.

(39) George, G. N.; Garrett, R. M.; Prince, R. C.; Rajagopalan, K. v. Coordination Chemistry at the Molybdenum Site of Sulfite Oxidase: Redox-Induced Structural Changes in the Cysteine 207 to Serine Mutant. *Inorganic Chemistry* **2004**, *43* (26), 8456–8460. https://doi.org/10.1021/ic0489847.

(40) Hille, R.; Hall, J.; Basu, P. The Mononuclear Molybdenum Enzymes. *Chemical Reviews* **2014**, *114* (7), 3963–4038. https://doi.org/10.1021/cr400443z.

6. Appendix A - Computational details of Orca and Gaussian09 calculations

Transition state (TS) calculations and geometry optimizations were performed using Orca 4.1.0.[1] The intrinsic reaction coordinate (IRC) calculations were performed using Gaussian 09 software[2] and used to confirm the TS geometry by computing the energy profiles of the paths connecting the TS to the optimized geometries of the reactants and products of the reaction.[3,4]

Input scripts for optimization and frequency of MsrP and DMSO reaction coordinate DFT calculations using Orca

```
! B3LYP def2-SVP Opt TightSCF Grid3 FinalGrid5 TightOpt

%basis

NewGTO Mo "def2-TZVP" end

end

%scf MaxIter 500 end

%maxcore 1000

%pal

nprocs 16

end


%geom

Calc_Hess true # Request an exact Hessian (here analytical) in the first optimization step

Recalc_Hess 10 # Recalculate the exact Hessian every 10 steps.

End


! Freq


# MsrP_reactants_gas_optfreq3

*xyz -1 1
```

P	-39.502906000000	-14.277907000000	75.287406000000
O	-39.284967000000	-12.718279000000	75.478237000000
O	-38.569466000000	-15.009075000000	76.404304000000
O	-39.225713000000	-14.807634000000	73.918234000000
C	-42.068321000000	-13.701832000000	75.852953000000
O	-40.947204000000	-14.589056000000	75.937446000000
C	-43.130697000000	-14.159879000000	74.827276000000
O	-44.209759000000	-14.728579000000	75.584865000000
C	-43.581517000000	-13.015999000000	73.931708000000
S	-42.279506000000	-12.232771000000	72.998938000000
C	-44.853633000000	-12.571256000000	73.873608000000
S	-45.290516000000	-11.134336000000	72.908249000000
N	-48.594408000000	-15.924579000000	76.334143000000
C	-49.867850000000	-15.682706000000	76.231981000000
N	-50.788918000000	-16.493045000000	76.885291000000
N	-50.364566000000	-14.675953000000	75.456991000000
C	-49.559556000000	-13.790049000000	74.690156000000
O	-50.090767000000	-12.899615000000	74.031267000000
N	-47.225242000000	-13.352522000000	74.052285000000
C	-45.920074000000	-13.277805000000	74.676499000000
C	-45.435881000000	-14.725342000000	74.904740000000
N	-46.401561000000	-15.420296000000	75.716391000000
C	-48.159926000000	-14.088566000000	74.786602000000
C	-47.740242000000	-15.138979000000	75.604937000000
H	-46.128942000000	-16.277196000000	76.182567000000
H	-38.987917000000	-12.269590000000	74.587148000000
H	-37.965396000000	-15.597182000000	75.929089000000
H	-41.716037000000	-12.688400000000	75.620504000000

H	-42.667500000000	-14.950251000000	74.202227000000
H	-50.330172000000	-17.106122000000	77.552894000000
H	-51.364650000000	-14.536706000000	75.348357000000
H	-47.580520000000	-12.493904000000	73.639854000000
H	-45.986516000000	-12.817484000000	75.689337000000
H	-45.315544000000	-15.203021000000	73.908904000000
H	-51.588778000000	-16.012223000000	77.288533000000
H	-42.547835000000	-13.699945000000	76.842906000000
N	-38.473642000000	-11.938084000000	73.092285000000
C	-39.186876000000	-11.085427000000	72.126980000000
C	-38.217522000000	-10.537027000000	71.082164000000
O	-37.015656000000	-10.646058000000	71.211669000000
C	-39.936573000000	-9.923801000000	72.827230000000
S	-41.293165000000	-9.171739000000	71.824248000000
H	-39.235691000000	-9.115584000000	73.097259000000
H	-37.476659000000	-11.702032000000	73.027566000000
H	-39.952270000000	-11.687571000000	71.611091000000
H	-38.659221000000	-10.023338000000	70.197431000000
H	-40.369734000000	-10.328469000000	73.751215000000
H	-38.555573000000	-12.923962000000	72.819680000000
Mo	-43.298747000000	-10.586305000000	71.649658000000
O	-43.436893000000	-11.156828000000	70.071654000000
O	-44.089962000000	-8.506995000000	72.001354000000
H	-44.729250000000	-8.582232000000	72.731514000000
H	-43.292022000000	-8.050671000000	72.349105000000
S	-40.355638000000	-10.338790000000	67.260288000000
O	-39.017346000000	-9.979450000000	67.886925000000
C	-40.951425000000	-11.850017000000	68.105931000000

H -41.924251000000 -12.150101000000 67.690128000000

H -41.055975000000 -11.665169000000 69.183096000000

H -40.189190000000 -12.616080000000 67.904975000000

C -41.580487000000 -9.167156000000 67.951910000000

H -41.345038000000 -8.189721000000 67.506767000000

H -41.449045000000 -9.135669000000 69.044532000000

H -42.601032000000 -9.482238000000 67.690298000000

*

! B3LYP def2-SVP Opt TightSCF Grid3 FinalGrid6 TightOpt

%basis

NewGTO Mo "def2-TZVP" end

end

%scf MaxIter 500 end

%maxcore 1000

%pal

nprocs 16

end

%geom

Calc_Hess true # Request an exact Hessian (here analytical) in the first optimization step

Recalc_Hess 10 # Recalculate the exact Hessian every 10 steps.

end

! Freq

MsrP_products_gas_optfreq6

*xyz -1 1

P -40.346801000000 -15.716726000000 79.471019000000

O	-41.393563000000	-15.189145000000	80.589135000000
O	-40.381915000000	-17.320102000000	79.689536000000
O	-38.998867000000	-15.102305000000	79.550488000000
C	-41.467022000000	-14.283476000000	77.546728000000
O	-41.175084000000	-15.578948000000	78.112581000000
C	-42.468666000000	-14.469534000000	76.415777000000
O	-43.669281000000	-14.946922000000	77.017964000000
C	-42.674703000000	-13.186069000000	75.613676000000
S	-41.219055000000	-12.397873000000	74.984198000000
C	-43.904740000000	-12.661892000000	75.392242000000
S	-44.109376000000	-11.110508000000	74.584683000000
N	-48.166940000000	-16.010684000000	76.775997000000
C	-49.366694000000	-15.794303000000	76.324758000000
N	-50.436831000000	-16.547013000000	76.787822000000
N	-49.640379000000	-14.807822000000	75.423640000000
C	-48.676013000000	-13.903067000000	74.918431000000
O	-49.038064000000	-13.069227000000	74.080856000000
N	-46.321751000000	-13.238960000000	75.122076000000
C	-45.136138000000	-13.347386000000	75.940260000000
C	-44.777914000000	-14.830810000000	76.170607000000
N	-45.903060000000	-15.468672000000	76.796758000000
C	-47.359699000000	-14.113220000000	75.453427000000
C	-47.165704000000	-15.186647000000	76.335405000000
H	-45.763563000000	-16.354306000000	77.269499000000
H	-40.912306000000	-14.714675000000	81.282546000000
H	-39.543933000000	-17.702335000000	79.390802000000
H	-40.541009000000	-13.829772000000	77.166256000000
H	-42.065031000000	-15.255710000000	75.741362000000

H	-50.121914000000	-17.349543000000	77.324850000000
H	-50.587962000000	-14.628671000000	75.104474000000
H	-46.217413000000	-13.024938000000	74.122187000000
H	-45.362083000000	-12.940691000000	76.947684000000
H	-44.542343000000	-15.285144000000	75.181381000000
H	-51.142154000000	-16.790635000000	76.097897000000
H	-41.909793000000	-13.631529000000	78.316685000000
N	-38.963622000000	-13.362004000000	70.427825000000
C	-39.284892000000	-12.031553000000	70.925625000000
C	-38.547240000000	-10.983818000000	70.122183000000
O	-38.028416000000	-11.197561000000	69.048462000000
C	-38.968777000000	-11.921950000000	72.433746000000
S	-39.556636000000	-10.370977000000	73.231991000000
H	-37.880124000000	-11.979261000000	72.595704000000
H	-38.723171000000	-13.286021000000	69.437492000000
H	-40.356804000000	-11.756321000000	70.805045000000
H	-38.535231000000	-9.966241000000	70.584615000000
H	-39.415918000000	-12.783211000000	72.952239000000
H	-39.773848000000	-13.974548000000	70.505943000000
Mo	-41.999579000000	-10.604401000000	73.415355000000
O	-42.383107000000	-11.147050000000	71.837134000000
O	-46.903215000000	-12.702445000000	72.312935000000
H	-47.757816000000	-12.651191000000	72.789780000000
H	-46.623950000000	-11.779666000000	72.185984000000
S	-45.967988000000	-10.423551000000	70.045021000000
O	-42.237921000000	-8.929551000000	73.612148000000
C	-44.594807000000	-9.234955000000	69.878397000000
H	-43.755384000000	-9.527042000000	70.526555000000

H -44.975260000000 -8.252775000000 70.195878000000

H -44.253358000000 -9.163332000000 68.832637000000

C -45.081822000000 -11.987921000000 69.732270000000

H -45.744594000000 -12.785490000000 70.095698000000

H -44.148558000000 -12.006591000000 70.315277000000

H -44.865917000000 -12.124020000000 68.659955000000

*

! B3LYP def2-SVP OptTS NumFreq TightSCF Grid3 FinalGrid6 TightOpt

%basis

NewGTO Mo "def2-TZVP" end

end

%scf MaxIter 500 end

%maxcore 1000

%pal

nprocs 16

end

%geom

Calc_Hess true # Request an exact Hessian (here analytical) in the first optimization step

NumHess true # Request numerical Hessian (analytical not available)

Recalc_Hess 10 # Recalculate the exact Hessian every 10 steps.

end

! Freq

MsrP_TS_optfreq4

*xyz -1 1

P -39.48437 -14.89228 76.94519

O	-38.92698	-13.42528	76.73706
O	-38.60738	-15.53562	78.15761
O	-39.48337	-15.77550	75.73892
C	-41.89679	-13.78743	77.31350
O	-40.88741	-14.71589	77.73017
C	-42.80658	-14.32988	76.19331
O	-44.02591	-14.79127	76.80661
C	-43.05606	-13.31119	75.08901
S	-41.61592	-12.59156	74.36578
C	-44.29084	-13.00648	74.63641
S	-44.52394	-11.90337	73.27061
N	-48.41922	-16.25444	76.52326
C	-49.59285	-16.22712	75.96294
N	-50.60818	-17.04197	76.43623
N	-49.87267	-15.45647	74.87110
C	-48.93840	-14.57924	74.26669
O	-49.29046	-13.90507	73.29530
N	-46.64233	-13.76585	74.41677
C	-45.50019	-13.61790	75.29202
C	-45.05728	-14.97711	75.87667
N	-46.18977	-15.57639	76.53806
C	-47.64324	-14.62943	74.87654
C	-47.42992	-15.48801	75.96316
H	-46.03396	-16.31276	77.21704
H	-38.60231	-13.26976	75.76319
H	-38.28159	-16.39267	77.84802
H	-41.41834	-12.85096	76.99375
H	-42.28707	-15.19878	75.74100

H	-50.37296	-17.45959	77.33131
H	-50.77991	-15.49149	74.41561
H	-46.43513	-13.79092	73.42018
H	-45.81418	-13.01111	76.16586
H	-44.69729	-15.61352	75.03735
H	-51.54721	-16.65566	76.40973
H	-42.52227	-13.59503	78.19724
N	-38.08593	-13.41197	74.21491
C	-38.60967	-12.63697	73.07634
C	-37.62910	-12.61006	71.92507
O	-36.52894	-13.11951	71.95799
C	-39.00567	-11.18096	73.44264
S	-40.20412	-10.39581	72.27578
H	-38.11252	-10.53141	73.46953
H	-37.06724	-13.47577	74.11629
H	-39.53130	-13.12251	72.71360
H	-37.98586	-12.03943	71.03352
H	-39.42552	-11.20147	74.45791
H	-38.43232	-14.37614	74.16526
Mo	-42.31147	-11.66992	72.21685
O	-42.10528	-12.90206	71.08639
O	-47.80815	-11.46341	72.35390
H	-48.34064	-12.24554	72.59603
H	-47.02690	-11.55390	72.92646
S	-44.36588	-9.52151	70.49259
O	-42.76661	-10.05487	71.18404
C	-45.28830	-11.04595	70.16056
H	-46.20227	-11.13337	70.77099

H -44.60533 -11.87697 70.41718

H -45.51542 -11.06026 69.08527

C -45.21073 -8.82188 71.93470

H -45.04872 -9.48229 72.79991

H -46.28631 -8.72364 71.72459

H -44.75328 -7.83814 72.10807

*

Input scripts for IRC calculations using Gaussian 09

%chk=MsrP_TS_IRC_gauss_reverse.chk

%nproc=16

%mem=2400MW

MaxDisk=1900MB

#

IRC=(CalcFC,Phase=(54,55),maxcycles=100,recorrect=never,stepsize=10,rever

se) b3lyp/gen geom=connectivity pseudo=read

*****

-1 1

P -39.48440000 -14.89230000 76.94520000

O -38.92700000 -13.42530000 76.73710000

O	-38.60740000	-15.53560000	78.15760000
O	-39.48340000	-15.77550000	75.73890000
C	-41.89680000	-13.78740000	77.31350000
O	-40.88740000	-14.71590000	77.73020000
C	-42.80660000	-14.32990000	76.19330000
O	-44.02590000	-14.79130000	76.80660000
C	-43.05610000	-13.31120000	75.08900000
S	-41.61590000	-12.59160000	74.36580000
C	-44.29080000	-13.00650000	74.63640000
S	-44.52390000	-11.90340000	73.27060000
N	-48.41920000	-16.25440000	76.52330000
C	-49.59290000	-16.22710000	75.96290000
N	-50.60820000	-17.04200000	76.43620000
N	-49.87270000	-15.45650000	74.87110000
C	-48.93840000	-14.57920000	74.26670000
O	-49.29050000	-13.90510000	73.29530000
N	-46.64230000	-13.76580000	74.41680000
C	-45.50020000	-13.61790000	75.29200000

C	-45.05730000	-14.97710000	75.87670000
N	-46.18980000	-15.57640000	76.53810000
C	-47.64320000	-14.62940000	74.87650000
C	-47.42990000	-15.48800000	75.96320000
H	-46.03400000	-16.31280000	77.21700000
H	-38.60230000	-13.26980000	75.76320000
H	-38.28160000	-16.39270000	77.84800000
H	-41.41830000	-12.85100000	76.99370000
H	-42.28710000	-15.19880000	75.74100000
H	-50.37300000	-17.45960000	77.33130000
H	-50.77990000	-15.49150000	74.41560000
H	-46.43510000	-13.79090000	73.42020000
H	-45.81420000	-13.01110000	76.16590000
H	-44.69730000	-15.61350000	75.03730000
H	-51.54720000	-16.65570000	76.40970000
H	-42.52230000	-13.59500000	78.19720000
N	-38.08590000	-13.41200000	74.21490000
C	-38.60970000	-12.63700000	73.07630000

C	-37.62910000	-12.61010000	71.92510000
O	-36.52890000	-13.11950000	71.95800000
C	-39.00570000	-11.18100000	73.44260000
S	-40.20410000	-10.39580000	72.27580000
H	-38.11250000	-10.53140000	73.46950000
H	-37.06720000	-13.47580000	74.11630000
H	-39.53130000	-13.12250000	72.71360000
H	-37.98590000	-12.03940000	71.03350000
H	-39.42550000	-11.20150000	74.45790000
H	-38.43230000	-14.37610000	74.16530000
Mo	-42.31150000	-11.66990000	72.21690000
O	-42.10530000	-12.90210000	71.08640000
O	-47.80820000	-11.46340000	72.35390000
H	-48.34060000	-12.24550000	72.59600000
H	-47.02690000	-11.55390000	72.92650000
S	-44.36590000	-9.52150000	70.49260000
O	-42.76660000	-10.05490000	71.18400000
C	-45.28830000	-11.04600000	70.16060000

H	-46.20230000	-11.13340000	70.77100000
H	-44.60530000	-11.87700000	70.41720000
H	-45.51540000	-11.06030000	69.08530000
C	-45.21070000	-8.82190000	71.93470000
H	-45.04870000	-9.48230000	72.79990000
H	-46.28630000	-8.72360000	71.72460000
H	-44.75330000	-7.83810000	72.10810000

1 4 2.0 2 1.0 6 1.0 3 1.0

2 26 1.0

3 27 1.0

4

5 7 1.0 28 1.0 6 1.0 36 1.0

6

7 9 1.0 29 1.0 8 1.0

8 21 1.0

9 10 1.0 11 2.0

10 49 1.0

11 12 1.0 20 1.0

12 49 1.0

13 14 1.5 24 1.5

14 16 1.5 15 1.0

15 35 1.0 30 1.0

16 17 1.5 31 1.0

17 18 2.0 23 1.5

18

19 32 1.0 23 1.0 20 1.0

20 21 1.0 33 1.0

21 34 1.0 22 1.0

22 24 1.0 25 1.0

23 24 1.5

24

25

26

27

28

29

30

31

32

33

34

35

36

37 38 1.0 44 1.0 48 1.0

38 39 1.0 45 1.0 41 1.0

39 46 1.0 40 2.0

40

41 42 1.0 43 1.0 47 1.0

42 49 1.0

43

44

45

46

47

48

49 50 1.0 55 1.0

50

51 52 1.0 53 1.0

52

53

54 56 1.0 55 1.0 60 1.0

55

56 59 1.0 58 1.0 57 1.0

57

58

59

60 62 1.0 63 1.0 61 1.0

61

62

63

Mo 0

LANL2DZ

****

N P S C O H 0

6-31G*

****

Mo 0

LANL2

%chk=MsrP_TS_IRC_gauss_forward.chk

%nproc=16

%mem=2400MW

MaxDisk=1900MB

#

IRC=(CalcFC,Phase=(54,55),maxcycles=100,recorrect=never,stepsize=10,forwa

rd) b3lyp/gen geom=connectivity pseudo=read

*****

-1 1

P	-39.48440000	-14.89230000	76.94520000
O	-38.92700000	-13.42530000	76.73710000
O	-38.60740000	-15.53560000	78.15760000
O	-39.48340000	-15.77550000	75.73890000
C	-41.89680000	-13.78740000	77.31350000
O	-40.88740000	-14.71590000	77.73020000
C	-42.80660000	-14.32990000	76.19330000
O	-44.02590000	-14.79130000	76.80660000
C	-43.05610000	-13.31120000	75.08900000
S	-41.61590000	-12.59160000	74.36580000
C	-44.29080000	-13.00650000	74.63640000
S	-44.52390000	-11.90340000	73.27060000
N	-48.41920000	-16.25440000	76.52330000
C	-49.59290000	-16.22710000	75.96290000
N	-50.60820000	-17.04200000	76.43620000
N	-49.87270000	-15.45650000	74.87110000

C	-48.93840000	-14.57920000	74.26670000
O	-49.29050000	-13.90510000	73.29530000
N	-46.64230000	-13.76580000	74.41680000
C	-45.50020000	-13.61790000	75.29200000
C	-45.05730000	-14.97710000	75.87670000
N	-46.18980000	-15.57640000	76.53810000
C	-47.64320000	-14.62940000	74.87650000
C	-47.42990000	-15.48800000	75.96320000
H	-46.03400000	-16.31280000	77.21700000
H	-38.60230000	-13.26980000	75.76320000
H	-38.28160000	-16.39270000	77.84800000
H	-41.41830000	-12.85100000	76.99370000
H	-42.28710000	-15.19880000	75.74100000
H	-50.37300000	-17.45960000	77.33130000
H	-50.77990000	-15.49150000	74.41560000
H	-46.43510000	-13.79090000	73.42020000
H	-45.81420000	-13.01110000	76.16590000
H	-44.69730000	-15.61350000	75.03730000

H	-51.54720000	-16.65570000	76.40970000
H	-42.52230000	-13.59500000	78.19720000
N	-38.08590000	-13.41200000	74.21490000
C	-38.60970000	-12.63700000	73.07630000
C	-37.62910000	-12.61010000	71.92510000
O	-36.52890000	-13.11950000	71.95800000
C	-39.00570000	-11.18100000	73.44260000
S	-40.20410000	-10.39580000	72.27580000
H	-38.11250000	-10.53140000	73.46950000
H	-37.06720000	-13.47580000	74.11630000
H	-39.53130000	-13.12250000	72.71360000
H	-37.98590000	-12.03940000	71.03350000
H	-39.42550000	-11.20150000	74.45790000
H	-38.43230000	-14.37610000	74.16530000
Mo	-42.31150000	-11.66990000	72.21690000
O	-42.10530000	-12.90210000	71.08640000
O	-47.80820000	-11.46340000	72.35390000
H	-48.34060000	-12.24550000	72.59600000

H -47.02690000 -11.55390000 72.92650000

S -44.36590000 -9.52150000 70.49260000

O -42.76660000 -10.05490000 71.18400000

C -45.28830000 -11.04600000 70.16060000

H -46.20230000 -11.13340000 70.77100000

H -44.60530000 -11.87700000 70.41720000

H -45.51540000 -11.06030000 69.08530000

C -45.21070000 -8.82190000 71.93470000

H -45.04870000 -9.48230000 72.79990000

H -46.28630000 -8.72360000 71.72460000

H -44.75330000 -7.83810000 72.10810000

1 4 2.0 2 1.0 6 1.0 3 1.0

2 26 1.0

3 27 1.0

4

5 7 1.0 28 1.0 6 1.0 36 1.0

6

7 9 1.0 29 1.0 8 1.0

8 21 1.0

9 10 1.0 11 2.0

10 49 1.0

11 12 1.0 20 1.0

12 49 1.0

13 14 1.5 24 1.5

14 16 1.5 15 1.0

15 35 1.0 30 1.0

16 17 1.5 31 1.0

17 18 2.0 23 1.5

18

19 32 1.0 23 1.0 20 1.0

20 21 1.0 33 1.0

21 34 1.0 22 1.0

22 24 1.0 25 1.0

23 24 1.5

24

25

26

27

28

29

30

31

32

33

34

35

36

37 38 1.0 44 1.0 48 1.0

38 39 1.0 45 1.0 41 1.0

39 46 1.0 40 2.0

40

41 42 1.0 43 1.0 47 1.0

42 49 1.0

43

44

45

46

47

48

49 50 1.0 55 1.0

50

51 52 1.0 53 1.0

52

53

54 56 1.0 55 1.0 60 1.0

55

56 59 1.0 58 1.0 57 1.0

57

58

59

60 62 1.0 63 1.0 61 1.0

61

62

63

Mo 0

LANL2DZ

****

N P S C O H 0

6-31G*

****

Mo 0

LANL2

Optimized coordinates of the TS using Orca (DMSO and MsrP)

P -39.48437 -14.89228 76.94519

O -38.92698 -13.42528 76.73706

O -38.60738 -15.53562 78.15761

O -39.48337 -15.77550 75.73892

C -41.89679 -13.78743 77.31350

O -40.88741 -14.71589 77.73017

C -42.80658 -14.32988 76.19331

O -44.02591 -14.79127 76.80661

C -43.05606 -13.31119 75.08901

S -41.61592 -12.59156 74.36578

C -44.29084 -13.00648 74.63641

S -44.52394 -11.90337 73.27061

N -48.41922 -16.25444 76.52326

C -49.59285 -16.22712 75.96294

N -50.60818 -17.04197 76.43623

N -49.87267 -15.45647 74.87110

C -48.93840 -14.57924 74.26669

O -49.29046 -13.90507 73.29530

N -46.64233 -13.76585 74.41677

C -45.50019 -13.61790 75.29202

C -45.05728 -14.97711 75.87667

N -46.18977 -15.57639 76.53806

C -47.64324 -14.62943 74.87654

C -47.42992 -15.48801 75.96316

H -46.03396 -16.31276 77.21704

H -38.60231 -13.26976 75.76319

H -38.28159 -16.39267 77.84802

H -41.41834 -12.85096 76.99375

H -42.28707 -15.19878 75.74100

H -50.37296 -17.45959 77.33131

H -50.77991 -15.49149 74.41561

H -46.43513 -13.79092 73.42018

H -45.81418 -13.01111 76.16586

H -44.69729 -15.61352 75.03735

H -51.54721 -16.65566 76.40973

H -42.52227 -13.59503 78.19724

N -38.08593 -13.41197 74.21491

C -38.60967 -12.63697 73.07634

C -37.62910 -12.61006 71.92507

O -36.52894 -13.11951 71.95799

C -39.00567 -11.18096 73.44264

S -40.20412 -10.39581 72.27578

H -38.11252 -10.53141 73.46953

H -37.06724 -13.47577 74.11629

H -39.53130 -13.12251 72.71360

H -37.98586 -12.03943 71.03352

H -39.42552 -11.20147 74.45791

H -38.43232 -14.37614 74.16526

Mo -42.31147 -11.66992 72.21685

O -42.10528 -12.90206 71.08639

O -47.80815 -11.46341 72.35390

H -48.34064 -12.24554 72.59603

H -47.02690 -11.55390 72.92646

S -44.36588 -9.52151 70.49259

O -42.76661 -10.05487 71.18404

C -45.28830 -11.04595 70.16056

H -46.20227 -11.13337 70.77099

H -44.60533 -11.87697 70.41718

H -45.51542 -11.06026 69.08527

C -45.21073 -8.82188 71.93470

H -45.04872 -9.48229 72.79991

H -46.28631 -8.72364 71.72459

H -44.75328 -7.83814 72.10807

Vibrational frequencies of the optimized TS geometry

VIBRATIONAL FREQUENCIES

0: 0.00 cm**-1

1: 0.00 cm**-1

2: 0.00 cm**-1

3: 0.00 cm**-1

4: 0.00 cm**-1

5: 0.00 cm**-1

6: -567.66 cm**-1 ***imaginary mode***

7: 12.42 cm**-1

8: 13.67 cm**-1

9: 27.05 cm**-1

10: 34.42 cm**-1

11: 41.36 cm**-1

12: 43.14 cm**-1

13: 49.33 cm**-1

14: 56.02 cm**-1

15: 60.45 cm**-1

16: 62.86 cm**-1

17: 75.10 cm**-1

18: 76.87 cm**-1

19: 81.77 cm**-1

20: 89.64 cm**-1

21: 106.61 cm**-1

22: 111.49 cm**-1

23: 113.28 cm**-1

24: 122.49 cm**-1

25: 127.85 cm**-1

26: 134.97 cm**-1

27: 136.54 cm**-1

28: 139.75 cm**-1

29: 147.25 cm**-1

30: 153.83 cm**-1

31: 163.84 cm**-1

32: 171.16 cm**-1

33: 175.68 cm**-1

34: 182.65 cm**-1

35: 183.70 cm**-1

36: 185.25 cm**-1

37: 204.93 cm**-1

38: 208.73 cm**-1

39: 218.22 cm**-1

40: 230.56 cm**-1

41: 240.46 cm**-1

42: 248.65 cm**-1

43: 251.46 cm**-1

44: 275.86 cm**-1

45: 285.35 cm**-1

46: 289.90 cm**-1

47: 297.61 cm**-1

48: 308.54 cm**-1

49: 311.49 cm**-1

50: 317.19 cm**-1

51: 324.69 cm**-1

52: 329.87 cm**-1

53: 349.12 cm**-1

54: 352.59 cm**-1

55: 355.33 cm**-1

56: 359.51 cm**-1

57: 365.29 cm**-1

58: 373.03 cm**-1

59: 377.95 cm**-1

60: 390.52 cm**-1

61: 394.73 cm**-1

62: 408.67 cm**-1

63: 417.93 cm**-1

64: 428.10 cm**-1

65: 445.49 cm**-1

66: 449.89 cm**-1

67: 460.01 cm**-1

68: 467.56 cm**-1

69: 476.14 cm**-1

70: 489.25 cm**-1

71: 497.59 cm**-1

72: 503.83 cm**-1

73: 516.87 cm**-1

74: 546.64 cm**-1

75: 556.41 cm**-1

76: 571.76 cm**-1

77: 580.51 cm**-1

78: 584.93 cm**-1

79: 590.08 cm**-1

80: 605.85 cm**-1

81: 622.69 cm**-1

82: 650.94 cm**-1

83: 670.23 cm**-1

84: 671.43 cm**-1

85: 696.19 cm**-1

86: 712.64 cm**-1

87: 713.38 cm**-1

88: 722.84 cm**-1

89: 725.29 cm**-1

90: 733.63 cm**-1

91: 743.12 cm**-1

92: 753.76 cm**-1

93: 779.51 cm**-1

94: 820.06 cm**-1

95: 860.58 cm**-1

96: 864.29 cm**-1

97: 880.73 cm**-1

98: 916.96 cm**-1

99: 933.14 cm**-1

100: 934.77 cm**-1

101: 940.20 cm**-1

102: 949.23 cm**-1

103: 970.13 cm**-1

104: 990.27 cm**-1

105: 995.97 cm**-1

106: 1004.99 cm**-1

107: 1012.31 cm**-1

108: 1016.16 cm**-1

109: 1033.63 cm**-1

110: 1038.78 cm**-1

111: 1052.67 cm**-1

112: 1053.42 cm**-1

113: 1058.64 cm**-1

114: 1086.63 cm**-1

115: 1100.53 cm**-1

116: 1115.69 cm**-1

117: 1121.65 cm**-1

118: 1130.87 cm**-1

119: 1138.80 cm**-1

120: 1147.60 cm**-1

121: 1159.65 cm**-1

122: 1186.86 cm**-1

123: 1188.48 cm**-1

124: 1191.97 cm**-1

125: 1202.60 cm**-1

126: 1248.46 cm**-1

127: 1252.11 cm**-1

128: 1255.16 cm**-1

129: 1282.14 cm**-1

130: 1287.05 cm**-1

131: 1296.00 cm**-1

132: 1298.52 cm**-1

133: 1300.80 cm**-1

134: 1312.45 cm**-1

135: 1324.08 cm**-1

136: 1335.61 cm**-1

137: 1339.97 cm**-1

138: 1350.04 cm**-1

139: 1367.39 cm**-1

140: 1378.85 cm**-1

141: 1379.66 cm**-1

142: 1384.61 cm**-1

143: 1401.23 cm**-1

144: 1420.30 cm**-1

145: 1425.88 cm**-1

146: 1428.55 cm**-1

147: 1433.71 cm**-1

148: 1444.74 cm**-1

149: 1449.20 cm**-1

150: 1453.39 cm**-1

151: 1458.04 cm**-1

152: 1462.93 cm**-1

153: 1515.16 cm**-1

154: 1550.86 cm**-1

155: 1595.90 cm**-1

156: 1628.00 cm**-1

157: 1633.70 cm**-1

158: 1651.21 cm**-1

159: 1674.00 cm**-1

160: 1683.85 cm**-1

161: 1761.71 cm**-1

162: 1815.27 cm**-1

163: 2538.16 cm**-1

164: 2926.27 cm**-1

165: 2949.25 cm**-1

166: 2966.37 cm**-1

167: 2985.11 cm**-1

168: 2990.76 cm**-1

169: 3023.78 cm**-1

170: 3026.28 cm**-1

171: 3055.15 cm**-1

172: 3070.56 cm**-1

173: 3093.26 cm**-1

174: 3110.59 cm**-1

175: 3137.00 cm**-1

176: 3140.16 cm**-1

177: 3147.25 cm**-1

178: 3162.30 cm**-1

179: 3429.83 cm**-1

180: 3498.20 cm**-1

181: 3538.56 cm**-1

182: 3550.37 cm**-1

183: 3595.07 cm**-1

184: 3623.17 cm**-1

185: 3658.49 cm**-1

186: 3660.50 cm**-1

187: 3737.63 cm**-1

188: 3830.08 cm**-1

Total SCF energy of the optimized TS geometry

TOTAL SCF ENERGY

Total Energy : -3667.67027583 Eh -99802.38206 eV

Optimized coordinates of the reactants using Orca (DMSO and MsrP)

P	-39.50291	-14.27791	75.28741
O	-39.28497	-12.71828	75.47824
O	-38.56947	-15.00907	76.40430
O	-39.22571	-14.80763	73.91823
C	-42.06832	-13.70183	75.85295
O	-40.94720	-14.58906	75.93745
C	-43.13070	-14.15988	74.82728
O	-44.20976	-14.72858	75.58486
C	-43.58152	-13.01600	73.93171

S	-42.27951	-12.23277	72.99894
C	-44.85363	-12.57126	73.87361
S	-45.29052	-11.13434	72.90825
N	-48.59441	-15.92458	76.33414
C	-49.86785	-15.68271	76.23198
N	-50.78892	-16.49304	76.88529
N	-50.36457	-14.67595	75.45699
C	-49.55956	-13.79005	74.69016
O	-50.09077	-12.89962	74.03127
N	-47.22524	-13.35252	74.05228
C	-45.92007	-13.27781	74.67650
C	-45.43588	-14.72534	74.90474
N	-46.40156	-15.42030	75.71639
C	-48.15993	-14.08857	74.78660
C	-47.74024	-15.13898	75.60494
H	-46.12894	-16.27720	76.18257
H	-38.98792	-12.26959	74.58715
H	-37.96540	-15.59718	75.92909

H	-41.71604	-12.68840	75.62050
H	-42.66750	-14.95025	74.20223
H	-50.33017	-17.10612	77.55289
H	-51.36465	-14.53671	75.34836
H	-47.58052	-12.49390	73.63985
H	-45.98652	-12.81748	75.68934
H	-45.31554	-15.20302	73.90890
H	-51.58878	-16.01222	77.28853
H	-42.54783	-13.69994	76.84291
N	-38.47364	-11.93808	73.09229
C	-39.18688	-11.08543	72.12698
C	-38.21752	-10.53703	71.08216
O	-37.01566	-10.64606	71.21167
C	-39.93657	-9.92380	72.82723
S	-41.29317	-9.17174	71.82425
H	-39.23569	-9.11558	73.09726
H	-37.47666	-11.70203	73.02757
H	-39.95227	-11.68757	71.61109

H	-38.65922	-10.02334	70.19743
H	-40.36973	-10.32847	73.75122
H	-38.55557	-12.92396	72.81968
Mo	-43.29875	-10.58630	71.64966
O	-43.43689	-11.15683	70.07165
O	-44.08996	-8.50699	72.00135
H	-44.72925	-8.58223	72.73151
H	-43.29202	-8.05067	72.34910
S	-40.35564	-10.33879	67.26029
O	-39.01735	-9.97945	67.88693
C	-40.95143	-11.85002	68.10593
H	-41.92425	-12.15010	67.69013
H	-41.05597	-11.66517	69.18310
H	-40.18919	-12.61608	67.90497
C	-41.58049	-9.16716	67.95191
H	-41.34504	-8.18972	67.50677
H	-41.44904	-9.13567	69.04453
H	-42.60103	-9.48224	67.69030

Vibrational frequencies of the optimized reactants geometry

VIBRATIONAL FREQUENCIES

0: 0.00 cm**-1

1: 0.00 cm**-1

2: 0.00 cm**-1

3: 0.00 cm**-1

4: 0.00 cm**-1

5: 0.00 cm**-1

6: 11.43 cm**-1

7: 14.68 cm**-1

8: 23.85 cm**-1

9: 33.70 cm**-1

10: 40.24 cm**-1

11: 43.49 cm**-1

12: 47.66 cm**-1

13: 51.77 cm**-1

14: 52.59 cm**-1

15: 59.29 cm**-1

16: 62.32 cm**-1

17: 67.05 cm**-1

18: 70.66 cm**-1

19: 77.50 cm**-1

20: 85.30 cm**-1

21: 91.92 cm**-1

22: 95.32 cm**-1

23: 105.09 cm**-1

24: 117.33 cm**-1

25: 125.85 cm**-1

26: 127.80 cm**-1

27: 135.24 cm**-1

28: 148.54 cm**-1

29: 163.61 cm**-1

30: 168.49 cm**-1

31: 174.43 cm**-1

32: 178.57 cm**-1

33: 178.95 cm**-1

34: 180.03 cm**-1

35: 183.77 cm**-1

36: 195.36 cm**-1

37: 200.54 cm**-1

38: 218.22 cm**-1

39: 221.55 cm**-1

40: 224.89 cm**-1

41: 233.13 cm**-1

42: 242.96 cm**-1

43: 263.84 cm**-1

44: 266.34 cm**-1

45: 284.35 cm**-1

46: 289.51 cm**-1

47: 301.91 cm**-1

48: 306.60 cm**-1

49: 309.56 cm**-1

50: 330.80 cm**-1

51: 340.44 cm**-1

52: 345.71 cm**-1

53: 353.20 cm**-1

54: 357.61 cm**-1

55: 364.29 cm**-1

56: 364.80 cm**-1

57: 367.50 cm**-1

58: 369.03 cm**-1

59: 385.09 cm**-1

60: 389.50 cm**-1

61: 394.39 cm**-1

62: 406.09 cm**-1

63: 417.40 cm**-1

64: 432.09 cm**-1

65: 437.42 cm**-1

66: 445.74 cm**-1

67: 458.87 cm**-1

68: 482.54 cm**-1

69: 496.77 cm**-1

70: 507.60 cm**-1

71: 519.95 cm**-1

72: 539.21 cm**-1

73: 559.92 cm**-1

74: 577.52 cm**-1

75: 581.00 cm**-1

76: 590.16 cm**-1

77: 598.07 cm**-1

78: 602.52 cm**-1

79: 622.03 cm**-1

80: 631.88 cm**-1

81: 647.23 cm**-1

82: 663.21 cm**-1

83: 668.83 cm**-1

84: 688.25 cm**-1

85: 707.94 cm**-1

86: 712.43 cm**-1

87: 714.08 cm**-1

88: 719.87 cm**-1

89: 730.92 cm**-1

90: 746.82 cm**-1

91: 749.40 cm**-1

92: 806.86 cm**-1

93: 811.16 cm**-1

94: 854.59 cm**-1

95: 874.84 cm**-1

96: 877.48 cm**-1

97: 889.40 cm**-1

98: 891.35 cm**-1

99: 922.23 cm**-1

100: 948.05 cm**-1

101: 954.02 cm**-1

102: 961.74 cm**-1

103: 973.84 cm**-1

104: 996.12 cm**-1

105: 1006.62 cm**-1

106: 1017.07 cm**-1

107: 1020.60 cm**-1

108: 1025.20 cm**-1

109: 1032.77 cm**-1

110: 1047.97 cm**-1

111: 1054.59 cm**-1

112: 1068.24 cm**-1

113: 1072.93 cm**-1

114: 1101.40 cm**-1

115: 1110.41 cm**-1

116: 1122.14 cm**-1

117: 1126.15 cm**-1

118: 1134.02 cm**-1

119: 1145.74 cm**-1

120: 1148.48 cm**-1

121: 1158.76 cm**-1

122: 1179.20 cm**-1

123: 1185.32 cm**-1

124: 1198.15 cm**-1

125: 1210.22 cm**-1

126: 1249.74 cm**-1

127: 1254.40 cm**-1

128: 1272.46 cm**-1

129: 1278.90 cm**-1

130: 1281.40 cm**-1

131: 1298.74 cm**-1

132: 1301.66 cm**-1

133: 1304.07 cm**-1

134: 1310.30 cm**-1

135: 1311.19 cm**-1

136: 1323.45 cm**-1

137: 1337.53 cm**-1

138: 1343.26 cm**-1

139: 1356.22 cm**-1

140: 1389.52 cm**-1

141: 1389.85 cm**-1

142: 1400.14 cm**-1

143: 1406.87 cm**-1

144: 1418.54 cm**-1

145: 1420.50 cm**-1

146: 1428.27 cm**-1

147: 1429.52 cm**-1

148: 1440.65 cm**-1

149: 1447.71 cm**-1

150: 1450.34 cm**-1

151: 1471.23 cm**-1

152: 1481.38 cm**-1

153: 1519.10 cm**-1

154: 1550.08 cm**-1

155: 1573.58 cm**-1

156: 1598.78 cm**-1

157: 1632.29 cm**-1

158: 1633.72 cm**-1

159: 1638.59 cm**-1

160: 1685.50 cm**-1

161: 1782.92 cm**-1

162: 1804.30 cm**-1

163: 2400.90 cm**-1

164: 2899.99 cm**-1

165: 2943.19 cm**-1

166: 2959.89 cm**-1

167: 2987.68 cm**-1

168: 3030.76 cm**-1

169: 3034.97 cm**-1

170: 3035.72 cm**-1

171: 3048.58 cm**-1

172: 3077.28 cm**-1

173: 3106.87 cm**-1

174: 3125.94 cm**-1

175: 3150.43 cm**-1

176: 3163.14 cm**-1

177: 3166.23 cm**-1

178: 3178.80 cm**-1

179: 3429.15 cm**-1

180: 3473.50 cm**-1

181: 3499.15 cm**-1

182: 3539.61 cm**-1

183: 3572.75 cm**-1

184: 3596.67 cm**-1

185: 3628.61 cm**-1

186: 3648.20 cm**-1

187: 3753.35 cm**-1

188: 3827.28 cm**-1

Total SCF energy of the optimized reactants geometry

TOTAL SCF ENERGY

Total Energy : -3667.67397207 Eh -99802.48264 eV

Optimized coordinates of the products using Orca (DMS and MsrP)

P	-40.34680	-15.71673	79.47102
O	-41.39356	-15.18914	80.58913
O	-40.38191	-17.32010	79.68954
O	-38.99887	-15.10230	79.55049
C	-41.46702	-14.28348	77.54673
O	-41.17508	-15.57895	78.11258
C	-42.46867	-14.46953	76.41578
O	-43.66928	-14.94692	77.01796
C	-42.67470	-13.18607	75.61368
S	-41.21905	-12.39787	74.98420
C	-43.90474	-12.66189	75.39224
S	-44.10938	-11.11051	74.58468
N	-48.16694	-16.01068	76.77600
C	-49.36669	-15.79430	76.32476
N	-50.43683	-16.54701	76.78782
N	-49.64038	-14.80782	75.42364
C	-48.67601	-13.90307	74.91843
O	-49.03806	-13.06923	74.08086

N	-46.32175	-13.23896	75.12208
C	-45.13614	-13.34739	75.94026
C	-44.77791	-14.83081	76.17061
N	-45.90306	-15.46867	76.79676
C	-47.35970	-14.11322	75.45343
C	-47.16570	-15.18665	76.33540
H	-45.76356	-16.35431	77.26950
H	-40.91231	-14.71467	81.28255
H	-39.54393	-17.70234	79.39080
H	-40.54101	-13.82977	77.16626
H	-42.06503	-15.25571	75.74136
H	-50.12191	-17.34954	77.32485
H	-50.58796	-14.62867	75.10447
H	-46.21741	-13.02494	74.12219
H	-45.36208	-12.94069	76.94768
H	-44.54234	-15.28514	75.18138
H	-51.14215	-16.79064	76.09790
H	-41.90979	-13.63153	78.31669

N	-38.96362	-13.36200	70.42782
C	-39.28489	-12.03155	70.92562
C	-38.54724	-10.98382	70.12218
O	-38.02842	-11.19756	69.04846
C	-38.96878	-11.92195	72.43375
S	-39.55664	-10.37098	73.23199
H	-37.88012	-11.97926	72.59570
H	-38.72317	-13.28602	69.43749
H	-40.35680	-11.75632	70.80505
H	-38.53523	-9.96624	70.58461
H	-39.41592	-12.78321	72.95224
H	-39.77385	-13.97455	70.50594
Mo	-41.99958	-10.60440	73.41536
O	-42.38311	-11.14705	71.83713
O	-46.90322	-12.70245	72.31293
H	-47.75782	-12.65119	72.78978
H	-46.62395	-11.77967	72.18598
S	-45.96799	-10.42355	70.04502

O	-42.23792	-8.92955	73.61215
C	-44.59481	-9.23495	69.87840
H	-43.75538	-9.52704	70.52656
H	-44.97526	-8.25277	70.19588
H	-44.25336	-9.16333	68.83264
C	-45.08182	-11.98792	69.73227
H	-45.74459	-12.78549	70.09570
H	-44.14856	-12.00659	70.31528
H	-44.86592	-12.12402	68.65995

Vibrational frequencies of the optimized products geometry

VIBRATIONAL FREQUENCIES

0: 0.00 cm**-1

1: 0.00 cm**-1

2: 0.00 cm**-1

3: 0.00 cm**-1

4: 0.00 cm**-1

5: 0.00 cm**-1

6: 4.83 cm**-1

7: 8.86 cm**-1

8: 11.54 cm**-1

9: 16.69 cm**-1

10: 17.78 cm**-1

11: 24.42 cm**-1

12: 29.27 cm**-1

13: 33.39 cm**-1

14: 35.98 cm**-1

15: 45.79 cm**-1

16: 48.99 cm**-1

17: 50.86 cm**-1

18: 61.56 cm**-1

19: 62.88 cm**-1

20: 73.01 cm**-1

21: 74.47 cm**-1

22: 78.01 cm**-1

23: 89.29 cm**-1

24: 96.89 cm**-1

25: 105.13 cm**-1

26: 107.41 cm**-1

27: 117.69 cm**-1

28: 129.84 cm**-1

29: 138.19 cm**-1

30: 146.91 cm**-1

31: 149.30 cm**-1

32: 157.00 cm**-1

33: 172.68 cm**-1

34: 176.51 cm**-1

35: 180.45 cm**-1

36: 183.58 cm**-1

37: 185.69 cm**-1

38: 197.68 cm**-1

39: 203.67 cm**-1

40: 212.22 cm**-1

41: 220.99 cm**-1

42: 223.04 cm**-1

43: 231.93 cm**-1

44: 234.62 cm**-1

45: 237.98 cm**-1

46: 239.70 cm**-1

47: 258.67 cm**-1

48: 270.02 cm**-1

49: 289.96 cm**-1

50: 297.25 cm**-1

51: 300.36 cm**-1

52: 303.41 cm**-1

53: 306.86 cm**-1

54: 322.30 cm**-1

55: 327.72 cm**-1

56: 337.69 cm**-1

57: 359.84 cm**-1

58: 368.68 cm**-1

59: 372.68 cm**-1

60: 376.22 cm**-1

61: 377.51 cm**-1

62: 394.57 cm**-1

63: 414.92 cm**-1

64: 416.81 cm**-1

65: 419.09 cm**-1

66: 423.57 cm**-1

67: 434.94 cm**-1

68: 438.10 cm**-1

69: 449.65 cm**-1

70: 481.90 cm**-1

71: 482.96 cm**-1

72: 504.17 cm**-1

73: 516.81 cm**-1

74: 549.34 cm**-1

75: 566.51 cm**-1

76: 579.47 cm**-1

77: 594.55 cm**-1

78: 601.34 cm**-1

79: 612.82 cm**-1

80: 636.04 cm**-1

81: 650.65 cm**-1

82: 667.08 cm**-1

83: 677.14 cm**-1

84: 685.02 cm**-1

85: 685.41 cm**-1

86: 708.62 cm**-1

87: 724.48 cm**-1

88: 734.09 cm**-1

89: 735.31 cm**-1

90: 746.97 cm**-1

91: 749.29 cm**-1

92: 768.95 cm**-1

93: 807.92 cm**-1

94: 818.59 cm**-1

95: 846.73 cm**-1

96: 869.95 cm**-1

97: 877.84 cm**-1

98: 901.22 cm**-1

99: 910.17 cm**-1

100: 923.19 cm**-1

101: 924.05 cm**-1

102: 945.49 cm**-1

103: 946.72 cm**-1

104: 959.83 cm**-1

105: 983.86 cm**-1

106: 995.60 cm**-1

107: 1008.97 cm**-1

108: 1011.94 cm**-1

109: 1028.27 cm**-1

110: 1040.11 cm**-1

111: 1042.22 cm**-1

112: 1052.64 cm**-1

113: 1054.90 cm**-1

114: 1056.57 cm**-1

115: 1074.44 cm**-1

116: 1085.78 cm**-1

117: 1120.27 cm**-1

118: 1121.34 cm**-1

119: 1125.06 cm**-1

120: 1142.01 cm**-1

121: 1158.57 cm**-1

122: 1175.12 cm**-1

123: 1191.03 cm**-1

124: 1196.01 cm**-1

125: 1206.83 cm**-1

126: 1216.74 cm**-1

127: 1237.52 cm**-1

128: 1255.74 cm**-1

129: 1267.11 cm**-1

130: 1282.97 cm**-1

131: 1295.32 cm**-1

132: 1305.05 cm**-1

133: 1306.41 cm**-1

134: 1315.28 cm**-1

135: 1324.05 cm**-1

136: 1333.42 cm**-1

137: 1339.36 cm**-1

138: 1342.41 cm**-1

139: 1352.89 cm**-1

140: 1366.82 cm**-1

141: 1381.72 cm**-1

142: 1382.37 cm**-1

143: 1406.95 cm**-1

144: 1410.63 cm**-1

145: 1431.03 cm**-1

146: 1437.70 cm**-1

147: 1449.37 cm**-1

148: 1451.19 cm**-1

149: 1466.73 cm**-1

150: 1469.96 cm**-1

151: 1475.15 cm**-1

152: 1508.97 cm**-1

153: 1516.75 cm**-1

154: 1551.14 cm**-1

155: 1596.04 cm**-1

156: 1600.25 cm**-1

157: 1623.70 cm**-1

158: 1631.97 cm**-1

159: 1642.37 cm**-1

160: 1682.85 cm**-1

161: 1753.22 cm**-1

162: 1819.93 cm**-1

163: 2917.94 cm**-1

164: 2936.18 cm**-1

165: 2944.92 cm**-1

166: 2949.85 cm**-1

167: 2961.41 cm**-1

168: 3019.94 cm**-1

169: 3022.15 cm**-1

170: 3050.00 cm**-1

171: 3059.78 cm**-1

172: 3109.70 cm**-1

173: 3118.59 cm**-1

174: 3124.99 cm**-1

175: 3137.43 cm**-1

176: 3148.72 cm**-1

177: 3156.81 cm**-1

178: 3377.15 cm**-1

179: 3478.81 cm**-1

180: 3543.66 cm**-1

181: 3572.14 cm**-1

182: 3584.13 cm**-1

183: 3594.88 cm**-1

184: 3624.12 cm**-1

185: 3652.74 cm**-1

186: 3753.33 cm**-1

187: 3825.97 cm**-1

188: 3827.55 cm**-1

Total SCF energy of the optimized products geometry

TOTAL SCF ENERGY

Total Energy : -3667.72762790 Eh -99803.94269 eV

A1. References

(1) Neese, F. The ORCA Program System. *Wiley Interdiscip. Rev. Comput. Mol. Sci.* **2012**, *2* (1), 73–78. https://doi.org/10.1002/wcms.81.

(2) Frisch, Æ.; Plata, R. E.; Singleton, D. A. Gaussian 09W Reference. *J. Am. Chem. Soc.* **2009**, *137*, 3811–3826.

(3) Fukui, K. A Formulation of the Reaction Coordinate. *J. Phys. Chem.* **1970**, *74* (23), 4161–4163.

(4) Fukui, K. The Path of Chemical Reactions -The IRC Approach. *Acc. Chem. Res.* **1981**, *14* (12). https://doi.org/10.1021/cen-v046n004.p005.